12-2017

A New Multiscale Modeling Framework for Lithium-Ion Battery Dynamics: Theory, Experiments, and Comparative Study with the Doyle-Fuller-Newman Model

Harikesh Arunachalam
Clemson University

A New Multiscale Modeling Framework for Lithium-Ion Battery Dynamics: Theory, Experiments, and Comparative Study with the Doyle-Fuller-Newman Model

---

A Dissertation
Presented to
the Graduate School of
Clemson University

In Partial Fulfillment
of the Requirements for the Degree
Doctor of Philosophy
Automotive Engineering

---

by
Harikesh Arunachalam
December 2017

Accepted by:
Dr. Simona Onori, Committee Chair
Dr. Ilenia Battiato
Dr. Mark Hoffman
Dr. Robert Prucka
Dr. Fadi Abu-Farha

Abstract

Technological advancements and globalization in recent decades have largely been responsible for the ever-increasing energy and power demands across different industrial sectors. This has led to an extensive use of fossil fuel based resources such as gasoline and diesel, especially in the transportation industry [1]. The consequences of this utilization are excessive emission of greenhouse gases and degradation of air quality, which have raised significant environmental concerns. Added to this, concerns over the eventual depletion of fossil fuels has accelerated the exploration and development of new energy sources. At the same time, increasingly stringent regulations have been imposed to enhance the fuel efficiency and minimize emissions in automobiles. Efforts to meet current and future regulation targets have led to the development of new technologies, some of which are: a) vehicle electrification [2], b) gasoline direct injection technology [3], c) variable valve timing [4], d) advanced exhaust gas recirculation [5], and e) selective catalytic reduction for NO_x [6]. On the energy front, wind and solar technologies have been vastly explored [7], but these technologies are time-dependent and intermittent in nature and must be supplemented by energy storage devices. Lithium-ion batteries have been considered the most preferred technology for grid energy storage and electrified transportation because of their higher energy and power densities, better efficiency, and longer lifespan in comparison with other energy storage devices such as lead acid, nickel metal hydride, and nickel cadmium [8].

Lithium-ion batteries are the most dominant technology today in small scale applications such as portable phones and computers [9]. However, their wide-scale adoption in automotive and grid energy storage applications has been hampered by concerns associated with battery life, safety, and reliability. A lack of comprehensive understanding of battery behavior across different environments and operating conditions make it challenging to extract their best performance. Currently, significant trade-off are being made to optimize battery performance, such as over-sizing and under-utilization in automotive applications. While sensors are used to evaluate battery performance and regulate their operation, their fundamental limitation

lies in the inability to measure battery internal states such as state-of-charge (SoC) or state-of-health (SoH). The aforementioned issues with lithium-ion batteries can addressed to a large extent with the help of mathematical modeling. They play an important role in the design and utilization of batteries in an efficient manner with existing technologies, because of their ability to predict battery behavior with minimal expenditure of time and materials [10]. While empirical mathematical models are computationally efficient, they rely on a significant amount of experimental data and calibration effort to predict future battery behavior. In addition, such models do not consider the underlying physicochemical transport processes and hence cannot predict battery degradation. Moreover, the knowledge acquired from such models cannot be generalized across different battery chemistry and geometry. This elucidates the need for fundamental physics-based mathematical models to aid in the development of advanced control strategies through model-based control and virtual sensor deployment. Such models can capture the underlying transport phenomena across various length and time scales, and enhance performance and longevity of batteries while ensuring safe operation.

The overarching aim of this dissertation is to present a multiscale modeling approach that captures the behavior of such devices with high fidelity, starting from fundamental principles. The application of this modeling approach is focused on porous lithium-ion batteries. The major outcome of this work is to facilitate the development of advanced and comprehensive battery management systems by: a) developing a high fidelity multiscale electrochemical modeling framework for lithium-ion batteries, b) investigating the temperature-influenced and aging-influenced multiscale dynamics for different battery chemistry and operating conditions, c) formulating a methodology to analytically determine effective ionic transport properties using the electrode microstructure, and d) numerical simulation of the developed physics-based model and comparison analysis with the conventionally used Doyle-Fuller-Newman (DFN) electrochemical model.

The new multiscale model presented in this dissertation has been derived using a rigorous homogenization approach which uses asymptotic expansions of variables to determine the macroscopic formulation of pore-scale governing transport equations. The conditions that allow successful upscaling from pore-to-macro scales are schematically represented using 2-D electrode and electrolyte phase diagrams. These phase diagrams are used to assess the predictability of macroscale models for different electrode chemistry and battery operating conditions. The effective transport coefficients of the homogenized model are determined by resolving a unit cell closure variable problem in the electrode microstructure, instead of conventionally employed empirical formulations. The equations of the developed full order homogenized multiscale (FHM) model are implemented and resolved using the finite element software COMSOL Multiphysics®. Numerical simulations are presented to demonstrate the enhanced predictability of the FHM against the traditionally

used DFN model, particularly at higher temperatures of battery operation. Model parameter identification is performed by co-simulation studies involving COMSOL Multiphysics®and MATLAB®software using the Particle Swarm Optimization (PSO) technique. The parameter identification studies are performed using data from laboratory experiments conducted on 18650 cylindrical lithium-ion cells of nickel-manganese-cobalt oxide (NMC) cathode chemistry.

Acknowledgments

I express my sincere gratitude to my advisor and mentor, Dr. Simona Onori, for offering me a position in her research group despite the fact that I formerly specialized outside her fields of interest. She instilled confidence in my abilities and provided resources and complete support to pursue challenging research on batteries and gasoline particulate filters. Her feedback and suggestions have significantly improved my technical writing and critical thinking skills over the years. Because of her guidance and support, I was able to secure the Student Best Paper Award at the 2017 IEEE Conference on Control Technology and Applications. She has been very patient with me, especially the past year as I worked towards the completion of my dissertation. Looking back at the years that have passed, I consider myself very fortunate to have an advisor like Dr. Onori who made me a productive person. She has set an excellent example as a diligent and successful academician, and I am very proud to have witnessed some of her professional achievements during my education at Clemson University.

I am very grateful to Dr. Ilenia Battiato for serving as my co-advisor over the entire course of my Ph.D. Her technical insights and suggestions have been very helpful when I have faced hurdles during research. I will always remember her guidance and meticulous feedback during the initial phase of my Ph.D., which involved highly advanced and intimidating mathematical derivations. I would also like to thank my Ph.D. committee members, Dr. Mark Hoffman, Dr. Robert Prucka, and Dr. Fadi Abu-Farha for agreeing to serve as my Ph.D. committee members and for their suggestions and insightful comments that enhanced my dissertation work. Dr. Hoffman has also mentored me over the past year with my project work and research associated with gasoline particulate filters. Without his valuable suggestions and technical feedback, it would have been very difficult to complete my designated tasks in a timely and efficient manner.

This journey is not complete without the support of my friends and colleagues. Special thanks to Anirudh Allam for helping me with course work, experiments, simulations, technical articles, and for all our discussions over the last four years. In no specific order, I'd like to sincerely thank my friends in

Greenville for giving me strength during rough days, sharing my joyous occasions and accomplishments, and making the past four years very memorable: Shreyas Naik, Satadru Dey, Jasprit Singh Gill, Kousaalya Bakthavatchalam, Sai Aditya Pradeep, Rohit Koli, Abhilash Pechetty, and Rakesh Iyer. I can never forget my friends and visiting scholars from Italy: Stefano Marelli, Carlo Taborelli, Stefano Sabatini, Simone Gelmini, and Gabriele Pozzato. Getting to know you all was one of the best things that happened to me at Clemson. Your moral support and encouragement have been invaluable. This list is endless, and I acknowledge the support of all my previous mentors and colleagues.

No words would suffice to express my indebtedness to my parents, Dr. Arunachalam Jayaraman and Mrs. Lalitha Srinivasan, my younger sister, Prasiddha Arunachalam, and my relatives. I owe all my achievements, including this Ph.D., to your prayers, sacrifice, love, and understanding. You have been my biggest driving force and motivation to embrace bigger challenges. With you by my side, I will continue to work harder and aim for greater heights. I sincerely thank the Almighty for the successful completion of this dissertation.

Table of Contents

List of Tables

List of Figures

List of Abbreviations

BACh	Battery Aging and Characterization
BMS	Battery Management System
CC	Constant-Current
CD	Charge-Depleting
CPU	Central Processing Unit
CS	Charge-Sustaining
CV	Constant-Voltage
DFN	Doyle-Fuller-Newman
eSPM	enhanced Single Particle Model
ECM	Equivalent Circuit Model
EKF	Extended Kalman Filter
FEV	Full Electric Vehicle
FHM	Full-order Homogenized Macroscale
HEV	Hybrid Electric Vehicle
HPPC	Hybrid Pulse Power Characterization
LCO	Lithium Cobalt Oxide
LFP	Lithium Ferrous Phosphate
LMO	Lithium Manganese Dioxide
LTO	Lithium Titanate

NCA	Nickel Cobalt Aluminum Oxide
NMC	Nickel Manganese Cobalt Oxide
OCP	Open Circuit Potential
P2D	Pseudo Two-Dimensional
PDE	Partial Differential Equation
PHEV	Plug-in Hybrid Electric Vehicle
PNP	Poisson-Nernst-Planck
PSO	Particle Swarm Optimization
REV	Representative Elementary Volume
RMS	Root Mean Square
SEI	Solid-Electrolyte-Interface
SoC	State-of-Charge
SoH	State-of-Health
SPM	Single Particle Model

Nomenclature

α $[-]$	Dimensionless exponent that is a function of the transport parameter Pe_e
$\langle \mathcal{A} \rangle$	Local average of a variable $\mathcal{A}$ in the porous medium
$\hat{\mathcal{B}}^{\varepsilon}$	Representation of the electrolyte solution phase of the porous matrix
β $[-]$	Dimensionless exponent that is a function of the transport parameter Da_e
$\boldsymbol{\chi}^{e}$ $[-]$	Electrolyte closure variable that is resolved to determine effective transport properties
$\boldsymbol{\chi}^{s}$ $[-]$	Electrode closure variable that is resolved to determine effective transport properties
γ $[-]$	Dimensionless exponent that is a function of the transport parameter Da_s
$\hat{\Gamma}^{\varepsilon}$	Representation of the surface boundary separating the active material and the electrolyte phases
∇	Gradient operator
δ $[-]$	Dimensionless exponent that is a function of the transport parameter Pe_s
δ_{SEI} [m]	Thickness of the SEI layer
η_e $[-]$	Electrolyte volume fraction
η_f $[-]$	Binder material volume fraction
η_s $[-]$	Active material volume fraction
ε $[-]$	Scale-separation parameter, defined as the ratio of ℓ and L
f $\left[\mathrm{s}^{-1}\right]$	Frequency of data acquisition using the Arbin BT-2000 tester
$f_{\pm}$ $[-]$	Activity coefficient
$\mathcal{K}^{\star}$ $[-]$	Dimensionless effective reaction rate constant
$\hat{\Omega}$	Representation of the porous matrix of a battery electrode

$\bar{\phi}_s$ [V]	Averaged electrostatic potential in the active material phase of an electrode
$\bar{\phi}_e$ [V]	Averaged electrostatic potential in the electrolyte phase
$\hat{\phi}_\varepsilon^e$ [V]	Electrostatic potential in the electrolyte phase
$\hat{\phi}_\varepsilon^s$ [V]	Electrostatic potential in the active material phase
$\hat{\mathcal{S}}^\varepsilon$	Representation of the active material phase of the porous matrix
ρ_{SEI} [kg/m^3]	Density of the SEI layer
τ_{r} $[-]$	Dimensionless reaction time variable
τ_{me} $[-]$	Dimensionless electromigration time variable
τ_{ms} $[-]$	Dimensionless active material conduction time variable
θ	Representation of the vector of identification parameters
$\hat{Y}$	Representation of the spatially periodic unit cells in a battery electrode
a_j [m^{-1}]	Electroactive surface area per unit volume of an electrode
A_{cell} [m^2]	Cross-sectional area of the electrode in a cell
$brugg$ $[-]$	Bruggeman exponent used to calculate the effective ionic properties for the DFN model
$c_{e,init}$ $\left[\mathrm{molm}^{-3}\right]$	Initial concentration of lithium in the electrolyte phase
c_s $\left[\mathrm{molm}^{-3}\right]$	Pore-scale lithium concentration in the active particles of an electrode
$c_{s,n,max}$ $\left[\mathrm{molm}^{-3}\right]$	Maximum anode lithium storage concentration
$c_{s,p,max}$ $\left[\mathrm{molm}^{-3}\right]$	Maximum cathode lithium storage concentration
$c_{s,surf,n}$ $\left[\mathrm{molm}^{-3}\right]$	Lithium concentration at the surface of an anode spherical active particle
$c_{s,surf,p}$ $\left[\mathrm{molm}^{-3}\right]$	Lithium concentration at the surface of a cathode spherical active particle
$\bar{c}_e$ $\left[\mathrm{molm}^{-3}\right]$	Averaged lithium-ion concentration in the electrolyte phase
$\bar{c}_s$ $\left[\mathrm{molm}^{-3}\right]$	Averaged concentration of lithium in the active material phase on an electrode
$\hat{c}_\varepsilon^e$ $\left[\mathrm{molm}^{-3}\right]$	Concentration of lithium ions in the electrolyte phase
$\hat{c}_\varepsilon^s$ $\left[\mathrm{molm}^{-3}\right]$	Concentration of lithium ions in the active material phase
$\hat{c}_{\mathrm{max}}^s$ $\left[\mathrm{molm}^{-3}\right]$	Maximum concentration of lithium that can be stored in the active materials
Da_e $[-]$	Damköhler number, defined as the ratio of electrolyte diffusion to reaction time scales
Da_s $[-]$	Damköhler number, defined as the ratio of electrode diffusion to reaction time scales

D^e $\left[\mathrm{m^2 s^{-1}}\right]$	Characteristic value of the pore-scale electrolyte interdiffusion tensor
D^e_{ag} $\left[\mathrm{m^2 s^{-1}}\right]$	Pore-scale electrolyte diffusion that is influenced by aging
D^{eff}_e $\left[\mathrm{m^2 s^{-1}}\right]$	Effective electrolyte diffusion coefficient
D^s $\left[\mathrm{m^2 s^{-1}}\right]$	Characteristic value of the pore-scale active material interdiffusion tensor
D^{eff}_s $\left[\mathrm{m^2 s^{-1}}\right]$	Effective electrode diffusion coefficient
$\hat{\mathbf{D}}^e$ $\left[\mathrm{m^2 s^{-1}}\right]$	Interdiffusion tensor in the electrolyte phase
$\mathbf{D}^{eff}_e$ $\left[\mathrm{m^2 s^{-1}}\right]$	Effective electrolyte diffusion tensor
$\hat{\mathbf{D}}^s$ $\left[\mathrm{m^2 s^{-1}}\right]$	Interdiffusion tensor in the active material phase
Ea_r $\left[\mathrm{Jmol^{-1}}\right]$	Electrode reaction rate activation energy
F $\left[\mathrm{Vs\Omega^{-1}mol^{-1}}\right]$	Faraday constant
i_s [A/m^2]	Side-reaction current density
I_{app} [A]	Applied current
$\mathbf{I}$	Identity matrix
j	This suffix represents a property of the anode n, the separator s, or the cathode p
J	Cost function
J_{Li} [A/m^3]	Intercalation current density
k $\left[\mathrm{Vm\Omega^{-1}mol^{-1}}\right]$	Electrochemical reaction rate constant that describes the kinetics of lithium-ion transfer
K^e $\left[\mathrm{m^2 s^{-1}}\right]$	Characteristic value of the electrolyte conductivity tensor
K^e_{ag} $\left[\Omega^{-1}\mathrm{m^{-1}}\right]$	Pore-scale electrolyte conductivity that is influenced by aging
K^{eff}_e $\left[\Omega^{-1}\mathrm{m^{-1}}\right]$	Effective electrolyte conductivity coefficient
K^s $\left[\mathrm{m^2 s^{-1}}\right]$	Characteristic value of the active material conductivity tensor
$\hat{\mathbf{K}}^e$ $\left[\Omega^{-1}\mathrm{m^{-1}}\right]$	Electric conductivity tensor in the electrolyte phase
$\mathbf{K}^{eff}_e$ $\left[\Omega^{-1}\mathrm{m^{-1}}\right]$	Effective electrolyte conductivity tensor
$\hat{\mathbf{K}}^s$ $\left[\Omega^{-1}\mathrm{m^{-1}}\right]$	Electric conductivity tensor in the active material phase
ℓ [m]	Characteristic microscopic length scale
L [m]	Characteristic macroscopic length scale

L_{cell} [m]	Cumulative sum of the thickness of the anode, separator, and cathode
L_{neg} [m]	Thickness of the anode
L_{pos} [m]	Thickness of the cathode
L_{sep} [m]	Thickness of the separator
M_{SEI} [kg/mol]	Molar mass of the SEI layer
$\mathbf{n}_e$ $[-]$	Outward unit normal vector to $\hat{\Gamma}^{\varepsilon}$ pointing from the electrolyte towards the active particle
$\mathbf{n}_s$ $[-]$	Outward unit normal vector to $\hat{\Gamma}^{\varepsilon}$ pointing from the active particle towards the electrolyte
N $[-]$	Total number of data samples
Pe_e $[-]$	Electric Péclet number, defined as the ratio of electrolyte diffusion to electromigration time scales
Pe_s $[-]$	Electric Péclet number, defined as the ratio of electrode diffusion to conduction time scales
Q_{cell} [Ah]	Energy capacity of a lithium-ion cell
r [m]	Radial coordinate
R $\left[\text{Jmol}^{-1}\text{K}^{-1}\right]$	Universal gas constant
R_c $[\Omega]$	Contact resistance at the current collectors
R_s [m]	Radius of the active particle in an electrode
S_n [m^2]	Electroactive surface area of an electrode
t_+ $[-]$	Transference number
$\hat{t}$ [s]	Time variable
$\hat{t}_{D^e}$ [s]	Electrolyte diffusion time scale
$\hat{t}_{D^s}$ [s]	Active material diffusion time scale
$\hat{t}_{M^e}$ [s]	Electrolyte electromigration time scale
$\hat{t}_{M^s}$ [s]	Active material conduction time scale
$\hat{t}_R$ [s]	Reaction time scale
T [K]	Temperature

x [m]	Cartesian coordinate
$x_{0\%}$ $[-]$	Stoichiometric coefficient of an electrode at 0% SoC
$x_{100\%}$ $[-]$	Stoichiometric coefficient of an electrode at 100% SoC
$\bar{x}$ $[-]$	Normalized Cartesian coordinate
$\hat{\mathbf{x}}$ [m]	Spatial variable
$\mathbf{x}$ $[-]$	Dimensionless spatial variable
$\hat{U}$ [V]	Electrode open circuit potential
V_{exp} [V]	Experimentally measured cell voltage response
V_{mod} [V]	Model-predicted cell voltage response
$x_{n,init}$ $[-]$	Initial stoichiometric coefficient of the anode
$x_{p,init}$ $[-]$	Initial stoichiometric coefficient of the cathode
$\mathbf{y}$ $[-]$	Dimensionless fast space variable
z $[-]$	Valence number

Chapter 1

Introduction

1.1 Motivation

The transportation sector has witnessed many technological advancements in recent years to enhance fuel efficiency and reduce vehicular emissions [2–6, 21]. These have been initiated by stringent fuel economy and emissions regulations that stem from increasing concerns over greenhouse gas emissions, depleting air quality, and the eventual depletion of fossil based resources [1]. Among these technologies, electrification of the vehicle powertrain has been widely implemented in the automotive industry. Lithium-ion batteries, electrochemical energy storage devices, have improved in energy and power density from research and development efforts [22, 23], and the most preferred technology today for electric and hybrid propulsion systems. The ragone plot in Fig. 1.1 depicts the enhanced abilities of lithium-ion batteries in comparison with energy storage technologies such as super capacitors, lead-acid batteries, nickel-cadmium batteries, and nickel metal hydride batteries. This makes lithium-ion technology ideal for consumer electronics, automotive, and grid energy storage sectors [8]. The global energy demand for lithium-ion technology is forecasted to double to 124 GWh in the year 2020 from 61 GWh in the year 2015 [24].

From a material perspective, lithium-ion technology has begun to reach its theoretical energy limits [25]. Yet, growth of the global electric vehicle market has been slower than initially predicted in the beginning of this decade [26]. This is attributed primarily to the shortcomings of the current state of battery technology. Lithium-ion battery packs used in automotive applications today are oversized and underutilized to meet vehicle life expectations [27]. This conservative strategy to ensure that batteries work through their designed lifecycles has resulted in suboptimal performance due to larger, heavier, and expensive battery sys-

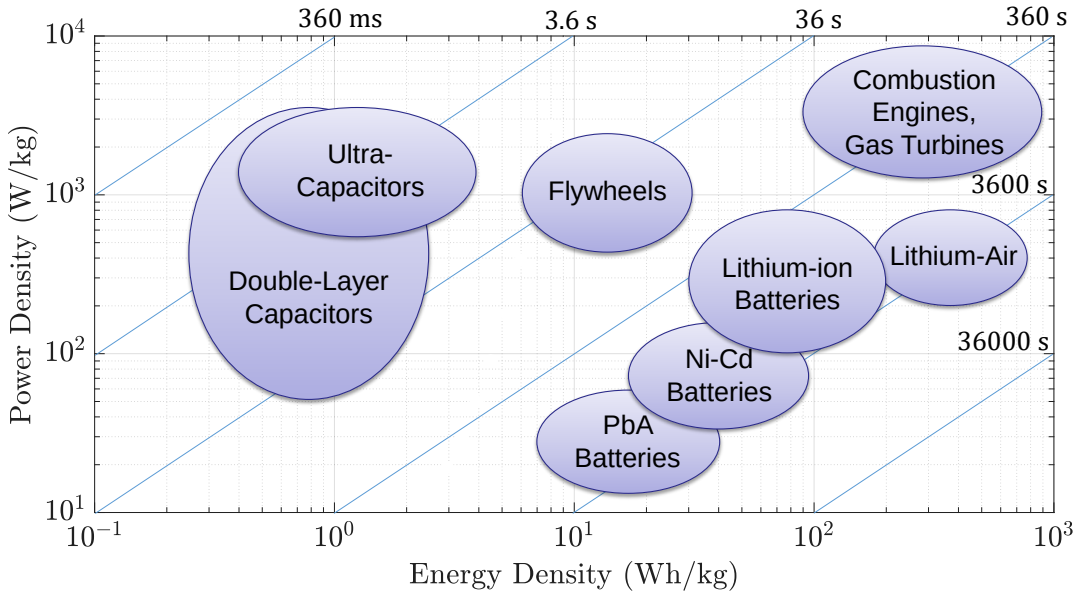

Figure 1.1: Ragone plot comparing the energy and power densities of different energy storage and vehicle propulsion technologies. The plot is developed based on information acquired from [18, 19].

tems. Adding to that, safety concerns and performance degradation have become the biggest hindrance for the full market penetration of batteries for vehicle electrification [28]. The most critical factor that has led to the conservative use of lithium-ion batteries is a lack of comprehensive understanding of their behavior across different operating environments. The transition from small scale electronic applications to large scale vehicular applications with much higher power and energy demands has been hampered by the relative lack of understanding of scaling effects, which impact battery performance and electrochemical and mechanical responses [29].

Efficient, safe, and optimal utilization of batteries for large-scale applications is achievable through the use of a sophisticated battery management system (BMS). A BMS is responsible for the safe and reliable operation of batteries. Its functions involve battery operation within specified voltage and current limits, prevention of over-charging, over-discharging, and over-heating, cell balancing, battery safety, and the prevention of battery abuse, fast degradation, and thermal runaway [30]. To optimize battery performance and prolong useful life using a BMS, accurate estimation of battery state-of-charge (SoC) and prediction of the battery state-of-health (SoH) [31] is required.

Battery internal states such as SoC and SoH cannot be measured directly on an vehicle. This reality is currently being addressed through the use of equivalent circuit models (ECMs) in BMSs that incorporate resistors and capacitor elements. ECMs are currently favored for real-time BMS applications because of

their computational efficiency. However, these models rely on a significant amount of experimental data and calibration effort to predict battery behavior [10]. Battery parameters are subject to change under different operating conditions and aging, and a BMS must account for these changes. ECMs do not account for the underlying transport phenomena, and hence cannot account for battery aging. In addition, the knowledge acquired from ECMs cannot be generalized for different battery chemistry and cell formats. The limitations of ECMs elucidate the need for physics-based models, which can predict transport phenomena in battery systems that span multiple length and time-scales.

Accurate prediction of battery behavior is dependent on how accurately the mathematical equations describe lithium transport, and how precisely the corresponding model parameters are measured, estimated, or identified [32, 33]. Advanced electrochemical modeling and estimation of battery internal states are vital to push batteries to operate at their physically permissible limits [34]. Simplified and reduced-order models that retain the accuracy of the original high fidelity models will minimize CPU run time in vehicle on-board applications, and can faciliate optimal BMS utilization in real-time [35, 36].

1.2 Background

The development of rechargeable lithium-ion batteries is widely credited to the efforts of Dr. John B. Goodenough and his colleagues at the University of Texas at Austin [37]. The first commercially available lithium-ion cell was composed of lithium cobalt oxide cathode and graphite anode. It was assembled by Yoshino of the Asahi Kasei Corporation and commercialized by SONY Corporation in the year 1990 for applications in portable phones and camcorders [38]. Gradually, their ability to provide a high energy and power densities led to the expansion of their applications to other portable electronic devices such as laptop computers, and power tool equipment [39]. Today, lithium-ion batteries are used as the primary energy storage device for electrified propulsion in vehicles developed by automotive manufacturers such as Tesla, General Motors, Toyota, Honda, etc. [40].

Figure 1.2 shows different commercially available lithium-ion cells of different formats that are utilized in a wide range of applications ranging from portable electronics to automobiles. A lithium-ion cell is defined as the smallest independent entity with all the functional capabilities of an energy storage device. A battery is defined as a combination of different cells of the same type and is designed for a targeted application. It can be as small as a group of 2 cells, or a module fabricated by combing several cells in series and/or parallel configurations, or an entire pack that is assembled using many module components. Regardless of the

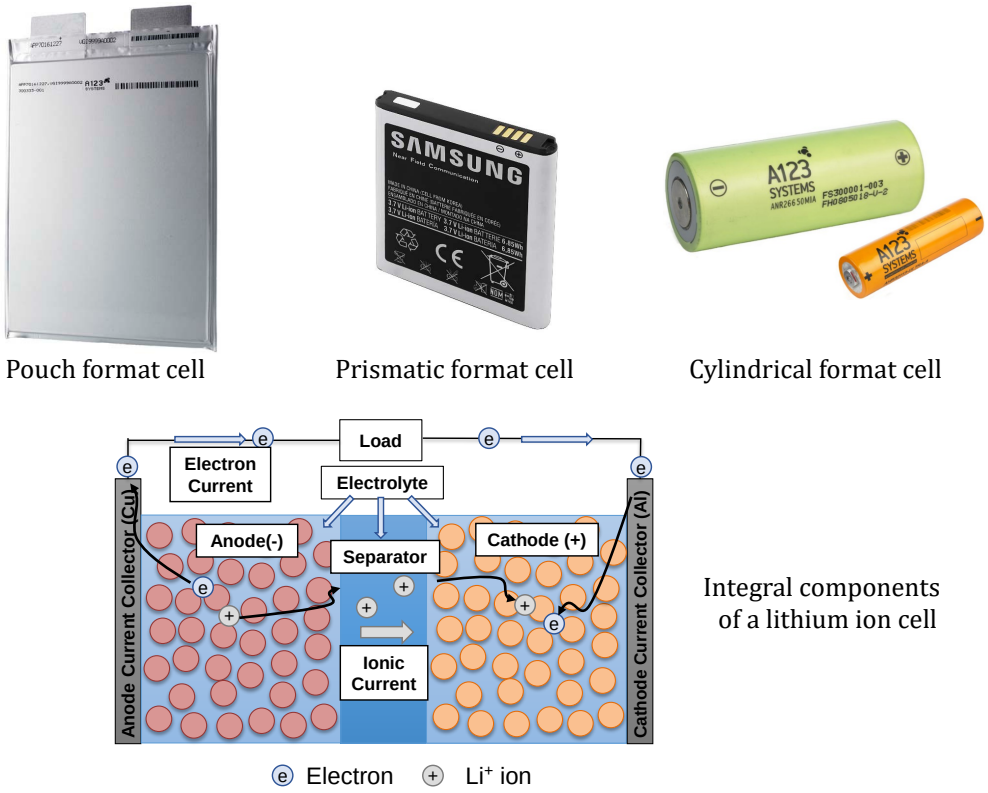

Figure 1.2: Commercially available lithium-ion cell formats for different applications, and a schematic representation of the integral cell components. Source of images: A123 Systems and Samsung Group.

format and chemistry, a lithium-ion cell is composed of four integral components: anode, cathode, separator, and electrolyte. The anode and cathode are the battery electrodes and are porous by design. They are primarily composed of layered structure materials (active particles) to store lithium. The porous matrix of these electrodes is composed of active particles surrounded by a concentrated electrolyte solution that includes binder materials to enhance conductivity. The anode and the cathode exist at different potentials. A separator is used as an electrical insulator between the electrodes to prevent internal short-circuit. It is made up of polymeric substrates, and is porous by design to accommodate the electrolyte solution. It allows only lithium-ions to be transported and ensures that electron transport takes place across the external circuit of the cell. The electrolyte solution is composed of organic solvents such as ethylene carbonate and dimethyl carbonate in specified proportions along with conducting salts such as lithium hexafluorophosphate. The electrolyte solution is present throughout the medium and enables lithium-ion transfer during battery operation.

When the two terminals of a lithium-ion battery are connected either to a load that draws current or a power supply that provides current, electron transport is initiated between the terminals of the battery

through the external circuit. A copper foil is typically utilized as the current collector at the anode and is connected to one end of this terminal. An aluminum foil serves as the current collector at the cathode and is connected to one end of this terminal. Lithium-ions are transferred from the anode to the cathode during discharge, and the reverse process occurs during charge. Some of the most prominent electrode technologies for automotive applications are lithium graphite (LiC_6) and lithium titanate ($Li_4Ti_5O_{12}$) for the anode [41], and lithium nickel cobalt aluminum oxide (NCA), lithium nickel manganese cobalt oxide (NMC), lithium manganese dioxide (LMO), and lithium ferrous phosphate (LFP) for the cathode [30].

1.2.1 Literature review: lithium-ion battery modeling

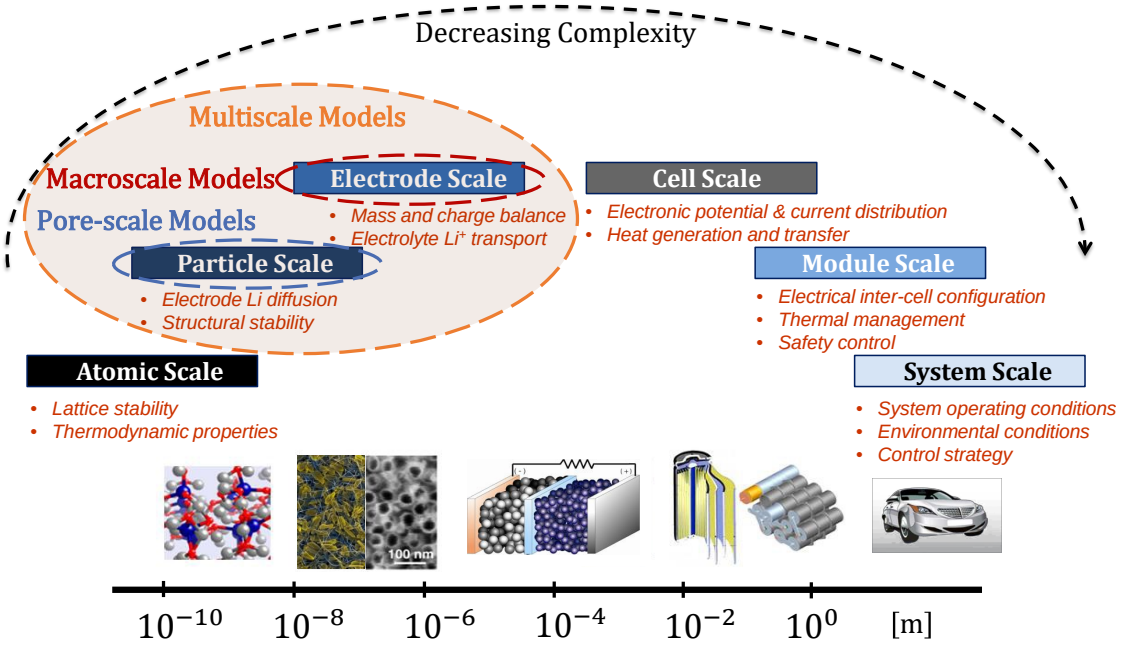

Figure 1.3: Classification of mathematical models to capture transport processes in lithium-ion batteries that span multiple length scales. This contents of this image have been obtained from [20].

Lithium-ion batteries involve highly non-linear transport processes, and exhibit physicochemical properties at multiple length scales, ranging from the *atomic* level to the *system* level in decreasing order of complexities [20], as depicted in Fig. 1.3. As such, ion transport can also be modeled on a multiplicity of length scales. *Atomic* scale models apply monte carlo simulations [42] and density functional theory [43] to investigate how crystal structure and particle size affect lithium transport. *Particle* scale models apply coupled stress-diffusion models [44] and finite element analysis [45] to determine the volume change and stress induced due to lithium transport and particle-particle interactions. At this *pore* scale, lithium transport in the

electrodes and the interface kinetics can be modeled using robust first principles of mass and charge conservations equations [46, 47] and 3-D finite element modeling techniques [48]. *Electrode* scale models [49, 50] describe lithium transport using averaged mass and charge transport equations, and are developed from pore-scale models using upscaling techniques [51, 52]. *Cell* scale [53, 54] and *module* scale models [55, 56] incorporate the effect of thermal dynamics by combining averaged mass and charge transport equations with a global energy balance equation. They are useful in examining the electrical behavior and heat evolution in cells and battery modules for various charging and discharging conditions. *Multiscale* models incorporate transport processes and effects that span two or more length scales. The multi-scale multi-domain model developed by National Renewable Energy Laboratory [57] couples transport dynamics at the *particle*, *electrode*, and *cell* scales to evaluate the electrical and thermal properties of different cell formats.

At the *system* level, equivalent circuit models (ECMs) [58–61] and reduced-order models [62–65] developed from *particle* and *electrode* scale models are used to characterize single cell and battery module/pack behavior, and develop model-based strategies for identification, estimation, control, and diagnostic purposes [66–70]. The simplicity of ECMs makes them conducive for real-time BMS applications. They have also been used for the prediction of thermal dynamics. Electrical-thermal models have been developed for model parameter identification and estimation of battery SoC in cylindrical lithium-ion cells [71, 72]. Adaptive observers have been designed to estimate the core temperature in cylindrical LFP cells for health monitoring purposes [73, 74].

Analytical models have been developed for the prediction of degradation in lithium-ion batteries [75], and data from the experimental characterization of lithium-ion cells have ben used for the estimation of remaining useful life for hybrid electric vehicle (HEV) applications [76]. Other studies have combined aging models with ECMs to predict the cycle life of battery cells [77], and conduct offline battery model parameter estimation studies as a function of the battery SoH [69]. Semi-empirical models have been proposed to devise methodologies for battery health management and strategies to prolong battery useful life while minimizing energy consumption [78, 79]. A capacity degradation model was developed in [80] and validated using aging experiments conducted on LFP cylindrical cells. The model can be used to assess the state of the health of the battery and predict its end-of-life based on the current rates of charge/discharge and the SoC range of operation.

Despite their computational efficiency, the limitations of capturing thermal and aging dynamics using ECMs and other empirical approaches is that they require an extensive amount of experimental data and calibration effort to predict the future behavior of battery systems. Such models are based on fitting

data for specific battery operating conditions, and cannot be extrapolated for other conditions of battery use. In addition, they do not consider any of the underlying physicochemical process during battery operation, hence their accuracy in their predictability over the duration of battery life remains an open ended question. On the other hand, physics-based models at the *particle* and *electrode* scales provide higher accuracy due to their ability to incorporate electrochemical kinetics along with other transport phenomena such as diffusion and migration. Mathematicaly simplification and reformulation of such full order models have led to the development of the single particle model (SPM) and the enhanced single particle model (eSPM).

The SPM captures lithium diffusion at the *particle* scale, and was first developed to study the behavior of metal hydride batteries [81] and later extended for lithium-ion battery systems [82, 83]. The SPM assumes each electrode to be represented by a single spherical active particle with uniform current density and infinite electrode conductivity. Concentration and potential gradients in the electrolyte are considered to be uniform and time-invariant. As a result, only the electrode concentration dynamic equations are resolved to predict the battery response. However, these models are applicable for only low current rates of charge or discharge because the underlying assumptions of the model are violated at high current rates of operation [84]. To address some of the limitations of the SPM, the enhanced SPM was developed by incorporating the electrolyte dynamic equations in addition to the SPM model equations [85, 86].

Reduced-order models have been developed using the SPM [87] and the eSPM [88] for the estimation of battery SoC. Model-based techniques have been implemented to estimate battery SoC based on the extended Kalman filter (EKF) and using the equations of the SPM [89, 90] and other reduced-order models [91, 92]. Experimental validations of model-based SoC estimation techniques based on the EKF and using the equations of a reduced-order electrochemical model are presented in [93, 94]. Coupled electrochemical-thermal models have been developed based on the equations of the SPM for the design of non-linear observers to improve battery SoC estimation [95, 96]. Reduced-order models have also been developed from the SPM for studying long term battery degradation [97] and characterizing capacity fading dynamics [98]. Other electrochemical models to study the growth of the solid-electrolyte-interface (SEI) layer in the anode are presented in [99, 100].

Prior to the development of computer-aided engineering tools [101] for predicting battery dynamics at very small length scales, research was focused at addressing *system* level issues such as [84]: a) underutilization, b) capacity fading, c) lower energy density, and d) thermal runaway. Lithium-ion battery application gradually expanded from portable electronics to automotive applications, motivated by emerging mobility options to reduce dependency on oil-based resources. New electrode chemistry were developed for applications

based on energy and power demand, along with the fabrication of new cell formats to optimize cost, performance, and longevity. These factors enabled researchers to understand that lithium-ion battery performance is highly dependent on chemistry, temperature, current rates of charge/discharge, and the internal states [102]. Advancements in simulation tools and imaging techniques to study the electrode microstructure [103–106] helped in the identification and different battery degradation and aging mechanisms, which was not a concern prior to these developments. The conservative use of batteries to meet lifecycle targets in large scale applications undermines the impact of battery degradation and aging. While nominal temperature, current rate, and SoC range of operation are not detrimental to battery performance in the short term, exposure to high current rates and temperature of operation leads to irreversible battery damage over time. In HEVs, aging is a serious concern when battery size and capacity is compromised for vehicle cost and weight.

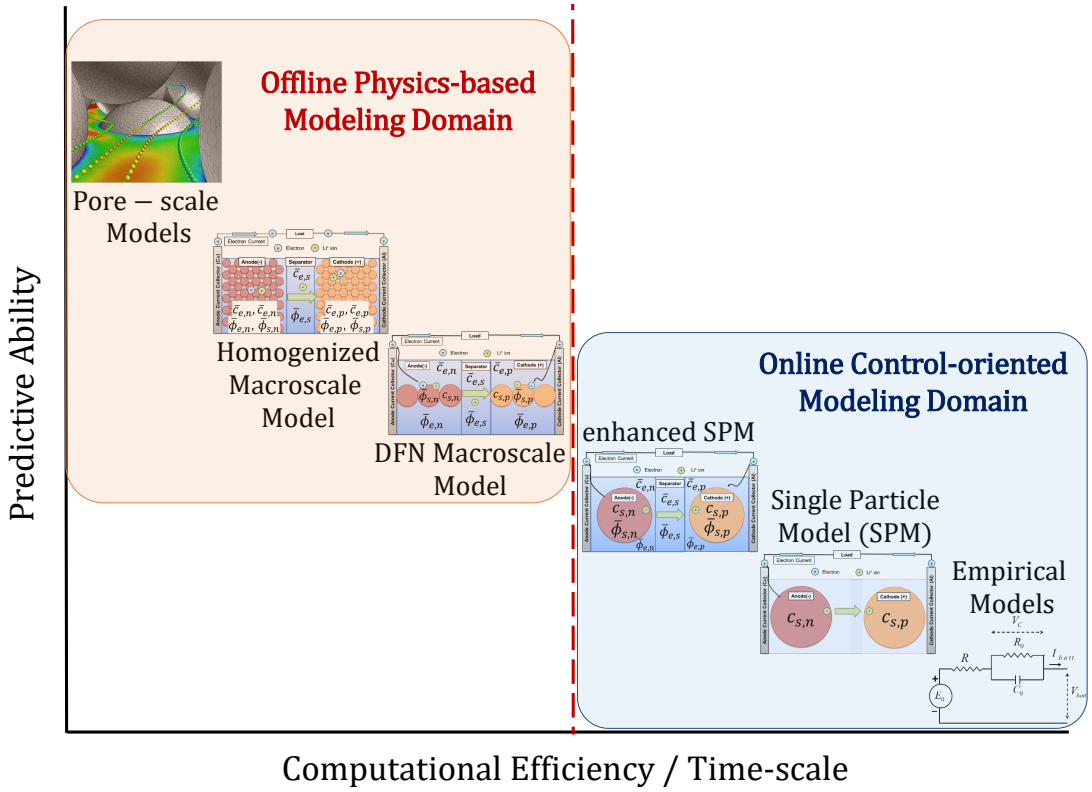

Figure 1.4: Predictability of different models to characterize lithium-ion battery behavior at different length scales. There is a need to estalish better communication between the two modeling domains and bring more physics into the current control and estimation efforts.

Figure 1.4 represents the predictability of different mathematical models for lithium-ion batteries. ECMs, SPM, and eSPM models are the most commonly used tools to develop model-based control strategies for online estimation applications. On the other hand, pore-scale and macroscale models with higher

predictability have significant numerical complexity and need to be resolved using offline approaches. One of the advantages of using physics-based models over ECMs is reduced calibration efforts to evaluate and characterize cell behavior using experiments. From a control standpoint, the limitations of the SPM and eSPM models are understood, but there has been no effort to supplement these limitations by incorporating additional physics. For instance, *atomic* and *particle* scale models [47, 107, 108] have been used for design and optimization of electrode morphology, but no studies have been reported on their use for model-based control applications.

Models that characterize battery behavior at the smaller length scales capture battery behavior better because they rely on only fundamental first principles to describing the underlying transport processes. Atomic and particle scale models characterize battery behavior at those length scales where critical aging mechanisms such as the SEI layer growth [109] and cyclic degradation [110] that lead to surface cracks, material fracture, and active material loss can be best described. Hence, there is a critical need to establish a communication and transfer of information from the physics-based to the control-oriented modeling domain. Incorporating information from atomic- and pore-scale models in control-oriented model design can enable the development of computationally tractable models and more accurate virtual sensors for estimation of the battery internal states. New challenges emerge with new technologies, and the addition of more physics into control-based design will lead to the development of a modeling framework that will enable researchers to address these challenges.

1.2.2 The DFN Model: Properly Applied or Abused?

"Essentially, all models are wrong, but some are useful."

- G. E. P. Box and N. R. Draper, *Empirical Model-Building and Response Surfaces (1987)*

When all transport phenomena cannot be experimentally verified within a system, one resorts to develop a model incorporating all relevant physico-chemical interactions, understand and explain the observations in the system behavior, and optimize the design and utilization of the system for a targeted application. The same is true in electrochemical batteries. While models have been effective for small scale battery applications, their predictability is not accurate with the scaling up of battery technology for large scale applications. An aspect of significant interest over the past decades is the efficient utilization and useful life enhancement of lithium-ion technology in the automotive sector.

Lithium-ion transport can be captured at the microscopic length scales using robust pore-scale models. However, their computational intensity renders them impractical as a predictive tool at the system level. Such limitations become dire when modeling battery lifetime and slow degradation processes over hundreds or thousands of cycles. The need for real-time estimation of battery SoC and SoH to guide control strategies in BMSs currently limits the application of more accurate and computationally intensive models in favour of simpler and computationally efficient macroscale (effective or continuum) models [111, 112]. Macroscopic models, which are approximate representations of the pore-scale physics, are particularly appealing for PDE-based control and estimation strategies of battery SoC and SoH.

Macroscale models are developed from pore-scale models using upscaling techniques [113–115]. Two well-known upscaling methods are *volume-averaging* [51] and *homogenization* [52]. In the volume-averaging technique, the variable of interest is first averaged over a representative elementary volume (REV). The REV is assumed to be a continuum representation of the underlying porous media. The pore-scale governing equations are then averaged in the REV so that they co-exist everywhere in the porous medium. The homogenization technique uses asymptotic expansion of variables to rigorously derive the effective formulation of the governing equations as the pore-scale asymptotically approaches to zero. The advantage of using homogenization over volume-averaging is that the resulting closure variables for effective transport parameters in the homogenized model are obtained by detailed numerical modeling of the electrode architecture, rather than using empirical approaches.

The electrochemical models used today have been derived from the work of Doyle $et.\ al.$ [49] using the volume averaging technique [116]. This isothermal macroscopic model is known as the Doyle-Fuller-Newman (DFN) model, and treats the electrode as a homogeneous medium. The widespread use of this model in different variations is attributed to the consideration of porous electrode and concentrated solution theories to describe mass and charge transport between electrodes, and Bulter-Volmer kinetics to describe the reaction dynamics [117]. This model is also known as the pseudo two-dimensional (P2D) model because the electrode active particles are assumed to be spherical in shape, ordered and monodispersed [15], and mass transport within these particles are resolved in spherical coordinates. However, one dimensional transport of mass and charge is assumed in the electrolyte phase.

Since the full order homogeneous DFN model is computationally intensive and cannot be directly implemented for real-time applications, research efforts over the years have led to the development of simplified [81,83] and reduced-order models [64,118] aimed at retaining the DFN model accuracy while improving computational efficiency. To improve the predictability of the transport models in accounting for temperature

effects during operation, electrochemical-thermal models [119] have been developed by coupling lumped cell temperature dynamic equations with the mass and charge conservation equations of the electrochemical model. Other extensions of isothermal transport models include capacity fading effects due to the SEI layer growth [120–122]. Advanced research efforts aided by enhanced computational capabilities in recent years have enabled the development of multiscale approaches to model the electrochemistry of lithium-ion batteries [57]. Yet, a comprehensive understanding of dynamical battery behavior has remained a complex problem over decades, and a major bottleneck in achieving diagnostic capabilities, safety, optimization, and control of battery systems.

Macroscale models overcome some of the computational limitations of pore-scale models by relying on assumptions and constraints that guarantee scale separation between the pore- and the continuum-scales. However, physical and electrochemical phenomena on one scale are often coupled to phenomena on a vastly different scale. For example, pore-scale molecular diffusion fundamentally affects lithium-ion mixing and heat generation at the electrode and cell scales [119]. Similarly, localised SEI layer growth in the pores over time scales spanning many orders of magnitude can lead to drastic porosity changes and long term impairment such as capacity fading in battery systems. Prior to the work outlined in this dissertation, there has been no published research that has rigorously established the conditions under which pore-scale equations describing migration, diffusion, and reaction of lithium ions correctly upscale to the classical macroscopic porous-electrode equations. The determination of battery operating conditions under which continuum approaches are a valid representation of microscopic processes is critical to achieve model predictivity of battery systems.

Since its development, the DFN model has been accepted with limited criticism and debate as the most reliable physics-based modeling tool available for lithium-ion technology. However, its limitations in predicting battery dynamics at operating conditions characterized by high discharge rates and operating temperatures is an aspect of research that has not been addressed. This is attributed to the fact that all the approximations and constraints that have facilitated the development of the DFN model, and battery operating regimes that lead to the violation of these conditions have not been documented in published literature. While the DFN model has been supplemented with thermal and aging models to improve its predictability, very few electrochemical modeling methodologies have since been formulated, and none of them have demonstrated any limitations of the DFN model nor any numerical simulations to supersede the DFN model in terms of predictability. The lack of other modeling methodologies has led battery researchers to adopt the same model in explaining every possible transport phenomena without prior assessment or justification.

Due to its computational complexity, the DFN model has been mathematically simplified to SPM and eSPM models and other reduced-order models through reformulation techniques for control, estimation, and diagnostic purposes. Hence the predictability of these computationally efficient models at best is limited to the accuracy of the DFN model. Different studies [22, 123–126] have presented computationally efficient DFN reformulations and validated their performance for different operating patterns against the full order DFN model as a benchmark. In most of these studies, battery operation is restricted to moderate temperatures and low current rates of operation. Such studies do not verify a priori the predictability of the full order DFN model for different electrode chemistry and aggressive battery operating conditions. As a result, the performance of such control-oriented models may not accurately reflect real-world battery response even though their performance is accurate with respect to the DFN model. Under these circumstances, model-based control strategies to maintain a safe envelope of battery operation will clearly limit their threshold of application to only those conditions for which the underlying model is accurate. These studies reflect the need to adopt other strategies to validate reduced-order models rather than abusing the full order DFN model in this process.

The DFN model has been formulated on the basis of certain underlying assumptions which are summarized in [15, 127, 128]. The most critical assumption among these concerns the particle geometry. Experimental investigations [129, 130] have proven that practical battery electrodes have non-spherical particle shapes which exhibit polydispersity. This means that the DFN model is capable of predicting battery dynamics better in electrodes that consist of spherical monodispersed particle shapes. For other battery electrode morphology, the DFN model must be used with caution. The volume averaging approach does not consider the active particle morphology and orientation while determining the effective transport parameters [131]. The effective transport properties are obtained using an empirical formula that depends only on the electrolyte volume fraction. However, the topology and the morphology of the electrode play a significant role in influencing these effective properties [116]. The complexity of this problem is understated, but must be seriously considered for the following reasons: (a) electrodes with the same volume fraction can have significantly different performance characteristics due to differences in topology, and (b) topology and morphology are not constant over the life of the battery because cyclic charging and discharging leads to volume changes, cracks, and differential stress/strain effects in the electrodes.

The limitations of the DFN model may be significantly amplified in the simplified and reduced-order model formulations. This will severely impact the accuracy of estimation of the battery battery internal states. That there is still a lack of deployment of physics-based models in real-world large scale battery applications

points to a need to address the following questions:

1. How accurate are macroscale models across different electrode chemistry and operating conditions?
2. Under what operating conditions do macroscale models provide an accurate reflection of battery dynamics, and what leads to a failure in the model predictability?
3. How can better battery models be developed to address safety issues, predict energy and power capabilities, and overcome limitations in battery utilization due to degradation and aging?

This discussion in no manner intends to undermine previous modeling contributions and efforts. Unequivocally, the development of the DFN model has been played an invaluable role and impact in the field of battery model development and model-based control strategies for estimation, control, and diagnostics. Rather, in the quest of understanding how to design and utilize batteries more effectively, this section serves to highlight specific attributes that are missing in macroscale transport models today, and motivates the work presented in this dissertation. The overarching goal is to understand when currently used models are good enough and when there is a need for using something different. Thus far, research efforts have not completely tackled the problem of identifying the right conditions of operation of the models that are being utilized. Unless this is addressed, lack of awareness of model utilization may lead to its implementation for the wrong applications. This dissertation aims to address the aforementioned questions through the development of a rigorously derived multiscale modeling framework for lithium-ion batteries, and eventually enable *better battery utilization through better model(ing)*.

1.3 Dissertation Outline

1.3.1 Objectives

The main objective of this research work is to develop a physics-based modeling framework for advanced BMS applications along with tools to assess model predictability. One of the major aims of this dissertation is to facilitate the synthesis of control-oriented mathematical models that predict battery behavior with higher fidelity than the models employed today. This will enable reliable estimation of the battery internal states (SoC and SoH) and predict the remaining useful life for optimizing performance and longevity. The versatility of the new modeling framework is evaluated across different electrode chemistry and operating regimes characterized by temperature and C-rates of operation. This research work can be categorized into

six sections: a) multi-scale modeling framework development, b) investigation of the veracity of macroscale models for different electrode chemistry and operating conditions characterized by temperature, C-rate of discharge, and capacity fading, c) determination of effective lithium ion transport properties, d) numerical implementation of the homogenized model equations using COMSOL Multiphysics®and model parameter identification using co-simulation studies involving COMSOL Multiphysics®and MATLAB®using a global optimization approach, and e) model performance assessment using data acquired from temperature-based experiments conducted on 18650 NMC lithium-ion cells.

1.3.2 Outline

This dissertation is structured as follows:

Chapter 2 presents the homogenization technique to derive macroscale mass and charge transport equations of lithium. The conditions that guarantee scale separation between the pore- and continuum scales are rigorously identified during the upscaling process. The region of validity of the continuum approximation of the pore-scale transport equations is graphically represented using 2-D phase diagrams. The details of the derivation of the homogenized model transport equations are presented in Appendices A and B. This is followed by a systematic approach to determine the effective ionic transport properties by resolving a closure variable in a unit cell of the electrode. The application of the phase diagrams to assess the validity of the macroscale mass and charge transport equations in relations to different electrode chemistry, cell temperatures, C-rates of discharge, and capacity fading due to aging dynamics over time, is elaborated in the later sections of this chapter.

Chapter 3 describes the equipment used to perform experiments and data acquisition on 18650 NMC cylindrical lithium-ion cells, design of experiments conducted at different cell temperatures, and the experimentally measured voltage response for different operating conditions. The selection of the different temperatures for the experimental characterization of the NMC cells was based on the results of an electrolyte phase diagram study, which is presented in 4.

Chapter 4 begins with a comparison of the lithium mass and charge transport equations of the full-order homogenized macroscale model (FHM) and the DFN model, along with a discussion of different factors that indicate higher predictability of the FHM model over the DFN model. The numerical implementation of the DFN model using the finite element modeling software COMSOL Multiphysics® is summarized, followed by a detailed description of the FHM model implementation in the same software platform. A user guide for the development of the FHM model is presented in Appendix C. This is followed by parameter identification

of the DFN and FHM models, performed using co-simulation studies involving COMSOL Multiphysics®and MATLAB®software using the Particle Swarm Optimization (PSO) technique. The geometric and stoichiometric parameters are first identified for the DFN and FHM models individually, and the average of these parameter values are used in both models. The electrode diffusion coefficients, reaction rate coefficients, and contact resistance are the five model parameters that are then identified for the FHM and DFN models as a function of temperature. The performance of both the models is assessed against experimental data, the details of which have been elaborated upon in Chapter 3. This chapter concludes with a discussion of the results from the parameter identification studies, and the summary of the results using a system level phase diagram to quantify the error in the predictability of both models as a function of the battery SoC and operating temperature.

Finally, Chapter 5 summarizes the conclusions from this dissertation and the potential direction of future work.

1.3.3 Contributions

The contributions of this dissertation have potential implications in the field of modeling, estimation, and control of lithium-ion batteries. In particular, the modeling framework development that is elaborated in this work will enable the development of advanced battery management systems through model-based control approaches. The key contributions of this dissertation are as follows:

1. Derivation of a physics-based multiscale model for lithium-ion batteries using *mathematical homogenization*, a rigorous upscaling technique applied to the pore-scale Poisson-Nernst-Planck (PNP) equations of mass and charge transport in the lithium-ion electrodes and the electrolyte.
2. Development of 2-D electrode and electrolyte phase diagrams and assessment of the predictability of the macroscale mass and charge transport equations across different operating conditions characterized by temperature, C-rate of discharge, and battery aging.
3. Development of a modeling approach to determine the effective electrolyte diffusion and conductivity coefficients by resolving a closure variable in the unit cell of the electrode microstructure.
4. Numerical implementation of the developed full order homogenized model of lithium mass and charge transport using the finite element software COMSOL Multiphysics®.
5. Identification of the parameters of the FHM and DFN models as a function of the operating temperature by conducting co-simulation studies involving COMSOL Multiphysics®and MATLAB®software

using the Particle Swarm Optimization (PSO) technique. The performance of the models is assessed against data obtained from experiments conducted on 18650 NMC cylindrical lithium-ion cells, and a schematic representation of the results of the identification studies using a system level phase diagram.

The peer-reviewed articles that were published over the course of this dissertation are listed below:

1. H. Arunachalam, S. Onori, and I. Battiato, "On veracity of macroscopic Lithium-ion battery models", *J. Electrochem. Soc.*, vol. 162, no. 10, pp. A1940-A1951, 2015.

2. H. Arunachalam, S. Onori, and I. Battiato, "Temperature-dependent multiscale-dynamics in Lithium-Ion battery electrochemical models", in *Proceedings of the 2015 American Control Conference*, pp. 305-210, IEEE, 2015.

3. H. Arunachalam, I. Battiato, and S. Onori, "Preliminary Investigation of Provability of Li-Ion Macroscale Models Subject to Capacity Fade", in *Proceedings of the 2016 Dynamic Systems and Control Conference*, ASME, 2016.

4. H. Arunachalam, S. Korneev, I. Battiato, and S. Onori, "Multiscale modeling approach to determine effective lithium-ion transport properties", in *Proceedings of the 2017 American Control Conference*, pp. 92-97, IEEE, 2017.

Chapter 2

Multiscale Electrochemical Modeling Framework Development

2.1 Introduction

This chapter elaborates upon the development of a multiscale electrochemical modeling framework that describes mass and charge transport of lithium in the electrode and electrolyte phases. Starting with a dimensionless formulation of the Poisson-Nernst-Planck (PNP) equations [132] that describe lithium-ion transport at the pore-scale, multiple-scale expansions technique [133] is applied to rigorously derive macroscopic dual-continua models and identify the physics-based conditions under which classical porous-electrode continuum models accurately describe lithium-ion micro-scale dynamics with the accuracy prescribed by the homogenization technique. Application of the homogenization technique to derive effective equations of mass and charge transport for lithium-ion batteries have been reported in literature [113, 134]. However, there are two key differences between the approach implemented by the authors of [113, 134] and the approach elaborated in this chapter:

1. The pore-scale equations describing mass transport of lithium within the active particles are not upscaled to an effective formulation. The authors of [113, 134] report that because of the much slower diffusion of lithium in the active particles compared to the rate of diffusion of lithium ions in the electrolyte, lithium transport in the electrodes can be adequately captured only at the pore-scale.

   No supporting hypothesis has been provided to justify this argument, and there have been no studies

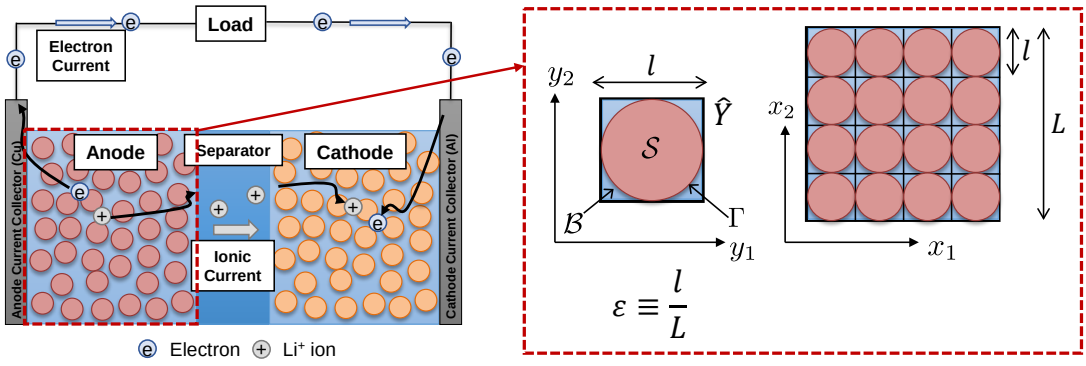

Figure 2.1: Representation of the porous electrode of a lithium-ion cell in the form of spatially periodic unit cell. Every unit cell $\hat{Y}$ is composed of active particles $\mathcal{S}$ and electrolyte solution $\mathcal{B}$ that are separated by an interface Γ.

reported that quantify the error associated with the upscaling of the electrode mass transport equation. This chapter presents the first-ever study to develop fully upscaled mass and charge transport equations of lithium-ion batteries along with a quantification of the predictability of the effective equations with respect to their pore-scale counterparts.

2. In [113, 134], the pore-scale equations of electrode charge transport and electrolyte mass and charge transport are upscaled in dimensional form. As a result, while the conditions that allow scale separation and successful upscaling were formulated, no rigorous analysis was presented to identify the conditions under which upscaled transport equations accurately represent pore-scale dynamics.

   In this chapter, the pore-scale mass and charge transport equations are first converted to dimensionless form. This enables the use of dimensionless parameters to represent the pore-scale transport processes, and summarize the applicability conditions in a schematic manner. Another advantage of this approach is that the conditions when macroscale models are accurate can be explained by comparing the time-scales of lithium transport mechanisms and understand which mechanisms dominate the others.

Following the derivation of the electrochemical model, a modeling approach is presented to determine the effective ionic transport properties in the battery medium by resolving a closure variable in a unit cell of the electrode microstructure. The later sections of this chapter are dedicated to the assessment of the predictability of macroscopic models across different electrode chemistry and battery operating conditions characterized by temperature, current rate of discharge, and aging mechanisms such as capacity fading due to the growth of the SEI layer.

2.2 Derivation of a homogenized electrochemical lithium-ion battery model

2.2.1 Pore-scale Governing Equations

Microscale transport of lithium ions is considered inside a battery electrode composed of a porous matrix $\hat{\Omega}$ with characteristic length L. The active particles are assumed to be microscopically arranged in the medium in the form of spatially periodic unit cells $\hat{Y}$ with a characteristic length ℓ, as illustrated in Fig. 2.1. The characteristic length at the pore-scale is defined as ℓ and is considered to be of the order of the diameter of the spherical active particles. ε, the scale-separation parameter, is defined as $\varepsilon \equiv \ell/L \ll 1$. The unit cell $\hat{Y} = \hat{\mathcal{B}} \cup \hat{\mathcal{S}}$ consists of the electrolyte space $\hat{\mathcal{B}}$ and the ion permeable solid matrix $\hat{\mathcal{S}}$ that are separated by the smooth surface $\hat{\Gamma}$. The pore spaces $\hat{\mathcal{B}}$ of each cell $\hat{Y}$ form a multi-connected pore-space domain $\hat{\mathcal{B}}^{\varepsilon} \subset \hat{\Omega}$ bounded by the smooth surface $\hat{\Gamma}^{\varepsilon}$. The mass and charge transport equations in the electrolyte and the electrode phases control the spatiotemporal evolution of the concentration of lithium ions $\hat{c}_{\varepsilon}^{i}(\mathbf{x}, t)$ (molm^{-3}) and the electrostatic potential $\hat{\phi}_{\varepsilon}^{i}(\mathbf{x}, t)$ (V) in the active particles $\{i = s\}$ and the electrolyte $\{i = e\}$. The set of governing equations are summarized in section §2.2.1.1 and section §2.2.1.2.

2.2.1.1 Electrolyte phase

The pore-scale transport equations of mass and charge transport incorporate the porous electrode [135] and concentrated solution theories for ion transport [117]. The conservation equations for lithium-ions in the concentrated electrolyte solution is developed from the generalized Poisson-Nernst-Planck equations for electrochemical systems with negligible convection, and is defined as [136]:

$$\frac{\partial \hat{c}_{\varepsilon}^{e}}{\partial \hat{t}} = -\hat{\nabla} \cdot \hat{N}_{e}, \tag{2.1}$$

where $\hat{N}_e$ $\left[\text{molm}^{-2}\text{s}^{-1}\right]$ is the flux of the positive lithium ions in the solution, and is expressed as [136]:

$$\hat{N}_{e} = -\mathbf{D}^{e}\hat{\nabla}\hat{c}_{\varepsilon}^{e} + t_{+}F^{-1}\hat{j}_{e}, \tag{2.2}$$

where $\hat{\mathbf{D}}^{e}$ $\left[\text{m}^{2}\text{s}^{-1}\right]$ is the interdiffusion coefficient in the electrolyte, t_+ is the transference number, F is Faraday constant, and $\hat{j}_e$ $\left[\text{Am}^{-2}\right]$ is the electric current density in the electrolyte phase, and is expressed

as [136]:

$$\hat{j}_e = -\hat{\mathbf{K}}^e \hat{\nabla} \hat{\phi}_\varepsilon^e - \left(\lambda t_+ RTF^{-1} \hat{\mathbf{K}}^e / \hat{c}_\varepsilon^e\right) \hat{\nabla} \hat{c}_\varepsilon^e, \tag{2.3}$$

where $\hat{\mathbf{K}}^e$ $\left[\Omega^{-1}\mathrm{m}^{-1}\right]$ is the electric conductivity in the electrolyte, $\hat{c}_{\text{max}}^s$ $\left[\mathrm{molm}^{-3}\right]$ is the maximum concentration of lithium that can be stored in the active particle, $f_\pm$ $[-]$ is the activity coefficient, $\lambda = 1 + \dfrac{\mathrm{d}\ln f_\pm}{\mathrm{d}\ln(\hat{c}_\varepsilon^e/\hat{c}_{\text{max}}^s)}$ $[-]$ is assumed to be a constant [137], R [$\mathrm{Jmol}^{-1}\mathrm{K}^{-1}$] is the universal gas constant, and T is temperature. Based on the condition of charge neutrality in the electrolyte solution between the lithium ions and the negative counter ions, the charge conservation equation in the electrolyte phase is defined as [136]:

$$\frac{\partial \hat{q}}{\partial \hat{t}} = \nabla \cdot \hat{j}_e = 0. \tag{2.4}$$

The intercalation reaction at the interface separating the active particle and the electrolyte phases is described by using the Butler Volmer theory [117], and the current density across the interface due to the intercalation reaction, i_{se} $\left[\mathrm{Am}^{-2}\right]$, is defined as [138]:

$$i_{se} = 2k\sqrt{\hat{c}_\varepsilon^e \hat{c}_\varepsilon^s (1 - \hat{c}_\varepsilon^s/\hat{c}_{\text{max}}^s)} \cdot \sinh[F(\hat{\phi}_\varepsilon^s - \hat{\phi}_\varepsilon^e - \hat{U})/2RT], \tag{2.5}$$

where k $\left[\mathrm{Vm}\Omega^{-1}\mathrm{mol}^{-1}\right]$ is the electrochemical reaction rate constant that describes the kinetics of lithium-ion transfer on Γ^ε, and $\hat{U}$ [V] is the electrode open circuit potential. It is assumed under all circumstances that the lithium-ions are either intercalated in the active particle are released into the electrolyte. This is in accordance with the consideration that there are no side-reactions involved in the porous electrodes. Assuming that there is no intercalation of any negative counter ions from the electrolyte, the total current across the active particle-electrolyte interface is only due to the transport of positive lithium ions. These conditions are formulated mathematically and expressed in the form of the following interface conditions [136]:

$$-\mathbf{n}_e \cdot \hat{N}_e = \frac{i_{se}}{F}, \tag{2.6a}$$

$$-\mathbf{n}_e \cdot \hat{j}_e = i_{se}, \tag{2.6b}$$

where $\mathbf{n}_e$ is the outward unit normal vector to $\hat{\Gamma}^\varepsilon$ pointing from the electrolyte towards the active particle. The mass and charge transport equations in the electrolyte phase $\mathbf{x} \in \hat{\mathcal{B}}^\varepsilon$ [138] can then be summarized as

follows [138]:

$$\frac{\partial \hat{c}_\varepsilon^e}{\partial \hat{t}} = \hat{\nabla} \cdot [(\hat{\mathbf{D}}^e + \lambda t_+^2 RTF^{-2}\hat{\mathbf{K}}^e/\hat{c}_\varepsilon^e)\hat{\nabla}\hat{c}_\varepsilon^e + t_+ F^{-1}\hat{\mathbf{K}}^e\hat{\nabla}\hat{\phi}_\varepsilon^e], \tag{2.7a}$$

$$0 = \hat{\nabla} \cdot [(\lambda t_+ RTF^{-1}\hat{\mathbf{K}}^e/\hat{c}_\varepsilon^e)\hat{\nabla}\hat{c}_\varepsilon^e + \hat{\mathbf{K}}^e\hat{\nabla}\hat{\phi}_\varepsilon^e], \tag{2.7b}$$

subject to

$$\mathbf{n}_e \cdot [(\hat{\mathbf{D}}^e + \lambda t_+^2 RTF^{-2}\hat{\mathbf{K}}^e/\hat{c}_\varepsilon^e)\hat{\nabla}\hat{c}_\varepsilon^e + t_+ F^{-1}\hat{\mathbf{K}}^e\hat{\nabla}\hat{\phi}_\varepsilon^e] = kF^{-1}\hat{f}(\hat{c}_\varepsilon^e, \hat{c}_\varepsilon^s, \hat{\phi}_\varepsilon^s, \hat{\phi}_\varepsilon^e), \tag{2.8a}$$

$$\mathbf{n}_e \cdot [(\lambda t_+ RTF^{-1}\hat{\mathbf{K}}^e/\hat{c}_\varepsilon^e)\hat{\nabla}\hat{c}_\varepsilon^e + \hat{\mathbf{K}}^e\hat{\nabla}\hat{\phi}_\varepsilon^e] = k\hat{f}(\hat{c}_\varepsilon^e, \hat{c}_\varepsilon^s, \hat{\phi}_\varepsilon^s, \hat{\phi}_\varepsilon^e), \tag{2.8b}$$

on the solid-electrolyte boundary Γ^ε, respectively. In (2.8),

$$\hat{f}(\hat{c}_\varepsilon^e, \hat{c}_\varepsilon^s, \hat{\phi}_\varepsilon^s, \hat{\phi}_\varepsilon^e) = 2\sqrt{\hat{c}_\varepsilon^e \hat{c}_\varepsilon^s (1 - \hat{c}_\varepsilon^s/\hat{c}_{\text{max}}^s)} \cdot \sinh[F(\hat{\phi}_\varepsilon^s - \hat{\phi}_\varepsilon^e - \hat{U})/2RT]. \tag{2.9}$$

2.2.1.2 Electrode phase

The mass and charge transport of lithium ions in the solid phase $\hat{\mathcal{S}}^\varepsilon$ are governed by the material balance and electroneutrality equations [138]. The equations for concentration and electric potential are based on general thermodynamic principles, similar to that in the electrolyte phase. Transport in the active materials is assumed to be isotropic on the microscopic scale [136]. It is also assumed that the transference number is zero in the active materials, since the electrical current is primarily driven by the transport of electrons. The net flux of lithium in an active particle is generally defined in terms of its thermodynamic driving force, and is expressed as [139]:

$$\hat{N}_s = -L_s \hat{\nabla}\mu_s, \tag{2.10}$$

where L_s is the kinetic coefficient and μ_s is the chemical potential of lithium in the active particles. It is assumed that the electric potential gradient is so small that it does not influence the mass flux of lithium [139]. Under this assumption, the chemical potential can be expressed in terms of the concentration of lithium in the solid phase, and equation (2.10) can be re-written in the form of a Fickian flux expression [139]:

$$\hat{N}_s = -\hat{\mathbf{D}}^s \hat{\nabla}\hat{c}_\varepsilon^s, \tag{2.11}$$

where $\hat{\mathbf{D}}^s$ $\left[\mathrm{m^2 s^{-1}}\right]$ is the interdiffusion coefficient in the active material. The distribution of electrostatic potential in the active materials is expressed using the current density, $\hat{j}_s$ $\left[\mathrm{Am^{-2}}\right]$, as [139]:

$$\hat{j}_s = -\hat{\mathbf{K}}^s \hat{\nabla} \hat{\phi}_\varepsilon^s, \tag{2.12}$$

where $\hat{\mathbf{K}}^s$ $\left[\Omega^{-1}\mathrm{m}^{-1}\right]$ is the electric conductivity in the active particles. The conservation of charge in the active material phase yields [139]:

$$\hat{\nabla} \cdot \hat{j}_s = 0. \tag{2.13}$$

At the interface between the active materials and the electrolyte phases, the electrostatic potential gradient and the flux of lithium in the active particles are governed by the charge-transfer intercalation reactions, and the conditions are mathematically formulated as [136, 140]:

$$\mathbf{n}_s \cdot \hat{N}_s = \frac{i_{se}}{F}, \tag{2.14a}$$

$$\mathbf{n}_s \cdot \hat{j}_s = i_{se}, \tag{2.14b}$$

where $\mathbf{n}_s$ is the outward unit normal vector to Γ^ε pointing from the active particle towards the electrolyte. The equations in the electrode phase can then be summarized as follows [138]:

$$\frac{\partial \hat{c}_\varepsilon^s}{\partial \hat{t}} = \hat{\nabla} \cdot (\hat{\mathbf{D}}^s \hat{\nabla} \hat{c}_\varepsilon^s), \qquad \hat{\mathbf{x}} \in \hat{\mathcal{S}}^\varepsilon, \tag{2.15a}$$

$$0 = \hat{\nabla} \cdot (\hat{\mathbf{K}}^s \hat{\nabla} \hat{\phi}_\varepsilon^s), \qquad \hat{\mathbf{x}} \in \hat{\mathcal{S}}^\varepsilon, \tag{2.15b}$$

subject to

$$-\mathbf{n}_s \cdot (\hat{\mathbf{D}}^s \hat{\nabla} \hat{c}_\varepsilon^s) = kF^{-1} \hat{f}(\hat{c}_\varepsilon^e, \hat{c}_\varepsilon^s, \hat{\phi}_\varepsilon^s, \hat{\phi}_\varepsilon^e), \qquad \hat{\mathbf{x}} \in \hat{\Gamma}^\varepsilon \tag{2.16a}$$

$$-\mathbf{n}_s \cdot (\hat{\mathbf{K}}^s \hat{\nabla} \hat{\phi}_\varepsilon^s) = k \hat{f}(\hat{c}_\varepsilon^e, \hat{c}_\varepsilon^s, \hat{\phi}_\varepsilon^s, \hat{\phi}_\varepsilon^e), \qquad \hat{\mathbf{x}} \in \hat{\Gamma}^\varepsilon \tag{2.16b}$$

respectively.

2.2.2 Dimensionless Formulation of Transport Equations

2.2.2.1 Transport Processes and Dimensionless Numbers

The transport processes occurring at the pore-scale include heterogenous reaction at the electrode-electrolyte interface $\hat{\Gamma}^{\varepsilon}$, and lithium diffusion and conduction in the electrode phase $\hat{\mathcal{S}}^{\varepsilon}$, and lithium-ion diffusion and electromigration in the electrolyte phase $\hat{\mathcal{B}}^{\varepsilon}$. The characteristic time scales associated with the different transport processes: heterogenous reaction, electrode diffusion and conduction, and ionic diffusion and electromigration, over a macroscopic length scale L, are

$$\hat{t}_R = \frac{LF}{k}, \quad \hat{t}_{D_j} = \frac{L^2}{D^i}, \quad \hat{t}_{M_j} = \frac{F^2 L^2 \hat{c}^s_{\text{max}}}{RTK^j}, \quad j = \{e, s\}, \tag{2.17}$$

respectively. In (2.17), $D^j = \mathcal{O}(\hat{\mathbf{D}}^j)$ and $K^j = \mathcal{O}(\hat{\mathbf{K}}^j)$, $j = \{e, s\}$, are the characteristic values of the interdiffusion and electric conductivity tensors $\hat{\mathbf{D}}^j$ and $\hat{\mathbf{K}}^j$ in the electrode ($j = s$) and the electrolyte ($j = s$), respectively. Dimensionless Damköhler and electric Péclet numbers are then defined as

$$\text{Da}_j := \frac{\hat{t}_{D_j}}{\hat{t}_R} = \frac{Lk}{FD^j} \quad \text{and} \quad \text{Pe}_j := \frac{\hat{t}_{D_j}}{\hat{t}_{M_j}} = \frac{RTK^j}{F^2 D^j \hat{c}^s_{\text{max}}}, \quad j = \{e, s\}. \tag{2.18}$$

These parameters provide information about the relative magnitude of ion transport processes in the electrolyte and the electrode phases. Let $c^j_{\varepsilon} := \hat{c}^j_{\varepsilon}/\hat{c}^s_{\text{max}}$ and $\phi^j_{\varepsilon} := \hat{\phi}^j_{\varepsilon} F/(2RT)$, $j = \{s, e\}$ be the dimensionless Li-ion concentration and electrostatic potential in the active particles ($j = s$) and the electrolyte ($j = e$). Then, the mass and charge transport equations can be cast in dimensionless form as follows.

2.2.2.2 Electrolyte Phase

The dimensionless form of the mass and charge transport equations in the electrolyte (2.7)-(2.8) is given by

$$\frac{\partial c^e_{\varepsilon}}{\partial t} = \nabla \cdot [(\mathbf{D}^e + \lambda t_+^2 \text{Pe}_e \mathbf{K}^e / c^e_{\varepsilon}) \nabla c^e_{\varepsilon} + 2\text{Pe}_e t_+ \mathbf{K}^e \nabla \phi^e_{\varepsilon}], \quad \mathbf{x} \in \mathcal{B}^{\varepsilon} \tag{2.19a}$$

$$0 = \nabla \cdot [(\lambda t_+ \mathbf{K}^e / c^e_{\varepsilon}) \nabla c^e_{\varepsilon} + 2\mathbf{K}^e \nabla \phi^e_{\varepsilon}], \quad \mathbf{x} \in \mathcal{B}^{\varepsilon} \tag{2.19b}$$

subject to

$$\mathbf{n}_e\cdot\left[(\mathbf{D}^e+\lambda t_+^2\mathrm{Pe}_e\mathbf{K}^e/c_\varepsilon^e)\nabla c_\varepsilon^e+2\mathrm{Pe}_e\ t_+\mathbf{K}^e\nabla\phi_\varepsilon^e\right]=\mathrm{Da}_e f(c_\varepsilon^e,c_\varepsilon^s,\phi_\varepsilon^s,\phi_\varepsilon^e), \tag{2.20a}$$

$$\mathbf{n}_e\cdot\left[(\mathrm{Pe}_e\lambda t_+\mathbf{K}^e/c_\varepsilon^e)\nabla c_\varepsilon^e+2\mathrm{Pe}_e\mathbf{K}^e\nabla\phi_\varepsilon^e\right]=\mathrm{Da}_e f(c_\varepsilon^e,c_\varepsilon^s,\phi_\varepsilon^s,\phi_\varepsilon^e), \tag{2.20b}$$

on Γ^ε, respectively. In (2.7) and (2.8), the dimensional spatial and time scales are nondimensionalized by the macroscopic length L and the diffusion time in the electrolyte phase $\hat{t}_{D_e}$ respectively, i.e. $\mathbf{x}=\hat{\mathbf{x}}/L$ and $t_e=\hat{t}/\hat{t}_{D_e}$; $\mathbf{D}^e=\hat{\mathbf{D}}^e/D^e$ and $\mathbf{K}^e=\hat{\mathbf{K}}^e/K^e$ are the dimensionless interdiffusion coefficient and the electric conductivity in the electrolyte. Also,

$$f(c_\varepsilon^e,c_\varepsilon^s,\phi_\varepsilon^e,\phi_\varepsilon^s)=2\sqrt{c_\varepsilon^e c_\varepsilon^s(1-c_\varepsilon^s)}\sinh(\phi_\varepsilon^s-\phi_\varepsilon^e-U) \tag{2.21}$$

where $U=F\hat{U}/(2RT)$ is the dimensionless open circuit potential. $\mathcal{B}^\varepsilon$ and $\mathcal{S}^\varepsilon$ represent the rescaled (non-dimensional) electrolyte and electrode phases, with Γ^ε the interface separating them.

2.2.2.3 Electrode Phase

In a similar manner, the dimensional transport equations in the electrode phase $\mathbf{x}\in\mathcal{S}^\varepsilon$, (2.15) and (2.16), are cast in dimensionless form as

$$\frac{\partial c_\varepsilon^s}{\partial t}=\mathrm{Da}_e\mathrm{Da}_s^{-1}\nabla\cdot(\mathbf{D}^s\nabla c_\varepsilon^s),\quad \mathbf{x}\in\mathcal{S}^\varepsilon \tag{2.22a}$$

$$0=\nabla\cdot(\mathbf{K}^s\nabla\phi_\varepsilon^s),\quad \mathbf{x}\in\mathcal{S}^\varepsilon \tag{2.22b}$$

subject to

$$-\mathbf{n}_s\cdot(\mathbf{D}^s\nabla c_\varepsilon^s)=\mathrm{Da}_s f(c_\varepsilon^e,c_\varepsilon^s,\phi_\varepsilon^s,\phi_\varepsilon^e),\quad \mathbf{x}\in\Gamma^\varepsilon \tag{2.23a}$$

$$-\mathbf{n}_s\cdot(2\mathrm{Pe}_s\,\mathbf{K}^s\nabla\phi_\varepsilon^s)=\mathrm{Da}_s f(c_\varepsilon^e,c_\varepsilon^s,\phi_\varepsilon^s,\phi_\varepsilon^e),\quad \mathbf{x}\in\Gamma^\varepsilon \tag{2.23b}$$

respectively.

Section §2.2.3 describes the multiple scale expansion technique that is used to derive a continuum (or) macroscopic approximation of the pore-scale equations, and identification of the conditions under which continuum equations are valid descriptors of pore-scale dynamics.

2.2.3 Homogenization via Multiple-Scale Expansions

The local averages of a quantity $\mathcal{A}(\mathbf{x})$ in the porous medium are defined as

$$\langle \mathcal{A} \rangle_e \equiv \frac{1}{|Y|} \int\limits_{\mathcal{B}(\mathbf{x})} \mathcal{A} \mathrm{d}\mathbf{y}, \quad \langle \mathcal{A} \rangle_s \equiv \frac{1}{|Y|} \int\limits_{\mathcal{S}(\mathbf{x})} \mathcal{A} \mathrm{d}\mathbf{y}, \tag{2.24}$$

$$\langle \mathcal{A} \rangle_{\mathcal{B}} \equiv \frac{1}{|\mathcal{B}|} \int\limits_{\mathcal{B}(\mathbf{x})} \mathcal{A} \mathrm{d}\mathbf{y}, \quad \langle \mathcal{A} \rangle_{\mathcal{S}} \equiv \frac{1}{|\mathcal{S}|} \int\limits_{\mathcal{S}(\mathbf{x})} \mathcal{A} \mathrm{d}\mathbf{y}, \tag{2.25}$$

$$\langle \mathcal{A} \rangle_{\Gamma} \equiv \frac{1}{|\Gamma|} \int\limits_{\Gamma(\mathbf{x})} \mathcal{A} \mathrm{d}\mathbf{y}, \tag{2.26}$$

where $\langle \mathcal{A} \rangle_e = \eta \langle \mathcal{A} \rangle_{\mathcal{B}}$, $\langle \mathcal{A} \rangle_s = (1-\eta) \langle \mathcal{A} \rangle_{\mathcal{S}}$ and $\eta = |\mathcal{B}|/|Y|$ is the electrode porosity. Using the method of multiple-scale expansions, a fast space variable $\mathbf{y}$ defined in the unit cell Y, $\mathbf{y} \in Y$, is introduced along with three time variables. One of the three time variables is related to reaction τ_{r}, one to conduction in the electrode phase $\tau_{\mathrm{m}s}$, and one to electromigration in the electrolyte phase $\tau_{\mathrm{m}e}$:

$$\mathbf{y} := \varepsilon^{-1}\mathbf{x}, \quad \tau_{\mathrm{r}} := \hat{t}_R^{-1}\hat{t} = \mathrm{Da}_e t, \quad \tau_{\mathrm{m}j} := \hat{t}_{M_s}^{-1}\hat{t} = \mathrm{Pe}_j \mathrm{Da}_e \mathrm{Da}_j^{-1} t, \quad j = \{e, s\} \tag{2.27}$$

where $t = \hat{t}/\hat{t}_{D_e}$ is a dimensionless time variable. No Einstein notation convention is implied if a repeated index is present. Replacing any pore scale quantity $\psi_\varepsilon(\mathbf{x}, t)$ (e.g. concentration, electrostatic potential in either phase) with $\psi(\mathbf{x}, \mathbf{y}, t, \tau_{\mathrm{r}}, \boldsymbol{\tau}_{\mathrm{m}})$ provides the following relations for the space and time derivatives,

$$\nabla \psi_\varepsilon = \nabla_{\mathbf{x}} \psi + \varepsilon^{-1} \nabla_{\mathbf{y}} \psi \tag{2.28a}$$

$$\frac{\partial \psi_\varepsilon}{\partial t} = \frac{\partial \psi}{\partial t} + \mathrm{Da}_e \frac{\partial \psi}{\partial \tau_{\mathrm{r}}} + \mathrm{Pe}_e \left(\frac{\partial \psi}{\partial \tau_{\mathrm{m}e}} + \frac{\mathrm{Da}_e}{\mathrm{Da}_s} \frac{\partial \psi}{\partial \tau_{\mathrm{m}s}} \right). \tag{2.28b}$$

Additionally, ψ is represented as an asymptotic series in integer powers of ε:

$$\psi(\mathbf{x}, \mathbf{y}, t, \tau_{\mathrm{r}}, \boldsymbol{\tau}_{\mathrm{m}}) = \sum_{n=0}^{\infty} \varepsilon^n \psi_n(\mathbf{x}, \mathbf{y}, t, \tau_{\mathrm{r}}, \boldsymbol{\tau}_{\mathrm{m}}), \tag{2.29}$$

where ψ_n, $n = 0, 1, \cdots$ are Y-periodic functions in $\mathbf{y}$. Finally, the dimensionless transport parameters are defined in terms of the scale separation parameter ε:

$$\mathrm{Pe}_e = \varepsilon^{-\alpha}, \quad \mathrm{Da}_e = \varepsilon^{\beta}, \quad \mathrm{Da}_s = \varepsilon^{\gamma}, \quad \mathrm{Pe}_s = \varepsilon^{-\delta}, \tag{2.30}$$

where the exponents α, β, γ and δ determine the system behavior in the electrolyte and electrode phases.

2.2.3.1 Upscaled Transport Equations in the Electrolyte

In Appendix A, it is shown in an elaborated manner that lithium ion transport in the electrolyte phase described by (2.19a)–(2.20b) can be homogenized, i.e., approximated up to order ε^2, by the following effective mass and charge transport equations:

$$\begin{aligned}\eta\partial_t\langle c^e\rangle_{\mathcal{B}} =&\nabla_{\mathbf{x}}\cdot[(\mathbf{D}^{e\star\star}+\varepsilon^{-\alpha}\lambda t_+^2\mathbf{K}^{e\star\star}/\langle c^e\rangle)\nabla_{\mathbf{x}}\langle c^e\rangle_{\mathcal{B}}+2\varepsilon^{-\alpha}t_+\mathbf{K}^{e\star\star}\nabla_{\mathbf{x}}\langle\phi^e\rangle_{\mathcal{B}}]\\&+2\eta\varepsilon^{-1}\mathcal{K}^{\star}\mathrm{Da}_e f(\langle c^e\rangle_{\mathcal{B}},\langle c^s\rangle_s,\langle\phi^e\rangle_{\mathcal{B}},\langle\phi^s\rangle_s),\end{aligned}\tag{2.31}$$

and

$$\begin{aligned}&\mathrm{Pe}_e\nabla_{\mathbf{x}}\cdot[(\lambda t_+\mathbf{K}^{e\star\star}/\langle c^e\rangle)\nabla_{\mathbf{x}}\langle c^e\rangle_{\mathcal{B}}+2\mathbf{K}^{e\star\star}\nabla_{\mathbf{x}}\langle\phi^e\rangle_{\mathcal{B}}]\\&=2\eta\varepsilon^{-1}\mathcal{K}^{\star}\mathrm{Da}_e f(\langle c^e\rangle_{\mathcal{B}},\langle c^s\rangle_s,\langle\phi^e\rangle_{\mathcal{B}},\langle\phi^s\rangle_s),\end{aligned}\tag{2.32}$$

where

$$f(\langle c^e\rangle_{\mathcal{B}},\langle c^s\rangle_s,\langle\phi^e\rangle_{\mathcal{B}},\langle\phi^s\rangle_s)=2\sqrt{\langle c^e\rangle_{\mathcal{B}}\langle c^s\rangle_s(1-\langle c^s\rangle_s)}\sinh(\langle\phi^s\rangle_s-\langle\phi^e\rangle_{\mathcal{B}}-U)\tag{2.33}$$

provided the following conditions are satisfied:

1) $\varepsilon\ll 1$,

2) $\mathrm{Da}_e<1$,

3) $\mathrm{Pe}_e<1$,

4) $\mathrm{Da}_e/\mathrm{Pe}_e<1$,

5) $\langle\boldsymbol{\chi}^e\rangle_{\Gamma}\approx\langle\boldsymbol{\chi}^e\rangle_{\mathcal{B}}$.

In (2.31) and (2.32), the dimensionless effective reaction rate constant in the electrolyte phase $\mathcal{K}^{\star}$ is determined by the pore geometry,

$$\mathcal{K}^{\star}=\frac{|\Gamma|}{|\mathcal{B}|},\tag{2.34}$$

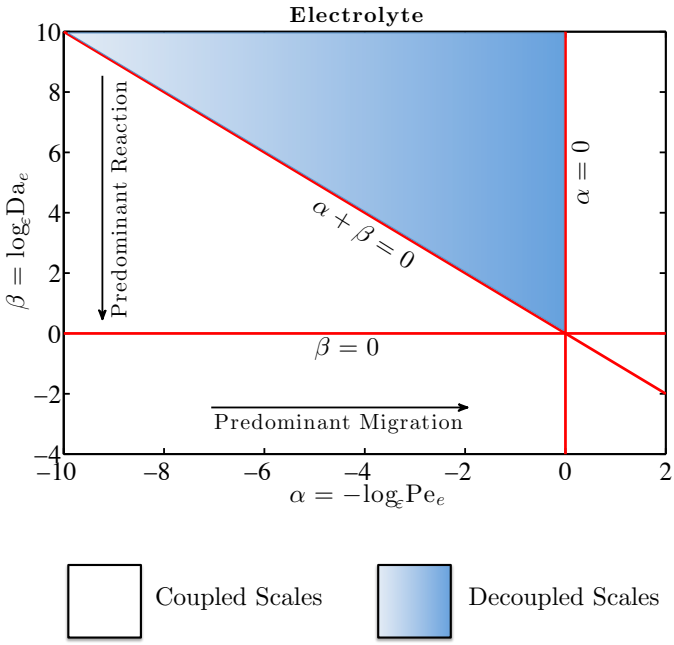

Figure 2.2: Phase diagram specifying the range of applicability of the upscaled equation for the diffusion-migration-reaction of lithium ions in the electrolyte in terms of Pe_e and Da_e. The blue region identifies the conditions under which the macro-scale equations hold. In the white region, micro- and macro-scale equations are coupled and need to be solved simultaneously. Diffusion, migration, and reaction are of the same order of magnitude at the point $(\alpha, \beta) = (0, 0)$.

and the dispersion tensors are given by:

$$\begin{aligned} \mathbf{D}^{e\star\star} &= \langle \mathbf{D}^e (\mathbf{I} + \nabla_{\mathbf{y}} \boldsymbol{\chi}^e) \rangle_e, \\ \mathbf{K}^{e\star\star} &= \langle \mathbf{K}^e (\mathbf{I} + \nabla_{\mathbf{y}} \boldsymbol{\chi}^e) \rangle_e, \end{aligned} \tag{2.35}$$

where $\mathbf{I}$ is the identity matrix. The closure variable, $\boldsymbol{\chi}^e(\mathbf{y})$, has zero mean, $\langle \boldsymbol{\chi}^e \rangle_e = \mathbf{0}$, and is defined as a solution to the local problem

$$\nabla_{\mathbf{y}} \cdot (\nabla_{\mathbf{y}} \boldsymbol{\chi}^e + \mathbf{I}) = 0, \qquad \mathbf{y} \in \mathcal{B}, \tag{2.36a}$$

$$\mathbf{n}_e \cdot (\nabla_{\mathbf{y}} \boldsymbol{\chi}^e + \mathbf{I}) = 0, \qquad \mathbf{y} \in \Gamma. \tag{2.36b}$$

Constraints 1)–4) ensure the separation of scales. While constraint 1) is almost always met in practical applications since the pore size is generally much smaller that the electrode dimension, constraints 2)–4) depend on the relative importance of the diffusion, electromigration, and reaction mechanisms, i.e. they impose con-

straints on the transport regimes that can be appropriately modeled by the continuum scale equations (2.31) and (2.32) within errors of order ε^2. These conditions are summarized in the form of an electrolyte phase diagram in Fig. 2.2, where the line $\beta = 0$ refers to $\mathrm{Da}_e = 1$ and the half-space $\beta > 0$ refers to $\mathrm{Da}_e < 1$ because $\varepsilon < 1$; the line $\alpha = 0$ refers to $\mathrm{Pe}_e = 1$ and the half-space $\alpha_e < 0$ refers to $\mathrm{Pe}_e < 1$; the line $\alpha + \beta = 0$ refers to $\mathrm{Da}_e/\mathrm{Pe}_e = 1$; and the half-space underneath this line refers to $\mathrm{Da}_e/\mathrm{Pe}_e < 1$. Constraint 5) is not necessary for scale separation, but facilitates the derivation of the effective parameters (2.34) and (2.35). As shown in Appendix A, this constraint enables the interchanging of the surface and volume averages, $\langle c_1^e \rangle_\Gamma \approx \langle c_1^e \rangle_{\mathcal{B}}$ and $\langle \phi_1^e \rangle_\Gamma \approx \langle \phi_1^e \rangle_{\mathcal{B}}$, within errors on the order of ε^2.

2.2.3.2 Upscaled Transport Equations in the Electrode

In Appendix B, it is shown that the microscale reactive transport processes described by (2.22)–(2.23) can also be homogenized, i.e., approximated up to order ε^2 in the solid phase by the following effective mass and charge transport equations:

$$\partial_t \langle c^s \rangle_s = \nabla_{\mathbf{x}} \cdot (\mathbf{D}^{s\star\star} \nabla_{\mathbf{x}} \langle c^s \rangle_s) - \varepsilon^{-1} \eta \mathrm{Da}_s \mathcal{K}^\star f(\langle c^e \rangle_{\mathcal{B}}, \langle c^s \rangle_s, \langle \phi^e \rangle_{\mathcal{B}}, \langle \phi^s \rangle_s), \tag{2.37}$$

and

$$2\mathrm{Pe}_s \nabla_{\mathbf{x}} \cdot (\mathbf{K}^{s\star\star} \nabla_{\mathbf{x}} \langle \phi^s \rangle_s) = \varepsilon^{-1} \eta \mathrm{Da}_s \mathcal{K}^\star f(\langle c^e \rangle_{\mathcal{B}}, \langle c^s \rangle_s, \langle \phi^e \rangle_{\mathcal{B}}, \langle \phi^s \rangle_s), \tag{2.38}$$

for $\mathbf{x} \in \Omega$, provided the following additional conditions are satisfied:

1) $\mathrm{Da}_s < 1$,

2) $\mathrm{Da}_s/\mathrm{Pe}_s < 1$,

3) $\langle \boldsymbol{\chi}^s \rangle_\Gamma \approx \langle \boldsymbol{\chi}^s \rangle_s$.

In (2.37) and (2.38), the dimensionless parameter $\mathcal{K}^\star$ is defined by (2.34) and the effective diffusion and conductivity tensors are given by

$$\begin{aligned} \mathbf{D}^{s\star\star} &= \langle \mathbf{D}^s (\mathbf{I} + \nabla_{\mathbf{y}} \boldsymbol{\chi}^s) \rangle_s \\ \mathbf{K}^{s\star\star} &= \langle \mathbf{K}^s (\mathbf{I} + \nabla_{\mathbf{y}} \boldsymbol{\chi}^s) \rangle_s \end{aligned} \tag{2.39}$$

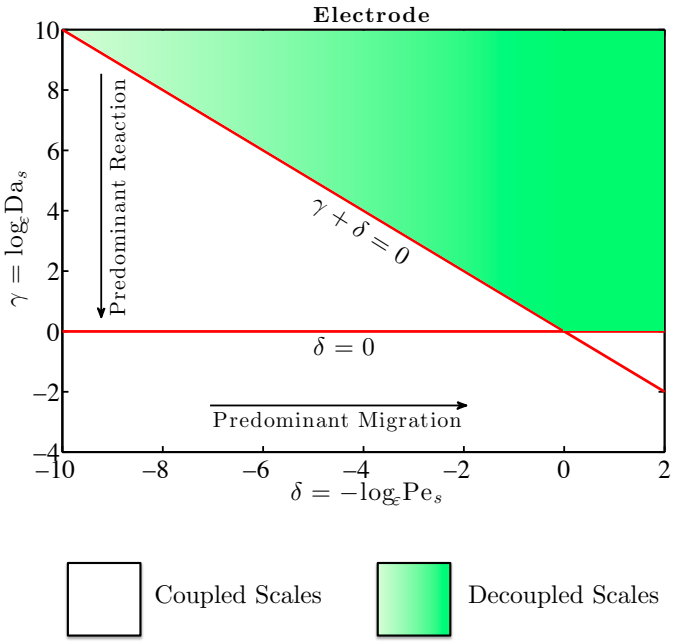

Figure 2.3: Phase diagram specifying the range of applicability of the upscaled equation for the diffusion-reaction of lithium ions in the electrode in terms of Pe_s and Da_s. The green region identifies the conditions under which the macro-scale equations hold. In the white region, micro- and macro-scale equations are coupled and need to be solved simultaneously. Diffusion and reaction are of the same order of magnitude at the point $(\delta, \gamma) = (0, 0)$.

The closure variable, $\boldsymbol{\chi}^s(\mathbf{y})$, has zero mean, $\langle \boldsymbol{\chi}^s \rangle_s = \mathbf{0}$, and is defined as a solution of the local problem

$$\nabla_{\mathbf{y}} \cdot [\mathbf{D}^s(\mathbf{I} + \nabla_{\mathbf{y}} \boldsymbol{\chi}^s)] = 0, \qquad \mathbf{y} \in \mathcal{S}, \tag{2.40a}$$

$$\mathbf{n}_s \cdot [\mathbf{D}^s(\mathbf{I} + \nabla_{\mathbf{y}} \boldsymbol{\chi}^s)] = 0, \qquad \mathbf{y} \in \Gamma. \tag{2.40b}$$

Constraints 2)–3) ensure separation of scales, and depend on the relative importance of the solid phase diffusion, conduction, and reaction mechanisms of transport. Condition 3) simply facilitates the derivation of the effective tensor (2.39). These constraints are summarised in the form of an electrode phase diagram in Fig. 2.3.

2.2.3.3 Physical Interpretation of Applicability Conditions of Macroscopic Models

The constraints identified in section §2.2.3.1 and section §2.2.3.2 impose conditions on the relative magnitude of the main processes controlling lithium-ion transport at the microscale: diffusion and conduction within electrode active particles, ionic diffusion and electromigration in the electrolyte solution, and heteroge-

nous reaction at the electrolyte-electrode interface. The constraints $\mathrm{Da}_e < 1$ and $\mathrm{Da}_s < 1$ require that the intercalation reaction be slower than diffusion processes both in the electrolyte and the electrode. Similarly, $\mathrm{Pe}_e < 1$ requires that diffusion processes in the electrolyte be faster than electromigration. Both conditions guarantee that lithium ions are uniformly distributed, i.e. well mixed, both in the pore-space occupied by the electrolyte and within the electrode active particles at the unit cell scale.

Under well-mixed conditions, i.e. when lithium-ion concentration is locally uniform, a dual-continua macroscale model can describe processes at the micro scale within errors of order $\mathcal{O}(\varepsilon^2)$ as prescribed by the homogenization approach. On the other hand, under diffusion-limited conditions, or high resistance to mass transport, concentration gradients are formed at the sub-pore scale, and the predictability of continuum scale models, which replace pore-scale quantities with their spatial averages, cannot no longer be guaranteed. These findings are consistent with the widespread observation that classical macroscopic approximations loose predictive power under high C-rate [1] operating conditions [142], when a strong current imbalance between electrodes generates sharp concentration gradients at the sub-pore level.

The importance of lack of sub-pore scale mixing was already pointed out by [119], where sub-grid concentration gradients were associated with generation of highly localized heat of mixing. The constraints $\mathrm{Da}_e/\mathrm{Pe}_e < 1$ and $\mathrm{Da}_s/\mathrm{Pe}_s < 1$ suggest that elecromigration can play a favourable role in improving the sub-pore scale mixing in presence of high mass transfer resistance, or diffusion-limited regimes. Finally, the dependence of Pe_e and Pe_s on the operating temperature, see (2.18), demonstrates that isothermal conditions are not sufficient to guarantee macroscale model accuracy: operating the same battery at a higher temperature may lead to the violation of $\mathrm{Pe}_e < 1$ and/or $\mathrm{Pe}_s < 1$, once a critical temperature is reached. A more thorough analysis of temperature-dependent breakdown for different battery chemistry is discussed in section §2.2.3.1. The following section presents a multiscale modeling approach to resolve the electrolyte closure variable problem (2.36) in the unit cell of an electrode microstructure, and utilize the results to determine the effective electrolyte diffusion and conductivity tensors defined in (2.35).

[1] C-rate is defined as the rate of charge or discharge current in normalized form:

$$\text{C-rate} = \frac{I}{Q_{nom}}[1/h]$$

where I is the battery current and Q_{nom} is the rated capacity of the battery. The general expression C/hh indicates that the number of hours to completely discharge the battery at a constant current is hh [141].

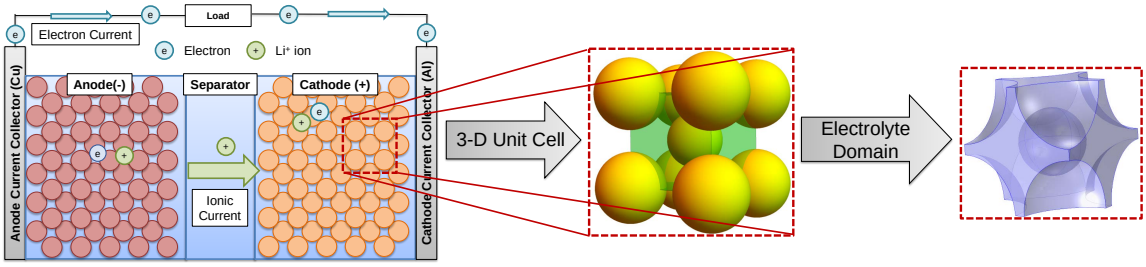

Figure 2.4: Representation of a lithium-ion battery (left), the corresponding 3-D electrode microstructure (middle), and the unit cell in which the closure variable is resolved (right).

2.3 Determination of effective lithium-ion ionic transport properties

2.3.1 Significance of the closure variable

The effective diffusion and conductivity parameters of the homogenized model, defined in (2.35), are resolved by a multiscale approach where the pore-scale closure problem, defined in (2.36), is resolved in the unit cell of the electrodes. This approach allows the incorporation of the microstructural grain distribution in order to estimate the effective parameters. Garcia $et.\ al.$ [143] and Tartakovsky $et.\ al.$ [144] have demonstrated the impact of the underlying electrode morphology on the performance of electrochemical energy storage devices and elucidate the need for optimizing their geometrical configuration. The topology of the porous electrodes is critical for the estimation of their effective material transport properties. The advantage of the closure variable is its ability to assess material performance for different topological structures on the pore-scale. Such information is not captured using empirical approaches such as the such as the Bruggeman approximation [145] which is utilized by the DFN model to approximate the effective diffusion and conductivity coefficients.

2.3.2 Resolution of the unit cell closure problem

The closure variable accounts of the impact of the pore-scale structure and can be determined using offline calculations. As a result, the closure problem can be resolved as a pre-processing step and the effective parameter values can be directly used in the homogenized model equations (2.37) and (2.38). Numerical simulation for the closure problem is performed in a cubic unit cell containing spherical active particles using the computational fluid dynamics solver OpenFOAM [146]. Fig. 2.4 shows the schematic representation of a lithium-ion battery. In this study,spherical active particles were selected to make a direct comparison with the effective parameter values using Bruggeman theory. The cubic unit cell of the electrode is of dimensions

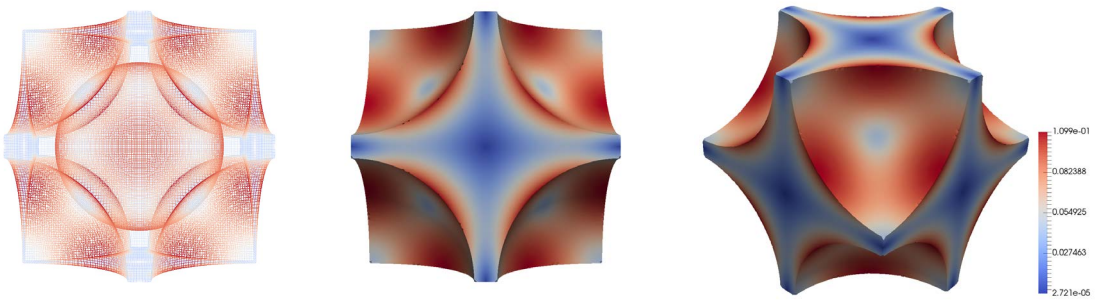

Figure 2.5: Schematic representation of the mesh used to solve for closure variable (left). The 2-D (middle) and 3-D (right) plots represent the magnitude of the resolved closure variable. The porosity of the unit cell considered in this study is equal to 0.40.

$\{10.94\mu\text{m}, 10.94\mu\text{m}, 10.94\mu\text{m}\}$, consists of spherical particles of radius 5μm with centers at each corner of the unit cell, and a spherical particle at the center of the unit cell. This geometrical configuration results in an electrolyte volume fraction of 0.4. Since the closure variable $\boldsymbol{\chi}^e(\mathbf{y})$ is solved in the fast variable $\mathbf{y}$, the size of the unit cell is $\{1,1,1\}$. The dimensions of the spherical particles within the unit cell are also normalized, and they have a dimensionless radius of 0.46. Fig. 2.4 also illustrates the spherical particle configuration in the unit cell and the domain of the electrolyte in a representative unit cell of the electrode.

The closure variable, $\boldsymbol{\chi}^e(\mathbf{y})$, defined in (2.36), is solved in the electrolyte domain of the unit cell using $laplacianFoam$. The mesh in which the finite volume analysis is performed is prepared with $snappyHexMesh$, with standard sets of parameters, and is shown in Fig. 2.5. The discretized equations are solved using standard linear solvers. The boundary conditions for the closure problem are implemented through the extension $groovyBC$ of the OpenFOAM library $swak4Foam$. The boundary condition for the closure variable is imposed at the interface separating the spherical active particles and the electrolyte. Figure 2.5 represents the distribution of the resolved closure variable in the electrolyte domain. The superficial average values of the x-, y-, and z-components of $\boldsymbol{\chi}^e(\mathbf{y})$ are respectively $6.43e-6$, $6.40e-6$, and $6.38e-6$. The results obtained are consistent with the definition of the closure variable, since they satisfy the zero mean criteria, $\langle\boldsymbol{\chi}^e\rangle = \mathbf{0}$, with a numerical accuracy in the unit cell.

The pore-scale diffusion coefficient, $D_{e,j}$, and the pore-scale conductivity coefficient, $K_{e,j}$, are assumed to be constant. $j = \{n, p\}$ represents the electrode under consideration. As a result, the effective diffusion tensor, $\mathbf{D}_{e,j}^{eff}$ and the effective conductivity tensor, $\mathbf{K}_{e,j}^{eff}$, can be determined by computing the superficial average of the tensor $(\mathbf{I} + \nabla_{\mathbf{y}}\boldsymbol{\chi}^e)$. The superficial average of this tensor results in the following

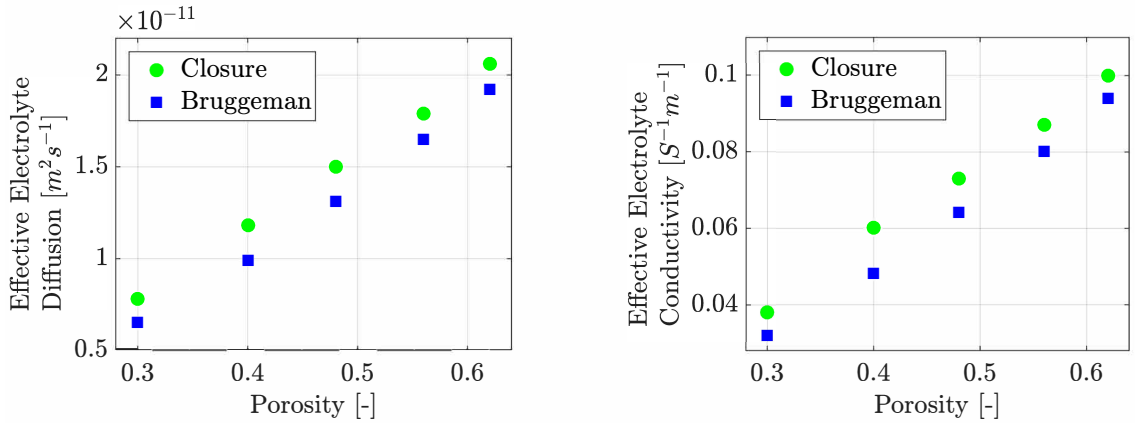

Figure 2.6: Comparison of the effective electrolyte diffusion (left) and effective electrolyte conductivity (right) calculated using the closure and the Bruggeman approach. Effective transport properties increase with porosity, and higher effective parameter values are obtained using the closure approach.

matrix:

$$\begin{bmatrix} 0.299 & -6.63e-10 & -3.62e-7 \\ -4.34e-10 & 0.299 & -1.36e-10 \\ -2.87e-7 & 3e-10 & 0.299 \end{bmatrix} \tag{2.41}$$

The tensor in (2.41) is essentially diagonal, with negligible off-diagonal components. It is also noted that the tensor is isotropic, due to the symmetric nature of the unit cell in which the closure variable was resolved. As a result, the tensor can be expressed as $0.299\ \mathbf{I}$, where $\mathbf{I}$ is the identity matrix. The effective diffusion and conductivity parameters obtained from the closure variable are compared with with the parameter values obtained using the Bruggeman theory [145]. The values of the parameters, $D_{e,j} = 3.94e-11\ m^2 s^{-1}$, and $K_{e,j} = 0.192\ S^{-1}m^{-1}$ are obtained from literature [147]. The effective transport parameters is obtained by

the product of the pore-scale transport coefficients with the tensor $0.299\ \mathbf{I}$:

$$\begin{aligned}
\mathbf{D}_{e,j}^{eff} &= \big(0.299 \cdot 3.94e-11\big)\ \mathbf{I} \quad m^2 s^{-1} \\
&= 1.18e-11\ \mathbf{I} \quad m^2 s^{-1}, \\
\mathbf{K}_{e,j}^{eff} &= \big(0.299 \cdot 0.192\big)\ \mathbf{I} \quad S^{-1} m^{-1} \\
&= 0.060\ \mathbf{I} \quad S^{-1} m^{-1}
\end{aligned} \tag{2.42}$$

The effective electrolyte diffusion and conductivity transport parameters determined by the Bruggeman theory are obtained as follows [148]:

$$\begin{aligned}
D_{e,j}^{eff} &= D_{e,j} \cdot \eta_{e,j}^{1.5} = 3.94e-11 \cdot (0.4)^{1.5} = 0.99e-11 \quad m^2 s^{-1}, \\
K_{e,j}^{eff} &= K_{e,j} \cdot \eta_{e,j}^{1.5} = 0.192 \cdot (0.4)^{1.5} = \ 0.048 \quad S^{-1} m^{-1}
\end{aligned} \tag{2.43}$$

Comparison with an isotropic diagonal element of the closure-based effective parameters indicates that the Bruggeman theory underpredicts the effective parameter values in the electrolyte medium. This can be observed by comparing the results shown in (2.42) and (2.43). This analysis can be extended in a similar manner to determine the effective transport parameters in any electrode and separator, provided information about the unit cell morphology is available through imaging techniques. The closure problem was resolved for the following values of porosity: $\{0.30, 0.40, 0.48, 0.56, 0.62\}$ using a unit cell configuration similar to that shown in Fig. 2.4. In each case, the values of effective diffusion and conductivity were calculated for the closure and the Bruggeman approach. The results of this study are summarized in Fig. 2.6, where the diagonal element of the effective parameter from the closure approach and the effective parameter value from the Bruggeman approach are plotted as a function of the porosity. Both approaches indicate that the effective transport parameters increase with porosity, with the closure-based approach resulting in higher effective parameter values. The results indicate that the geometry of the unit cell strongly influences the effective transport parameters. For the spherical particle geometry, which is one of the simplest structures that can be considered, the Bruggeman theory still under-predicted the effective parameter values by about 20% for a unit cell porosity of 0.40. Such influence of the electrode geometry on the effective parameters could be even more pronounced for complex non-spherical active particles.

2.4 Assessment of the veracity of macroscale electrochemical battery models

Different studies [142, 149, 150] have focused on the development of control strategies and estimation of battery SoC and SoH using electrochemical models. Some of the most popular models on which Partial Differential Equation (PDE) control and estimation strategies are based upon reduced-order formulations [151] and simplified versions [152] of the DFN model. Such models have the advantage of being relatively simple for controller/observer design as they are classical macroscopic/upscaled models which treat the complex porous structure and the electrolyte as superimposed fully-connected continua.

For example, the single particle model (SPM) is based on the key idea that the solid phase of each electrode can be idealized as a single spherical particle, while the electrolyte lithium-ion concentration is constant in space and time [152]. Its governing equations are therefore reduced to the Fick's law in spherical coordinates and can be readily derived from (2.31)-(2.32) and (2.37)-(2.38) under the appropriate model assumptions (e.g. constant $\langle c_e \rangle_{\mathcal{B}}$ and negligible electromigration). Similarly, the DFN model electrolyte transport equations can be obtained from (2.31)-(2.32) by relaxing the assumption that $\langle c_e \rangle_{\mathcal{B}}$ is approximately constant and including the full mass transport equation in the electrolyte phase (2.31), while assuming negligible electromigration.

As such, these macroscopic models formulations are based on the fundamental, and often untested, assumption that separation of scales occurs and, consequently, macroscopic representations of averaged quantities can describe pore-scale processes with an accuracy prescribed by mathematical homogenization. Yet, since their validity is limited to the same constraints identified in section §2.2.3.1 and section §2.2.3.2, they should be used with caution when the sufficient conditions listed above are violated. In sections §2.4.1-§2.4.4, the application of the phase diagrams in Fig. 2.2 and Fig. 2.3 is demonstrated to *a priori* estimate macroscale model accuracy compared to their pore-scale counterparts for different commercially used battery electrodes across different operating temperatures, current rates, and battery aging.

2.4.1 Case Study: Commercial Lithium-ion Batteries

In this section, the validity of the macroscale models is investigated for a series of commercially available batteries in relation to: 1) different electrode chemistry, and 2) different conditions of operation characterized by temperature and current rates of discharge. In particular, the accuracy of continuum-scale models is compared with respect to either their fully resolved (3-D) counterparts (or) with experiment data

as reported in a number of studies [11–17]. More importantly, the predictive performance of the macroscale models is related to the applicability regimes defined in Fig. (2.2) and Fig. (2.3). These phase diagrams serve as a screening tool to *a priori* evaluate continuum model predictivity under variable C-rates of operation.

2.4.1.1 Chemistry dependence of macroscale models

The battery cell parameter data used in this case study are summarized in Table 2.1, based on a variety of electrode and electrolyte compositions at room temperature conditions (T = 298K), and obtained from published literature [11–17]. The different electrodes investigated in this study are: lithium graphite anode (Li_xC_6), lithium cobalt oxide cathode or LCO ($LiCoO_2$), lithium ferrous phosphate cathode or LFP ($LiFePO_4$), lithium titanate anode or LTO ($Li_4Ti_5O_{12}$), lithium nickel manganese cobalt oxide cathode or NMC ($LiNi_{1/3}Mn_{1/3}Co_{1/3}O_2$), and lithium nickel cobalt aluminum oxide cathode or NCA ($Li_xNi_yCo_zAl_{1-y-z}O_2$). The dimensions of the electrode geometry and transport parameters listed in Table 2.1 are: [m] for ℓ and L, [m^2s^{-1}] for D^e anf D^s, [$\Omega^{-1}m^{-1}$] for K^e and K^s, [A·m·mol^{-1}] for k, and [$molm^{-3}$] for c_{max}. ε is a dimensionless quantity. The dimensionless parameters α, β, γ and δ in the electrolyte and electrode phases, calculated using (2.18) and (2.30), are reported in Table 2.2 and plotted on the corresponding phase diagram for the electrolyte and electrode, Fig. 2.7 and Fig. 2.8, respectively.

Among the twelve electrode chemistry considered in this analysis [11–17], ten possess electrolyte effective transport coefficients, i.e. dimensionless numbers (α, β), which do not violate the applicability conditions of macroscale models, see Fig. 2.7. The theory developed in Section 2.2.3 ensures that the homogenized equations in the electrolyte will be able to accurately capture the dynamics at the pore-scale: this is consistent with the numerical simulations performed in [11–17], where DFN-type macroscale models have been successfully used to model transport in the electrolyte phase. On the contrary, two data points (solid symbols in Fig. 2.7), corresponding to LTO and NMC chemistry [16, 17], lie outside of the range of applicability. For these two electrode chemistry, it is not guaranteed that the homogenized equations (2.31) and (2.32) describing electrolyte transport will be effective in capturing the pore-scale transport processes. Again, this is confirmed by the results presented in [16, 17], where a DFN-type model response could not accurately capture experimental data, see Fig. 6 in [17]. Such a discrepancy is understandable: LTO has a very fast intercalation reaction rate (between 6 and 9 orders of magnitude faster than the other chemistry), which leads to mass transport limitations (or reaction-dominated regimes) and lack of pore-scale mixing.

Figure 2.8 shows the data points corresponding to the (δ, γ) values for the battery chemistry electrodes listed in Table 2.1 and calculated in Table 2.2.

Table 2.1: Lithium-ion battery parameters for both electrode and electrolyte phases as reported in [11–17]. The characteristic time scale associated with the heterogeneous reaction is defined according to the unit of k reported in each source, before applying (2.18) to determine the Damköhler numbers Da_e and Da_s.

Electrode	ℓ	L	ε	k	c^s_{max}	D^e	K^e	D^s	K^s	Source
Graphite	1.02e-6	9.85e-5	1.04e-2	6.15e-4	26000	3.94e-11	0.192	9.89e-14	100	[11]
Graphite	2.5e-5	1.62e-4	0.154	7.5e-4	28200	2.93e-10	1.29	1e-13	100	[12]
Graphite	2e-6	7.9e-5	0.025	3.02e-4	31540	2.3e-10	1.323	3.9e-14	2	[13]
Graphite	2e-5	1.13e-4	0.177	3.11e-4	26000	2.6e-10	1	3.9e-14	100	[14]
Graphite	2e-6	3.7e-5	0.054	1.75e-2	16,100	2.6e-10	5.676	2e-16	100	[15]
LCO	2e-5	1.05e-4	0.190	4.36e-4	51000	2.6e-10	1	1e-13	100	[14]
LFP	3.31e-8	9.5e-5	3.48e-4	1.15e-4	22806	3.94e-11	0.192	4.29e-18	0.49	[11]
LFP	2e-6	1.12e-4	0.152	5.68e-4	26390	2.3e-10	1.323	1.25e-15	0.01	[13]
LTO	1.075e-8	9.6e-5	1.12e-4	1.49e7	51385	2e-10	0.38	6.8e-15	100	[16, 17]
NMC	2.4e-6	8.6e-5	0.028	9.92e-3	51385	2e-10	0.38	2.5e-16	139	[16, 17]
NCA	8e-6	8.6e-5	0.093	5.5e-3	49195	2.93e-10	1.29	2e-13	10	[12]
NCA	2.5e-6	2.9e-5	0.086	9.76e-3	23,900	2.6e-1	5.676	3.7e-16	10	[15]

All the data points lie outside the range of applicability of the upscaled equations of lithium-ion transport in the electrode phase, therefore suggesting that full pore-scale models have to be employed to accurately capture lithium-ion transport in the active particles. This is consistent with the numerical approaches used in [11–17], where no upscaled model is used to model lithium transport in active particles, and the transport in the solid electrode is resolved at the microscale using spherical coordinates. It is worth noticing that, since bounds on α, β, γ and δ have to be *concurrently* satisfied, the numerical simulations matched well the experiments only when the conditions on (α, β) were not violated, as discussed earlier.

2.4.1.2 Influence of the operating conditions on macroscale models

Figures 2.7 and 2.8 illustrate the distribution of the dimensionless transport parameters α, β, γ and δ at room temperature in the phase diagrams and enable the *a priori* assessment of the validity of DFN-type macroscale models across different battery chemistry. Such models, on the other hand, might also fail when used for the *proper chemistry* (i.e., the chemistry for which the corresponding α and β data points fall in the applicability regime regions at room temperature) but *improper operating conditions*. For this reason, the

Table 2.2: Dimensionless transport parameters calculated from (2.18) and (2.30) for the different battery chemistry listed in Table 2.1.

Electrode	Da_e [-]	Pe_e [-]	α [-]	β [-]	Da_s [-]	Pe_s [-]	δ [-]	γ [-]	Source
Graphite	1.59e-2	4.98e-2	-0.66	0.91	6.35	1.03e4	2.02	-0.40	[11]
Graphite	4.3e-3	4.16e-2	-1.70	2.92	1.26	9.44e3	4.90	-1.36	[12]
Graphite	1.08e-3	4.85e-2	-0.82	1.86	6.35	4.33e2	1.65	-0.50	[13]
Graphite	1.4e-3	3.94e-2	-1.87	3.79	9.34	2.62e4	5.88	-1.29	[14]
Graphite	2.58e-2	3.61e-1	-0.35	1.25	3.36e4	8.27e6	5.46	-3.57	[15]
LCO	1.82e-3	2.01e-2	-2.36	3.80	4.74	5.22e3	5.16	-0.94	[14]
LFP	2.87e-3	5.68e-2	-0.36	0.74	2.64e4	1.33e6	1.77	-1.28	[11]
LFP	2.87e-3	5.8e-2	-0.71	1.45	5.28e2	8.07e1	1.09	-1.56	[13]
LTO	7.4e7	9.84e-3	-0.51	-1.99	2.18e12	7.62e4	1.24	-3.12	[16, 17]
NMC	4.42e-2	9.84e-3	-1.29	0.87	3.54e4	2.88e6	4.16	-2.93	[16, 17]
NCA	1.67e-2	2.38e-2	-1.57	1.72	2.45	2.70e2	2.36	-1.35	[12]
NCA	1.13e-2	2.43e-1	-0.58	1.83	7.93e3	3.01e5	5.15	-3.66	[15]

veracity of the upscaled equations of mass and charge transport in the electrolyte across battery cell operating conditions is also investigated. In particular, the study presented here focuses on temperature and C-rate of operation and utilizes the electrode-electrolyte system described in [153]. In this work, the authors compared the performance of their (continuum-scale) numerical simulations with experimental data for lithium-ion cells with $\mathrm{Li}_y\mathrm{Mn}_2\mathrm{O}_4$ and $\mathrm{LiNi}_{0.8}\mathrm{Co}_{0.15}\mathrm{Al}_{0.05}\mathrm{O}_2$ cathode materials at different C-rates ranging from C/25 to 10C. The phase diagram analysis is conducted for the $\mathrm{Li}_y\mathrm{Mn}_2\mathrm{O}_4$ cathode material, and can be extended in a similat manner to describe the predictability of macroscale models for the $\mathrm{LiNi}_{0.8}\mathrm{Co}_{0.15}\mathrm{Al}_{0.05}\mathrm{O}_2$ cathode.

The case study analysis relies on the premise that temperature is one of the primary factors that influences the ability of macroscale transport models in capturing battery dynamics at high C-rates. In fact, the battery cell temperature strongly influences transport parameters in the electrolyte phase: k (reaction rate constant), D^e (the electrolyte diffusion coefficient), and K^e (the electrolyte conductivity coefficient). When the influence of temperature on k is much more pronounced than on D^e and K^e, as will be verified in the case of battery operation at high C-rates, ionic diffusion is no longer the dominant mode of transport. In this case, the homogenized transport equations do not accurately capture transport at the pore-scale.

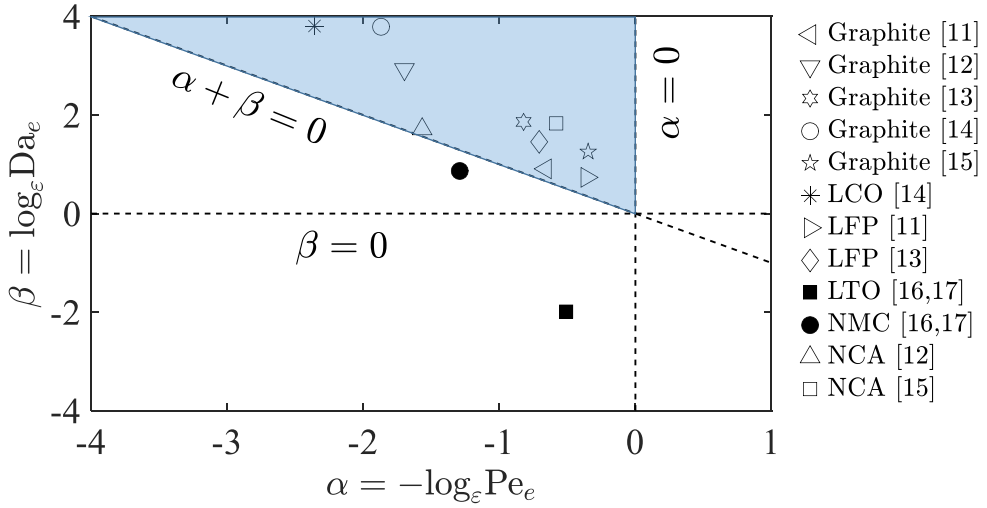

Figure 2.7: Values of the dimensionless parameters (α, β) for the most commonly used lithium-ion battery materials. These values, determined at room temperature (298K), lie either inside the electrolyte applicability regime

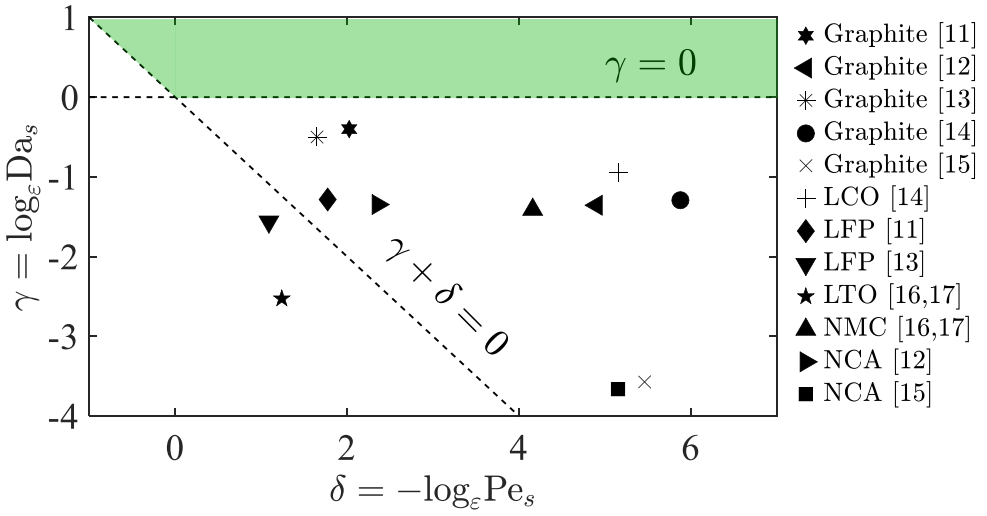

Figure 2.8: Values of the dimensionless parameters (δ, γ) for the most commonly used lithium-ion battery materials. These values, determined at room temperature (298K), all lie outside the electrode applicability regime region.

A single and constant value for the reaction rate k was considered in [153]. Yet, experimental evidence shows significant cell temperature variations in terms of C-rate [154–159]. The analysis presented here is conducted for three different C-rates: low (C/25), medium (1C), and high (10C). Following experimental

data [154–159], the temperature increase, starting from room temperature, can be estimated as follows: from 298K to 299K for C/25 rate of discharge, from 298K to 306K for 1 C-rate of discharge and from 298K to 333K at 10 C-rate of discharge. The reaction rate constant at room temperature (T_{ref} =298K), k_{ref}, is estimated using the following relationship:

$$I_{app} = 2 \cdot k_{ref} \cdot \sqrt{\hat{c}_{\varepsilon}^{e} \hat{c}_{\varepsilon}^{s} \big(1 - \frac{\hat{c}_{\varepsilon}^{s}}{\hat{c}_{\max}^{s}}\big)} \cdot \sinh[F(\hat{\phi}_{\varepsilon}^{s} - \hat{\phi}_{\varepsilon}^{e} - \hat{U})/2RT_{ref}] \tag{2.44}$$

where I_{app} (A/m^2), the applied current density, is provided in [160] for each C-rate, and summarized in Table 2.3. The electrochemical reaction rate constant $k(T)$ for a given electrode system can be described as a function of temperature using the Arrhenius equation, as reported in [56]:

$$k(T) = k_{ref} \, \exp\Big[\frac{Ea_r}{R}\Big(\frac{1}{T_{ref}} - \frac{1}{T}\Big)\Big], \tag{2.45}$$

where $k(T)$ is the reaction rate constant of a given electrode at the desired temperature T. In (2.48), Ea_r is the electrode reaction rate activation energy. Following [161], the value of Ea_r is set to 78.24 kJ/mol at a reference temperature of 298K . Using (2.48), the values of k are computed for different temperature conditions, and used to determine the parameter values α and β as a function of temperature. Similarly,

Table 2.3: Reference reaction rate constants k_{ref} for lithium manganate cathode in terms of applied current I_{app}.

C-rate [1/h]	I_{app} [A/m^2]	k_{ref} [A·m·mol^{-1}]
C/25	0.34	2.03e-5
1C	8.5	5.07e-4
10C	85	5.07e-3

the diffusion and conductivity coefficients, D^e and K^e, vary as a function of both temperature and lithium concentration in the electrolyte phase. For an estimate of D^e and K^e values at the reference temperature T_{ref}, the approach used by [153] has been implemented, where:

$$D^e = 6.5 \cdot 10^{-10} \exp\big(-0.7\frac{\hat{c}_{\varepsilon}^{e}}{1000}\big), \tag{2.46}$$

and

$$K^e = 0.84\Big(\frac{1.134(\hat{c}_\varepsilon^e/1000)}{1+0.2(\hat{c}_\varepsilon^e/1000)+0.08(\hat{c}_\varepsilon^e/1000)^4}+0.1\Big), \tag{2.47}$$

Based on [153], the electrolyte concentration varies in the range of 1,000 to 2,000 mol/m^3 over the entire duration of the simulations. As a result, an averaged value is considered for lithium concentration in the electrolyte: $\hat{c}_\varepsilon^e = 1500$ mol/m^3. This leads to reference values of 2.41e-10 m^2/s and 0.922 S/m for D^e and K^e, respectively. Since no analytical dependence on temperature is available for D^e and K^e, a curve fitting procedure was applied on figures 13 and 14 in [162] to determine $D^e(T)$ and $K^e(T)$. A summary of the estimated parameters for different C-rates and temperature ranges is presented in Table 2.4. The values of the electrode geometrical parameters, ℓ and L, are respectively 3.4e-6 [m] and 100e-6 [m], which yields a valaue of 0.034 for the scale separation parameter ε. From the above calculations, the temperature-dependent trajectories of data points (α,β) were determined at the temperature intervals characteristic of each C-rate. Table 2.4 summarizes the variation of parameters α and β as a function of the operating conditions for the three C-rates of interest. The data points and their variation with temperature and C-rate are schematically represented in Fig. 2.9.

Figure 2.9 (top) illustrates that at 1/25 C-rate of discharge, there is minimal temperature increase over the duration of a discharge event. The magnitude of parameter α remains invariant, while β increases slightly due to an increase in the Da$_e$ number. The behavior of the system (as a function of temperature) is linear with β. The data points satisfy the constraints on α and β. Hence, the upscaled equations for lithium mass transport should provide an accurate description of the pore scale behavior. This is consistent with the simulation results from a continuum-scale simulator obtained in [153], where there is a perfect match between the model and the experimental response.

At 1 C-rate of discharge, illustrated in Fig. 2.9 (middle), there is a moderate increase in temperature over the duration of the simulation cycle. The magnitude of parameter α remains invariant, while β increases at a moderate rate due to a faster increase in the Da$_e$ number. The behavior of this system is linear in α and β. At elevated temperatures, the effect of increase in the reaction rate constant k dominates any increase of D^e and K^e. The data points satisfy the constraints on α and β over the range of operating temperature conditions. Hence the homogenized set of transport equations used in [153] still provide an accurate description of the pore scale behavior, leading to good correlation with experimental data.

At 10 C-rate of discharge, illustrated in Fig. 2.9 (bottom), there is a very significant increase in the

Table 2.4: Dimensionless transport parameters of $Li_yMn_2O_4$ cathode for different C-rates and temperatures.

C-rate [1/h]	k	T [K]	D^e	K^e	Da_e [-]	Pe_e [-]	α [-]	β [-]
C/25	2.03e-5	298	2.41e-10	0.922	8.72e-5	4.26e-2	-0.93	2.76
C/25	2.07e-5	298.2	2.41e-10	0.922	8.91e-5	4.26e-2	-0.93	2.76
C/25	2.12e-5	298.4	2.41e-10	0.922	9.1e-5	4.27e-2	-0.93	2.75
C/25	2.16e-5	298.6	2.41e-10	0.922	9.29e-5	4.27e-2	-0.93	2.75
C/25	2.25e-5	299.0	2.41e-10	0.922	9.69e-5	4.27e-2	-0.93	2.73
1C	5.07e-4	298	2.41e-10	0.922	2.18e-3	4.26e-2	-0.93	1.81
1C	6.26e-4	300	2.55e-10	0.972	2.55e-3	4.28e-2	-0.93	1.77
1C	7.70e-4	302	2.69e-10	1.022	2.97e-3	4.29e-2	-0.93	1.72
1C	9.45e-4	304	2.82e-10	1.072	3.47e-3	4.31e-2	-0.93	1.67
1C	1.16e-3	306	2.96e-10	1.122	4.05e-3	4.33e-2	-0.93	1.63
10C	5.07e-3	298	2.41e-10	0.922	2.18e-2	4.26e-2	-0.93	1.13
10C	8.54e-3	303	2.75e-10	1.047	3.21e-2	4.30e-2	-0.93	1.02
10C	2.30e-2	313	3.44e-10	1.297	6.93e-2	4.41e-2	-0.92	0.79
10C	5.84e-2	323	4.13e-10	1.547	1.47e-1	4.52e-2	-0.92	0.57
10C	1.40e-1	333	4.82e-10	1.797	3.01e-1	4.64e-2	-0.91	0.35

battery temperature over the operating conditions. There is a very small increase in α as the increase in D^e marginally dominates the increase in K^e, leading to an incremental increase in the Pe_e number. The reaction rate constant is 2 to 3 orders of magnitude higher than at lower C-rates, due to which the rate of decrease in β is higher than the rate of increase in α. For the $LiMn_2O_4$ cathode system, the macroscale transport equations are no longer accurate in describing microscale transport processes at temperatures 313K or higher. This is because the value of $\alpha + \beta$ is less than 0, which violates one of the three constraints on these two parameters. At high operating temperatures and C-rates, the lithium manganate cathode system is represented in a transport regime where the three lithium transport processes (reaction, diffusion, and electro-migration) are of the same order. In this scenario, very fast reaction kinetics lead to diffusion-limited regimes where

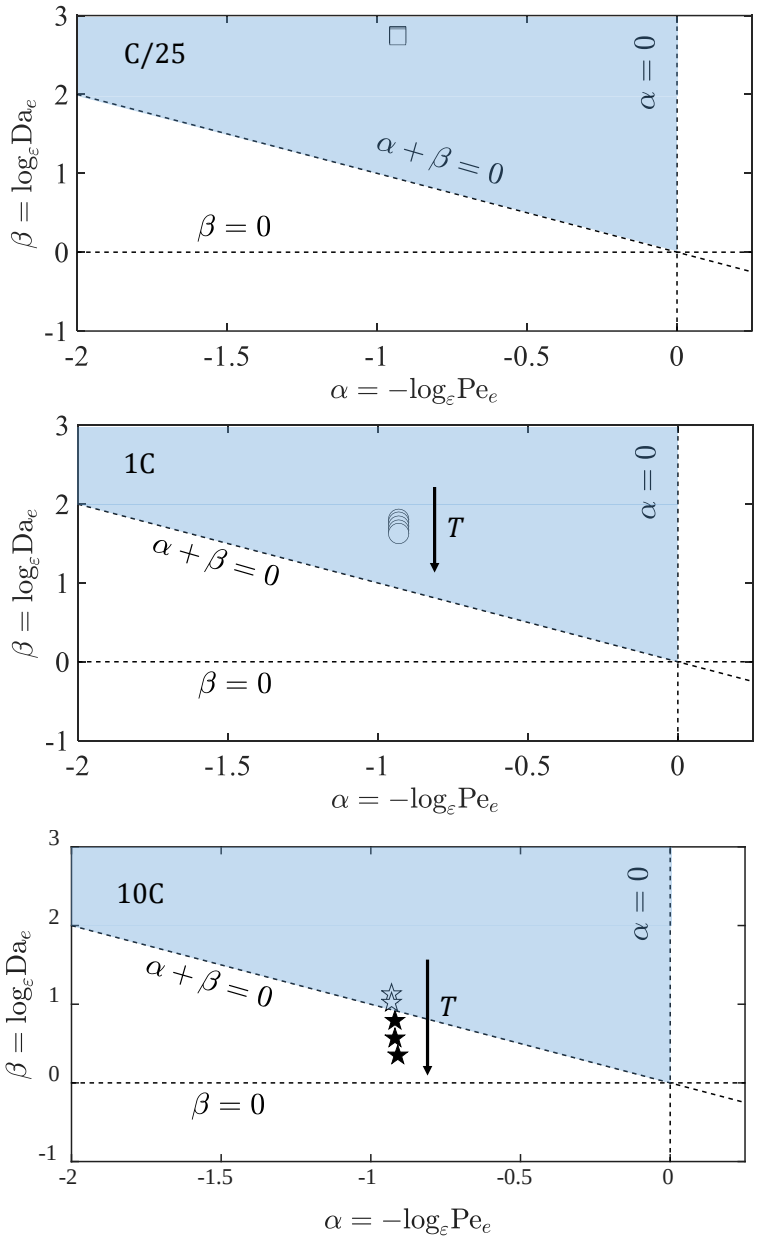

Figure 2.9: Phase diagram parameters (α,β) in lithium manganate cathode batteries for three C-rate of discharge: C/25 (top), 1C (middle), and 10C (bottom). Neglible temperature variation in the first scenario results in nearly constant α and β values inside the applicability regime, represented by square data points (empty symbols). In the second scenario, moderate temperature variation results in faster reaction kinetics and increase in β, while α is constant. The applicability constraints are satisfied, hence the circular data points lie within the blue region (empty symbols). The third scenario is characterized by rapid temperature increase and very fast reaction kinetics. This drives the data points out of the applicability regime beyond a critical temperature, and these conditions are depicted by the star shaped data points (filled symbols).

diffusion is no longer the dominant transport mechanism in the medium. As a result, macroscale equations describing electrolyte transport are vulnerable and can be invalidated due to lack of scale separation with respect to the pore-scale.

The performance prediction of continuum-scale models based on the phase diagram Fig. 2.9 (bottom) is, again, consistent with the analysis performed by [153], where the numerical solution obtained from macroscopic models cannot capture the experimental results. Under these circumstances, a multi-scale model is necessary to incorporates the effects of transport both at the pore-scale and the macroscopic scale. The approach implemented above is significant in terms of identifying the temperature of operation and C-rate of current charge/discharge as crucial parameters that dictate the dominance of one transport mechanism over the other(s) in the battery electrode/electrolyte medium. Standard DFN-type macroscopic models under scenarios similar to the one described above are invalid and may fail to capture microscale transport processes. *Better* battery models need to be developed to accurately predict battery response under these conditions.

2.4.2 Temperature-influenced Predictability of Macroscale Models

In the process of developing a more predictive model, there is a need to identify the operating conditions where effective macroscale transport equations would break down. The premise of this study is to determine *a priori* if there is a critical temperature of operation beyond which macroscopic transport equations are incapable of describing the microscale dynamics of a different battery systems. The values of parameters α and β are determined as a function of temperature for different electrodes to ascertain if DFN-type macroscopic models are the most appropriate modeling tools across different operating temperatures.

The key parameters of interest in this temperature-based phase diagram study are: the electrochemical reaction rate constant k [A $\cdot$ m$^{2.5}\cdot$mol$^{-1.5}$], the electrolyte pore-scale diffusion coefficient D^e [m$^2\cdot$s^{-1}], the electrolyte pore-scale conductivity coefficient K^e [S $\cdot$m^{-1}], battery operating temperature T [K], the scale separation parameter $\varepsilon = \ell/L$, and the maximum electrode lithium storage concentration c^s_{max} [mol $\cdot$ m^{-3}]. In the electrolyte phase, the separator is treated as an inherent property of the electrolyte. For this reason, the value for the macroscale characteristic length L is taken as the combined thickness of the electrode and separator, expressed in m. The value for the microscale characteristic length ℓ is taken as the average diameter of the active particles in the electrode, expressed in m. ℓ, L, and c^s_{max} are considered invariant with respect to temperature in this study. Following these consideration, the the effect of temperature is investigated on the transport parameters k, K^e, and D^e.

The initial phase of this study involved plotting the data points (α,β) in the phase diagram for

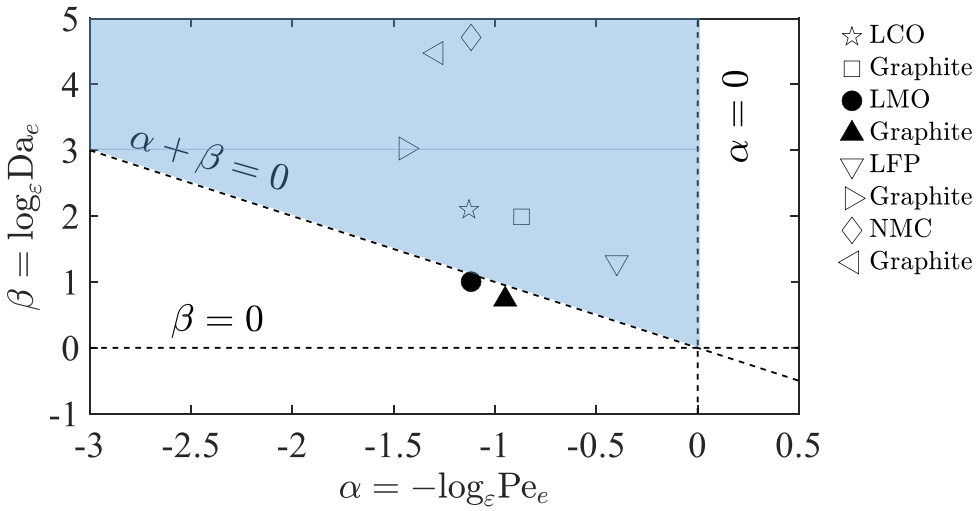

Figure 2.10: Electrolyte phase diagram representing the dimensionless parameters (α,β) evaluated at 25°C for commonly used lithium-ion battery electrodes. The data points with empty symbols in the blue region represent operation conditions where the applicability constraints are satisfied. The two data points with filled symbols in the white region represent operating conditions that violate the constraint ($\alpha + \beta \geq 0$).

eight different battery electrode chemistries whose key parameters were provided under room temperature conditions (298K). This is illustrated in Fig. 2.10. These battery compositions chosen in this study are the most commonly used cathode materials in commercial lithium-ion batteries. The first battery system consists of a graphite anode and LCO cathode, and the electrolyte is composed of 1.2 M of $LiPF_6$ salt dissolved in a 1:2 v/v mixture of ethylene carbonate and dimethyl carbonate (EC:2DMC). All parameter values for this system were obtained from [163] and [164]. The second battery system consists of graphite anode and lithium manganese dioxide (LMO) cathode, and the polymer electrolyte is comprised of $LiClO_4$ salt dissolved in polyethylene oxide. Parameter values for this system have been obtained from [165] and [166].

The third battery system consists of a graphite anode and LFP cathode. The parameter values have been procured from [167]. The fourth battery chemistry is composed of graphite anode and NMC cathode. The parameter values have been acquired from [168]. The phase diagram of Fig. 2.10 indicates that the battery systems composed of LFP, LCO, and NMC cathodes have parameters that fall in the shaded region of our phase diagram in Fig. 2.2. This implies that the macroscale mass transport equation is capable of describing the porous medium composed of these materials. However, the system containing LMO cathode and graphite anode must also utilize the microscale equations in order to describe electrolyte transport dynamics in the medium. When compared with the other three chemistries, this observation is attributed to a combination of

two factors: the lower value of the scaling parameter ε coupled with faster kinetics of lithium transport at the reaction interface. This implies that the active material and porous electrode structure play an important role in determining the validity of the electrochemical model at a given operating condition.

To emphasize the importance of these two factors, another lithium ion battery chemistry composed of lithium manganate cathode and lithium graphite anode is studied. The electrolyte is composed of 1.0 M of $LiPF_6$ salt dissolved in a 3:7 v/v mixture of ethylene carbonate and ethyl methyl carbonate. The values for ionic conductivity in the electrolyte have been reported as a function of temperature in [169]. Valøen and Reimers have reported the variation in the ionic diffusion coefficient for this system for different temperatures in [162]. By applying a cubic spline interpolation, the ionic diffusivity were computed for intermediate operating temperatures in the regions of interest in this study. The values obtained were in agreement with those reported by Nyman *et al.* in [170].

The electrochemical reaction rate constant k for a given electrode system is described as a function of temperature using the Arrhenius equation [158, 171]:

$$k_j(T) = k_{j,ref} \cdot exp\Big[\frac{Ea_{r,j}}{R}\Big(\frac{1}{T_{ref}} - \frac{1}{T}\Big)\Big]. \tag{2.48}$$

$k_j(T)$ and $k_{j,ref}$ are the reaction rate constants of electrode j at the desired temperature T and the reference temperature T_{ref}, respectively. $Ea_{r,j}$ is the reaction rate activation energy of electrode j. For the system of electrodes considered in this study, the values of $k_{j,ref}$ and $Ea_{r,j}$ are provided in [172] for a reference temperature of 298K. The parameter values necessary to determine α and β for this system are also presented here. Using (2.48), the values of k are computed for different temperatures of interest.

The phase diagrams for graphite anode and LMO cathode are presented in Fig. 2.11 and Fig. 2.12, respectively. In this case, both the systems exhibit a similar behavior. The magnitude of parameters α and β increase at a nearly equal rate with the operating temperature, since a line joining these data points would almost be parallel with the line α + β = 0. This indicates that the behavior of the system (as a function of temperature) is a linear function in α and β. At elevated temperatures, the effect of increase in k is compensated by the increase in D^e, leading to only a small change in β. Similarly, the small change in α at elevated temperatures is a result of increase in K^e compensated by increase in D^e. For these systems, the data points satisfy the constraints on α and β over the range of operating temperature conditions. Hence the upscaled equations of lithium transport in the electrolyte should provide an accurate description of pore-scale behavior. In this system, increasing temperature caused data points (α,β) to shift further inside the domain

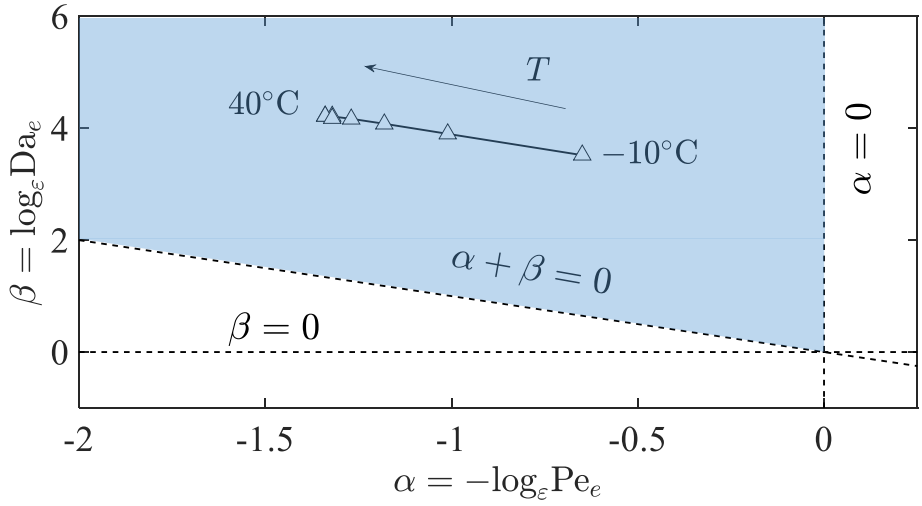

Figure 2.11: Representation of parameters α and β in the phase diagram for graphite anode as a function of temperature. The data points satisfy the applicability constraints for the range of temperatures considered. Hence the triangular data points (empty symbols) stay within the blue region.

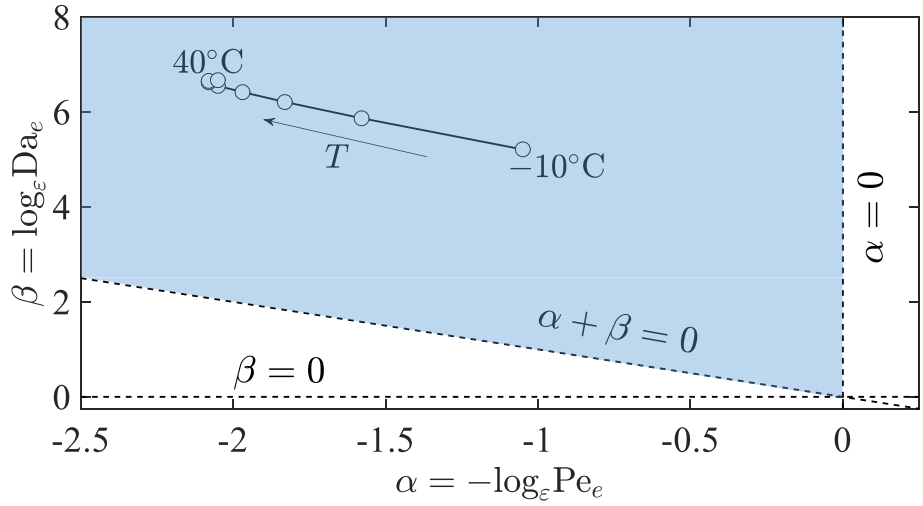

Figure 2.12: Representation of parameters α and β in the phase diagram for LMO cathode as a function of temperature. The data points satisfy the applicability constraints for the range of temperatures considered. Hence the circular data points (empty symbols) stay within the blue region.

of interest. It is also possible for the dimensionless parameters to exhibit a contrasting behavior. Such case studies are presented below by investigating the effect of increasing temperature for three different cathode

chemistries: NMC, LFP, and LCO. The electrolyte used in these systems consists of $LiPF_6$ salt dissolved in an organic solvent mixture of propylene carbonate, ethylene carbonate, and dimethyl carbonate.

The parameters necessary to compute α and β for the Li NMC battery system are derived from [173]. Since the electrolyte material considered is common for all the three cathode materials, the ionic diffusivity D^e and ionic conductivity K^e equations for LFP and LCO are also utilized from this journal. The phase diagram for the lithium nickel manganese cobalt oxide cathode system is presented in Fig. 2.13. Values for the reaction rate constant k for LFP are determined using the Arrhenius equation (2.48). The parameter values for LFP are provided in [167] and the value of the reaction rate activation energy is obtained from [174]. The phase diagram for the LFP cathode system is presented in Fig. 2.14. The reaction rate constant expression (2.48) is also used for the LCO system. The parameter values for LCO are provided in [175] and the value of the reaction rate activation energy is obtained from [176]. The phase diagram for the lithium cobalt oxide cathode system is presented in Fig. 2.15.

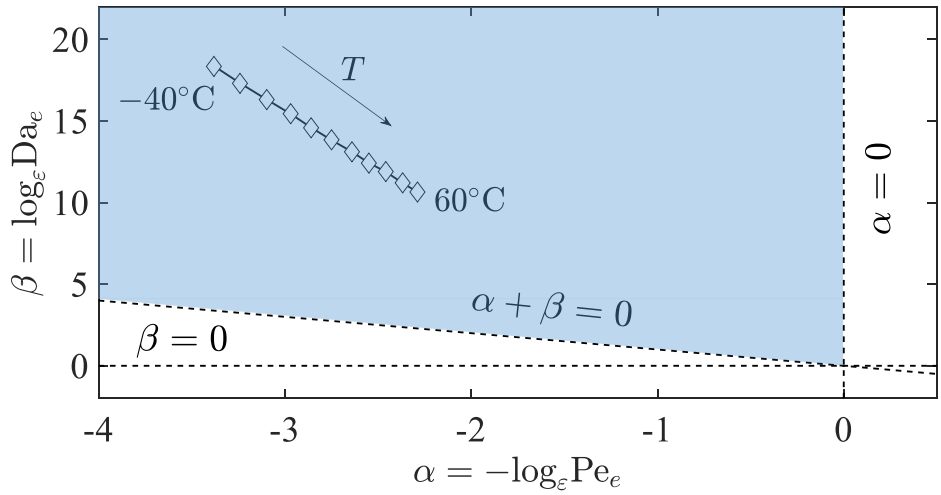

Figure 2.13: Representation of parameters α and β in the phase diagram for NMC cathode as a function of temperature. The data points satisfy the applicability constraints for the range of temperatures considered. Hence the rhombus data points (empty symbols) stay within the blue region.

In analyzing the phase diagrams depicted in Fig. 2.13 to Fig. 2.15, it is inferred that for all the three cathode systems, the value of α increased and the value of β decreased with increasing operating temperature. In comparison, the relatively very slow kinetics of reaction at the NMC-electrolyte interface resulted in significantly higher values for β for this system. For the LFP and LCO systems, the kinetics of the interface

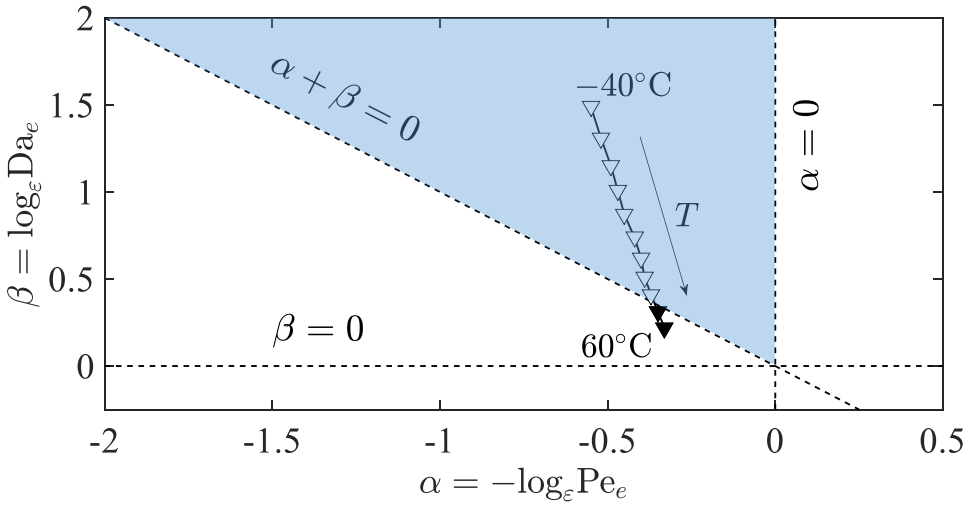

Figure 2.14: Representation of parameters α and β in the phase diagram for LFP cathode as a function of temperature. The applicability constraint ($\alpha+\beta \geq 0$) is violated beyond 50°C, and these operating conditions are represented by the triangular data points (filled symbols) in the white region.

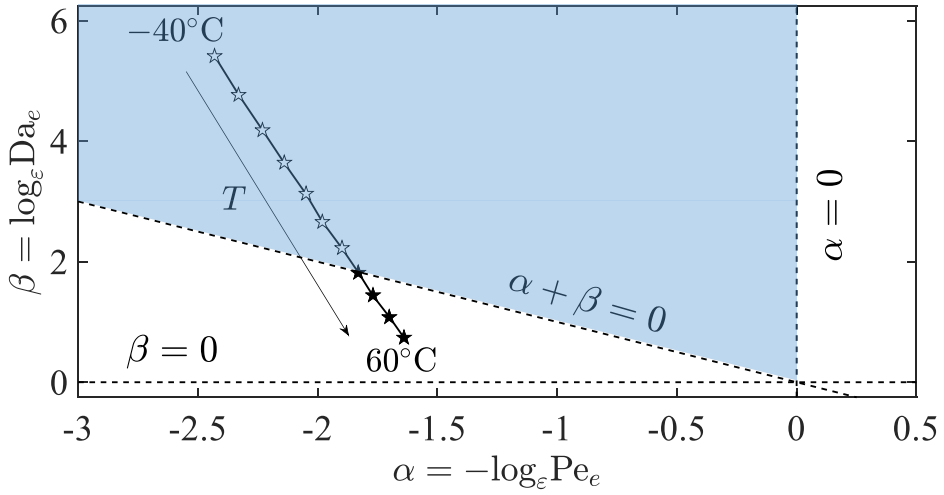

Figure 2.15: Representation of parameters α and β in the phase diagram for LCO cathode as a function of temperature. The applicability constraint ($\alpha+\beta \geq 0$) is violated beyond 30°C, and these operating conditions are represented by the star shaped data points (filled symbols) in the white region.

reaction were several order of magnitude higher than the Li NMC system, and with increasing temperature, the rate of decrease in β was higher than the rate of increase in α. For the NMC system, it is noted that the

upscaled equation of mass transport is valid for the entire range of operating temperatures considered. However, for the LFP system, the macroscale equation is no longer accurate in describing microscale transport processes at temperatures 323K and higher. For the LCO system, beyond 303K, the microscale equation of mass transport must be simultaneously solved with the upscaled equation. This is because the value of $\alpha + \beta$ is less than 0.

For the battery chemical compositions considered in this study, it is observed that α and β vary linearly with temperature. The key transport parameters k, K^e, and D^e exhibit an exponential behavior with temperature, and the logarithmic dependence of α and β on the scale separating parameter ε results in a linear relationship of the data points with temperature. The NMC cathode system can be represented in the transport regime where diffusion and migration are of the same order (comparable) and dominate the reaction transport mechanism. The upscaled equations of such systems can also be reduced to a simpler form. The LFP and LCO system are represented in the transport regime where all three lithium transport processes are of the same order. Macroscale equations describing such systems are vulnerable to the effect of the operating temperature and may fail to describe battery physics at the microscopic level.

2.4.3 Impact of Capacity Fading on Pore-scale Transport Parameters

As batteries age, their performance degrades due to capacity and power fading. Capacity fade is the loss of cyclable lithium ions as a result of electrode degradation and leads to the depletion of the electrode energy storage capacity. Lithium-ion batteries age differently as a consequence of their operating patterns. Their utilization behavior greatly determines the extent of capacity fading due to cyclic aging and the eventual end of life of the battery. Among the different aging mechanisms, the SEI layer growth has been the most influential cause of battery capacity degradation. Many studies have identified this growth at the anode during galvanostatic and dynamic operating conditions.

During cycling, the SEI layer forms between the anode and electrolyte. Initially, this layer acts as a protective barrier, allowing lithium ion transfer while keeping the electrolyte separated physically from the anode. The continued growth that occurs during cycling will increase the resistive layer and remove active lithium from the cycling system. Gradually, this leads to diminishing energy and power capacity of the battery. This study evaluates the predictability of macroscopic models as a function of the battery state-of-health (SoH), and is initiated by formulating mathematical expressions to determine the transport parameters Da_e and Pe_e as a function of battery aging due to the SEI layer growth.

The capacity fade analysis explored in this study is based on the work of Prada *et. al.* in [177]. The evolution of the SEI layer at the anode surface in [177] is based on solvent diffusion and single particle approximation [160]. A lumped parameter approach is used to describe the variation in the negative electrode porosity. No active material deformation is considered, and the loss of cyclic lithium ions is the main capacity loss mechanism. Assuming that the loss of cell capacity Q_{cell} is exclusively due to the loss of cyclable Li-ions in the negative electrode due to the side reaction after de-lithiation, then [177]

$$\frac{dQ_{cell}}{dt} = S_n \cdot i_s, \tag{2.49}$$

where S_n is the electroactive surface area of the negative electrode and i_s is the current density of the side-reaction leading to the formation of the SEI layer. S_n is related to the geometrical parameters of the electrode as [177]

$$S_n = 3 \cdot \eta_{s,n} \cdot L_{neg} \cdot A_{cell}/R_{s,n}. \tag{2.50}$$

In (2.50), $\eta_{s,n}$ is the anode porosity, L_{neg} is the thickness of the anode, A_{cell} is the cell cross-sectional area, and $R_{s,n}$ is the radius of the anode active particle. The growth rate of the SEI layer can be expressed using the current density of the SEI layer side-reaction current, [177]

$$\frac{\delta_{SEI}}{dt} = -\frac{i_s}{2F} \cdot \frac{M_{SEI}}{\rho_{SEI}}, \tag{2.51}$$

with M_{SEI} the molar mass of the SEI layer, ρ_{SEI} the density of the SEI layer. Combining (2.49), (2.50), and (2.51), an expression for the SEI layer growth is postulated as a function of time:

$$\delta_{SEI,t} = \delta_{SEI,0} + \frac{M_{SEI}}{2 \cdot F \cdot S_n \cdot \rho_{SEI}} \cdot (Q_0 - Q_t) \tag{2.52}$$

where $\delta_{SEI,0}$ and Q_0 are the initial SEI layer thickness and capacity, and $\delta_{SEI,t}$ and Q_t are the SEI layer thickness and capacity at a later time $t > 0$. (2.52) is postulated based on the knowledge of the initial SEI layer thickness. In most cases, as indicated in [177], this value is estimated. The battery capacity is determined by considering that the anode provides all the cyclic lithium ions that travel across the electrolyte to the cathode. Assuming discharge conditions, Q_t is expressed in terms of the applied current, I_{app}, and the time at the

beginning and end of discharge, t_0 and t_f, respectively as follows,

$$Q_t = \int_{t_0}^{t_f} I_{app} \cdot dt \tag{2.53}$$

Q_t can be expressed in terms of the maximum lithium-ion concentration in the anode, $c^s_{max,n,t}$, as [177]

$$Q_t = \eta_{s,n} \cdot z \cdot c^s_{max,n,t} \cdot A_{cell} \cdot L_{neg} \cdot F \cdot \big(x_{100\%,n} - x_{0\%,n}\big). \tag{2.54}$$

In (2.54), z is the valence number, $x_{100\%,n}$ is the stoichiometric coefficient at 100% SoC, and $x_{0\%,n}$ is the stoichiometric coefficient at 0% SoC. The value of $c^s_{max,n,t}$ as a function of aging can be determined by equating the cell capacity from the assessment tests in the expression for Q_t.

The effective electrolyte conductivity, $K^{eff}_{e,n}$, decreases due to cell aging according to the following relationship, due to the growth of the SEI layer thickness at the outer surface of the anode active material [177]

$$K^{eff}_{e,n} = K^e \cdot \left\{1 - \eta_{f,n} - \eta_{s,n}\left(1 + \frac{3\delta_{SEI,t}}{R_{s,n}}\right)\right\}^{1.5} \tag{2.55}$$

In the above expression, $\eta_{f,n}$ is the porosity of the filler material in the anode, and K^e is the electrolyte conductivity in the microscale. The power factor of 1.5 is obtained by incorporating the Bruggeman relationship to determine the effective conductivity in the electrolyte [177]. An expression is then postulated for the microscopic electrolyte conductivity K^e_{ag}, in which aging effects are incorporated using the following relationship:

$$K^{eff}_{e,n} = K^e_{ag} \cdot (\eta_{e,n})^{1.5} \tag{2.56}$$

No description has been reported till date in published literature on the impact of SEI layer growth on pore-scale parameters. Since their impact on effective transport parameters has been described in [177], this information is incorporated while postulating the expression (2.56). Combining (2.55) and (2.56),

$$K^e_{ag} = \frac{K^e}{(\eta_{e,n})^{1.5}} \cdot \left\{1 - \eta_{f,n} - \eta_{s,n}\left(1 + \frac{3\delta_{SEI,t}}{R_{s,n}}\right)\right\}^{1.5}. \tag{2.57}$$

Similarly, a parameter D^e_{ag} is postulated for the electrolyte diffusion as a function of aging. The effective

electrolyte diffusivity of lithium ions in the anode, $D_{e,n}^{eff}$, decreases due to cell aging as: [177]

$$D_{e,n}^{eff} = D^e \cdot \left\{1 - \eta_{f,n} - \eta_{s,n}\left(1 + \frac{3\delta_{SEI,t}}{R_{s,n}}\right)\right\}^{1.5}. \tag{2.58}$$

Therefore, the microscopic electrolyte diffusion D_{ag}^e which incorporates the effect of the SEI layer growth (aging) is

$$D_{ag}^e = \frac{D^e}{(\eta_{e,n})^{1.5}} \cdot \left\{1 - \eta_{f,n} - \eta_{s,n}\left(1 + \frac{3\delta_{SEI,t}}{R_{s,n}}\right)\right\}^{1.5}. \tag{2.59}$$

For isothermal macroscopic models which do not incorporate aging effects, the microscopic transport parameters are re-defined considering the the effect of aging using (2.57) and (2.59). The Damköhler and Péclet numbers for the electrolyte are then defined as a function of the aging parameters:

$$\text{Da}_e = \frac{L_{neg}k}{FD_{ag}^e} = \frac{L_{neg}k}{FD^e} \cdot \frac{(\eta_{e,n})^{1.5}}{\left\{1 - \eta_{f,n} - \eta_{s,n}\left(1 + \frac{3\delta_{SEI,t}}{R_{s,n}}\right)\right\}^{1.5}}, \tag{2.60}$$

$$\text{Pe}_e = \frac{RTK_{ag}^e}{D_{ag}^e F^2 c_{max,n,t}^s} = \frac{RTK^e}{D^e F^2 c_{max,n,t}^s}. \tag{2.61}$$

2.4.4 Aging-influenced Predictability of Macroscale Models

The subsection investigates the the impact of the SEI layer growth on the applicability conditions of macroscale electrolyte transport equations by conducting an analytical study of moderate and aggressive battery galvanostatic discharge as a function of the battery SoH. The phase diagram analysis has been until now implemented to study the robustness of macroscopic models at a given state of health. This study focuses on evaluating the ability of macroscopic models to predict the behavior of battery cells as they age. Data for this study is obtained from [178]. Accelerated aging experimental tests were conducted on lithium-ion pouch cells of blended cathodes NMC-LMO (nickel-manganese-cobalt oxide-lithium manganese dioxide). Intermittent cell characterization tests (capacity test in discharge, and hybrid pulse power characterization (HPPC)) were conducted to assess the energy and power capability of these cells as a function of their SoH. Experimental data from these capacity tests have been utilized for this analysis. The following assumptions have been made to facilitate this study:

1. The effect of the relaxation phase of the pulse train event on the growth of the SEI layer is negligible compared to the positive and negative pulse events during cyclic aging.

2. The assessment tests conducted for cell characterization have minimal impact on the SEI layer growth compared to the accelerated aging experiment.

3. The SEI layer is formed only at the anode during charging/discharging events, and is assumed to uniformly grow at the outer surface of the active anode particle.

The target application for the lithium-ion pouch cells analyzed in this study is plug-in hybrid electric vehicles (PHEVs), which operate under charge-depleting (CD) and charge-sustaining modes (CS). The power demand of the CD and CS micro-cycles described in [178] indicates that the pouch-cell under investigation operates in discharge mode between C-rates of 1 and 10. The phase diagram analysis is conducted for two current rates of galvanostatic discharge of the pouch cell: 1 C-rate (moderate) and 10 C-rate (high). The galvanostatic discharge is considered to begin with a battery SoC of 100%. This analysis is used to evaluate model predictability when the cell is tested at two different health conditions: 100% SoH (fresh) and 86% SoH (aged).

Model parameters used to assess the veracity of macroscale models as a function of the pouch cell SoH were obtained from [53, 158, 179]. This analysis investigates the impact of C-rate of operation, temperature, and SoH on the micro-scale transport parameters (k, D^e, and K^e). The reaction rate constant at room temperature (T_{ref} = 298K) is determined from the applied current I_{app} using the expression:

$$\frac{I_{app}}{A_{cell}} = 2 \cdot k_{ref} \cdot \sqrt{\hat{c}_\varepsilon^e \hat{c}_\varepsilon^s \left(1 - \frac{\hat{c}_\varepsilon^s}{c_{max}^s}\right)} \cdot \sinh[F(\hat{\phi}_\varepsilon^s - \hat{\phi}_\varepsilon^e - \hat{U})/2RT_{ref}]. \tag{2.62}$$

The stoichiometric coefficient x is used to determine the value of c_ε^s from the cell SoC and c_{max}^s. The value of c_ε^e is set to 1,000 mol/m^3. The value of the cell overpotential is taken as 100mV for this analysis based on values reported in [158]. The scale separation parameter $\varepsilon = \frac{2R_{s,n}}{L_{neg}}$ is the ratio of the anode particle diameter (25μm) and anode thickness (162μm).

In order to determine Da$_e$ as a function of aging, k must be determined as $c_{max,n,t}^s$ decreases with the SEI layer growth. The anode reaction rate constant $k_{ref,n}$ is determined assuming galvanostatic discharge at the anode. Table (2.5) presents the values of $k_{ref,n}$ determined as a function of the C-rate of discharge and $c_{max,n,t}^s$. Table (2.6) summarizes the results of the capacity fading analysis performed on the lithium-ion pouch cell. Using this information, the variation of the phase diagram parameters (α,β) is determined for galvanostatic discharge at 1 C-rate and 10 C-rate for a fresh pouch-cell (SoH = 100%) and an aged pouch-cell (SoH = 86%). Based on prior experimental data [156, 158, 180, 181] and assuming the discharge to begin at an initial cell temperature of 298K, the cell temperature is estimated to increase from 298K to 306K for 1

Table 2.5: Reference reaction rate constant $k_{ref,n}$ in terms of the applied current I_{app} as a function of its SoH and C-rate.

SoH [%]	$c^s_{max,n,t}$ [mol/m^3]	C-rate [1/h]	$\frac{I_{app}}{A_{cell}}$ [A/m^2]	$k_{ref,n}$ [A·m/mol]
100	31,833	1	2.84	1.94e-4
86.4	27,499	1	2.84	2.09e-4
100	31,833	10	28.4	1.94e-3
86.4	27,499	10	28.4	2.08e-3

Table 2.6: Lithium-ion pouch cell parameters determined from capacity fading analysis.

Ah-throughput [kAh]	Q_t [Ah]	SoH [%]	$\delta_{SEI,t}$ [m]	$c^s_{max,n,t}$ [mol/m^3]	D^e_{ag} [m^2/s]	K^e_{ag} [Ω^{-1}m^{-1}]
0	14.98	100	0	31,833	2e-10	0.56
3.1	14.36	95.9	2.09e-7	30,516	1.83e-10	0.51
4.7	14.27	95.3	2.40e-7	30,325	1.8e-10	0.51
8.5	13.96	93.2	3.44e-7	29,666	1.72e-10	0.48
12.8	13.87	92.6	3.75e-7	29,475	1.7e-10	0.48
17.5	13.34	89.1	5.53e-7	28,349	1.56e-10	0.44
21	13.13	87.7	6.24e-7	27,903	1.5e-10	0.42
21.3	12.94	86.4	6.88e-7	27,499	1.46e-10	0.41

C-rate of discharge and from 298K to 333K for 10 C-rate of discharge.

The electrochemical transport parameters k, D^e, and K^e also vary as a function of temperature. The reaction rate constant, $k(T)$, is expressed as a function of temperature using the Arrhenius relationship [56]:

$$k(T) = k_{ref} \cdot \exp\Big[\frac{Ea_r}{R}\Big(\frac{1}{T_{ref}} - \frac{1}{T}\Big)\Big]. \tag{2.63}$$

Ea_r is the electrode reaction rate activation energy, and is set to a value of 78.24 kJ/mol [182]. As reported earlier, due to the lack of an analytical expression for the dependency of D^e and K^e on temperature, a curve fitting procedure was implemented to determine $D^e(T)$ and $K^e(T)$. Based on the determined pore-scale transport parameter values and the methodology described earlier, the temperature-dependent trajectory of the phase diagram coefficients (α,β) is computed at different temperature intervals that are characteristic of

Table 2.7: Variation of the electrolyte phase diagram parameters for different C-rate and temperature, as a function of their SoH.

SoH	C-rate	ε	k	T [K]	D^e_{ag}	K^e_{ag}	Da_e	Pe_e	α	β
100	1	0.154	1.94e-4	298	2e-10	0.56	1.63e-3	2.34e-2	-2.01	3.44
100	1	0.154	2.39e-4	300	2.14e-10	0.61	1.88e-3	2.40e-2	-2.00	3.36
100	1	0.154	2.95e-4	302	2.28e-10	0.66	2.17e-3	2.45e-2	-1.98	3.28
100	1	0.154	3.62e-4	304	2.42e-10	0.71	2.51e-3	2.50e-2	-1.97	3.20
100	1	0.154	4.43e-4	306	2.56e-10	0.76	2.90e-3	2.55e-2	-1.96	3.13
86.4	1	0.154	2.09e-4	298	1.45e-10	0.406	2.41e-3	2.71e-2	-1.93	3.22
86.4	1	0.154	2.57e-4	300	1.59e-10	0.456	2.72e-3	2.79e-2	-1.91	3.16
86.4	1	0.154	3.17e-4	302	1.73e-10	0.506	3.08e-3	2.87e-2	-1.90	3.10
86.4	1	0.154	3.89e-4	304	1.87e-10	0.556	3.49e-3	2.94e-2	-1.89	3.03
86.4	1	0.154	4.76e-4	306	2.01e-10	0.606	3.98e-3	3.00e-2	-1.88	2.96
100	10	0.154	1.94e-3	298	2e-10	0.56	1.63e-2	2.34e-2	-2.01	2.20
100	10	0.154	3.26e-3	303	2.35e-10	0.685	2.33e-2	2.48e-2	-1.98	2.01
100	10	0.154	8.79e-3	313	3.04e-10	0.93	4.86e-2	2.69e-2	-1.94	1.62
100	10	0.154	2.23e-2	323	3.73e-10	1.17	1e-1	2.84e-2	-1.91	1.23
100	10	0.154	5.35e-2	333	4.42e-10	1.42	2.03e-1	3e-2	-1.88	0.85
86.4	10	0.154	2.08e-3	298	1.45e-10	0.406	2.41e-2	2.71e-2	-1.93	1.99
86.4	10	0.154	3.51e-3	303	1.80e-10	0.53	3.27e-2	2.90e-2	-1.90	1.83
86.4	10	0.154	9.46e-3	313	2.49e-10	0.77	6.38e-2	3.14e-2	-1.85	1.47
86.4	10	0.154	2.40e-2	323	3.19e-10	1.02	1.26e-1	3.35e-2	-1.82	1.11
86.4	10	0.154	5.76e-2	333	3.88e-10	1.26	2.49e-1	3.51e-2	-1.79	0.74

the C-rate of operation and the cell SoH. The variation of parameters α and β as a function of the operating conditions is summarized in Table (2.7), and schematically represented in Fig. 2.16. The dimensions of the different transport parameters are: [K] for T, [A·m·mol^{-1}] for k, [m^{2}sec^{-1}] for D^e_{ag}, [Ω^{-1}m^{-1}] for K^e_{ag} , and [1/h] for C-rate. Battery SoH is expressed in [%], and the parameters, ε, Da_e, Pe_e, α, and β are dimensionless.

At a 1 C-rate, moderate increase in temperature during the discharge event results in a minor change

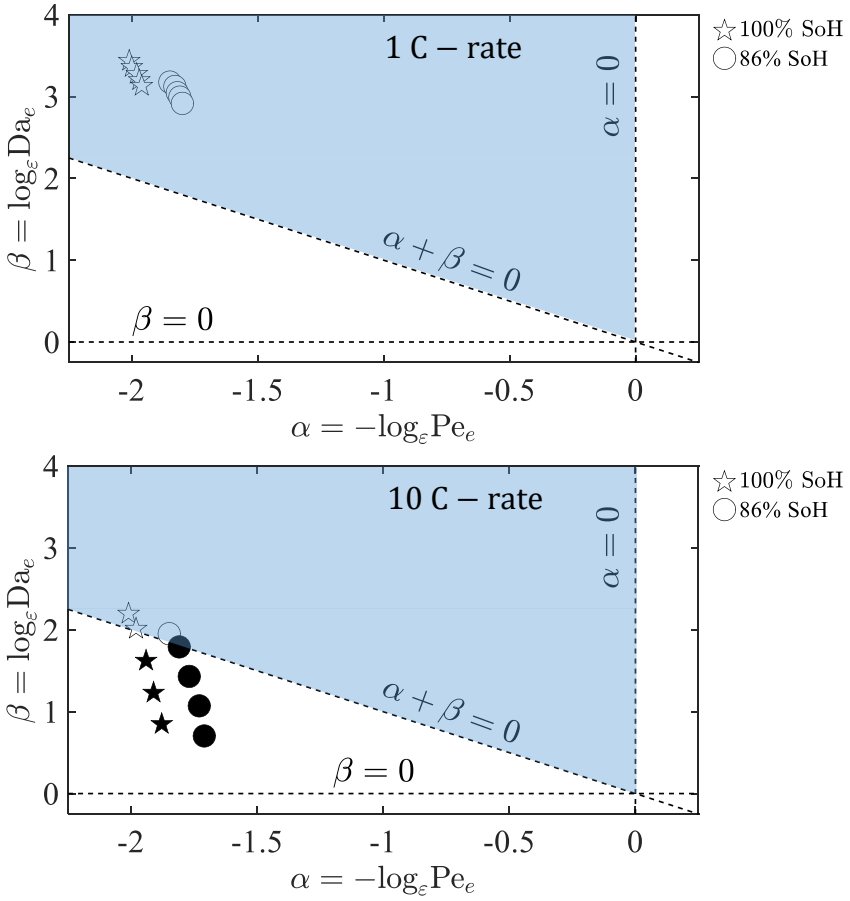

Figure 2.16: Variation with temperature of the data points (α,β) for constant current discharge at 1 C-rate and 10 C-rate, and with the battery at 100% SoH and 86% SoH. For 1 C-rate discharge, the temperature of the cell is estimated to increase from 298K to 306K. The applicability conditions are satisfied from beginning to end of discharge, but the circular data points are closer to the boundary of the applicability regime. For 10 C-rate discharge, the temperature of the cell is estimated to increase from 298K to 333K. The applicability conditions are violated during discharge, and represented by the star shaped and circular data points with filled symbols. This indicates that capacity fading will lead to diminishing macroscale model predictability.

in the parameter α compared to β. This is due to the faster rate of increase in reaction kinetics compared to the enhanced electrolyte diffusion and conductivity. The effect of cell operation at different SoH can be clearly observed in both parameters, as lower SoH pushes the parameter values closer to the boundary of the applicability regime (indicated by the dotted lines in Fig. 2.16). In both cases, the data points satisfy the constraints over the range of temperature increase. Hence macroscale transport models would be capable of capturing pore-scale dynamics accurately.

During 10 C-rate of discharge, significant increase in battery internal temperature leads to an accelerated decrease in β. The effect of increasing k dominates any increase in parameters D^e and K^e. The

condition $\alpha + \beta > 0$ is violated shortly after discharge begins. This is because fast reaction kinetic lead to the formation of diffusion-limited regimes. Such poorly mixed conditions leads to the lack of scale separation between the pore-scale and macroscale domains. Operating aged cells under aggressive conditions of discharge has a significant effect on the trajectory of (α,β). The data points for aged cell tend to violate the conditions of homogenizability faster, as shown in Fig. 2.16. Lower SoH battery operation lead the points closer to the limiting boundaries and invalidate macroscale models.

The proposed theory suggests that the predictability of macroscale models degrade as the battery SoH decreases over time. This is consistent with previous experimental/numerical studies, and can be explained by variation of the parameters Da_e and Pe_e as a function of aging using the applicability conditions:

1. The Péclet number Pe_e increases with aging due to the decrease in battery capacity Q_t, which leads to a decrease in $c^s_{max,n,t}$.
2. The Damkhöler number Da_e increases with aging due to the decrease in D^e_{ag}, which is the result of the SEI formation side-reaction.
3. The ratio of the Damkhöler and Péclet number, Da_e/Pe_e, increases with aging and is directly proportional to the ratio $\frac{c^s_{max,n,t}}{\left\{1-\eta_{f,n}-\eta_{s,n}\left(1+\frac{3\delta_{SEI}}{R_{s,n}}\right)\right\}^{1.5}}$.

In addition, decreasing $c^s_{max,n,t}$ leads to an increase in the rate constant $k_{ref,n}$ for the same current demand as the cell ages. As explained in [160], the applied current determines the total current density at the negative electrode. The total current density is a sum of the intercalation and the side-reaction current densities. As the growth of the SEI layer depletes cyclable lithium ions and increases the unwanted side-reaction dynamics, the intercalation current density must compensate for these losses in order to meet the required current demand. This results in an increase in the intercalation side-reaction kinetics. This study demonstrates that the ability of the phase diagrams in identifying when classical macroscopic models may fail to accurately capture battery dynamics with respect to degradation.

2.5 Conclusion

Lithium-ion transport involves diffusion, conduction, electromigration and heterogeneous reactions in geometrically complex porous electrodes. Macroscopic models, which are approximate representations of the pore-scale physics, offer advantageous due to their relative simplicity and limited computational burden in comparison with their pore-scale counterparts. These aspects renders them as suitable tools from which simplified and reduced-order model formulations can be developed for model-based control and estimation of battery SoC and SoH. However, macroscale models fail as predictive tools under operating conditions such as high C-rates and high temperatures. This critically impacts any control and estimation strategies developed based on these models.

Section §2.2 presents a rigorous derivation of macroscopic dual-continua models and the identification of sufficient conditions under which the averaged model equations describe micro-scale dynamics with an accuracy that is prescribed by the homogenization technique. The relative importance between the pore-scale transport processes can be quantified using electric Péclet Pe_j and Damköhler Da_j, $j = \{e, s\}$ numbers in the electrolyte and electrode phases. A significant outcome of this derivation, summarized in the form of two (Da,Pe)-based phase diagrams, is the development of an approach that establishes the robustness of macroscopic transport equations in describing the evolution of lithium concentration and potential in the electrolyte and electrode phases.

Section §2.3 presents a finite volume approach using OpenFOAM software to resolve the unit-cell closure problem for porous battery electrodes. The closure variable results are integrated in the homogenized model equations through the effective transport parameters. A significant outcome of this multiscale modeling approach is that it can be extended to determine the effective transport properties in realistic battery electrode structures obtained from imaging techniques.

Section §2.4 presents a detailed analytical study where the phase diagrams were implemented to evaluate the predictability of the macroscale transport models across different electrode chemistry and a wide spectrum of battery operation characterized by temperature, C-rate, and aging effects. § 2.4.1 summarized the distribution of phase diagram parameters (α,β) for commercially used battery electrode compositions, followed by a case study that determined the transport parameters Pe_e and Da_e for different operating conditions based on electrode composition, temperature, and C-rate. The performance predictions of continuum models based on the phase diagram analysis confirmed the results that were independently obtained from other numerical and experimental studies, i.e. a breakdown of continuum models at high C-rates.

In section §2.4.2, phase diagram analyses are presented to examine the temperature-dependent dynamics in lithium-ion battery electrodes. Different battery compositions are examined to determine the range of applicability of DFN-type models. The results indicate two major implications: 1) temperature is a critical parameter that governs transport processes in the electrode and induces the onset of multi-scale dynamics, and 2) standard macroscopic models may fail to describe micro-scale processes in batteries that are operated above critical temperature conditions. Section §2.4.3 and section §2.4.4 present a phase diagram study to evaluate the predictability of macroscale transport models throughout the useful life of a battery. Mathematical expressions for the dimensionless Damkhöler and Péclet numbers in the electrolyte phase are formulates as a function of battery aging due to the SEI layer growth. Results indicate that the predictability of macroscale models degrades with battery aging due to the side-reaction dynamics that affect pore-scale transport. The applicability conditions provide a quantitative framework to identify the onset of mass transport limitations as the battery SoH decreases over time.

The phase diagram analysis has been demonstrated to assess the predictability of macroscale models in capturing pore-scale battery dynamics under different operating conditions and SoH. The sufficient conditions identified on parameters Pe_j and Da_j, $j = \{e, s\}$ also highlight the importance of mixing at the sub-pore scale for continuum equations to be valid. Very fast reaction kinetics resulting from high operating temperatures would lead to diffusion-limited regimes, under which continuum models would be invalidated. Under these operating conditions, hybrid algorithms that account for a full coupling between the two scales must be employed instead to classical continuum models for accurate prediction of the battery response. Published literature has so far lacked such a systematic methodology to guide researchers on the use of the correct modeling tools for battery systems. Estimation strategies for battery SoC and SoH must account for model robustness and error. The outcomes of this chapter is envisioned to pave the way for developing strategies to prolong battery life through accurate modeling and control.

Chapter 3

Experimental Characterization of Lithium-ion Cells

3.1 Introduction

This chapter describes the testing equipment and presents the design of experiments conducted to evaluate the performance of the homogenized macroscale modeling framework. It starts with an overview of the features of the test equipment used to conduct current and voltage-based experiments on lithium-ion batteries under controlled cell surface temperatures. Cylindrical cells of 18650 geometrical format are utilized in these experiments. The cells are subjected to experiments at different cell surface temperatures. The anode in the 18650 cell is composed of lithium graphite, and the cathode is composed of layered structures of NMC transition metal oxide. A detailed description of the initial setup and testing of the two devices, Arbin BT-2000 tester and the Peltier junctions, is presented. The later part of this chapter summarizes the different types of experiments conducted on each cell chemistry, and a summary of the measured voltage response of different cells as a function of temperature and C-rate of discharge.

3.2 Testing equipment

Experiments were conducted in the Battery Aging and Characterization (BACh) Laboratory at the Department of Automotive Engineering, Clemson University. The experimental test setup is depicted in

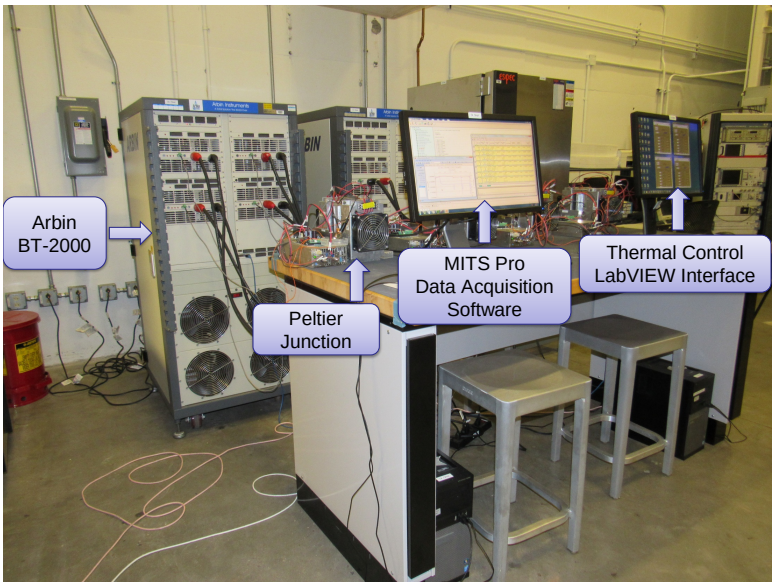

Figure 3.1: Experimental testing on lithium-ion battery cells at the BACh laboratory.

Fig. 3.1. The testing equipment consists of an Arbin BT-2000 testing station incorporating a programmable power supply and an electronic load, capable of performing charge-discharge cycles with high precision and data acquisition up to a rate of 100 Hz. The Arbin BT-2000 is completely software controlled, enabled by the use of MITS Pro data acquisition software to design test cycle input profiles, along with real-time data review and analysis. The cells under test are installed in the fixture of a Peltier junction heater/cooler system that controls the surface temperature of the cells in direct contact using the thermoelectric effect.

Arbin BT-2000

The Arbin BT-2000 is a multiple independent-channel operating system for testing battery cells and modules. The MITS Pro software system has built-in as well as user-defined control mechanisms for highly accurate programmable control of current, voltage, load, and power. The software platform enables around-the-clock safe and reliable testing of energy storage devices, thanks to the presence of the following safety features:

1. *Current limiting circuitry* to prevent the current from exceeding maximum range if the loaded device short circuits.
2. *Watchdog* feature that shuts the system down in the event of a major hardware or communication failure.
3. *Thermoswitches* that prevents overheating from a long-term over-current or breakdown of cooling fans.
4. *Software safety and step limits* to terminate the test in the event that current, voltage, and/or other

relevant test variables exceed their upper or lower threshold limits of allowable operation.

5. *Voltage clamp* to allow smooth transition from constant current to constant voltage during a charging or discharging event.

Table 3.1: Technical specifications of the Arbin BT-2000 tester used for the experimental characterization of lithium-ion cells.

Number of channels	4
Maximum current rating	±200 A
Medium current rating	±20 A
Low current rating	± 5 A
Voltage rating	0-6 V
Maximum power rating	±1.2 kW

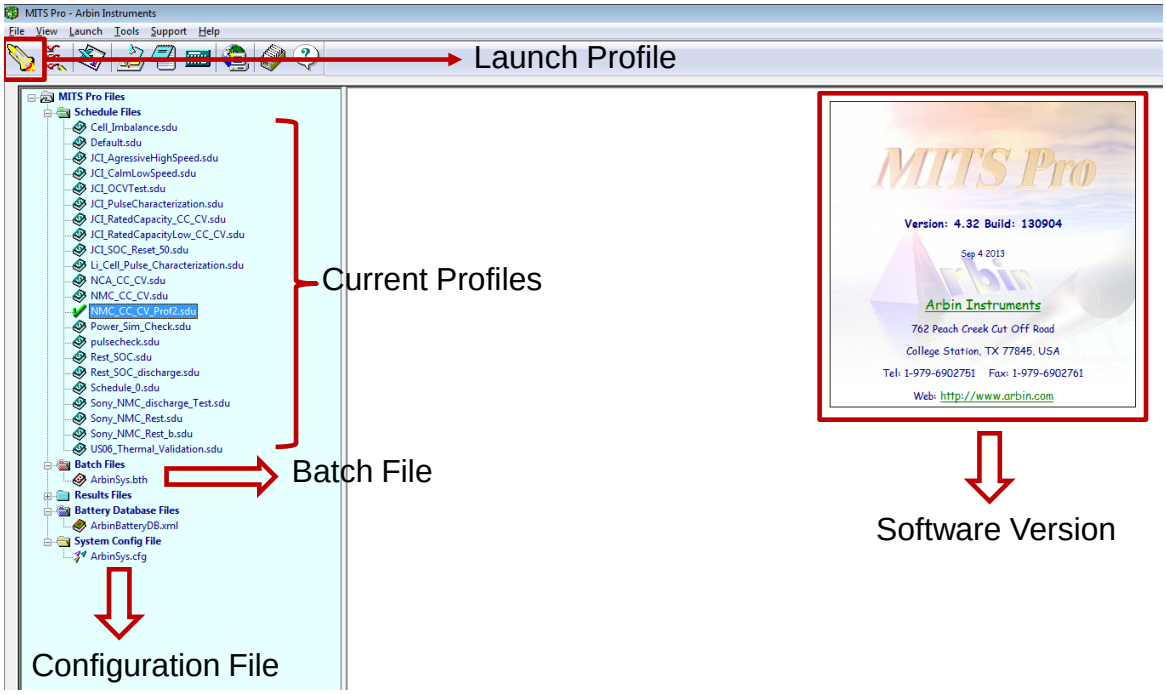

Figure 3.2: Features of the MITS Pro software platform to program and control the Arbin BT-2000 during experimental measurements.

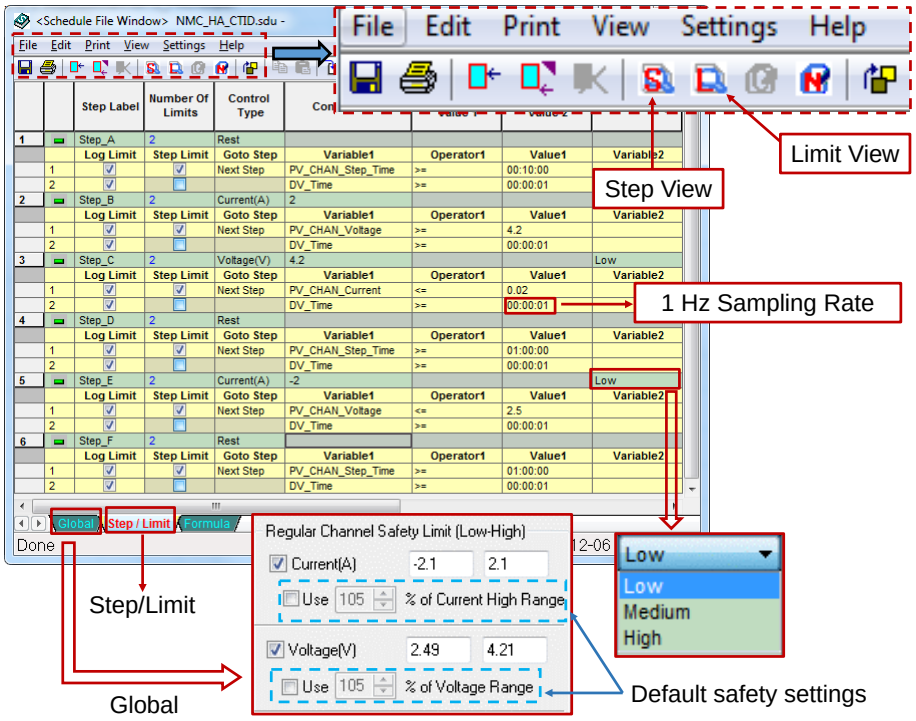

Figure 3.3: Schedule file designed for capacity test in discharge experiments on 18650 NMC cells.

The specifications of the Arbin BT-2000 equipment used for the experimental characterization of lithium-ion cells is presented in Table 3.1. The MITS Pro software platform ensures reliable operation of the Arbin BT-2000 with minimal supervision. An overview of the software interface is presented in Fig. 3.2. The batch file represents the experimental profiles that are set to run on each channel of the Arbin BT-2000. To execute the battery experiments, input current profiles are designed and saved in the form of schedule files. The configuration file is modified in the event of a system failure or calibration. The launch profile window is the master screen that reflects the current status of all running programs. The sign convention of the Arbin BT-2000 for current input is: *positive current* indicates *charging*, and *negative current* indicates *discharging*.

An experimental schedule file designed to perform a capacity test in discharge on a lithium-ion cell is illustrated in Fig. 3.3. The program is executed in a sequence of steps, beginning at *Step-A* and terminating at the end of *Step-F*. The step view summarizes the sequence of each experimental profile run, while the limit view elaborates the time limit (or) condition for the successful execution of each step in the profile of the experiment. At each step of the schedule file, the current range must be specified as either *low*, *medium*, or *high*, depending on the magnitude of the current, as specified in Table 3.1. For every step that is subjected to data acquisition, the sampling rate is specified. A sampling rate is f hertz means that each data point is

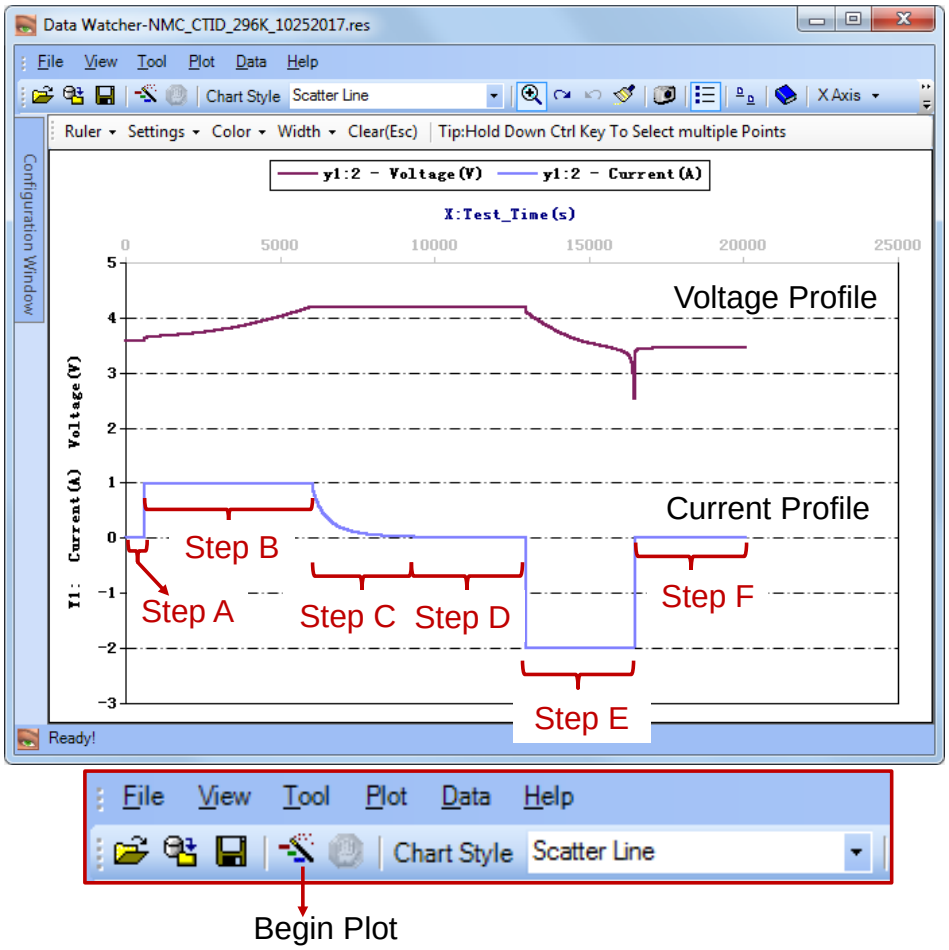

Figure 3.4: An illustration of the current profile and the measured voltage response from a capacity test in discharge experiment on an NMC cell, indicating the different steps of the schedule file.

collected at time steps of $(1/f)$ seconds. Under the *Global* tab, the upper and lower safety limits for current and voltage are specified for the experimental profile under consideration. In Fig. 3.3, the current limits are ± 2.1 A, and the upper and lower voltage limits are respectivelt 4.21 V and 2.49 V. By default, they are set to $\pm 105\%$ of the maximum values entered in the schedule file program, as shown in Fig. 3.3.

The first step, *Step_A*, in the experimental schedule file is the *Rest* phase. In the event that a wrong schedule file is loaded, it enables the user to terminate the test and rectify the error without affecting the state of the battery cell under test. A capacity test in discharge experiment starts by fully charging the battery to its upper allowable voltage limit of operation. This is executed using constant-current constant-voltage (CC-CV) charging. The second step,*Step_B*, represents constant-current charge. During the CC phase, the battery is charged from its initial state until it reaches its upper voltage limit. Table 3.2 provides the allowable limits

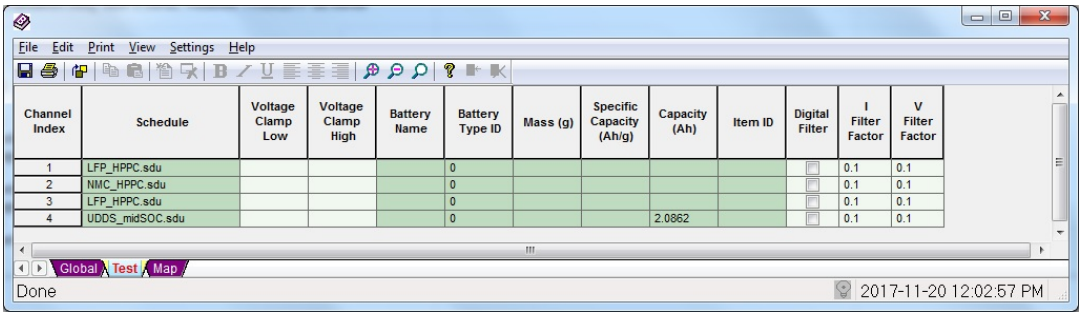

Figure 3.5: MITS Pro batch file that indicates the current schedule file that is setup for execution on each Arbin channel.

of voltage operation for the 18650 NMC cells. The third step, *Step_C*, represents the constant-voltage phase. When the CV phase is initiated, the voltage of the cell is held constant at its upper limit until the current value drops to 1% of its initial value at the beginning of the CV phase.

The fourth step, *Step_D*, is represents battery rest after complete charging. This rest provides the battery sufficient time to reach steady-state and thermal equilibrium with the surroundings. The fifth step, *Step_E*, represents the discharge phase of the experiment. The constant current capacity test experiment is initiated by discharging the battery between from its upper cut-off voltage to its lower cut-off voltage. The final step, *Step_F*, is a rest phase. When the battery reaches its lower operating voltage limit, the final step of the experiment begins, where the OCP of the cell is recorded as the battery is resting after discharge. The outcome of a capacity test in discharge experiment on an NMC cell is depicted in 3.4.

After creating the schedule file, the batch file is updated with information about the experiment that must be conducted on each Arbin channel. A typical batch file initialization is illustrated in Fig. 3.5. An advantage that the MITS Pro offers is the ability to design input profiles for current in the form of C-rate in addition to the magnitude of current in amperes. If the schedule file is designed for current input in terms of C-rate instead of amperes, then the capacity of the battery must be entered in the batch file, and the magnitude of current input during battery operation is accordingly determined by the software and commanded to the Arbin.

The final step prior to the beginning of experiments is to launch the schedule files. The master screen of the launch window is initiated after assigning specific input profiles for each Arbin channel and completing the electrical connections between the terminals of the Arbin channels the battery cell under experiment. Figure 3.6 represents a general outlook of the launch window, along with a display of the measured current and voltage values of two experiments in real-time. During the experiments, the launch window displays the

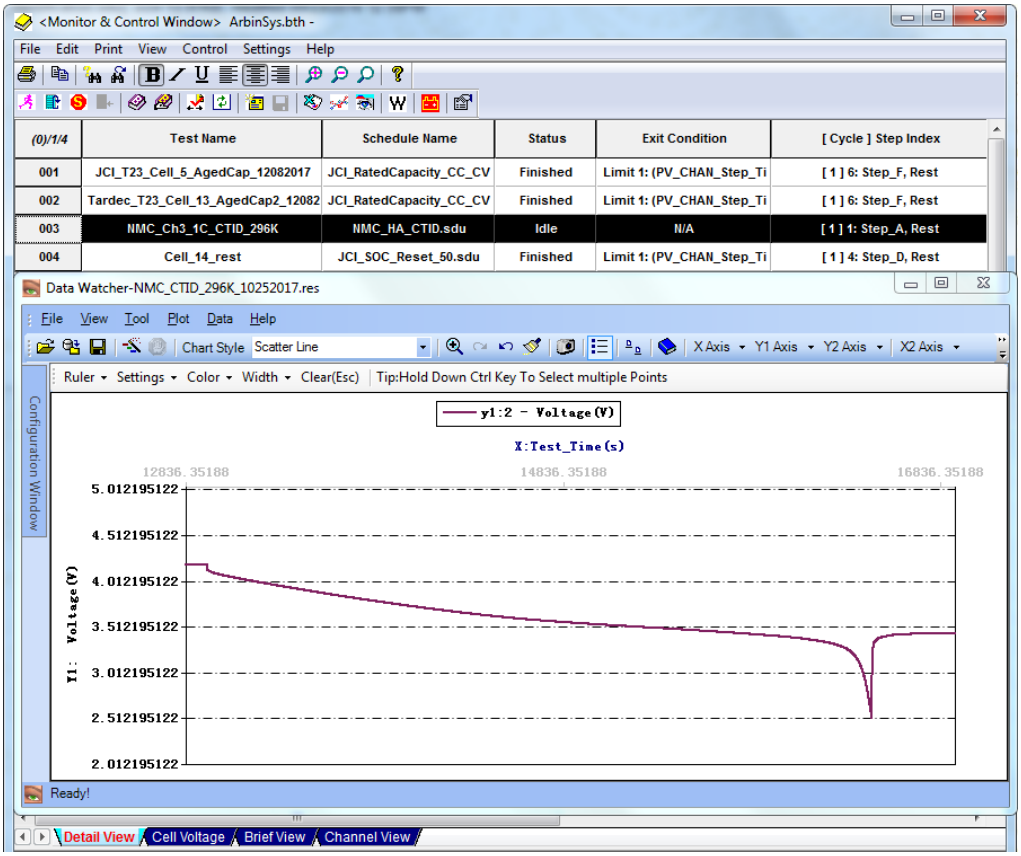

Figure 3.6: A snapshot of the MITS Pro launch window that describes the experiments running on each Arbin channel and their current status. Real-time review and analysis of experiments is enabled using the *Data Watcher* feature.

current status of each running experiment along with the battery phase, i.e. *charge*, *discharge*, or *rest*. The *Data Watcher* feature of MITS Pro enables real-time review and analysis of the measured current and voltage values during the experiments to verify nominal operation and detect any anomalies. After the experiments are completed, experimentally measured data can be exported from the Arbin environment in a spreadsheet format using the Microsoft®Excel®software tool for analysis and simulation studies.

Peltier Junction

The Peltier junction heater/cooler device is a dual purpose integrated system designed by CAR Technologies to facilitate the testing of both 18650 and 26650 cylindrical lithium-ion battery cells. It is designed to provide an effective control of the battery skin temperature in the range of -5°C to +55°C, and is used for the modeling and data analysis of battery cells for hybrid and electric vehicle applications. The thermoelectric assembly of a Peltier junction is represented in Fig. 3.7. The main components of the Peltier junction are:

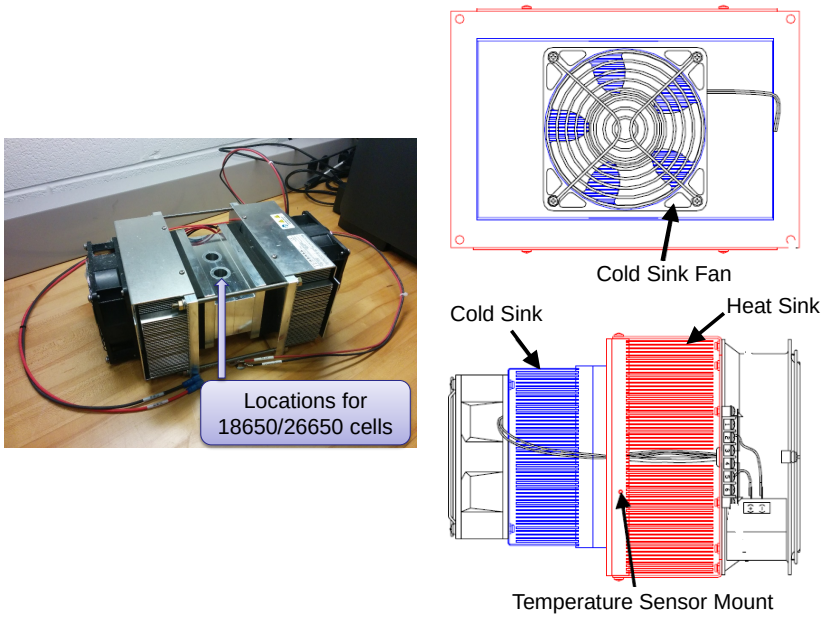

Figure 3.7: Peltier junction assembly used for controlled temperature experiments on cylindrical cells, and different components of the heating/cooling assembly.

1. *CP-110 Thermoelectric Cold Plate Cooler* that utilizes direct contact cooling for precision temperature control.

2. *TCC-36-25 RS232 Temperature Controller* that utilizes bi-directional, solid-state H-bridge operation for heating and cooling.

3. *MP-3193 Temperature Sensor* that acts as an over-temperature safety device. It is moisture resistant for applications with surface condensation issues, and has a large thermal contact area for accurate temperature measurements.

One of the advantages of the Peltier junction is its ability to be used either as a stand-alone device, or in conjunction with a computer using a LabVIEW program interface. For all the experiments conducted, the Peltier junction was controlled using the LabVIEW program. To enable Peltier junction control using the software platform, three steps must be followed in sequence:

1. Step 1: Load default settings. In this step, the configuration parameters regulating the operation of the Peltier device are initially loaded for each thermoelectric device. Every Peltier junction has a dedicated communication port under which all default parameter values are loaded.

2. Step 2: Verify configuration settings. In this step, the configuration of each communication port is verified by re-loading the parameters from Step 1, and ensuring that the parameters are correctly loaded for optimal Peltier junction performance.

3. Step 3: Load controller screen. The third and final step prior to Peltier junction control is to load the thermal control platform. Once the communication port is selected, the controller gains, default temperature set point, and current thermal sensor measurement values are displayed on the screen.

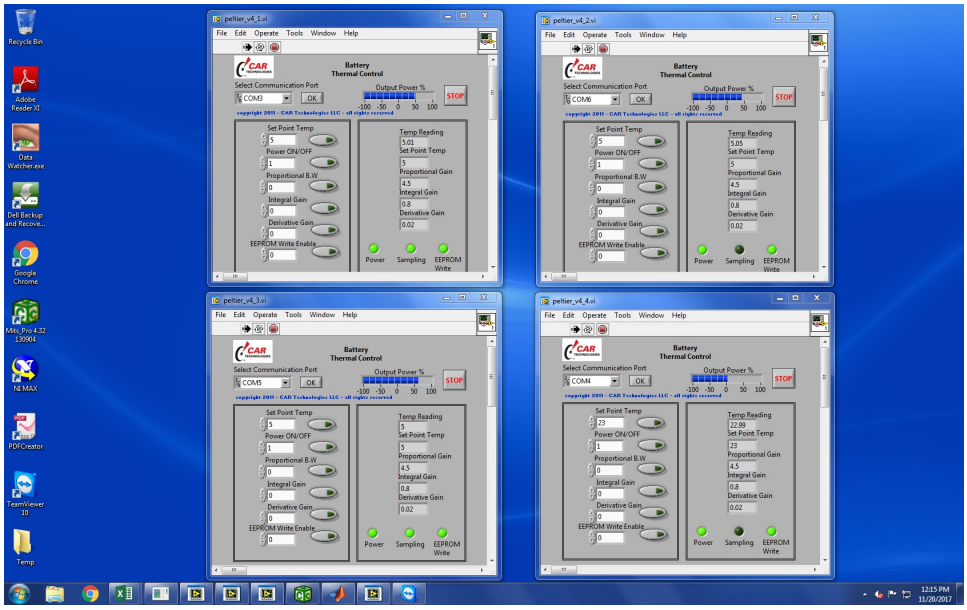

Figure 3.8: A snapshot illustrating the simultaneous operation and control of four Peltier junctions for battery temperature controlled experiments.

Figure 3.8 presents a snapshot of the thermal control of four battery systems using different Peltier junctions. Multiple Peltier junctions can be operated and controlled simultaneously using the same computer device, allowing to test simultaneously many cells at different temperatures. The LabVIEW program for battery thermal control using a Peltier junction is presented in Fig. 3.9. Each Peltier junction is driven by an isolated power supply device. By manually setting the value under the *Power ON/OFF* tab to 1 in the controller and activating the tab, the thermoelectric junctions are supplied power to perform their designated operation.

To test a cell at a temperature T_{des}, the value of T_{des} is manually entered under the *Set Point Temp* tab and activated. The difference between the desired and current temperature values drives the direction of current inside the Peltier junction to either cool or heat the fixture where the battery cell is mounted. The thermal control program utilizes a proportionalintegralderivative controller to achieve the desired tempera-

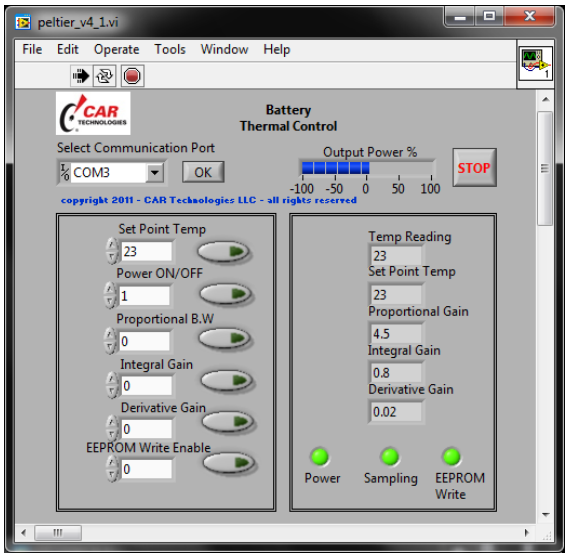

Figure 3.9: Battery thermal control LabVIEW program used for the operation of a Peltier junction.

ture. As the temperature reaches towards its target value, the current provided to the thermoelectric junctions is regulated accordingly, indicating the PID control in action. After the completion of the experiments, the Peltier devices are turned off by commanding the power to zero in the thermal control screen. Before turning off the device, the set point must be reverted back to room temperature conditions. The BACh laboratory also hosts a ESPEC BTX-475 environmental chamber with the ability to maintain ambient conditions within a temperature range of -70°C to 180°C, and relative humidity within a range of 10% to 95%. However, the Peltier junctions were used for the experimental characterization of the 18650 cells because they are more efficient in terms of the overall duration of testing.

3.3 Lithium-Ion Cell Experiments

Both the Arbin BT-2000 and the Peltier thermoelectric devices were utilized in conjunction for experiments on 18650 lithium-ion cells. The NMC cells used for experimental characterization are shown in Fig. 3.10 and their technical specifications are summarized in Table 3.2. Constant current capacity test in discharge experiments are conducted at five different temperatures: 5°C, 23°C, 40°C, 45°C, and 52°C. The selection of these temperature values for the experiments is based on the predictions of an electrolyte phase diagram study for the anode and cathode of an 18650 NMC cell, which is elaborated in section §4.6.1 of chapter 4. The cell is installed in the fixture of the Peltier junction, as shown in Fig. 3.10, and soaked for

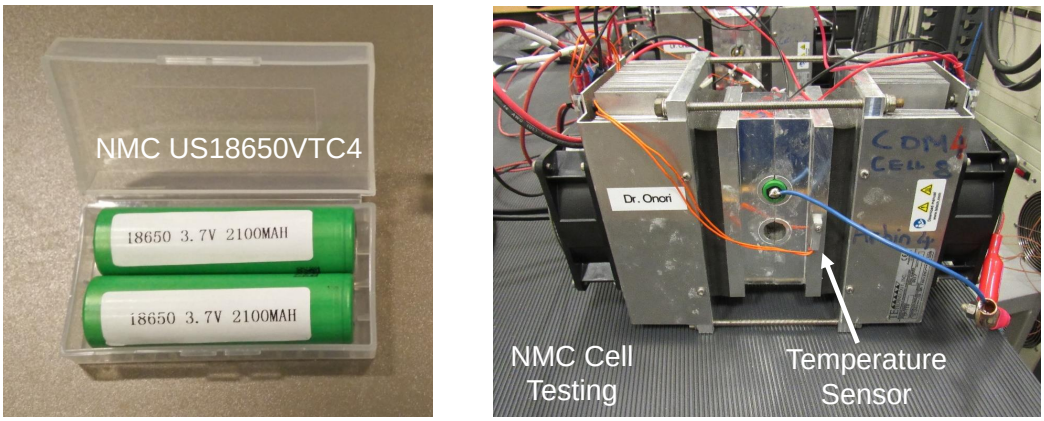

Figure 3.10: Temperature controlled experiments on 18650 lithium-ion cells using the Peltier junction.

Table 3.2: Technical specifications of NMC US18650VTC4 lithium-ion cells.

Type of Cell	NMC US18650VTC4
Nominal Capacity	2100 mAh
Recommended standard charging method	2.0 A to 4.2 V CCCV, 90 min
Maximum continuous discharge current	30 A
Cyclic performance	60% of initial capacity after 500 cycles of 5 C-rate discharge
Upper cut-off voltage at 23°C	4.20 V
Lower cut-off voltage at 23°C	2.50 V
Operating temperature range	-20°C to +60°C

three (3) hours to achieve thermal equilibrium at each targeted temperature of operation.

The results of the NMC cell capacity test is summarized in Fig. 3.11. The magnitude of the constant current in discharge used for the NMC cell is 2 A. Table 3.3 summarizes the experimentally measured capacity of the NMC cell from the discharge experiments.

Table 3.3: Measured capacity values of the 18650 NMC cell from the constant current discharge experiments.

Temperature	Measured NMC Cell Capacity
5°C	1739.1 mAh
23°C	1952.9 mAh
40°C	2059.6 mAh
45°C	2127.4 mAh
52°C	2150.8 mAh

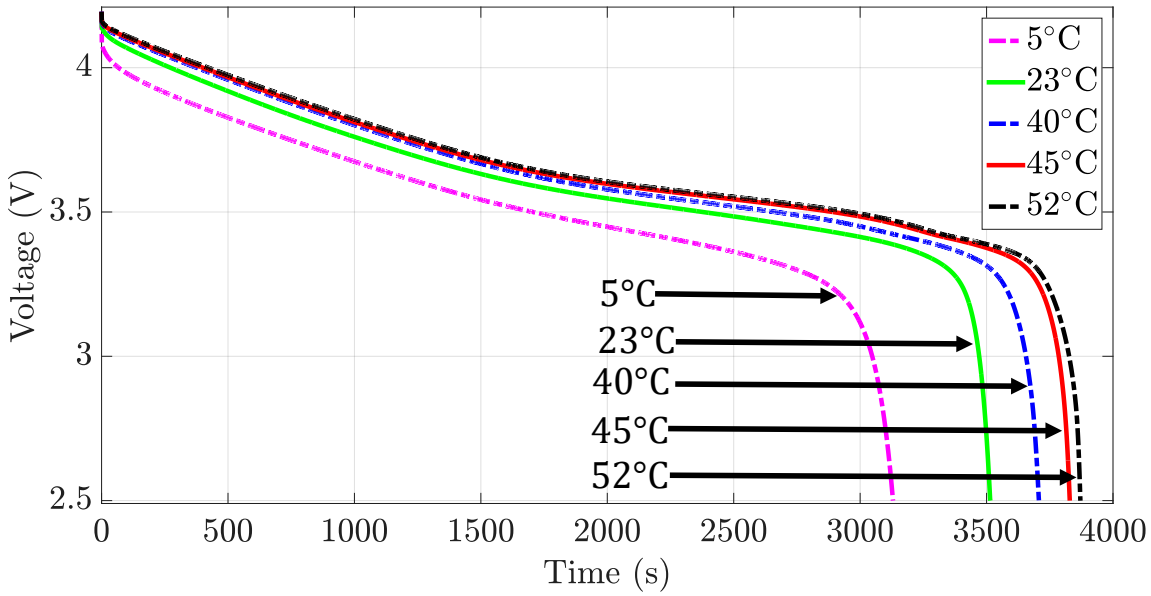

Figure 3.11: Voltage response of an 18650 cylindrical NMC cell as a function of time obtained from 2 A constant current discharge experiments conducted at different temperatures.

Chapter 4

Comparative Studies on the DFN and FHM Macroscale Models

4.1 Introduction

This chapter elaborates upon the numerical implementation of the homogenized macroscale model equations derived in Chapter 2. A comparison of the mass and charge transport equations of the DFN and FHM model is presented in the next section, along with a discussion of different factors that indicate enhanced predictability of battery behavior using the FHM model equations. The section that follows is a summary of the numerical implementation of the DFN model using a model developed by Plett *et. al* [183] using the finite element modeling software COMSOL Multiphysics®. This model is utilized for comparative studies, and is summarized for completeness in this dissertation. A detailed explanation of the implementation of this model can be found in [183]. Following the summary of the DFN model, the numerical implementation of the FHM model is elaborated in the subsequent section. The later part of this chapter then presents an approach to identify the parameters of the DFN and FHM models by conducting co-simulation studies involving COMSOL Multiphysics®and MATLAB®software using the Particle Swarm Optimization (PSO) technique. The performance of both models is assessed against experimental data, the details of which are presented in Chapter 3. The results of the identification studies are analyzed using electrolyte phase diagrams and comparison of the model-predicted electrode dynamics. A system level phase diagram is used to quantify the error in the DFN and FHM model-predicted voltage as a function of the cell SoC and operating temperature. Appendix C

describe the procedure to develop the FHM COMSOL model and conduct the co-simulation studies.

4.2 Comparison Analysis: DFN and FHM Model Equations

This section discusses the similarities and differences between the mass and charge transport governing equations of the DFN model, obtained from [65], and the FHM model. The DFN model is developed using the volume-averaging technique, while the FHM model is rigorously derived using mathematical homogenization. One of the major outcomes of the application of the homogenization theory to lithium-ion batteries is the ability to assess the veracity of macroscale models on temperature-influenced battery dynamics. The dimensional transport equations of the DFN and FHM models are summarized in Table 4.1. n, s, and p represent the anode, separator, and cathode, respectively. The separator does not contain any active particles, hence there is no intercalation current density in the separator.

4.2.1 Mass transport in the electrode

Fick's law of diffusion is used to define the governing equation for electrode mass transport. The DFN model assumes spherical particle shape for electrode concentration dynamics. The electrode concentration is represented as $c_{s,j}$ to denote that it is a pore-scale quantity. The FHM model electrode mass transport equation is derived from Fick's law of diffusion without making any assumption about the particle shape. The concentration term of the homogenized model is a quantity that is averaged over the unit cell.

In the DFN model, the term $D_{s,j}$ represents the pore-scale diffusion coefficient, whereas in the homogenized equation, $\mathbf{D}_{s,j}^{eff}$ represents the effective diffusion tensor. It is obtained by resolving the closure variable $\boldsymbol{\chi}^s(\mathbf{y})$ in the electrode phase of the unit cell using the set of equations defined in (2.40). $\mathbf{y}$ is a fast space variable in the unit cell Y, $\mathbf{y} \in Y$, and is defined as $\mathbf{y} = \varepsilon^{-1}\mathbf{x}$, where $\mathbf{x}$ is the variable in the macroscale domain. $D_{s,j}$ is the pore-scale electrode diffusion coefficient and is assumed to be constant at a given temperature. The diagonal components of the tensor $\mathbf{D}_{s,j}^{eff}$ are identified for the FHM model. In the DFN model, the pore-scale electrode mass transport equation is used in conjunction with macroscale equations of transport in the electrolyte phase. The justification for this combined implementation of equations at different length scales has not been adequately addressed. In Chapter 2, the applicability conditions in the electrode phase revealed a lack of scale-separation between the *pore* and *macro* scales for different cathode materials. Under these circumstances, either full pore-scale or fully coupled micro-macroscopic equations of mass transport are necessary for accurate modeling of active material transport.

Table 4.1: Mass and charge transport equations of the DFN and FHM macroscale models.

DFN Model	FHM Model
Electrode Mass Transport Equation; $j = (n, p)$	
$\frac{\partial c_{s,j}(x,r,t)}{\partial t} = \frac{1}{r^2}\frac{\partial}{\partial r}\left(D_{s,j} r^2 \frac{\partial c_{s,j}(x,r,t)}{\partial r}\right)$	$\frac{\partial \bar{c}_{s,j}}{\partial t} = \nabla \cdot \left[\mathbf{D}_{s,j}^{eff} \nabla \bar{c}_{s,j}\right] - \frac{1}{F} J_{Li,j}$
Electrolyte Mass Transport Equation; $j = (n, s, p)$	
$\eta_{e,j}\frac{\partial \bar{c}_{e,j}(x,t)}{\partial t} = \frac{\partial}{\partial x}\left(D_{e,j}^{eff}\frac{\partial \bar{c}_{e,j}(x,t)}{\partial x}\right) + \frac{(1-t_+)}{F} J_{Li,j}(x,t)$	$\eta_{e,j}\frac{\partial \bar{c}_{e,j}}{\partial t} = \nabla \cdot \left[\left\{\mathbf{D}_{e,j}^{eff} + \frac{RT\lambda t_+^2}{F^2 \bar{c}_{e,j}}\mathbf{K}_{e,j}^{eff}\right\}\nabla \bar{c}_{e,j}\right] + \nabla \cdot \left[\left\{\frac{t_+}{F}\mathbf{K}_{e,j}^{eff}\right\}\nabla \bar{\phi}_{e,j}\right] + \frac{1}{F} J_{Li,j}$
Electrode Charge Transport Equation; $j = (n, p)$	
$K_{s,j}^{eff}\frac{\partial^2 \bar{\phi}_{s,j}(x,t)}{\partial x^2} = J_{Li,j}(x,t)$	$\nabla \cdot \left[\mathbf{K}_{s,j}^{eff} \nabla \bar{\phi}_{s,j}\right] = J_{Li,j}$
Electrolyte Charge Transport Equation; $j = (n, s, p)$	
$-K_{e,j}^{eff}\frac{\partial^2 \bar{\phi}_{e,j}(x,t)}{\partial x^2} - \frac{2K_{e,j}^{eff}(x,t)RT(1-t_+)}{F}\frac{\partial^2 \ln \bar{c}_{e,j}}{\partial x^2} = J_{Li,j}(x,t)$	$\nabla \cdot \left[\left\{\frac{RT\lambda t_+}{F\bar{c}_{e,j}}\mathbf{K}_{e,j}^{eff}\right\}\nabla \bar{c}_{e,j} + \mathbf{K}_{e,j}^{eff}\nabla \bar{\phi}_{e,j}\right] = -J_{Li,j}$
Intercalation Current Density; $j = (n, p)$	
$J_{Li,j}(x,t) = a_j k_{0,j} \cdot \sqrt{c_{s,surf,j} \cdot \bar{c}_{e,j}(x,t)} \cdot \sqrt{\left(c_{s,max,j} - c_{s,surf,j}\right)} \cdot 2\sinh\left[\frac{0.5F}{RT}\left(\bar{\phi}_{s,j} - \bar{\phi}_{e,j} - U_{0,j}\right)\right],$ $J_{Li,s}(x,t) = 0$	$J_{Li,j} = \frac{\varepsilon_j^{-1}\mathcal{K}_\dagger^* \eta_{e,j}}{L_j} \cdot k_j \cdot \sqrt{\bar{c}_{e,j} \cdot \bar{c}_{s,j}} \cdot \sqrt{\left(1 - \frac{\bar{c}_{s,j}}{c_{s,max,j}}\right)} \cdot 2\sinh\left(\frac{F}{2RT}\left[\bar{\phi}_{s,j} - \bar{\phi}_{e,j} - U_{0,j}\right]\right)$ $J_{Li,s} = 0$

4.2.2 Mass transport in the electrolyte

The electrolyte phase lithium-ion transport equation is based on the concentrated solution theory. The difference between the DFN and FHM model equations can be summarized as follows:

1. The DFN model considers the effect of only diffusion in electrolyte mass balance, whereas the FHM model considers the effect of both diffusion and electromigration.

2. The DFN model approximates effective diffusion and conductivity coefficients based on the asymmetrical Bruggeman effective-medium model [145], also known as the Bruggeman theory. The effective

diffusion coefficient is mathematically represented in the DFN model as [148]:

$$D_{e,j}^{eff} = D_{e,j} \cdot \eta_{e,j}^{brugg}, \tag{4.1}$$

where $brugg$ is the Bruggeman exponent, and is typically considered to be equal to 1.5 for perfectly spherical particles [148]. On the other hand, the effective diffusion and conductivity coefficients of the homogenized model, $\mathbf{D}_{e,j}^{eff}$ and $\mathbf{K}_{e,j}^{eff}$, are obtained by resolving the closure variable $\boldsymbol{\chi}^e(\mathbf{y})$ in the electrolyte phase of the unit cell using the set of equations defined in (2.36). $D_{e,j}$ and $K_{e,j}$ are the pore-scale diffusion and conductivity coefficients, respectively. The Bruggeman approximation works well only for the case of dilute electrolyte solutions. Du $et.\ al.$ [184] report significant deviation of the effective transport coefficients from the Bruggeman approximation when experiments are compared to pore-scale simulations of battery dynamics.

4.2.3 Charge transport in the electrode and electrolyte

The solid phase lithium-ion potential is obtained using the charge conservation equation described by Ohm's law, and modeled as a 1-D transport equation in the DFN model. The effective electrode conductivity in the DFN model is expressed in terms of the electrode porosity as [148]:

$$K_{s,j}^{eff} = K_{s,j} \cdot \eta_{s,j}^{brugg}, \tag{4.2}$$

On the other hand, the FHM model incorporates the in the homogenized the effective solid-phase conductivity parameter, obtained by resolving the closure variable $\boldsymbol{\chi}^s(\mathbf{y})$. $K_{s,j}$ is the pore-scale conductivity coefficient and is assumed to be constant at a given temperature. The equation for the electrolyte phase lithium-ion charge transport is obtained by combining Kirchhoff's law with Ohm's law. The effective electrolyte conductivity is mathematically represented using the Bruggeman theory as [148]:

$$K_{e,j}^{eff} = K_{e,j} \cdot \eta_{e,j}^{brugg}, \tag{4.3}$$

where the Bruggeman coefficient is assumed to be equal to 1.5 [148]. On the other hand, the effective electrolyte conductivity $\mathbf{K}_{e,j}^{eff}$ is determined by resolving the closure variable $\boldsymbol{\chi}^e(\mathbf{y})$.

4.2.4 Remarks

1. The homogenization technique, represents pore-scale quantities as an asymptotic series in powers of the scale separation parameter ε[1]. On the other hand, the DFN model approximates the pore-scale PNP equations such that only the zeroth order terms of an asymptotic series expansion are accounted for [113].

2. The DFN model has an order of accuracy of ε and must rely on significantly small ratio of length scales between the micro and macro media [113], while the homogenization model has an accuracy of the order of ε^2 [185].

3. The DFN model accounts for only spherically shaped active particle in the determination of the effective parameters. As evidenced by the scanning electron microscope images of the structure of lithium cobalt oxide cathode and graphite anode [148], the homogenized electrode material balance equation is better suited for resolving concentration dynamics in these electrodes.

4. The homogenization technique provides a more robust approach to determine the effective transport parameters when the analytical expressions, such as the Bruggeman relationship, are invalidated.

4.3 Numerical Implementation of the DFN Model

The implementation of the DFN model using the finite element solver COMSOL Multiphysics®is summarized in this section. The model is developed by Plett *et. al* [183] and is summarized here for completeness and to facilitate the comparison studies presented in this chapter. The developers of this model considered COMSOL for its user friendly interface and the flexibility in the evaluation of battery dynamics across different current and temperature conditions of operation. This is a *pseudo two-dimensional* battery model since the electrolyte mass and charge transport, along with electrode charge transport are modeled along the direction perpendicular to the current collectors (1-D) while electrode mass transport is resolved in a *pseudo* radial direction from the center to the surface of each active particle, which are assumed to be spherical in shape. The implementation of the DFN model in COMSOL can be visualized with the help of Fig. 4.1. To accommodate the convenience of utilizing different geometrical configurations in the DFN model with-

[1]The scale separation parameter ε is defined as the ratio of the characteristic length scale l of the unit cell Y, and the characteristic length scale L of the porous electrode: $\varepsilon \equiv \frac{l}{L}$. For porous battery electrodes, L is typically of the order of the thickness of the electrode under consideration.

out the need to resize the designed geometry, for instance the electrode thickness values, normalized length values were utilized in the model instead of natural length values.

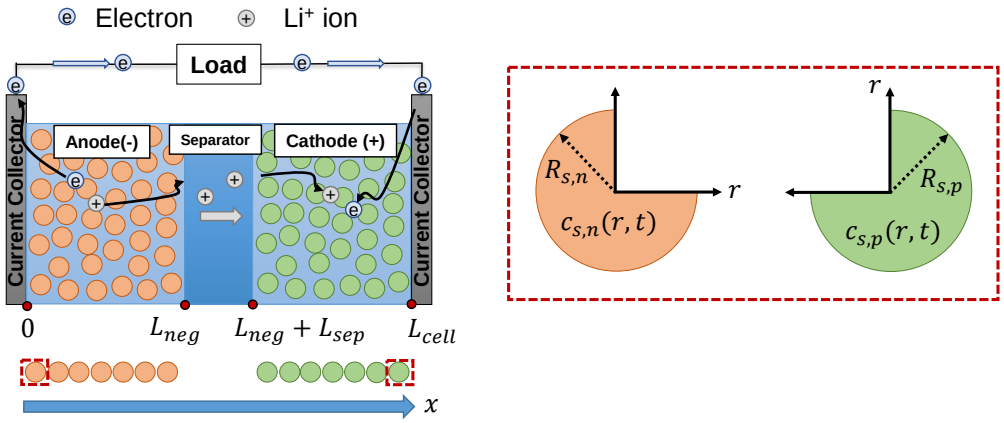

Figure 4.1: Visualization of the implementation of the DFN model in COMSOL. Electrolyte concentration along with the potential variables are resolved in 1-D in the direction of electrode thickness. Electrode concentration is resolved along the radial direction of every active particle that is considered in the direction perpendicular to the current collectors.

L_{neg}, L_{sep}, and L_{pos} represent the thickness of the anode, separator, and cathode regions of the lithium-ion battery, respectively. The sum of these three parameters is equal to L_{cell}. The symbol $\bar{x}$ is used to represent position with respect to the normalized length while x is retained to represent the physical position. The advantage offered by normalization is that regardless of the values of L_{neg}, L_{sep}, and L_{pos}, the dimension of each region inside the battery is equal to 1.0. In general, the normalized variable can be defined in terms of the natural variable as

$$\bar{x}_{region} = \frac{x}{L_{region}} + \text{constant}. \tag{4.4}$$

As a result, the derivative terms can be transformed to the normalized coordinate system using the relationship

$$\frac{\partial(\cdot)}{\partial x} = \frac{1}{L_{region}} \frac{\partial(\cdot)}{\partial \bar{x}} \tag{4.5}$$

The electrode mass conservation equation is resolved in the *pseudo* radial direction, r, instead of the Cartesian linear dimension, x. At every x location in the anode and the cathode, the concentration profile of lithium within the active particles, from center to the surface, is determined using the spherical coordinate

formulation. This process is first initiated by normalizing the radial dimension:

$$\bar{r} = \frac{r}{R_{s,j}}, \quad j = \{n, p\}, \tag{4.6}$$

which then leads to the following transformation of the derivative term in the normalized coordinate system:

$$\frac{\partial(\cdot)}{\partial r} = \frac{1}{R_{s,j}} \frac{\partial(\cdot)}{\partial \bar{r}}. \tag{4.7}$$

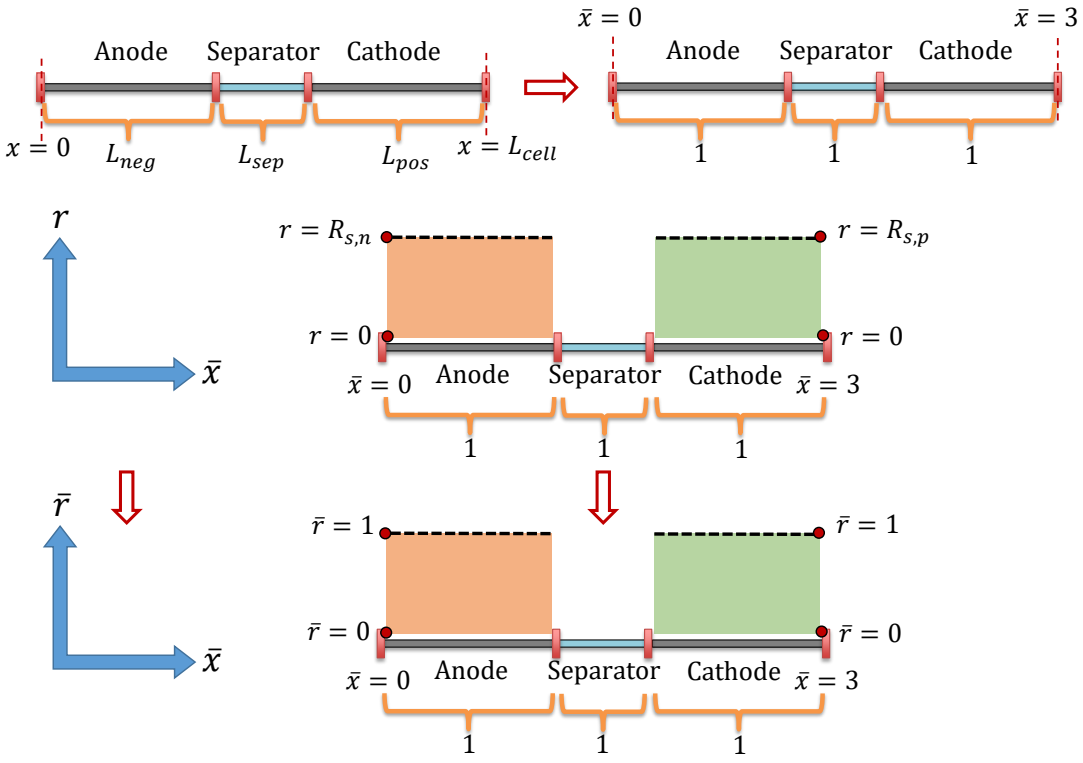

Figure 4.2: Illustration of the normalization of the linear x and radial r coordinates during the implementation of the DFN model equations.

Figure 4.2 schematically represents the normalization of the linear and radial coordinate dimensions for the implementation of the DFN model equations. It must be noted that in COMSOL, x is utilized to represent the normalized linear coordinate $\bar{x}$, and y is utilized instead of $\bar{r}$ as the representation of the normalized radial coordinate. In the *pseudo* radial direction, $y = 0$ represents the center of the spherical active particle, i.e. $r = 0$, while $y = 1$ represents the outer surface of the spherical active particle, i.e. $r = R_{s,j}$. In the DFN

Table 4.2: General and normalized mass and charge transport equations of the DFN macroscale model. The normalized equations are implemented in COMSOL.

General DFN Model	Normalized DFN Model
Electrode Mass Transport Equation; $j = (n, p)$	
$\frac{\partial c_{s,j}(x,r,t)}{\partial t} = \frac{1}{r^2}\frac{\partial}{\partial r}\left(D_{s,j} r^2 \frac{\partial c_{s,j}(x,r,t)}{\partial r}\right)$	$\bar{r}^2 R_{s,j} \frac{\partial c_{s,j}(\bar{x},\bar{r},t)}{\partial t} = \frac{1}{\partial \bar{r}}\left(D_{s,j}\frac{\bar{r}^2}{R_{s,j}} \frac{\partial c_{s,j}(\bar{x},\bar{r},t)}{\partial \bar{r}}\right)$
Electrolyte Mass Transport Equation; $j = (n, s, p)$	
$\eta_{e,j}\frac{\partial \bar{c}_{e,j}(x,t)}{\partial t} = \frac{\partial}{\partial x}\left(D_{e,j}^{eff}\frac{\partial \bar{c}_{e,j}(x,t)}{\partial x}\right) + \frac{(1-t_+)}{F} J_{Li,j}(x,t)$	$\eta_{e,j}\frac{\partial \bar{c}_{e,j}(\bar{x},t)}{\partial t} = \frac{1}{(L_{region})^2}\frac{\partial}{\partial \bar{x}}\left(D_{e,j}^{eff}\frac{\partial \bar{c}_{e,j}(\bar{x},t)}{\partial \bar{x}}\right) + \frac{(1-t_+)}{F} J_{Li,j}(\bar{x},t)$
Electrode Charge Transport Equation; $j = (n, p)$	
$K_{s,j}^{eff}\frac{\partial^2 \bar{\phi}_{s,j}(x,t)}{\partial x^2} = J_{Li,j}(x,t)$	$K_{s,j}^{eff}\frac{\partial^2 \bar{\phi}_{s,j}(\bar{x},t)}{\partial \bar{x}^2} = (L_{region})^2 J_{Li,j}(\bar{x},t)$
Electrolyte Charge Transport Equation; $j = (n, s, p)$	
$-K_{e,j}^{eff}\frac{\partial^2 \bar{\phi}_{e,j}(x,t)}{\partial x^2} - \frac{2K_{e,j}^{eff}(x,t)RT(1-t_+)}{F}\frac{\partial^2 \ln \bar{c}_{e,j}}{\partial x^2} = J_{Li,j}(x,t)$	$-K_{e,j}^{eff}\frac{\partial^2 \bar{\phi}_{e,j}(\bar{x},t)}{\partial \bar{x}^2} - \frac{2K_{e,j}^{eff}(\bar{x},t)RT(1-t_+)}{F}\frac{\partial^2 \ln \bar{c}_{e,j}}{\partial \bar{x}^2} = (L_{region})^2 J_{Li,j}(\bar{x},t)$

model, there is no consideration of lithium diffusion within the solid in the linear direction x. Solid phase lithium diffusion is considered in the "vertical" y direction (or) the radial direction. The electrolyte mass and charge transport equations are normalized similar to the electrode charge transport equation. Table 4.2 summarizes the normalized mass and charge transport equations of the DFN model that is implemented in COMSOL.

Table 4.3: Boundary conditions of the variables $\bar{\phi}_s$, $\bar{\phi}_e$, and $\bar{c}_e$ of the DFN model.

Variable	Location: $x = 0$	Location: $x = L_{neg}$	Location: $x = L_{neg} + L_{sep}$	Location: $x = L_{cell}$
$\bar{\phi}_s$	Constraint: $\bar{\phi}_{s,n} = 0$	$\frac{\partial \bar{\phi}_{s,n}}{\partial x} = 0$	$\frac{\partial \bar{\phi}_{s,p}}{\partial x} = 0$	$K_{s,p}^{eff}\frac{\partial \bar{\phi}_{s,p}}{\partial x} = -\frac{I_{app}}{A_{cell}}$
$\bar{\phi}_e$	$K_{e,n}^{eff}\left[\frac{\partial \bar{\phi}_{e,n}}{\partial x} + \frac{2RT(1-t_+)}{F}\frac{\partial \ln \bar{c}_{e,n}}{\partial x}\right] = 0$	Not required due to continuity	Not required due to continuity	$K_{e,p}^{eff}\left[\frac{\partial \bar{\phi}_{e,p}}{\partial x} + \frac{2RT(1-t_+)}{F}\frac{\partial \ln \bar{c}_{e,p}}{\partial x}\right] = 0$
$\bar{c}_e$	$\frac{\partial \bar{c}_{e,n}}{\partial x} = 0$	Not required due to continuity	Not required due to continuity	$\frac{\partial \bar{c}_{e,p}}{\partial x} = 0$

Table 4.4: Initial conditions of the four variables of the DFN model.

Variable	Anode	Separator	Cathode
$\bar{\phi}_s$	$\bar{\phi}_{s,n} = 0$	Not applicable	$\bar{\phi}_{s,p}\,(t=0) = \left[U_{0,p}(x_{p,init}) - U_{0,n}(x_{n,init})\right]$
$\bar{\phi}_e$	$\bar{\phi}_{e,n}\,(t=0) = 0$	$\bar{\phi}_{e,sep}\,(t=0) = 0$	$\bar{\phi}_{e,p}\,(t=0) = 0$
c_s	$c_{s,n}\,(t=0) = x_{n,init} \cdot c_{s,n,max}$	Not applicable	$c_{s,p}\,(t=0) = x_{p,init} \cdot c_{s,p,max}$
$\bar{c}_e$	$\bar{c}_{e,n}\,(t=0) = c_{e,init}$	$\bar{c}_{e,sep}\,(t=0) = c_{e,init}$	$\bar{c}_{e,p}\,(t=0) = c_{e,init}$

The boundary conditions of the variables $\bar{\phi}_s$, $\bar{\phi}_e$, and $\bar{c}_e$ of the DFN model are summarized in Table 4.3. I_{app} refers to the applied current and A_{cell} refers to the cross-sectional area of the electrode in a cell. Since c_s is resolved in the radial direction, the boundary conditions that apply for c_s at the center and the outer surface of each spherical active particle are:

$$\left.\frac{\partial c_{s,j}}{\partial r}\right|_{r=0} = 0 \quad \text{and} \quad D_{s,j}\left.\frac{\partial c_{s,j}}{\partial r}\right|_{r=R_{s,j}} = -\frac{J_{Li,j}}{a_j \cdot F}, \quad j = \{n, p\}. \tag{4.8}$$

The initial conditions for the four variables of the DFN model are summarized in Table 4.4. $x_{n,init}$ and $x_{p,init}$ are anode and cathode stoichiometric coefficients, respectively, that indicate the total amount of lithium stored in the active particls of each electrode during the beginning of simulation. $c_{e,init}$ is the initial concentration of electrolyte inside the medium, and is considered to be the same everywhere when the battery is at steady-state. The non-linear partial differential equations (PDEs) of the model are coupled through the intercalation current density. In addition to this coupling, the charge conservation equation in the electrolyte consists of both the electrolyte concentration and potential variables. Individual physics-based study interfaces are used for each model variable, wherein the general form of the particular PDE is input along with all the boundary and initial conditions, and any constraints that apply to that particular variable. While the variables $\bar{\phi}_s$, $\bar{\phi}_e$, and $\bar{c}_e$ are resolved in a 1-D setting, the variable c_s is resolved in a 2-D setting where one direction is the linear x and the other direction is the radial y. However, as mentioned earlier, solid-phase lithium is not considered in the x direction, hence the xx, xy, and yx components of the solid phase diffusion tensor are set to zero.

Even though all four variable of the DFN model are resolved simultaneously, the variable c_s is resolved in a different computational domain. In order to transfer the results from one domain to the other 3

variables and vice-sersa, the *linear extrusion operator* functionality is utilized in COMSOL to establish a mapping between the two regions. When $\bar{\phi}_s$, $\bar{\phi}_e$, and $\bar{c}_e$ are solved in the 1-D domain, their resolved values are treated as the source and transferred to the destination surface boundary of the 2-D domain where c_s is resolved. The surface boundary of the 2-D domain is represented using the black dotted lines in Fig. 4.2. The same approach is implemented when c_s is solved in the source 2-D domain and its resolved values are transferred to the destination 1-D domain. For the 1-D domain,a predefined physics-based *fine* mesh is utilized for discretization while a customized user-controlled mesh is utilized for the 2-D domain. The DFN model variables are resolved for a specified input current profile using a time-dependent study in COMSOL. Fixed time-step is used during the simulation studies, and the obtained results are exported from the COMSOL environment in a spreadsheet format for review and analysis.

4.4 Numerical Implementation of the FHM Model

The implementation of the FHM model in COMSOL Multiphysics®is discussed in this section. A detailed user guide that elaborates upon the procedure to develop the FHM model from the initiation phase to the final solver configuration setup prior to simulation is presented. The development of this model in COMSOL facilitates the comparison studies conducted to assess the performance of the DFN and FHM models using the same computational platform. The FHM model can be developed in 2-D or 3-D, provided intricate geometrical information and details of the electrode morphology in the 18650 cylindrical cells is available. This information is generally not provided by the manufacturer. Taking into consideration that an unbiased comparison of both the DFN and FHM models must be made, the FHM model is developed in a one-dimensional setting. Unlike the DFN model where a *pseudo* dimension is defined to resolve c_s, the FHM model is developed as a completely 1-D model where all four variables are resolved in the direction perpendicular to the current collectors. The implementation of the FHM model in COMSOL can be visualized with the help of Fig. 4.3.

It must be noted that in the DFN model, the variable c_s is resolved using a pore-scale mass transport equation that is simplified in spherical coordinates. However, in the FHM model, the variable $\bar{c}_s$ is an averaged transport variable that is resolved using an *effective* or *upscaled* mass tranport equation. Hence there is no need to implement the use of a *pseudo* dimension during the resolution of the FHM model equations. In addition, it is observed that there is no specific need to utilize normalized length values while resolving the FHM model, since COMSOL did not indicate any added computational demand or inconveniences cause

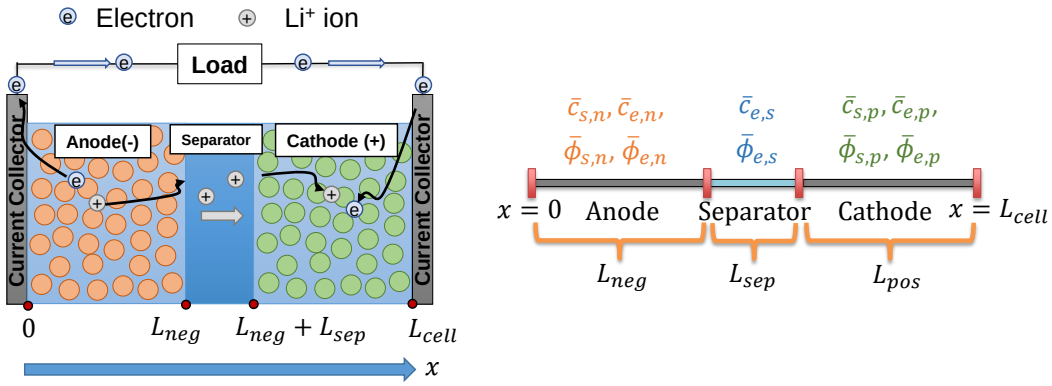

Figure 4.3: Illustration of the FHM model implementation using COMSOL. The variables of the model that are resolved in specific regions of the battery medium in 1-D are specified in the image shown.

Table 4.5: Boundary conditions of the variables $\bar{c}_s$, $\bar{\phi}_s$, $\bar{c}_e$, and $\bar{\phi}_e$ of the FHM model.

Variable	Location: $x = 0$	Location: $x = L_{neg}$	Location: $x = L_{neg} + L_{sep}$	Location: $x = L_{cell}$
$\bar{c}_s$	$D_{s,n}^{eff} \frac{\partial \bar{c}_{s,n}}{\partial x} = 0$	$D_{s,n}^{eff} \frac{\bar{c}_{s,n}}{\partial x} = -\frac{J_{Li,n}}{F \cdot L_{neg}}$	$D_{s,p}^{eff} \frac{\bar{c}_{s,p}}{\partial x} = -\frac{J_{Li,p}}{F \cdot L_{pos}}$	$D_{s,p}^{eff} \frac{\partial \bar{c}_{s,p}}{\partial x} = 0$
$\bar{\phi}_s$	Constraint: $\bar{\phi}_{s,n} = 0$	$\frac{\partial \bar{\phi}_{s,n}}{\partial x} = 0$	$\frac{\partial \bar{\phi}_{s,p}}{\partial x} = 0$	$K_{s,p}^{eff} \frac{\partial \bar{\phi}_s}{\partial x} = -\frac{I_{app}}{A_{cell}}$
$\bar{c}_e$	$\frac{\partial \bar{c}_{e,n}}{\partial x} = 0$	Not required due to continuity	Not required due to continuity	$\frac{\partial \bar{c}_{e,p}}{\partial x} = 0$
$\bar{\phi}_e$	$K_{e,n}^{eff} \left[\frac{\partial \bar{\phi}_{e,n}}{\partial x} + \frac{RTt_+}{F} \frac{\partial \ln \bar{c}_{e,n}}{\partial x} \right] = 0$	Not required due to continuity	Not required due to continuity	$K_{e,p}^{eff} \left[\frac{\partial \bar{\phi}_{e,p}}{\partial x} + \frac{RTt_+}{F} \frac{\partial \ln \bar{c}_{e,p}}{\partial x} \right] = 0$

due to the presence of natural dimensionalized length values. Hence the FHM model equations summarized in Table 4.1 are implemented in 1-D coordinates. While no additional modifications are required, the diffusion and conductivity tensors in 3-D notation are now reduced to scalar values in the 1-D formulation of the FHM model equations. Effective electrode diffusion and conductivity are represented by D_s^{eff} and K_s^{eff}, respectively and are assumed to be concentration-independent entities. Electrolyte diffusion and conductivity are represented by D_e^{eff} and K_e^{eff}, respectively and are concentration-dependent entities. The boundary conditions and initial conditions of the variables $\bar{c}_s$, $\bar{\phi}_s$, $\bar{c}_e$, and $\bar{\phi}_e$ are specified in Table 4.5 and Table 4.6, respectively.

It must be noted in the FHM model that in addition to the coupling of the non-linear PDEs of the model through the intercalation current density, both the mass and charge conservation equations in the electrolyte phase consist of the electrolyte concentration and potential variables. Similar to the DFN

Table 4.6: Initial conditions of the four variables of the FHM model.

Variable	Anode	Separator	Cathode
$\bar{\phi}_s$	$\bar{\phi}_{s,n} = 0$	Not applicable	$\bar{\phi}_{s,p}\,(t=0) = \left[U_{0,p}(x_{p,init}) - U_{0,n}(x_{n,init})\right]$
$\bar{\phi}_e$	$\bar{\phi}_{e,n}\,(t=0) = 0$	$\bar{\phi}_{e,sep}\,(t=0) = 0$	$\bar{\phi}_{e,p}\,(t=0) = 0$
$\bar{c}_s$	$\bar{c}_{s,n}\,(t=0) = x_{n,init} \cdot c_{s,n,max}$	Not applicable	$\bar{c}_{s,p}\,(t=0) = x_{p,init} \cdot c_{s,p,max}$
$\bar{c}_e$	$\bar{c}_{e,n}\,(t=0) = c_{e,init}$	$\bar{c}_{e,sep}\,(t=0) = c_{e,init}$	$\bar{c}_{e,p}\,(t=0) = c_{e,init}$

model implementation, individual physics-based study interfaces are used for each FHM model variable. The general form of the PDE is input along with the associated boundary conditions, initial conditions, and any constraints that apply to each model variable. The FHM model variables are also resolved for an input current profile using a time-dependent study and fixed time-step during simulations. The terminal voltage of the cell in both the DFN and the FHM models is determined using the expression:

$$V(t) = \bar{\phi}_s(L_{cell}, t) - \bar{\phi}_s(0, t) - R_c \cdot I_{app}(t), \tag{4.9}$$

where R_c is the contact resistance at the current collectors. This is the model-predicted output of cell voltage from the simulations and is compared with the experimentally measured voltage response. To facilitate consistent and reliable results for cell chemistry and prevent any numerical stability issues that result from the generation of complex numbers during simulation, the following steps were implemented in the FHM COMSOL model:

1. The graphite anode and NMC cathode open circuit potential (OCP) values for the simulation of the 18650 NMC cell behavior were obtained from literature [88]. An interpolation function is used in COMSOL to express the OCP of each electrode as a function of their respective stoichiometric coefficient.

2. The pore-scale electrolyte diffusion and conductivity coefficients as a function of concentration and temperature were obtained from literature [162] using linear interpolation. The effective diffusion and conductivity values for the DFN model were obtained using the Bruggeman approach [148]. For the FHM model, the effective ionic transport properties were calculated by resolving the closure variable problem, as explained in section §2.3.

3. To prevent numerical instabilities due to the terms in square root in the intercalation current density, the following stopping criteria were imposed during simulations to prevent the generation of complex numbers:

Stopping Criteria 1	$\bar{c}_{s,n} \leq 32 \left[\text{mol/m}^3\right]$
Stopping Criteria 2	$\bar{c}_{s,p} \geq \left(c_{s,p,max} - 32\right) \left[\text{mol/m}^3\right]$
Stopping Criteria 3	$\left(\bar{\phi}_s(L_{cell}, t) - \bar{\phi}_s(0, t) - R_c \cdot I_{app}(t)\right) \leq 2.50 \text{ [V]}$

   At every time instant, the values of $\bar{c}_{s,n}$ and $\bar{c}_{s,p}$ were monitored at the locations $x = L_{neg}$ and $x = L_{neg} + L_{sep}$ respectively, since the minimum and maximum concentrations in the two electrodes were first attained at these locations. This is performed using an integration function in COMSOL to update the concentration values at these locations during every time step.

4. All four variables of the FHM model are resolved simultaneously at each time step, and successive iterations are performed until convergence is achieved. To ensure that that there are no convergence related issues, particularly during model parameter identification where initial parameter guess is provided to COMSOL through an external source, the termination technique for convergence is based on a tolerance value of 0.001, and the maximum number of iterations is increased to 800 from a default value of 4.

The applied current $I_{app}(t)$ is provided as an input in COMSOL using the interpolation function. The aforementioned steps to improve stability and convergence are also implemented in the DFN COMSOL model. In this case, stopping criteria 1 and 2 were based on the values of the surface concentration $c_{s,surf,n}$ and $c_{s,surf,p}$, respectively. The locations where these variables were monitored at every time step is the same as that in the FHM model. The next section describes the approach implemented to identify the parameters of the DFN and the FHM models using experimental data.

4.5 Model Parameter Identification Approach

This section elaborates upon the identification studies conducted to determine the parameters of the DFN and the FHM models using an integrated Matlab®and COMSOL Multiphysics®co-simulation framework. The parameters of both models were identified by selecting a specific experimental data set and minimizing the error between the measured voltage response and the model-predicted voltage for a specified

current input using an objective function. A total of 18 parameters of the DFN and FHM models are identified using experimental data, with the vector of parameters, θ, being:

$$\theta_{DFN} = \big[L_{neg}\ L_{sep}\ L_{pos}\ A_{cell}\ D_{s,n}\ D_{s,p}\ k_{0,n}\ k_{0,p}\ R_c \\ x_{n,init}\ x_{p,init}\ c_{s,n,max}\ c_{s,p,max}\ \eta_n\ \eta_p\ \eta_{e,n}\ \eta_{e,sep}\ \eta_{e,p}\big]^T \tag{4.10}$$

for the DFN model and

$$\theta_{FHM} = \big[L_{neg}\ L_{sep}\ L_{pos}\ A_{cell}\ D_{s,n}^{eff}\ D_{s,p}^{eff}\ k_n\ k_p\ R_c \\ x_{n,init}\ x_{p,init}\ c_{s,n,max}\ c_{s,p,max}\ \eta_n\ \eta_p\ \eta_{e,n}\ \eta_{e,sep}\ \eta_{e,p}\big]^T \tag{4.11}$$

for the FHM model. The vector of parameters for both the models are identified using the Particle Swarm Optimization algorithm [186]. PSO is a non-gradient based evolutionary computational approach based on the social behavior of certain animal species [35]. It is designed to achieve the global minumum for a designed objective/fitness function by moving a population of possible solutions, constituting the *swarm*, through a multi-dimensional solution hyperspace in an iterative fashion [187]. The objective of the parameter identification study is to determine the element values of the vector θ, such that the model-predicted voltage output matches the experimentally measured voltage as closely as possible. Mathematically, this is defined using the cost function:

$$J(\theta) = \sqrt{\left\{ \frac{1}{N} \sum_{i=1}^{N} \Big(V_{exp}(i) - V_{mod}(\theta; i) \Big)^2 \right\}}, \tag{4.12}$$

where V_{exp} is the experimentally measured voltage response of the lithium-ion cell, V_{mod} is the model-predicted voltage that is a function of θ, N is the total number of data samples, and i is the time index. The mathematical expression for the cost function is a representation of the root mean square (RMS) error.

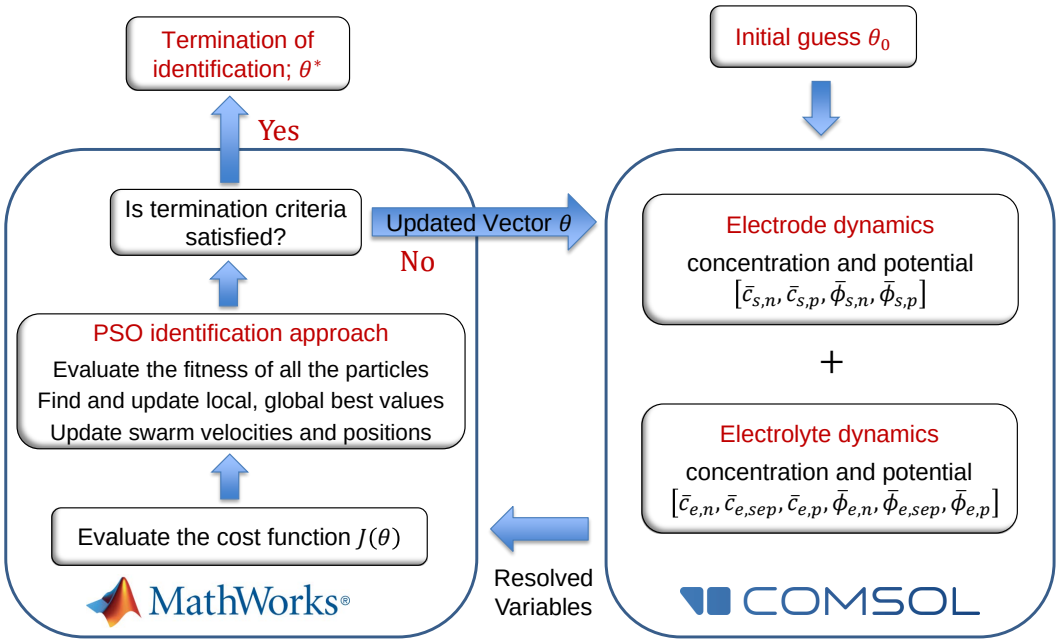

Figure 4.4: Flowchart describing the iterative process of parameter identification for the FHM model in the co-simulation framework involving COMSOL Multiphysics® and Matlab®.

Figure 4.4 describes the co-simulation flowchart for the parameter identification studies conducted on the FHM model using COMSOL Multiphysics® and Matlab®. The variables $\bar{c}_{s,n}$ and $\bar{c}_{s,p}$ are replaced with $c_{s,n}$ and $c_{s,p}$ for the DFN model. The PSO-based identification is initiated by providing an initial guess for the vector θ. A suitable initial guess is determined based on values reported in literature and minor modifications through trial and error. The PSO initializes the particles with random position and velocity vectors. The initial guess is provided to the COMSOL model, the four model variables are resolved for the provided input parameter vector θ, and the results are exported to the Matlab® framework.

The PSO algorithm begins with an evaluation of the fitness function for each particle. At the end of these evaluations, the individual and global best fitness values are recorded. For each particle, the local best fitness value is set as its current fitness value, and the local best position is set as its current position. In subsequent iterations, if a particle's fitness value is better than the individual best fitness value, then the current fitness value is assigned the individual best value. Otherwise, the individual best value remains unchanged. The best fitness value among all the particles is assigned as the global best value. Then, using the individual and global best fitness values, the position and velocity of each swarm particle is updated for the next iteration. If the termination criteria is satisfied, the identification study is terminated by exiting

the loop and the optimized vector of parameter values, $\theta^{\star}$ is saved as the output of the identification study. Otherwise, the updated vector of parameters θ is provided to COMSOL® for the next iteration and the process is continued.

The common elements of the vector θ in the DFN and the FHM models comprise anode thickness L_{neg}, separator thickness L_{sep}, cathode thickness L_{pos}, cross-sectional area of the cell A_{cell}, contact resistance R_c, anode and cathode stoichiometric coefficients $x_{n,init}$ and $x_{p,init}$, the maximum anode and cathode lithium storage concentrations $c_{s,n,max}$ and $C_{s,p,max}$, the anode and cathode active material volume fractions η_n and η_p, and the electrolyte volume fraction in the anode, separator, and cathode represented respectively by $\eta_{e,n}$, $\eta_{e,sep}$, and $\eta_{e,p}$. The identification range of these 14 parameters for the 18650 NMC cells have been desgined based on values reported in literature [88], and are reported in Table 4.7. The radius of the active particles in the anode and cathode were kept constant at a value of 5 μm for both the models.

The parameter identification approach to determine model parameters is implemented as follows:

Table 4.7: The range of variation of the common parameters of both models during the identification process.

Parameter	Identification Range	Parameter	Identification Range
L_{neg}	$[45e-6, 55e-6]$	$c_{s,n,max}$	$[26000, 31500]$
L_{sep}	$[20e-6, 32e-6]$	$c_{s,p,max}$	$[45000, 50000]$
L_{pos}	$[35e-6, 45e-6]$	η_n	$[0.54, 0.66]$
A_{cell}	$[0.1006, 0.1120]$	η_p	$[0.50, 0.60]$
R_c	$[0.024, 0.036]$	$\eta_{e,n}$	$[0.28, 0.36]$
$x_{n,init}$	$[0.75, 0.80]$	$\eta_{e,sep}$	$[0.35, 0.45]$
$x_{p,init}$	$[0.31, 0.36]$	$\eta_{e,p}$	$[0.28, 0.36]$

1. Step 1: The parameter identification study is conducted using the PSO algorithm [186], with a population size of 200 and 10 total generations. The termination criteria is defined as either 2200 completed iterations (or) the completion of 5 successive generations without any improvement in the cost function. Table 4.8 summarizes the details of the parameter identification study using the PSO algorithm.

2. Step 2: The 18 parameters represented in θ were individually identified for both models using data from 2 A constant current capacity test in discharge experiment conducted at room temperature (23°C). The anode and cathode conductivity coefficients were maintained constant, since prior identification studies [188] observed that they had no impact on model-predicted voltage response. Their true values were obtained from literature [7] and kept unchanged in subsequent identification studies.

Table 4.8: Details of the parameter identification study.

PSO Option	Value/Setting
options.PopulationSize	200
options.Generations	10
options.Vectorized	off
options.TolFun	0.5e-6
options.StallGenLimit	5
options.CognitiveAttraction	0.3
options.SocialAttraction	3.6
options.BoundaryMethod	absorb

3. Step 3: The 13 geometric and stoichiometric parameters identified for the DFN and FHM models were averaged. These parameters characterize the design of the cell, and are optimized by the manufacturer for a target application. This information is generally not provided by the manufacturers. Identification is a non-destructive approach to determine these parameters. However, it is not justified to make use of different values for these parameters on the basis of different models, when in reality they possess a unique value. To address this issue while enabling unbiased simulations and identification studies, the averaged values of these 13 parameters are used in both the models, and are summarized in Table 4.9.

4. Step 4: The 13 averaged parameter values are invariant with respect to temperature and kept fixed for all the subsequent identification studies. Since the averaging of parameters compromises the predictability of both the models, the identification study in Step 1 is repeated to optimized the other 5 parameters: the two electrode diffusion coefficients, the two reaction rate constants, and the contact resistance. Table 4.10 reports the identification range used for these parameters.

5. Step 5: In predicting battery dynamics at other thermal conditions of cell operation, only the aforementioned 5 parameters are identified as a function of temperature. The same cost function is utilized in all the identification studies to minimize the model-predicted error in the output cell voltage. The results from the identification of these five parameters as a function of temperature are reported in Table 4.11.

Table 4.9: The individually identified geometric and stoichiometric parameters of the DFN and FHM models, and their average values.

Parameter	DFN Model Identified Value	FHM Model Identified Value	Average
L_{neg} [m]	$50.60e-6$	$51.60e-6$	$51.1e-6$
L_{sep} [m]	$31.0e-6$	$24.9e-6$	$28e-6$
L_{pos} [m]	$40.8e-6$	$39.4e-6$	$40.1e-6$
A_{cell} [m^2]	0.1058	0.1026	0.1042
$x_{n,init}$ [$-$]	0.7878	0.7748	0.7813
$x_{p,init}$ [$-$]	0.3507	0.3402	0.3455
$c_{s,n,max}$ [mol/m^3]	29970	27611	28791
$c_{s,p,max}$ [mol/m^3]	46264	47852	47058
$\eta_{s,n}$ [$-$]	0.5813	0.6599	0.6206
$\eta_{s,p}$ [$-$]	0.5729	0.5724	0.5727
$\eta_{e,n}$ [$-$]	0.3037	0.2939	0.2988
$\eta_{e,sep}$ [$-$]	0.4320	0.3888	0.4104
$\eta_{e,p}$ [$-$]	0.2841	0.3035	0.2938

Table 4.10: The identification range of the 5 parameters used for the 23°C experimental data set.

DFN Parameter	Identification Range	FHM Parameter	Identification Range
$D_{s,n}$	$[1.8e-14, 5.0e-14]$	$D_{s,n}^{eff}$	$[8e-12, 4e-11]$
$D_{s,p}$	$[2.7e-14, 6.0e-14]$	$D_{s,p}^{eff}$	$[1e-11, 6e-11]$
$k_{0,n}$	$[3e-4, 14e-4]$	k_n	$[6e-5, 1e-4]$
$k_{0,p}$	$[2e-4, 10e-4]$	k_p	$[3e-5, 8e-5]$
R_c	$[0.024, 0.030]$	R_c	$[0.024, 0.030]$

The parameter identification studies were conducted on a Dell Precision T5810 desktop computer with 32.0 GB random access memory and Intel(R) Xeon(R) CPU E5-1650 v3 3.50 GHz processor. The parameter identification study using the FHM model and 23°C data took $65,048$ s to complete, while the DFN model identification study using the 23°C data took $86,709$ s to complete. The longer simulation time per iteration of the DFN model is attributed to the resolution of the model variables in two computational domains (radial and linear). The FHM model is computationally more efficient because of the resolution of all four model variables in only one computational domain (linear).

Table 4.11: The identified values of the five parameters of the DFN and FHM models using different temperature-based experimental data sets.

DFN Parameter	5°C	23°C	40°C	45°C	52°C
$D_{s,n}$ [$m^2 \cdot s^{-1}$]	$2.78e-14$	$3.50e-14$	$7.73e-14$	$9.27e-14$	$1.11e-13$
$D_{s,p}$ [$m^2 \cdot s^{-1}$]	$7.93e-14$	$1.42e-13$	$4.32e-13$	$5.64e-13$	$8.23e-13$
$k_{0,n}$ [$A \cdot m^{2.5} \cdot mol^{-1.5}$]	$2.01e-6$	$2.98e-5$	$1.64e-4$	$2.04e-4$	$2.80e-4$
$k_{0,p}$ [$A \cdot m^{2.5} \cdot mol^{-1.5}$]	$9.14e-7$	$1.72e-5$	$2.52e-5$	$4.20e-5$	$6.86e-5$
R_c [Ω]	0.060	0.030	0.021	0.018	0.015
FHM Parameter	5°C	23°C	40°C	45°C	52°C
$D_{s,n}^{eff}$ [$m^2 \cdot s^{-1}$]	$2.73e-11$	$3.30e-11$	$7.38e-11$	$1.82e-10$	$2.73e-10$
$D_{s,p}^{eff}$ [$m^2 \cdot s^{-1}$]	$4.33e-11$	$6.40e-11$	$8.41e-11$	$1.26e-11$	$1.21e-10$
k_n [$A \cdot m \cdot mol^{-1}$]	$1.23e-4$	$1.44e-4$	$1.49e-4$	$1.55e-4$	$1.77e-4$
k_p [$A \cdot m \cdot mol^{-1}$]	$9.69e-5$	$1.05e-4$	$2.15e-4$	$2.64e-4$	$2.71e-4$
R_c [Ω]	0.054	0.032	0.018	0.016	0.015

4.6 Results and Discussion

The results of the parameter identification study using the five experimental data sets are presented in Fig. 4.5. The RMS error between the experimental and model-predicted voltage response of both models are reported in Table 4.12. It can be observed that the performance of both models in predicting battery behavior is accurate at 5°C and 23°C. At higher temperatures of battery operation, the DFN model loses its accuracy towards the end of discharge. On the other hand, the FHM model predicts cell dynamics until the end of the discharge curve.

Table 4.12: Comparison of FHM and DFN model performance against experimental data.

Temperature	FHM Model RMS Error	DFN Model RMS Error
5°C	16.40 mV	20.60 mV
23°C	21.60 mV	22.10 mV
40°C	21.00 mV	75.80 mV
45°C	19.00 mV	83.90 mV
52°C	17.00 mV	87.80 mV

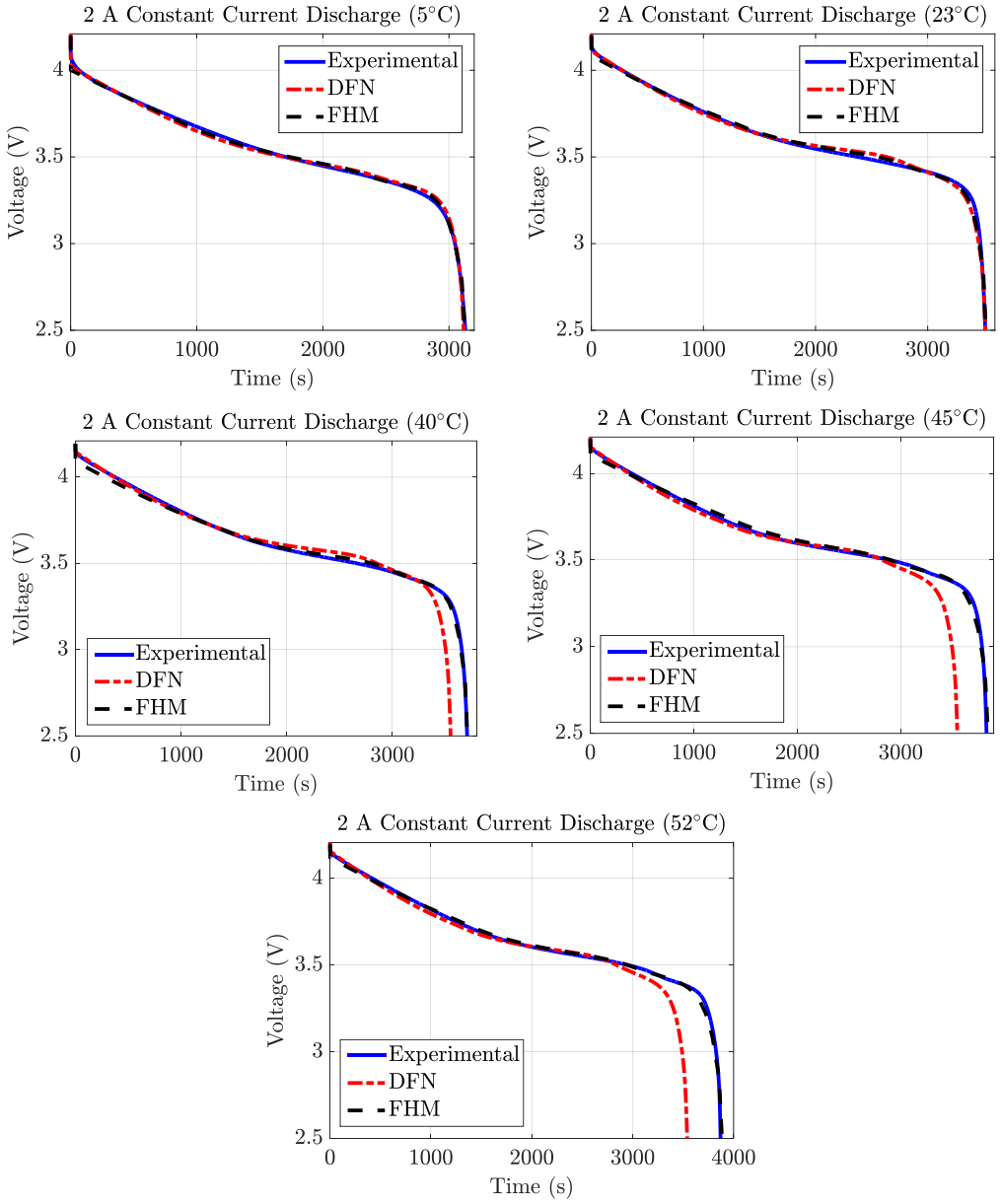

Figure 4.5: Performance of the DFN and FHM models against experimental data at different temperatures.

The performance of the DFN and FHM models is investigated by analyzing the simulation results of lithium concentration dynamics in the anode and cathode, illustrated in Fig. 4.6. Locations $x = L_{neg}$ and $x = L_{neg} + L_{sep}$ are selected for observation because anode electrode concentration is lowest at $x = L_{neg}$ and cathode concentration is highest at $x = L_{neg}+L_{sep}$ during cell discharge. The total duration of discharge during the 2 A constant constant experiments was 3829 s at 45°C and 3871 s at 52°C. At both temperatures,

in comparison with the FHM model, the DFN model predicts a faster rate of lithium depletion in the anode as well as faster rate of lithium deposition in the cathode. Lithium concentration is depleted to approximately 32 [mol/m^3] at around $t = 3550$ s in the anode, indicated by the red dashed line. Around the same time, lithium is nearly fully deposited to approximately 47030 [mol/m^3] in the cathode, indicated by the blue dashed line. This leads to the violation of stopping criteria 1 and 2 in the DFN model. As a result, battery dynamics is not captured for the complete range of discharge. The FHM model is able to predict battery behavior until the end of discharge, indicated by the black and magenta dash-dotted lines. Stopping criteria conditions 1 and 2 are not violated during the simulation of the FHM model for 45°C and 52°C.

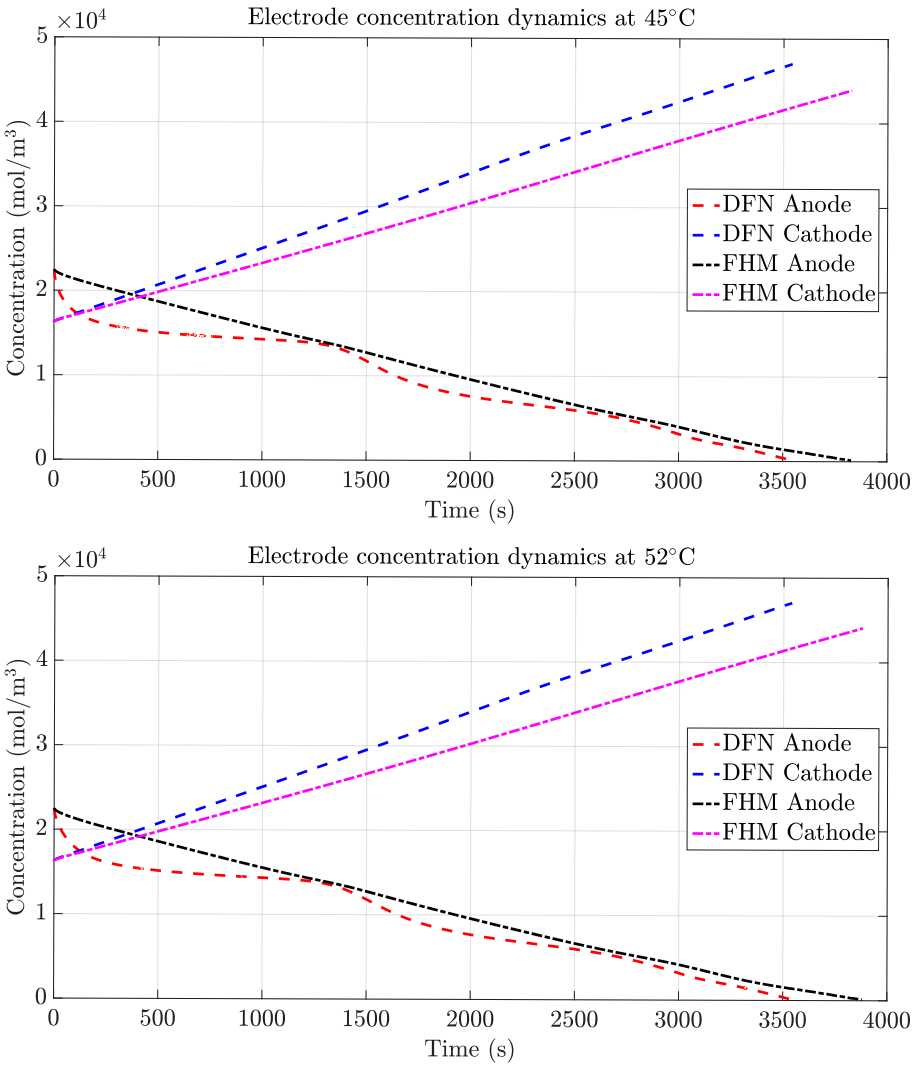

Figure 4.6: Electrode concentration dynamics predicted by the DFN and FHM models at the locations $x = L_{neg}$ and $x = L_{neg} + L_{sep}$.

Table 4.13: Dimensionless transport parameters Pe_e and Da_e calculated for the graphite anode.

DFN Model (Graphite Anode)						
Temperature [K]	D_e [$\text{m}^2\cdot\text{s}^{-1}$]	K_e [$\Omega^{-1}\text{m}^{-1}$]	Da_e [-]	Pe_e [-]	α [-]	β [-]
296	2.22e-10	1.00	1.21e-2	4.14e-2	-2.17	3.01
303	2.68e-10	1.15	2.08e-2	4.03e-2	-2.18	2.63
308	3.12e-10	1.32	2.96e-2	4.04e-2	-2.18	2.39
313	3.56e-10	1.46	4.23e-3	3.98e-2	-2.19	2.15
318	4.01e-10	1.63	6.03e-2	4.01e-2	-2.19	1.91
323	4.47e-10	1.77	8.55e-2	3.97e-2	-2.20	1.67
328	4.89e-10	1.89	1.22e-1	3.93e-2	-2.20	1.43
FHM Model (Graphite Anode)						
Temperature [K]	D_e [$\text{m}^2\cdot\text{s}^{-1}$]	K_e [$\Omega^{-1}\text{m}^{-1}$]	Da_e [-]	Pe_e [-]	α [-]	β [-]
296	2.22e-10	1.00	3.44e-4	4.14e-2	-2.19	5.47
303	2.68e-10	1.15	4.79e-4	4.03e-2	-2.20	5.25
308	3.12e-10	1.32	1.03e-3	4.04e-2	-2.20	4.72
313	3.56e-10	1.46	1.47e-3	3.98e-2	-2.21	4.48
318	4.01e-10	1.63	2.09e-3	4.01e-2	-2.21	4.23
323	4.47e-10	1.77	2.96e-3	3.97e-2	-2.22	3.99
328	4.89e-10	1.89	4.23e-3	3.93e-2	-2.22	3.75

4.6.1 Phase Diagram Analysis - *Pore-Scale* to *System Level*

In this subsection, the observations made from an electrolyte phase diagram analysis is presented. This study is conducted to assess the validity of the applicability constraints of macroscale models in predicting 18650 NMC cell behavior. The values of the phase diagram parameters (α,β) were plotted as a function of different cell operating temperatures, ranging from 23°C to 55°C. The pore-scale transport parameters identified using 23°C experimental data and summarized in Tables 4.9 and 4.11 were considered as the starting point. The phase diagram study after the completion of the first identification study at 23°C, in order to understand the critical temperature at which the applicability constraints are violated. For higher operating temperatures, a reliable estimate of the temperature-dependent rate constant k_j, $j = \big(n, p\big)$ value was calculated using the Arrhenius equation (2.48) and information from [172]. Pore-scale electrolyte diffusion and conductivity were computed at a reference concentration value of 1200 [mol/m^3] for different temperatures using linear interpolation of the experimentally measured coefficients presented in [162]. This value was considered as the initial electrolyte lithium concentration in the DFN and FHM models for all the parameter identification studies.

The dimensionless Péclet number Pe_e and the dimensionless Damkhöler number Da_e are computed

for the cell electrodes at different temperatures of cell operation. The dimensionless transport parameters are calculated using the approach presented in section §2.4. Table 4.13 reports the values of the phase diagram parameters computed for the graphite anode, and the electrolyte phase diagram corresponding to this analysis is illustrated in Fig. 4.7a.

Table 4.14: Dimensionless transport parameters Pe_e and Da_e are calculated for the NMC cathode.

DFN Model (NMC Cathode)						
Temperature [K]	D_e [$\text{m}^2\cdot\text{s}^{-1}$]	K_e [$\Omega^{-1}\text{m}^{-1}$]	Da_e [-]	Pe_e [-]	α [-]	β [-]
296	2.22e-10	1.00	7.00e-3	2.53e-2	-3.10	4.18
303	2.68e-10	1.15	1.21e-2	2.47e-2	-3.12	3.72
308	3.12e-10	1.32	1.72e-2	2.47e-2	-3.11	3.42
313	3.56e-10	1.46	2.45e-2	2.44e-2	-3.13	3.12
318	4.01e-10	1.63	3.50e-2	2.45e-2	-3.12	2.82
323	4.47e-10	1.77	4.96e-2	2.43e-2	-3.13	2.53
328	4.89e-10	1.89	7.07e-2	2.41e-2	-3.14	2.23
FHM Model (NMC Cathode)						
Temperature [K]	D_e [$\text{m}^2\cdot\text{s}^{-1}$]	K_e [$\Omega^{-1}\text{m}^{-1}$]	Da_e [-]	Pe_e [-]	α [-]	β [-]
296	2.22e-10	1.00	1.97e-4	2.53e-2	-3.10	7.19
303	2.68e-10	1.15	4.67e-4	2.47e-2	-3.12	6.46
308	3.12e-10	1.32	6.65e-4	2.47e-2	-3.11	6.16
313	3.56e-10	1.46	9.49e-4	2.44e-2	-3.13	5.86
318	4.01e-10	1.63	1.35e-3	2.45e-2	-3.12	5.56
323	4.47e-10	1.77	1.92e-3	2.43e-2	-3.13	5.27
328	4.89e-10	1.89	2.73e-3	2.41e-2	-3.14	4.97

Similarly, Table 4.14 provides the values of the phase diagram parameters (α,β) for the NMC cathode, and the results are schematically represented in Fig. 4.7b. It can be observed from both the phase diagrams that the points (α,β) of the DFN model transport parameters violate the applicability constraint ($\alpha + \beta \geq 0$) at temperatures of 40°C and beyond. Under all operating temperature conditions, the points (α,β) of the FHM model satisfy all the applicability constraints, and hence the points stay within the blue shaded region. Based on these results, five operating temperatures were selected for conducting experiments: a) the phase diagram transition temperature (40°C), b) 5°C and 23°C (two conditions below the transition temperature), and c) 45°C and 52°C (two conditions above the transition temperature).

The phase diagram plots shown in Fig. 4.7a and Fig. 4.7b are a predictive tool to single out the conditions of battery operating where model predictability is guaranteed, i.e. macroscale modeling error is bounded with respect to its pore-scale counterpart equations. When data points (α,β) of these phase diagrams

fall out of the applicability regime (defined by the blue shaded region), macroscale modeling electrolyte equation error is no longer bounded. Under these circumstances, it is important to provide a quantitative assessment of the error in the prediction of macroscale models using information from measurable system level quantities such as temperature, voltage, and current. Most of the parameters required to determine the phase diagram parameters (α,β) are either identified or estimated, but not experimentally measured. As a result, the 2-D phase diagrams are not directly utilizable as a predictive tool at the system level.

To address this issue, a system-level 3-D phase diagram is proposed that quantifies the theoretical predictability of macroscopic models within certain specified bounds for different operating conditions. This phase diagram correlates the percentage error between the experimentally measured and model-predicted cell voltage as a function of: a) the battery SoC and b) the cell temperature. This normalized voltage error is mathematically determined using the expression:

$$\%\text{ Voltage Error} = \sqrt{\left\{ \frac{1}{N} \sum_{i=1}^{N} \Big(V_{exp}(i) - V_{mod}(\theta; i) \Big)^2 \right\}} \cdot \frac{100 \cdot N}{\sum_{i=1}^{N} V_{exp}(i)} \,. \tag{4.13}$$

Estimation studies on lithium-ion batteries reported in [189, 190] considered the underlying models to be accurate if the error in voltage prediction was within an RMS error of $\pm 2\%$.

The state-of-charge (SoC) of the cell was calculated using the Coulomb counting technique. Using the measured cell current during discharge, the cell SoC, $SoC(t)$, is determined using the mathematical expression:

$$SoC(t) = SoC_{ini} - \frac{1}{Q_{cell}} \cdot \int_{t_0}^{t_f} I_{app}(t) dt \,, \tag{4.14}$$

where SoC_{ini} is the initial cell SoC, Q_{cell} is the measured capacity of the cell for each experimental data set in units of [A·s], t_0 and t_f denote the time at the beginning and end of the experiment, and $I_{app}(t)$ is the applied current and is positive during discharge. For the capacity tests in discharge, $SoC_{ini} = 100\%$ and $t_0 = 0$ s.

Figure 4.7c illustrates the prediction error in cell voltage by the DFN and FHM models as a function of the cell SoC for the five different temperature-based experimental data sets. The accuracy in voltage prediction by the two models to within an RMS error of $\pm 2\%$ is indicated by data points that lie within the region that is shaded in *cyan*. At temperatures of 5°C and 23°C, the DFN and FHM models show good accuracy in voltage prediction in the cell SoC range of $\big[0.05, 1.00\big]$.

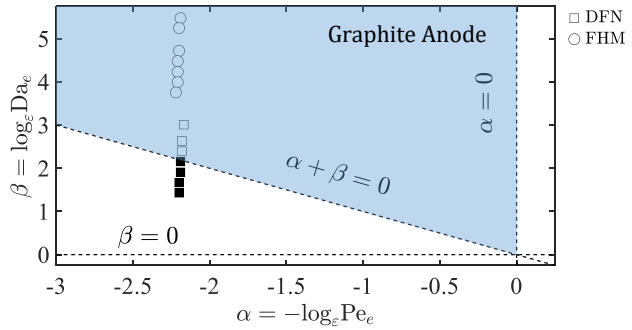

(a) Electrolyte phase diagram for the graphite anode of the 18650 cell.

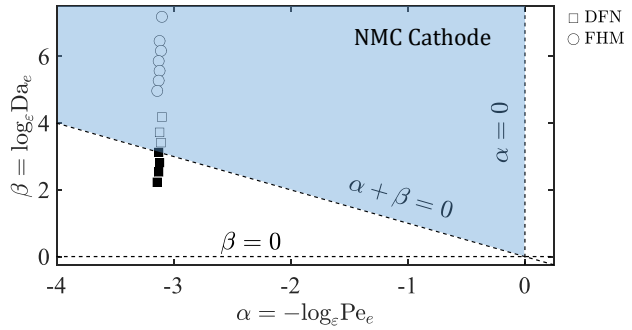

(b) Electrolyte phase diagram for the NMC cathode of the 18650 cell.

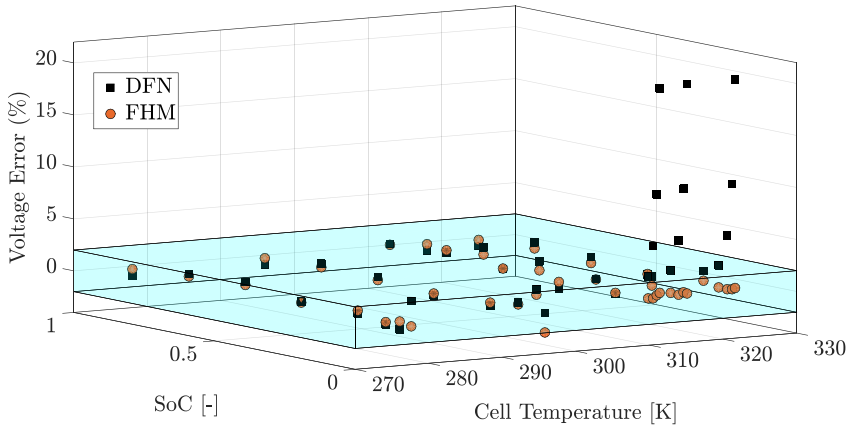

(c) Percentage RMS error in model-predicted voltage as a function of SoC and cell temperature.

Figure 4.7: The electrolyte phase diagrams (top and middle) assess the veracity of DFN and FHM macroscale models. The square and circular data points represent (α,β) values calculated for the DFN and FHM models, respectively. In the system level phase diagram (bottom), the black square data points represent the percentage RMS error in the DFN model-predicted voltage. The orange circular data points represent the percentage RMS error in the FHM model-predicted voltage. The data points in the bottom figure are plotted as a function of the cell SoC for five experimental data sets. The cell operating temperatures for the data points represented in this phase diagram are: 278K, 296K, 313K, 318K, and 325K.

Towards the end of the discharge curve, the DFN model has a voltage prediction error greater than 2% at SoC values of 1% and 3.5% for the 5°C and 23°C experimental data sets, respectively. The FHM model is always accurate to within 2% for the 5°C data set, and has an error of 2% at an SoC value of 0.5% for the 23°C experimental data set. The DFN model voltage prediction error exceeded 20% towards the end of cell discharge at 40°C, 45°C and 52°C. Under the same conditions, the FHM model retained less than 2% error. The DFN model error was greater than 2% at all SoC values below 8.30% for the 40°C data set, 13.40% for the 45°C data set, and 14.60% for the 52°C data set.

These observations validate the predictions made by the 2-D phase diagrams in Fig. 4.7a and Fig. 4.7b. Table 4.12 and Fig. 4.7c quantify the error in the predictability of the DFN and FHM models. For data points that lie within the applicability regime, the RMS error in voltage prediction is within 25 mV. For data points that violate the applicability constraints, the RMS error in voltage prediction exceeded 69 mV, as observed in the DFN model. These observations also indicate that significant caution must be exercised while implementing the DFN model and its simplified versions for model-based control applications, particularly full electric vehicles, where the battery cells operate over a wide range of SoC.

4.7 Conclusion

Accurate prediction of battery behavior across a wide range of operating temperatures and current rates of charge or discharge is dependent on a reliable description of battery internal transport processes. The fact that lithium-ion transport processes are highly non-linear and span multiple length scales indicates that ion transport can also be modeled on a multiplicity of scales. Macroscale battery models describing mass and charge transport are well suited as a reference model for developing model-based control and estimation strategies. The battery research community, for long, has considered the Doyle-Fuller-Newman (DFN) macroscale model [49, 191] as the benchmark to evaluate the predictability of reduced-order and simplified electrochemical models. However, macroscale models are approximate representations of micro-scale battery dynamics, and are vulnerable as predictive tools under specific operating conditions. One of the major contributions of this chapter is the identification of operating conditions under which the assumptions and approximations that facilitate the use of the DFN macroscale model are violated, leading to a loss of model predictability.

Section §4.2 presents a detailed comparison analysis of the mass and charge transport equations of the DFN and the FHM models. In the process, specific model attributes were highlighted to indicate enhance prediction capabilities of the FHM model over the DFN model. In particular, the electrolyte mass transport equation in the FHM model considers the effect of both diffusion and electromigration in the transport of lithium ions. In addition, the effective ionic transport parameters are determined using information from the geometric configuration of active particles in the unit cells, rather than relying on empirical formulations.

Section §4.3 summarizes the numerical implementation of the DFN model mass and charge transport equations using the finite element modeling software COMSOL Multiphysics®. The DFN model described in this chapter is developed by Plett *et. al* [183] and is a *pseudo two-dimensional* battery model. This is because electrode concentration is resolved in a *pseudo* radial direction as opposed to the other model variables that are resolved in the direction perpendicular to the current collectors. The equations of the DFN model were converted to a normalized form and setup in COMSOL prior to simulations. A *linear extrusion operator* function was used in COMSOL to facilitate the simultaneous resultion of all the four model variables and transfer information from one computational domain to the other at every time-step.

Section §4.4 presents a detailed discussion of the numerical implementation of the FHM model equations using COMSOL. The same software platform was utilized to validate the comparison studies on the performance of both models against experimental data. Unlike the DFN model, all the four model variables

of the FHM model are completely resolved in the direction perpendicular to the current collectors. The equations of the FHM model were resolved in dimensional form. The initial and boundary conditions of the FHM model are summarized in the form of tables. Different steps were implemented in the FHM model for reliable simulations and to prevent any numerical stability issues. Three different stopping criteria were imposed during the simulations such that no complex numbers were generated in the intercalation current density term, and battery operation was confined to its upper and lower voltage cut-off limits. The same stopping criterion was later incorporated in the DFN model. To ensure convergence at every time-step, the termination technique was based on a tolerance value of $1e-3$, and the maximum number of iterations were set to 800.

Section §4.5 elaborates the approach to determine the parameters of the DFN and FHM models using an integrated co-simulation framework involving COMSOL Multiphysics® and Matlab®. The particle swarm optimization (PSO) algorithm was used to identify the parameters of both models. A cost function was designed to minimize the error between experimentally measured and model-predicted voltage response the cell. A flowchart of the identification approach was presented to explain the closed-loop communication established between the two software platforms. The same geometric and stoichiometric parameters were used in both the models, and 5 temperature-dependent parameters were identified for both the models using constant current discharge experimental data sets conducted at five different temperatures: 5°C, 23°C, 40°C, 45°C, and 52°C. The values of the identified parameters of the DFN and FHM models using these data sets are summarized in the form of tables.

Section §4.6 summarizes the outcome of the parameter identification studies. An independent 2-D phase diagram analysis was conducted for 18650 NMC cells to identify the operating conditions where the applicability constraints are violated. Based on these observations, five temperatures were chosen to conduct NMC cell experiments. The results of the parameter identification studies are summarized using a 3-D system level phase diagram that quantifies the error in voltage prediction by both models as a function of the cell SoC and operating temperature. It is inferred from the results that the DFN model, which predicts battery dynamics accurately at 5°C and 23°C, fails to replicate the same at 40°C, 45°C, and 52°C towards the end of cell discharge.

The FHM model accurately predicts battery response under all temperature conditions. This observation was validated by two means: a) observing the model-predicted concentration dynamics at higher operating temperatures, and b) confirmation of the predictions of the 2-D electrolyte phase diagrams and quantification of the model prediction error under these conditions using a 3-D system level phase diagram.

The loss in the predictability of the DFN model is due to violation of the constraints that enable successful upscaling of the macroscale transport equations. At higher operating temperature, the dominance of reaction transport leads to the formation of diffusion-limited regimes. Under these circumstances, the system is no longer well-mixed, and macroscopic transport models become invalidated and incapable of capturing pore-scale dynamics.

These results have significant importance in the context of implementation of the DFN and its reduced-order formulations for full electric vehicle (FEV) applications. Battery cells in FEVs operate over a wide range of SoC. The poor predictability of the DFN model at higher temperatures can seriously compromise estimation and control strategies to regulate battery performance and longevity. A major contribution of this chapter is the development and validation of the enhanced predictability of the FHM model, which will enable the development of better physics-based control strategies to prolong battery life for battery management system applications.

Chapter 5

Conclusions and Future Work

This dissertation presented the theory, development, and experimental validation of a new multiscale modeling framework to characterize the mass and charge transport dynamics of lithium-ion batteries. The contents of this dissertation are summarized as follows:

1. Chapter 1 presented the motivation, background, and literature review for the development of physics-based models to characterize lithium-ion battery behavior on a multitude of length scales. The evolution in the prediction of battery behavior from using empirical models to models based on first principles of transport phenomena facilitated the advancement of model-based strategies for the estimation, control, and prognostics of battery systems. Despite this progress, battery systems remain conservatively utilized for large-scale applications and their full market penetration in this segment remains hampered due to various factors.

   The foundation of this dissertation was built on addressing some of the fundamental challenges associated with the physics-based models available today, such as: a) the lack of a systematic approach to quantify the error in modeling accuracy for different electrode chemistry, b) the absence of tools to identify the operating conditions under which models fail to provide an accurate description of battery dynamics, and c) the need to understand when currently used models are good enough for developing model-based battery management strategies, and when there is a need to develop something better.

2. Chapter 2 summarized the theory of the formulation of pore-scale equations based on first principles of mass and charge transport in the electrode and electrolyte phases of a porous lithium-ion battery. A

rigorous mathematical technique was applied to derive macroscopic formulations of the fundamental pore-scale transport equations. In the process, conditions were identified that allow successful upscaling of the pore-scale equations to the macroscale. The satisfaction of these applicability conditions bounds the modeling error using the macroscale equations to within a certain order of accuracy with respect to their pore-scale counterparts. These conditions were schematically represented using phase diagrams, which can be used to conduct analytical studies to *a priori* determine the predictability of macroscopic transport equations as a function of electrode chemistry, operating temperature, and capacity fading.

A multiscale modeling approach was presented to determine the effective ionic transport properties by resolving the electrolyte closure in the microstructure of the electrodes. This approach provides an advantage of determining transport properties in realistic battery electrodes using imaging techniques rather than relying on empirical formulations. Appendices A and B provided the detailed mathematical derivation of the transport equations of the homogenized model in the electrolyte and electrode phases, respectively.

3. Chapter 3 described the testing equipment used for the experimental characterization of lithium-ion cells. A design of experiment is presented to evaluated the performance of the full-order homogenized macroscale (FHM) model against experimental measurements at different temperatures of cell operation. 18650 lithium-ion cells of NMC and LFP chemistry were subjected to constant current discharge experiments at five different temperatures: 5°C, 23°C, 40°C, 45°C, and 52°C. The selection of these temperatures was based on an independent phase diagram study, summarized in Chapter 4, to evaluate the temperature-influenced veracity of macroscopic battery models. An Arbin BT-2000 tester was used to provide the current input and measure the voltage response of the cells, and these temperature-controlled experiments were performed by installing the cells in the fixture of a thermoelectric device called the Peltier junction. The setup and operation of these devices was elaborated in this chapter, and the experimentally measured cell response was summarized for the different cells as a function of temperature.

4. Chapter 4 presented a detailed comparison of the mass and charge transport equations of the FHM model with the commonly used Doyle-Fuller-Newman (DFN) model, highlighting different attributes that indicated higher predictability of the FHM model. The performance of the FHM and DFN models

was evaluated using the finite element modeling software COMSOL Multiphysics®. The DFN model was developed by Plett *et. al* [183], and made available as an open-source software. The implementation of this model was summarized with a description of the model equations, the initial conditions, and the boundary conditions. The development of the FHM model in COMSOL was elaborated in detail, starting with the model equations, the initial and boundary conditions, and a series of steps to ensure numerical stability of the model during simulations.

The performance of the DFN and FHM models were evaluated against data obtained from cell experiments at different temperatures of operation. The parameters of the DFN and the FHM models were identified by conducting parameter identification studies using an integrated co-simulation framework involving Matlab®and COMSOL Multiphysics®. The parameters were identified using the PSO technique, and the same geometric and stoichiometric parameter values were used in both the models. The diffusion, reaction-rate, and contact resistance were identified as a function of temperature. The results of the model parameter identification studies were discussed in detail in this chapter. Appendix C presented a detailed user guide for the development of the FHM model using COMSOL. Following the development of the model, the approach to conduct parameter identification studies, enabled by the use of the MATLAB® LiveLink™ feature of COMSOL, was elaborated at the end of this appendix.

One of the major contributions of the phase diagram studies presented in Chapter 2 is the identification of temperature as a critical parameter that governs the predictability of macroscale models such as the DFN model. Beyond critical temperatures of operation, the applicability conditions that enable successful upscaling of the DFN model equations using the volume averaging technique are violated, which results in a loss of model predictability. When diffusion-limited regimes are developed due to the dominance of reaction transport, the system is no longer well mixed and homogeneous, and the veracity of macroscale models cannot be guaranteed. The results from the parameter identification studies presented in Chapter 4 indicate the loss of DFN model predictability in predicting the voltage response at temperatures greater than 40° C in 18650 NMC cells.

The loss in the predictability of the DFN model at higher operating temperatures was initially inferred from an independent phase diagram study conducted for 18650 NMC cells. The information from the phase diagrams was utilized in the selection of different temperatures for cell characterization experiments. On the other hand, the FHM model accurately predicted battery voltage response under all the five temperatures of cell operation. The better predictability of the FHM model was confirmed using the phase diagrams,

and a comparison of the electrode concentration dynamics predicted by the DFN and FHM models at higher cell temperatures. A system level phase diagram was developed to quantify the percentage error in the DFN and FHM model predictability as a function of cell SoC and temperature.

Results indicated that the DFN model loses predictability towards the end of the discharge curve, characterized by low SoC values. Sufficient caution must be exercised in the implementation of this model for applications that involve a wide range of battery SoC operations. This dissertation presented a higher fidelity multiscale modeling framework than the DFN model through the development and validation of the FHM model. Models obtained from the reformulation and/or simplification of FHM model transport equations will enable the development of more accurate and predictive physics-based control strategies to prolong battery useful life for BMS applications.

Potential recommendations for the direction of future work are listed below:

1. **Development of reduced-complexity models:** The computational intensity of a full-order homogenized macroscale renders it unsuitable for real-time estimation applications directly. The development of models obtained by the simplification of the mass and charge transport equations of the FHM model can facilitate better model-based control strategies.

2. **Model order reduction of the FHM model:** Model order reduction techniques on the DFN model [63, 65, 192–194] have been investigated for the development of model-based control strategies for BMS applications in real-time. However, the FHM model presents one of the first-ever case of a fully coupled and upscaled set of mass and charge transport equations for lithium-ion batteries. Given the better computational efficiency and predictability with respect to the DFN model, reduced order modeling techniques on the FHM transport equations can enable more accurate estimation studies.

3. **Electrochemical-thermal model development:** The FHM model is an isothermal model of mass and charge transport. For high current rate applications, it is important to consider temperature dependency in the prediction of the electrochemical response. A reliable and consistent prediction can be achieved by coupling the mass and charge transport equations with an energy balance equation to predict the rate of heat generation and estimate the core and surface temperature of battery cells. This will enable the development of enhanced thermal management strategies.

Appendices

Appendix A Homogenization in the electrolyte

After setting $c_\varepsilon^j(\mathbf{x},t) = c^j(\mathbf{x},\mathbf{y},t,\tau_{\rm r},\tau_{\rm me},\tau_{\rm ms})$ and $\phi_\varepsilon^j(\mathbf{x},t) = \phi^j(\mathbf{x},\mathbf{y},t,\tau_{\rm r},\tau_{\rm me},\tau_{\rm ms})$, $j = \{e,s\}$, equation (2.28) is combined with (2.19a) and (2.19b) to obtain

$$\begin{aligned}
&\frac{\partial c^e}{\partial t}+\mathrm{Da}_e\frac{\partial c^e}{\partial \tau_{\rm r}}+\mathrm{Pe}_e\left(\frac{\partial c^e}{\partial \tau_{me}}+\frac{\mathrm{Da}_e}{\mathrm{Da}_s}\frac{\partial c^e}{\partial \tau_{\rm ms}}\right)= \qquad (1)\\
&\quad=\nabla_{\mathbf{x}}\cdot\left[(\mathbf{D}^e+\lambda t_+^2\mathrm{Pe}_e\mathbf{K}^e/c^e)(\nabla_{\mathbf{x}}c^e+\varepsilon^{-1}\nabla_{\mathbf{y}}c^e)+2t_+\mathrm{Pe}_e\mathbf{K}^e(\nabla_{\mathbf{x}}\phi^e+\varepsilon^{-1}\nabla_{\mathbf{y}}\phi^e)\right]\\
&+\varepsilon^{-1}\nabla_{\mathbf{y}}\cdot\left[(\mathbf{D}^e+\lambda t_+^2\mathrm{Pe}_e\mathbf{K}^e/c^e)(\nabla_{\mathbf{x}}c^e+\varepsilon^{-1}\nabla_{\mathbf{y}}c^e)+2t_+\mathrm{Pe}_e\mathbf{K}^e(\nabla_{\mathbf{x}}\phi^e+\varepsilon^{-1}\nabla_{\mathbf{y}}\phi^e)\right]
\end{aligned}$$

and

$$\begin{aligned}
&\nabla_{\mathbf{x}}\cdot[(\lambda\, t_+\mathrm{Pe}_e\mathbf{K}^e/c_e)(\nabla_{\mathbf{x}}c^e+\varepsilon^{-1}\nabla_{\mathbf{y}}c^e)+2\mathbf{K}^e\mathrm{Pe}_e\,(\nabla_{\mathbf{x}}\phi^e+\varepsilon^{-1}\nabla_{\mathbf{y}}\phi^e)] \qquad (2)\\
&+\varepsilon^{-1}\nabla_{\mathbf{y}}\cdot\left[\mathbf{K}^e(\lambda\, t_+\mathrm{Pe}_e/c^e)(\nabla_{\mathbf{x}}c^e+\varepsilon^{-1}\nabla_{\mathbf{y}}c^e)+2\mathbf{K}^e\mathrm{Pe}_e\,(\nabla_{\mathbf{x}}\phi^e+\varepsilon^{-1}\nabla_{\mathbf{y}}\phi^e)\right]=0,
\end{aligned}$$

for $\mathbf{y}\in\mathcal{B}$, subject to

$$\begin{aligned}
&\mathbf{n}_e\cdot[(\mathbf{D}^e+\lambda t_+^2\mathrm{Pe}_e\mathbf{K}^e/c^e)(\nabla_{\mathbf{x}}c^e+\varepsilon^{-1}\nabla_{\mathbf{y}}c^e)+2t_+\mathrm{Pe}_e\mathbf{K}^e(\nabla_{\mathbf{x}}\phi^e+\varepsilon^{-1}\nabla_{\mathbf{y}}\phi^e)]\\
&=\mathrm{Da}_e f(c_\varepsilon^e,c_\varepsilon^s,\phi_\varepsilon^s,\phi_\varepsilon^e)\quad \mathbf{y}\in\Gamma, \qquad (3)
\end{aligned}$$

and

$$\begin{aligned}
&\mathbf{n}_e\cdot[(\lambda t_+\mathrm{Pe}_e\mathbf{K}^e/c^e)(\nabla_{\mathbf{x}}c^e+\varepsilon^{-1}\nabla_{\mathbf{y}}c^e)+2\mathrm{Pe}_e\mathbf{K}^e(\nabla_{\mathbf{x}}\phi^e+\varepsilon^{-1}\nabla_{\mathbf{y}}\phi^e)]\\
&=\mathrm{Da}_e f(c_\varepsilon^e,c_\varepsilon^s,\phi_\varepsilon^s,\phi_\varepsilon^e),\qquad \mathbf{y}\in\Gamma, \qquad (4)
\end{aligned}$$

respectively, where $f(c_\varepsilon^e,c_\varepsilon^s,\phi_\varepsilon^s,\phi_\varepsilon^e)$ is defined in (2.21).

A.1 Mass and charge transport asymptotic expansions

Substituting (2.29) and (2.30) into the mass transport equation in the electrolyte (2.19) leads to

$$
\begin{aligned}
&\varepsilon^{-2}\{-\nabla_{\mathbf{y}}\cdot[(\mathbf{D}^e+\varepsilon^{-\alpha}\lambda\, t_+^2\mathbf{K}^e/c_0^e)\nabla_{\mathbf{y}}c_0^e+2\varepsilon^{-\alpha}t_+\,\mathbf{K}^e\nabla_{\mathbf{y}}\phi_0^e)]\}+\\
&\varepsilon^{-1}\{\varepsilon^{1+\beta}\partial_{\tau_{\mathrm{r}}}c_0^e-\nabla_{\mathbf{x}}\cdot[(\mathbf{D}^e+\varepsilon^{-\alpha}\lambda\, t_+^2\mathbf{K}^e/c_0^e)\nabla_{\mathbf{y}}c_0^e+2\varepsilon^{-\alpha}t_+\mathbf{K}^e\nabla_{\mathbf{y}}\phi_0^e]\\
&\quad-\nabla_{\mathbf{y}}\cdot[(\mathbf{D}^e+\varepsilon^{-\alpha}\lambda\, t_+^2\mathbf{K}^e/c_0^e)(\nabla_{\mathbf{x}}c_0^e+\nabla_{\mathbf{y}}c_1^e)+\varepsilon^{-\alpha}\lambda\, t_+^2\mathbf{K}^e(c_1^e/c_0^e)/c_0^e\nabla_{\mathbf{y}}c_0^e\\
&\quad+2\varepsilon^{-\alpha}t_+\mathbf{K}^e(\nabla_{\mathbf{x}}\phi_0^e+\nabla_{\mathbf{y}}\phi_1^e)]\}\\
&\varepsilon^{0}\{\partial_t c_0^e+\varepsilon^{-\alpha}(\partial_{\tau_{\mathrm{me}}}c_0^e+\varepsilon^{\beta-\gamma}\partial_{\tau_{\mathrm{ms}}}c_0^e)+\varepsilon^{1+\beta}\partial_{\tau_{\mathrm{r}}}c_1^e\\
&\quad-\nabla_{\mathbf{x}}\cdot[(\mathbf{D}^e+\varepsilon^{-\alpha}\lambda t_+^2\mathbf{K}^e/c_0^e)(\nabla_{\mathbf{x}}c_0^e+\nabla_{\mathbf{y}}c_1^e)+\varepsilon^{-\alpha}\lambda t_+^2\mathbf{K}^e(c_1^e/c_0^e)/c_0^e\nabla_{\mathbf{y}}c_0^e\\
&\quad+2\varepsilon^{-\alpha}t_+\mathbf{K}^e(\nabla_{\mathbf{x}}\phi_0^e+\nabla_{\mathbf{y}}\phi_1^e)]-\nabla_{\mathbf{y}}\cdot[(\mathbf{D}^e+\varepsilon^{-\alpha}\lambda t_+^2\mathbf{K}^e/c_0^e)(\nabla_{\mathbf{x}}c_1^e+\nabla_{\mathbf{y}}c_2^e)\\
&\quad-\varepsilon^{-\alpha}\lambda t_+^2\mathbf{K}^e(c_1^e/c_0^e)/c_0^e(\nabla_{\mathbf{x}}c_0^e+\nabla_{\mathbf{y}}c_1^e)+\varepsilon^{-\alpha}\lambda t_+^2\mathbf{K}^e/c_0^e[(c_1^e/c_0^e)^2-c_2^e/c_0^e]\nabla_{\mathbf{y}}c_0^e\\
&\quad+2\varepsilon^{-\alpha}t_+\mathbf{K}^e(\nabla_{\mathbf{x}}\phi_1^e+\nabla_{\mathbf{y}}\phi_2^e)]\}=\mathcal{O}(\varepsilon),\qquad \mathbf{y}\in\mathcal{B},
\end{aligned}
\tag{5}
$$

where the nonlinear term in (2.19) is expanded in a Mclaurin series

$$
1/c^e\approx(c_0+\varepsilon c_1^e+\varepsilon^2c_2^e)^{-1}\approx\frac{1}{c_0}\left\{1-\varepsilon\frac{c_1^e}{c_0^e}+\varepsilon^2\left[\left(\frac{c_1^e}{c_0^e}\right)^2-\left(\frac{c_2^e}{c_0^e}\right)\right]\right\}. \tag{6}
$$

Similarly, the interface condition (3) can be written as

$$
\begin{aligned}
&\varepsilon^{-1}\{\mathbf{n}_e\cdot[(\mathbf{D}^e+\varepsilon^{-\alpha}\lambda t_+^2\mathbf{K}^e/c_0^e)\nabla_{\mathbf{y}}c_0^e+2\varepsilon^{-\alpha}t_+\mathbf{K}^e\nabla_{\mathbf{y}}\phi_0^e]\}+\\
&\varepsilon^{0}\{\mathbf{n}_e\cdot[(\mathbf{D}^e+\varepsilon^{-\alpha}\lambda t_+^2\mathbf{K}^e/c_0^e)(\nabla_{\mathbf{x}}c_0^e+\nabla_{\mathbf{y}}c_1^e)-\varepsilon^{-\alpha}\lambda t_+^2\mathbf{K}^e/c_0^e(c_1^e/c_0^e)\nabla_{\mathbf{y}}c_0^e)\\
&\qquad+2\varepsilon^{-\alpha}t_+\,\mathbf{K}^e(\nabla_{\mathbf{x}}\phi_0^e+\nabla_{\mathbf{y}}\phi_1^e)]-2\varepsilon^{\beta}A_0B_0)\}+\\
&\varepsilon\{\mathbf{n}_e\cdot[(\mathbf{D}^e+\varepsilon^{-\alpha}\lambda t_+^2\mathbf{K}^e/c_0^e)(\nabla_{\mathbf{x}}c_1^e+\nabla_{\mathbf{y}}c_2^e)+2\varepsilon^{-\alpha}t_+\mathbf{K}^e(\nabla_{\mathbf{x}}\phi_1^e+\nabla_{\mathbf{y}}\phi_2^e)\\
&\qquad-\varepsilon^{-\alpha}\lambda t_+^2\mathbf{K}^e/c_0^e(c_1^e/c_0^e)(\nabla_{\mathbf{x}}c_0^e+\nabla_{\mathbf{y}}c_1^e)+\varepsilon^{-\alpha}\lambda t_+^2\mathbf{K}^e/c_0^e[(c_1^e/c_0^e)^2-(c_2/c_0)]\nabla_{\mathbf{y}}c_0^e\\
&\qquad-2\varepsilon^{\beta}(A_0B_1+A_1B_0)]\}=\mathcal{O}(\varepsilon^2),\quad \mathbf{y}\in\Gamma,
\end{aligned}
\tag{7}
$$

since $\sinh(\phi^s - \phi^e - U) = \sinh(\phi_0^s - \phi_0^e - U) + \varepsilon(\phi_1^s - \phi_1^e)\cosh(\phi_0^s - \phi_0^e - U) + \mathcal{O}(\varepsilon^2)$, where

$$A_0 = \sinh(\phi_0^s - \phi_0^e - U), \tag{8a}$$

$$B_0 = \sqrt{c_0^e c_0^s (1 - c_0^s)}, \tag{8b}$$

$$A_1 = (\phi_1^s - \phi_1^e)\cosh(\phi_0^s - \phi_0^e - U), \tag{8c}$$

$$B_1 = \sqrt{c_0^e c_0^s (1 - c_0^s)}\Big[\frac{c_1^s}{2c_0^s} + \frac{c_1^e}{2c_0^e} - \frac{c_1^s}{2(1 - c_0^s)}\Big]. \tag{8d}$$

Combining (2.29) and (2.30) with the charge transport equation (2) and boundary condition (4) yields

$$\begin{aligned}
&\varepsilon^{-2}\{\nabla_{\mathbf{y}} \cdot [\lambda t_+ \mathbf{K}^e / c_0^e \nabla_{\mathbf{y}} c_0^e + 2\mathbf{K}^e \nabla_{\mathbf{y}} \phi_0^e]\} + \\
&\varepsilon^{-1}\{\nabla_{\mathbf{x}} \cdot [\lambda t_+ \mathbf{K}^e / c_0^e \nabla_{\mathbf{y}} c_0^e + 2\mathbf{K}^e \nabla_{\mathbf{y}} \phi_0^e] + \nabla_{\mathbf{y}} \cdot [\lambda t_+ \mathbf{K}^e / c_0^e (\nabla_{\mathbf{x}} c_0^e + \nabla_{\mathbf{y}} c_1^e) \\
&\quad - \lambda t_+ \mathbf{K}^e (c_1^e / c_0^e) / c_0^e \nabla_{\mathbf{y}} c_0^e + 2\mathbf{K}^e (\nabla_{\mathbf{x}} \phi_0^e + \nabla_{\mathbf{y}} \phi_1^e)]\} + \\
&\varepsilon^{0}\{\nabla_{\mathbf{x}} \cdot [\lambda t_+ \mathbf{K}^e / c_0^e (\nabla_{\mathbf{x}} c_0^e + \nabla_{\mathbf{y}} c_1^e) - \lambda t_+ \mathbf{K}^e (c_1^e / c_0^e) / c_0^e \nabla_{\mathbf{y}} c_0^e + 2\mathbf{K}^e (\nabla_{\mathbf{x}} \phi_0^e + \nabla_{\mathbf{y}} \phi_1^e) \\
&\quad + \nabla_{\mathbf{y}} \cdot [\lambda t_+ \mathbf{K}^e / c_0^e (\nabla_{\mathbf{x}} c_1^e + \nabla_{\mathbf{y}} c_2^e) - \lambda t_+ \mathbf{K}^e (c_1^e / c_0^e) / c_0^e (\nabla_{\mathbf{x}} c_0^e + \nabla_{\mathbf{y}} c_1^e) + \\
&\quad + \lambda t_+ \mathbf{K}^e / c_0^e [(c_1^e / c_0^e)^2 - c_2^e / c_0^e] \nabla_{\mathbf{y}} c_0^e + 2\mathbf{K}^e (\nabla_{\mathbf{x}} \phi_1^e + \nabla_{\mathbf{y}} \phi_2^e)]\} = \mathcal{O}(\varepsilon), \, \mathbf{y} \in \mathcal{B}
\end{aligned} \tag{9}$$

subject to

$$\begin{aligned}
&\varepsilon^{-1}\{\mathbf{n}_e \cdot [\varepsilon^{-\alpha} \lambda t_+ \mathbf{K}^e / c_0^e \nabla_{\mathbf{y}} c_0^e + 2\varepsilon^{-\alpha} \mathbf{K}^e \nabla_{\mathbf{y}} \phi_0^e]\} \\
&\varepsilon^{0}\{\mathbf{n}_e \cdot [\varepsilon^{-\alpha} \lambda t_+ \mathbf{K}^e / c_0^e (\nabla_{\mathbf{x}} c_0^e + \nabla_{\mathbf{y}} c_1^e) - \varepsilon^{-\alpha} \lambda t_+ \mathbf{K}^e / c_0^e (c_1^e / c_0^e) \nabla_{\mathbf{y}} c_0^e \\
&\qquad + 2\varepsilon^{-\alpha} \mathbf{K}^e (\nabla_{\mathbf{x}} \phi_0^e + \nabla_{\mathbf{y}} \phi_1^e) - 2\varepsilon^{\beta} A_0 B_0]\} + \\
&\varepsilon\{\mathbf{n}_e \cdot [\varepsilon^{-\alpha} \lambda t_+ \mathbf{K}^e / c_0^e (\nabla_{\mathbf{x}} c_1^e + \nabla_{\mathbf{y}} c_2^e) - \varepsilon^{-\alpha} \lambda t_+ \mathbf{K}^e / c_0 (c_1 / c_0) (\nabla_{\mathbf{x}} c_0^e + \nabla_{\mathbf{y}} c_1^e) \\
&\qquad + \varepsilon^{-\alpha} \lambda t_+ \mathbf{K}^e / c_0 [(c_1^e / c_0^e)^2 - c_2^e / c_0^e] \nabla_{\mathbf{y}} c_0^e + 2\varepsilon^{-\alpha} \mathbf{K}^e (\nabla_{\mathbf{x}} \phi_1^e + \nabla_{\mathbf{y}} \phi_2^e) \\
&\quad - 2\varepsilon^{\beta} (A_0 B_1 + A_1 B_0)\} = \mathcal{O}(\varepsilon^2), \quad \mathbf{y} \in \Gamma.
\end{aligned} \tag{10}$$

where A_0, A_1, B_0 and B_1 are defined in (8). The next step compares the terms of like order of ε.

A.2 Terms of order $\mathcal{O}\left(\varepsilon^{-2}\right)$

Collecting the leading-order terms in the mass transport equation and corresponding boundary condition (5) and (7) respectively, leads to

$$-\nabla_{\mathbf{y}} \cdot [(\mathbf{D}^e + \varepsilon^{-\alpha} \lambda\, t_+^2 \mathbf{K}^e / c_0^e) \nabla_{\mathbf{y}} c_0^e + 2\varepsilon^{-\alpha} t_+\, \mathbf{K}^e \nabla_{\mathbf{y}} \phi_0^e] = 0, \quad \mathbf{y} \in \mathcal{B}, \tag{11}$$

subject to

$$\mathbf{n}_e \cdot [(\mathbf{D}^e + \varepsilon^{-\alpha} \lambda t_+^2 \mathbf{K}^e / c_0^e) \nabla_{\mathbf{y}} c_0^e + 2\varepsilon^{-\alpha} t_+ \mathbf{K}^e \nabla_{\mathbf{y}} \phi_0^e)] = 0, \quad \mathbf{y} \in \Gamma. \tag{12}$$

Similarly, at the leading order the charge transport equation is

$$\nabla_{\mathbf{y}} \cdot (\lambda t_+ \mathbf{K}^e / c_0^e \nabla_{\mathbf{y}} c_0^e + 2\mathbf{K}^e \nabla_{\mathbf{y}} \phi_0^e) = 0, \quad \mathbf{y} \in \mathcal{B}, \tag{13}$$

subject to

$$\mathbf{n}_e \cdot (\lambda t_+ \mathbf{K}^e / c_0^e \nabla_{\mathbf{y}} c_0^e + 2\mathbf{K}^e \nabla_{\mathbf{y}} \phi_0^e) = 0, \quad \mathbf{y} \in \Gamma. \tag{14}$$

Homogeneity of (11)-(12) and (13)-(14), guarantees that c_0^e and ϕ_0^e are independent of $\mathbf{y}$, i.e.

$$c_0^e = c_0^e(\mathbf{x}, t, \tau_{\mathrm{r}}, \tau_{\mathrm{m}e}, \tau_{\mathrm{m}s}) \tag{15}$$

$$\phi_0^e = \phi_0^e(\mathbf{x}, t, \tau_{\mathrm{r}}, \tau_{\mathrm{m}e}, \tau_{\mathrm{m}s}) \tag{16}$$

A.3 Terms of order $\mathcal{O}\left(\varepsilon^{-1}\right)$

Since $\nabla_{\mathbf{y}} c_0^e \equiv \mathbf{0}$ and $\nabla_{\mathbf{y}} \phi_0^e \equiv \mathbf{0}$, the mass balance equation (5) at order $\mathcal{O}(\varepsilon^{-1})$ simplifies to

$$\begin{aligned} \varepsilon^{1+\beta} \partial_{\tau_{\mathrm{r}}} c_0^e - \nabla_{\mathbf{y}} \cdot [(\mathbf{D}^e + \varepsilon^{-\alpha} \lambda\, t_+^2 \mathbf{K}^e / c_0^e)(\nabla_{\mathbf{x}} c_0^e + \nabla_{\mathbf{y}} c_1^e) \\ + 2\varepsilon^{-\alpha} t_+ \mathbf{K}^e (\nabla_{\mathbf{x}} \phi_0^e + \nabla_{\mathbf{y}} \phi_1^e)] = 0, \qquad \mathbf{y} \in \mathcal{B}, \end{aligned} \tag{17}$$

subject to the interface condition

$$\mathbf{n}_e \cdot [(\mathbf{D}^e + \varepsilon^{-\alpha}\lambda t_+^2 \mathbf{K}^e/c_0^e)(\nabla_{\mathbf{x}} c_0^e + \nabla_{\mathbf{y}} c_1^e) + 2\varepsilon^{-\alpha} t_+ \mathbf{K}^e(\nabla_{\mathbf{x}}\phi_0^e + \nabla_{\mathbf{y}}\phi_1^e)] = 2\varepsilon^{\beta} A_0 B_0 \qquad \mathbf{y} \in \Gamma. \tag{18}$$

Integrating (17) over $\mathcal{B}$ with respect to $\mathbf{y}$, while accounting for the boundary condition (18), and the periodicity of the coefficients on the external boundary of the unit cell ∂Y yields

$$\varepsilon^{1+\beta}\partial_{\tau_{\mathrm{r}e}} c_0^e = 2\varepsilon^{\beta}\mathcal{K}^{\star} A_0 B_0, \tag{19}$$

where $\mathcal{K}^{\star}$ is defined by (2.34).

Combining (19) with (17) to eliminate the temporal derivative,

$$2\varepsilon^{\beta}\mathcal{K}^{\star} A_0 B_0 - \nabla_{\mathbf{y}} \cdot [(\mathbf{D}^e + \varepsilon^{-\alpha}\lambda\, t_+^2 \mathbf{K}^e/c_0^e)(\nabla_{\mathbf{x}} c_0^e + \nabla_{\mathbf{y}} c_1^e) + 2\varepsilon^{-\alpha} t_+ \mathbf{K}^e(\nabla_{\mathbf{x}}\phi_0^e + \nabla_{\mathbf{y}}\phi_1^e)] = 0. \tag{20}$$

Similarly, the charge balance equation (9) at $\mathcal{O}(\varepsilon^{-1})$ is

$$\nabla_{\mathbf{y}} \cdot [\lambda t_+ \mathbf{K}^e/c_0^e(\nabla_{\mathbf{x}} c_0^e + \nabla_{\mathbf{y}} c_1^e) + 2\mathbf{K}^e(\nabla_{\mathbf{x}}\phi_0^e + \nabla_{\mathbf{y}}\phi_1^e)] = 0,\ \mathbf{y} \in \mathcal{B}, \tag{21}$$

subject to

$$\mathbf{n}_e \cdot [\varepsilon^{-\alpha}\lambda t_+ \mathbf{K}^e/c_0^e(\nabla_{\mathbf{x}} c_0^e + \nabla_{\mathbf{y}} c_1^e) + 2\varepsilon^{-\alpha}\mathbf{K}^e(\nabla_{\mathbf{x}}\phi_0^e + \nabla_{\mathbf{y}}\phi_1^e) - 2\varepsilon^{\beta} A_0 B_0] = 0, \tag{22}$$

for $\mathbf{y} \in \Gamma$. Equations (18), (20), (21) and (22) form boundary value problems for both c_1^e and ϕ_1^e. Following the approach indicated [195] and [52, pp. 10, Eqs. 3.6–3.7], a solution exists in the following form:

$$\begin{aligned} c_1^e(\mathbf{x},\mathbf{y},t,\tau_{\mathrm{r}},\tau_{\mathrm{m}e},\tau_{\mathrm{m}s}) &= \boldsymbol{\chi}_1(\mathbf{y}) \cdot \nabla_{\mathbf{x}} c_0^e(\mathbf{x},t,\tau_{\mathrm{r}},\tau_{\mathrm{m}e},\tau_{\mathrm{m}s}) + \overline{c}_1^e(\mathbf{x},t,\tau_{\mathrm{r}},\tau_{\mathrm{m}e},\tau_{\mathrm{m}s}), \\ \phi_1^e(\mathbf{x},\mathbf{y},t,\tau_{\mathrm{r}},\tau_{\mathrm{m}e},\tau_{\mathrm{m}s}) &= \boldsymbol{\chi}_2(\mathbf{y}) \cdot \nabla_{\mathbf{x}} \phi_0^e(\mathbf{x},t,\tau_{\mathrm{r}},\tau_{\mathrm{m}e},\tau_{\mathrm{m}s}) + \overline{\phi}_1^e(\mathbf{x},t,\tau_{\mathrm{r}},\tau_{\mathrm{m}e},\tau_{\mathrm{m}s}). \end{aligned} \tag{23}$$

Substitution of (23) into (20) and (18) leads to

$$2\varepsilon^{\beta}\mathcal{K}^{\star}A_0B_0 - \nabla_{\mathbf{y}}\cdot[(\mathbf{D}^e + \varepsilon^{-\alpha}\lambda\, t_+^2\mathbf{K}^e/c_0^e)(\mathbf{I}+\nabla_{\mathbf{y}}\boldsymbol{\chi}_1)\nabla_{\mathbf{x}}c_0^e + 2\varepsilon^{-\alpha}t_+\mathbf{K}^e(\mathbf{I}+\nabla_{\mathbf{y}}\boldsymbol{\chi}_2)\nabla_{\mathbf{x}}\phi_0^e] = 0, \qquad \mathbf{y}\in\mathcal{B}, \tag{24a}$$

subject to $\langle\boldsymbol{\chi}_1\rangle_e = \langle\boldsymbol{\chi}_2\rangle_e = 0$ and

$$\mathbf{n}_e\cdot[(\mathbf{D}^e + \varepsilon^{-\alpha}\lambda t_+^2\mathbf{K}^e/c_0^e)(\mathbf{I}+\nabla_{\mathbf{y}}\boldsymbol{\chi}_1)\nabla_{\mathbf{x}}c_0^e + 2\varepsilon^{-\alpha}t_+\mathbf{K}^e(\mathbf{I}+\nabla_{\mathbf{y}}\boldsymbol{\chi}_2)\nabla_{\mathbf{x}}\phi_0^e] = 2\varepsilon^{\beta}A_0B_0 \qquad \mathbf{y}\in\Gamma, \tag{24b}$$

where $\mathbf{I}$ is the identity matrix, and $\boldsymbol{\chi}_1$ and $\boldsymbol{\chi}_2$ are periodic vector fields. Substitution of (23) into (21) and (22) leads to

$$\nabla_{\mathbf{y}}\cdot[\lambda t_+\mathbf{K}^e/c_0^e(\mathbf{I}+\nabla_{\mathbf{y}}\boldsymbol{\chi}_1)\nabla_{\mathbf{x}}c_0^e + 2\mathbf{K}^e(\mathbf{I}+\nabla_{\mathbf{y}}\boldsymbol{\chi}_2)\nabla_{\mathbf{x}}\phi_0^e] = 0, \tag{25a}$$

subject to

$$\mathbf{n}_e\cdot[\varepsilon^{-\alpha}\lambda t_+\mathbf{K}^e/c_0^e(\mathbf{I}+\nabla_{\mathbf{y}}\boldsymbol{\chi}_1)\nabla_{\mathbf{x}}c_0^e + 2\varepsilon^{-\alpha}\mathbf{K}^e(\mathbf{I}+\nabla_{\mathbf{y}}\boldsymbol{\chi}_2)\nabla_{\mathbf{x}}\phi_0^e - 2\varepsilon^{\beta}A_0B_0] = 0, \tag{25b}$$

Equations (24) and (25) define the closure variables $\boldsymbol{\chi}_1(\mathbf{y})$ and $\boldsymbol{\chi}_2(\mathbf{y})$. The coupling of $\boldsymbol{\chi}_1(\mathbf{y})$ and $\boldsymbol{\chi}_2(\mathbf{y})$ with $c_0^e(\mathbf{x})$, $\phi_0^e(\mathbf{x})$, $A_0(\mathbf{x})$ and $B_0(\mathbf{x})$ through the boundary value problems (24) and (25) is incompatible with the closure variables' general representation postulated in (23). This inconsistency is resolved by imposing the following constraints on the exponents α and β. If we choose $\beta > \max\{0,-\alpha\}$ and $\alpha < 0$, then the term $\mathcal{K}^{\star}A_0B_0$ is negligible relative to the smallest term in (24) and the nonlinear migration term $\varepsilon^{-\alpha}\lambda t_+^2\mathbf{K}^e/c_0^e$ relative to $\mathbf{D}^e$. Under these constraints, (24) and (25) simplify to

$$\nabla_{\mathbf{y}}\cdot[\mathbf{D}^e(\mathbf{I}+\nabla_{\mathbf{y}}\boldsymbol{\chi}_1)\nabla_{\mathbf{x}}c_0^e] = 0 \qquad \mathbf{y}\in\mathcal{B}, \tag{26a}$$

$$\mathbf{n}_e\cdot[\mathbf{D}^e(\mathbf{I}+\nabla_{\mathbf{y}}\boldsymbol{\chi}_1)\nabla_{\mathbf{x}}c_0^e] = 0 \qquad \mathbf{y}\in\Gamma, \tag{26b}$$

Equation (26) can be satisfied for all $\mathbf{x} \in \Omega$ if

$$\nabla_{\mathbf{y}} \cdot [\mathbf{D}^e(\mathbf{I} + \nabla_{\mathbf{y}}\boldsymbol{\chi}_1)] = 0, \qquad \mathbf{y} \in \mathcal{B} \tag{27a}$$

$$\mathbf{n}_e \cdot [\mathbf{D}^e(\mathbf{I} + \nabla_{\mathbf{y}}\boldsymbol{\chi}_1)] = 0, \qquad \mathbf{y} \in \Gamma. \tag{27b}$$

Similarly, (25) yields

$$\nabla_{\mathbf{y}} \cdot [\lambda t_+ \mathbf{K}^e(\mathbf{I} + \nabla_{\mathbf{y}}\boldsymbol{\chi}_1)] = 0, \qquad \mathbf{y} \in \mathcal{B} \tag{28a}$$

$$\mathbf{n}_e \cdot [\lambda t_+ \mathbf{K}^e(\mathbf{I} + \nabla_{\mathbf{y}}\boldsymbol{\chi}_1)] = 0, \qquad \mathbf{y} \in \Gamma \tag{28b}$$

and

$$\nabla_{\mathbf{y}} \cdot [\mathbf{K}^e(\mathbf{I} + \nabla_{\mathbf{y}}\boldsymbol{\chi}_2)] = 0, \qquad \mathbf{y} \in \mathcal{B} \tag{29a}$$

$$\mathbf{n}_e \cdot [\mathbf{K}^e(\mathbf{I} + \nabla_{\mathbf{y}}\boldsymbol{\chi}_2)] = 0, \qquad \mathbf{y} \in \Gamma \tag{29b}$$

Consistency of (27) with (28) implies

$$\nabla_{\mathbf{y}} \cdot (\mathbf{I} + \nabla_{\mathbf{y}}\boldsymbol{\chi}_1) = 0, \qquad \mathbf{y} \in \mathcal{B} \tag{30a}$$

$$\mathbf{n}_e \cdot (\mathbf{I} + \nabla_{\mathbf{y}}\boldsymbol{\chi}_1) = 0, \qquad \mathbf{y} \in \Gamma \tag{30b}$$

In (29), the conductivity tensor $\mathbf{K}^e$ is a function of concentration c^e and potential ϕ^e. With an order ε approximation $\mathbf{K}^e \approx \mathbf{K}^e(c_0^e, \phi_0^e)$. Then, (29) can be simplified to

$$\nabla_{\mathbf{y}} \cdot (\mathbf{I} + \nabla_{\mathbf{y}}\boldsymbol{\chi}_2) = 0, \qquad \mathbf{y} \in \mathcal{B} \tag{31a}$$

$$\mathbf{n}_e \cdot (\mathbf{I} + \nabla_{\mathbf{y}}\boldsymbol{\chi}_2) = 0, \qquad \mathbf{y} \in \Gamma \tag{31b}$$

As a result, $\boldsymbol{\chi}_1(\mathbf{y}) = \boldsymbol{\chi}_2(\mathbf{y}) =: \boldsymbol{\chi}^e(\mathbf{y})$. The treatment of the closure variable is consistent with the approach employed in [196]. The closure variable $\boldsymbol{\chi}^e(\mathbf{y})$ defines the cell problem and describes the behavior of the effective diffusion and conductivity tensors. Recalling the definitions of Da_e and Pe_e in (2.30) enables reformulation of the conditions in terms of α and β in the form of constraints 2)–4) of §2.2.3.1. Having identified the conditions that guarantee homogenizability, the next step is to complete the derivation of the effective mass transport equation (2.31).

A.4 Terms of order $\mathcal{O}(1)$

Collecting the zeroth-order term in the mass balance equation (5) and first-order term in the corresponding boundary condition (7), leads to

$$\begin{aligned}
&\partial_t c_0^e + \varepsilon^{-\alpha}(\partial_{\tau_{\mathrm{me}}} c_0^e + \varepsilon^{\beta-\gamma}\partial_{\tau_{\mathrm{m}s}} c_0^e) + \varepsilon^{1+\beta}\partial_{\tau_{\mathrm{r}}} c_1^e \\
&\quad - \nabla_{\mathbf{x}} \cdot [(\mathbf{D}^e + \varepsilon^{-\alpha}\lambda t_+^2 \mathbf{K}^e / c_0^e)(\nabla_{\mathbf{x}} c_0^e + \nabla_{\mathbf{y}} c_1^e) + 2\varepsilon^{-\alpha} t_+ \mathbf{K}^e (\nabla_{\mathbf{x}} \phi_0^e + \nabla_{\mathbf{y}} \phi_1^e)] \\
&\quad - \nabla_{\mathbf{y}} \cdot [(\mathbf{D}^e + \varepsilon^{-\alpha}\lambda t_+^2 \mathbf{K}^e / c_0^e)(\nabla_{\mathbf{x}} c_1^e + \nabla_{\mathbf{y}} c_2^e) + 2\varepsilon^{-\alpha} t_+ \mathbf{K}^e (\nabla_{\mathbf{x}} \phi_1^e + \nabla_{\mathbf{y}} \phi_2^e) \\
&\quad - \varepsilon^{-\alpha}\lambda t_+^2 \mathbf{K}^e (c_1^e / c_0^e) / c_0^e (\nabla_{\mathbf{x}} c_0^e + \nabla_{\mathbf{y}} c_1^e)] = 0
\end{aligned} \tag{32}$$

subject to

$$\begin{aligned}
&\mathbf{n}_e \cdot [(\mathbf{D}^e + \varepsilon^{-\alpha}\lambda t_+^2 \mathbf{K}^e / c_0^e)(\nabla_{\mathbf{x}} c_1^e + \nabla_{\mathbf{y}} c_2^e) + 2\varepsilon^{-\alpha} t_+ \mathbf{K}^e (\nabla_{\mathbf{x}} \phi_1^e + \nabla_{\mathbf{y}} \phi_2^e) \\
&\quad - \varepsilon^{-\alpha}\lambda t_+^2 \mathbf{K}^e / c_0^e (c_1^e / c_0^e)(\nabla_{\mathbf{x}} c_0^e + \nabla_{\mathbf{y}} c_1^e) = 2\varepsilon^{\beta}(A_0 B_1 + A_1 B_0)]
\end{aligned} \tag{33}$$

since $\nabla_{\mathbf{y}} c_0^e = 0$. Integrating (32) over $\mathcal{B}$ with respect to $\mathbf{y}$ and using the boundary condition (33) leads to

$$\begin{aligned}
&\partial_t \langle c_0^e \rangle_{\mathcal{B}} + \varepsilon^{-\alpha}(\partial_{\tau_{\mathrm{me}}} \langle c_0^e \rangle_{\mathcal{B}} + \varepsilon^{\beta-\gamma}\partial_{\tau_{\mathrm{ms}}} \langle c_0^e \rangle_{\mathcal{B}}) + \varepsilon^{1+\beta}\partial_{\tau_{\mathrm{r}}} \langle c_1^e \rangle_{\mathcal{B}} \\
&- \eta^{-1} \nabla_{\mathbf{x}} \cdot [(\mathbf{D}^{e\star\star} + \varepsilon^{-\alpha}\lambda t_+^2 \mathbf{K}^{e\star\star} / \langle c_0^e \rangle_{\mathcal{B}}) \nabla_{\mathbf{x}} \langle c_0^e \rangle_{\mathcal{B}} + 2\varepsilon^{-\alpha} t_+ \mathbf{K}^{e\star\star} \nabla_{\mathbf{x}} \langle \phi_0^e \rangle_{\mathcal{B}}] \\
&- 2\varepsilon^{\beta} \mathcal{K}^{\star} (\langle A_0 \rangle_{\mathcal{B}} \langle B_1 \rangle_{\Gamma} + \langle A_1 \rangle_{\Gamma} \langle B_0 \rangle_{\mathcal{B}}) = 0
\end{aligned} \tag{34}$$

where $\mathcal{K}^{\star} = |\Gamma|/|\mathcal{B}|$, $\mathbf{D}^{e\star\star} = \langle \mathbf{D}^e (\mathbf{I} + \nabla_{\mathbf{y}} \boldsymbol{\chi}^e) \rangle_e$, $\mathbf{K}^{e\star\star} = \langle \mathbf{K}^e (\mathbf{I} + \nabla_{\mathbf{y}} \boldsymbol{\chi}^e) \rangle_e$ and

$$\langle A_1 \rangle_{\Gamma} = (\langle \phi_1^s \rangle_{\Gamma} - \langle \phi_1^e \rangle_{\Gamma}) \cosh(\langle \phi_0^s \rangle_{\mathcal{B}} - \langle \phi_0^e \rangle_{\mathcal{B}} - U), \tag{35a}$$

$$\langle B_1 \rangle_{\Gamma} = \sqrt{\langle c_0^e \rangle_{\mathcal{B}} \langle c_0^s \rangle_{\mathcal{B}} (1 - \langle c_0^s \rangle_{\mathcal{B}})} \left[\frac{\langle c_1^s \rangle_{\Gamma}}{2\langle c_0^s \rangle_{\mathcal{B}}} + \frac{\langle c_1^e \rangle_{\Gamma}}{2\langle c_0^e \rangle_{\mathcal{B}}} - \frac{\langle c_1^s \rangle_{\Gamma}}{2(1 - \langle c_0^s \rangle_{\mathcal{B}})} \right]. \tag{35b}$$

It must be noted that

$$\begin{aligned}
\langle c^e \rangle_{\mathcal{B}} &= \langle c_0^e \rangle_{\mathcal{B}} + \varepsilon \langle c_1^e \rangle_{\mathcal{B}} + \mathcal{O}(\varepsilon^2), \\
\langle \phi^e \rangle_{\mathcal{B}} &= \langle \phi_0^e \rangle_{\mathcal{B}} + \varepsilon \langle \phi_1^e \rangle_{\mathcal{B}} + \mathcal{O}(\varepsilon^2).
\end{aligned} \tag{36}$$

Multiplying the temporal derivative of (36) by ε yields

$$\varepsilon\partial_t\langle c^e\rangle_{\mathcal{B}} = \varepsilon\partial_t\langle c_0^e\rangle_{\mathcal{B}} + \varepsilon^{1+\beta}\partial_{\tau_{\mathrm{r}}}\langle c_0^e\rangle_{\mathcal{B}} + \varepsilon^{1-\alpha}(\partial_{\tau_{\mathrm{me}}}\langle c_0^e\rangle_{\mathcal{B}} + \varepsilon^{\beta-\gamma}\partial_{\tau_{\mathrm{ms}}}\langle c_0^e\rangle_{\mathcal{B}}) + \mathcal{O}(\varepsilon^2) \tag{37}$$

Multiplying (34) by ε, adding the result to (19), and using (37), the following equation is obtained:

$$\begin{aligned}\varepsilon\partial_t\langle c^e\rangle_{\mathcal{B}} =&\varepsilon\eta^{-1}\nabla_{\mathbf{x}}\cdot[(\mathbf{D}^{e\star\star} + \varepsilon^{-\alpha}\lambda t_+^2\mathbf{K}^{e\star\star}/\langle c_0^e\rangle)\nabla_{\mathbf{x}}\langle c_0^e\rangle_{\mathcal{B}} + 2\varepsilon^{-\alpha}t_+\mathbf{K}^{e\star\star}\nabla_{\mathbf{x}}\langle\phi_0^e\rangle_{\mathcal{B}}]\\ &+ 2\varepsilon^{\beta}\mathcal{K}^{\star}[\langle A_0\rangle_{\mathcal{B}}\langle B_0\rangle_{\mathcal{B}} + \varepsilon(\langle A_0\rangle_{\mathcal{B}}\langle B_1\rangle_{\Gamma} + \langle A_1\rangle_{\Gamma}\langle B_0\rangle_{\mathcal{B}})]\end{aligned} \tag{38}$$

Combining this result with the expansions $\varepsilon\langle c^e\rangle_{\mathcal{B}} = \varepsilon\langle c_0^e\rangle_{\mathcal{B}} + \mathcal{O}(\varepsilon^2) = \varepsilon c_0^e + \mathcal{O}(\varepsilon^2)$ and $\varepsilon\langle\phi^e\rangle_{\mathcal{B}} = \varepsilon\langle\phi_0^e\rangle_{\mathcal{B}} + \mathcal{O}(\varepsilon^2) = \varepsilon\phi_0^e + \mathcal{O}(\varepsilon^2)$ while recalling the definitions of Da and Pe in (2.30) and assuming $\langle\psi^s\rangle_{\Gamma} \approx \langle\psi^s\rangle_s$ and $\langle\psi^e\rangle_{\Gamma} \approx \langle\psi^e\rangle_{\mathcal{B}}$, where $\psi = \{c, \phi\}$, leads to

$$\begin{aligned}\eta\partial_t\langle c^e\rangle_{\mathcal{B}} =&\nabla_{\mathbf{x}}\cdot[(\mathbf{D}^{e\star\star} + \varepsilon^{-\alpha}\lambda t_+^2\mathbf{K}^{e\star\star}/\langle c^e\rangle)\nabla_{\mathbf{x}}\langle c^e\rangle_{\mathcal{B}} + 2\varepsilon^{-\alpha}t_+\mathbf{K}^{e\star\star}\nabla_{\mathbf{x}}\langle\phi^e\rangle_{\mathcal{B}}]\\ &+ 2\eta\varepsilon^{-1}\mathcal{K}^{\star}\mathrm{Da}_e f(\langle c^e\rangle_{\mathcal{B}}, \langle c^s\rangle_s, \langle\phi^e\rangle_{\mathcal{B}}, \langle\phi^s\rangle_s),\end{aligned} \tag{39}$$

since

$$f(\langle c^e\rangle_{\mathcal{B}}, \langle c^s\rangle_s, \langle\phi^e\rangle_{\mathcal{B}}, \langle\phi^s\rangle_s) \approx \langle A_0\rangle_{\mathcal{B}}\langle B_0\rangle_{\mathcal{B}} + \varepsilon(\langle A_0\rangle_{\mathcal{B}}\langle B_1\rangle_{\Gamma} + \langle A_1\rangle_{\Gamma}\langle B_0\rangle_{\mathcal{B}}) + \mathcal{O}(\varepsilon^2) \tag{40}$$

where $f(\langle c^e\rangle_{\mathcal{B}}, \langle c^s\rangle_s, \langle\phi^e\rangle_{\mathcal{B}}, \langle\phi^s\rangle_s)$ is defined by (2.33).

Similarly, collecting $\mathcal{O}(1)-$terms in the charge balance equation in the electrolyte (9) and $\mathcal{O}(\varepsilon)-$terms in the boundary condition (10) while accounting for $\nabla_{\mathbf{y}}c_0^e = 0$, leads to

$$\begin{aligned}&\nabla_{\mathbf{x}}\cdot[\lambda t_+\mathbf{K}^e/c_0^e(\nabla_{\mathbf{x}}c_0^e + \nabla_{\mathbf{y}}c_1^e) + 2\mathbf{K}^e(\nabla_{\mathbf{x}}\phi_0^e + \nabla_{\mathbf{y}}\phi_1^e) +\\ &\nabla_{\mathbf{y}}\cdot[\lambda t_+\mathbf{K}^e/c_0^e(\nabla_{\mathbf{x}}c_1^e + \nabla_{\mathbf{y}}c_2^e) - \lambda t_+\mathbf{K}^e(c_1^e/c_0^e)/c_0^e(\nabla_{\mathbf{x}}c_0^e + \nabla_{\mathbf{y}}c_1^e) +\\ &\quad + 2\mathbf{K}^e(\nabla_{\mathbf{x}}\phi_1^e + \nabla_{\mathbf{y}}\phi_2^e)] = 0,\end{aligned} \tag{41}$$

subject to

$$\mathbf{n}_e \cdot [\lambda t_+ \mathbf{K}^e / c_0^e (\nabla_{\mathbf{x}} c_1^e + \nabla_{\mathbf{y}} c_2^e) - \lambda t_+ \mathbf{K}^e / c_0 (c_1/c_0)(\nabla_{\mathbf{x}} c_0^e + \nabla_{\mathbf{y}} c_1^e) + 2\mathbf{K}^e (\nabla_{\mathbf{x}} \phi_1^e + \nabla_{\mathbf{y}} \phi_2^e)] = 2\varepsilon^{\alpha+\beta}(A_0 B_1 + A_1 B_0). \tag{42}$$

Both equations (41) and its boundary condition (42) are multiplied by ε, and added to (21) and (22) respectively, and the resulting equation is integrated over $\mathcal{B}$ while employing the newly obtained boundary conditions. This leads to

$$\begin{aligned} &\varepsilon^{1-\alpha} \eta^{-1} \nabla_{\mathbf{x}} \cdot [(\lambda t_+ \mathbf{K}^{e\star\star} / \langle c_0^e \rangle) \nabla_{\mathbf{x}} \langle c_0^e \rangle_{\mathcal{B}} + 2\mathbf{K}^{e\star\star} \nabla_{\mathbf{x}} \langle \phi_0^e \rangle_{\mathcal{B}}] \\ &= 2\varepsilon^{\beta} \mathcal{K}^{\star} [\langle A_0 \rangle_{\mathcal{B}} \langle B_0 \rangle_{\mathcal{B}} + \varepsilon (\langle A_0 \rangle_{\mathcal{B}} \langle B_1 \rangle_{\Gamma} + \langle A_1 \rangle_{\Gamma} \langle B_0 \rangle_{\mathcal{B}})] \end{aligned} \tag{43}$$

where $\mathbf{K}^{e\star\star} = \langle \mathbf{K}^e (\mathbf{I} + \nabla_{\mathbf{y}} \boldsymbol{\chi}^e) \rangle_e$. Following a similar procedure to that outlined for the mass transport equation, (43) can be written as

$$\begin{aligned} &\mathrm{Pe}_e \nabla_{\mathbf{x}} \cdot [(\lambda t_+ \mathbf{K}^{e\star\star} / \langle c^e \rangle) \nabla_{\mathbf{x}} \langle c^e \rangle_{\mathcal{B}} + 2\mathbf{K}^{e\star\star} \nabla_{\mathbf{x}} \langle \phi^e \rangle_{\mathcal{B}}] \\ &= 2\eta \varepsilon^{-1} \mathcal{K}^{\star} \mathrm{Da}_e f(\langle c^e \rangle_{\mathcal{B}}, \langle c^s \rangle_s, \langle \phi^e \rangle_{\mathcal{B}}, \langle \phi^s \rangle_s), \end{aligned} \tag{44}$$

where $f(\langle c^e \rangle_{\mathcal{B}}, \langle c^s \rangle_s, \langle \phi^e \rangle_{\mathcal{B}}, \langle \phi^s \rangle_s)$ is defined by (2.33).

Equations (39) and (44) govern the dynamics of $\langle c^e \rangle_{\mathcal{B}}$ and $\langle \phi^e \rangle_{\mathcal{B}}$ in the electrolyte up to errors of order ε^2.

Appendix B Homogenization in the electrode

The same procedure outline in Appendix A is followed for the derivation of the effective mass and charge transport equations in the electrode. The derivations are reported for completeness. After setting $c_\varepsilon^j(\mathbf{x},t) = c^j(\mathbf{x},\mathbf{y},t,\tau_{\rm r},\tau_{{\rm m}e},\tau_{{\rm m}s})$ and $\phi_\varepsilon^j(\mathbf{x},t) = \phi^j(\mathbf{x},\mathbf{y},t,\tau_{\rm r},\tau_{{\rm m}e},\tau_{{\rm m}s})$, $j = \{e,s\}$, equation (2.28) is combined with (2.22) and (2.23) to obtain

$$\frac{\partial c^s}{\partial t} + {\rm Da}_e\frac{\partial c^s}{\partial \tau_{\rm r}} + {\rm Pe}_e\left(\frac{\partial c^s}{\partial \tau_{{\rm m}e}} + \frac{{\rm Da}_e}{{\rm Da}_s}\frac{\partial c^s}{\partial \tau_{{\rm m}s}}\right) = {\rm Da}_e{\rm Da}_s^{-1}\nabla_{\mathbf{x}}\cdot[\mathbf{D}^s(\nabla_{\mathbf{x}}c^s + \varepsilon^{-1}\nabla_{\mathbf{y}}c^s)] + \varepsilon^{-1}{\rm Da}_e{\rm Da}_s^{-1}\nabla_{\mathbf{y}}\cdot[\mathbf{D}^s(\nabla_{\mathbf{x}}c^s + \varepsilon^{-1}\nabla_{\mathbf{y}}c^s)], \quad \mathbf{x}\in\mathcal{S}^\varepsilon \tag{45}$$

and

$$\nabla_{\mathbf{x}}\cdot[\mathbf{K}^s(\nabla_{\mathbf{x}}\phi^s + \varepsilon^{-1}\nabla_{\mathbf{y}}\phi^s)] + \varepsilon^{-1}\nabla_{\mathbf{y}}\cdot[\mathbf{K}^s(\nabla_{\mathbf{x}}\phi^s + \varepsilon^{-1}\nabla_{\mathbf{y}}\phi^s)] = 0, \quad \mathbf{x}\in\mathcal{S}^\varepsilon \tag{46}$$

subject to

$$-\mathbf{n}_s\cdot[\mathbf{D}^s(\nabla_{\mathbf{x}}c^s + \varepsilon^{-1}\nabla_{\mathbf{y}}c^s)] = {\rm Da}_s f(c_\varepsilon^e, c_\varepsilon^s, \phi_\varepsilon^s, \phi_\varepsilon^e), \quad \mathbf{x}\in\Gamma^\varepsilon \tag{47}$$

and

$$-\mathbf{n}_s\cdot[2{\rm Pe}_s\,\mathbf{K}^s(\nabla_{\mathbf{x}}\phi^s + \varepsilon^{-1}\nabla_{\mathbf{y}}\phi^s)] = {\rm Da}_s f(c_\varepsilon^e, c_\varepsilon^s, \phi_\varepsilon^s, \phi_\varepsilon^e), \quad \mathbf{x}\in\Gamma^\varepsilon \tag{48}$$

respectively, where $f(c_\varepsilon^e, c_\varepsilon^s, \phi_\varepsilon^s, \phi_\varepsilon^e)$ is defined in (2.21).

B.1 Mass and charge transport asymptotic expansions

Substituting (2.29) and (2.30) into the mass transport equation in the electrode (45) leads to

$$\begin{aligned}
&\varepsilon^{-2}\{-\varepsilon^{\beta-\gamma}\nabla_{\mathbf{y}}\cdot(\mathbf{D}^s\nabla_{\mathbf{y}}c_0^s)\}+\\
&\varepsilon^{-1}\{\varepsilon^{1+\beta}\partial_{\tau_{\rm r}}c_0^s - \varepsilon^{\beta-\gamma}\nabla_{\mathbf{x}}\cdot(\mathbf{D}^s\nabla_{\mathbf{y}}c_0^s) - \varepsilon^{\beta-\gamma}\nabla_{\mathbf{y}}\cdot[\mathbf{D}^s(\nabla_{\mathbf{x}}c_0^s + \nabla_{\mathbf{y}}c_1^s)]\}\\
&\quad\varepsilon^0\{\partial_t c_0^s + \varepsilon^{-\alpha}(\partial_{\tau_{{\rm m}e}}c_0^s + \varepsilon^{\beta-\gamma}\partial_{\tau_{{\rm m}s}}c_0^s) + \varepsilon^{1+\beta}\partial_{\tau_{\rm r}}c_1^s - \varepsilon^{\beta-\gamma}\nabla_{\mathbf{x}}\cdot[\mathbf{D}^s(\nabla_{\mathbf{x}}c_0^s + \nabla_{\mathbf{y}}c_1^s)\\
&\qquad - \varepsilon^{\beta-\gamma}\nabla_{\mathbf{y}}\cdot[\mathbf{D}^s(\nabla_{\mathbf{x}}c_1^s + \nabla_{\mathbf{y}}c_2^s)]\} = \mathcal{O}(\varepsilon), \qquad \mathbf{y}\in\mathcal{S},
\end{aligned} \tag{49}$$

subject to

$$\varepsilon^{-1}\{\mathbf{n}_s \cdot (\mathbf{D}^s \nabla_{\mathbf{y}} c_0^s)\} + \varepsilon^0 \{\mathbf{n}_s \cdot [\mathbf{D}^s (\nabla_{\mathbf{x}} c_0^s + \nabla_{\mathbf{y}} c_1^s)] + 2\varepsilon^\gamma A_0 B_0)\} +$$
$$\varepsilon\{\mathbf{n}_s \cdot [\mathbf{D}^s (\nabla_{\mathbf{x}} c_1^s + \nabla_{\mathbf{y}} c_2^s)] + 2\varepsilon^\gamma (A_0 B_1 + A_1 B_0)]\} = \mathcal{O}(\varepsilon^2), \quad \mathbf{y} \in \Gamma, \tag{50}$$

where A_0, A_1, B_0 and B_1 are defined in (8). Similarly, the charge transport equation (46) and the boundary condition (48) combined with (2.29) and (2.30) yield

$$\varepsilon^{-2}\{\nabla_{\mathbf{y}} \cdot (\mathbf{K}^s \nabla_{\mathbf{y}} \phi_0^s)\} + \varepsilon^{-1}\{\nabla_{\mathbf{x}} \cdot (\mathbf{K}^s \nabla_{\mathbf{y}} \phi_0^s) + \nabla_{\mathbf{y}} \cdot [\mathbf{K}^s (\nabla_{\mathbf{x}} \phi_0^s + \nabla_{\mathbf{y}} \phi_1^s)]\} +$$
$$\varepsilon^0\{\nabla_{\mathbf{x}} \cdot [\mathbf{K}^s (\nabla_{\mathbf{x}} \phi_0^s + \nabla_{\mathbf{y}} \phi_1^s) + \nabla_{\mathbf{y}} \cdot [\mathbf{K}^s (\nabla_{\mathbf{x}} \phi_1^s + \nabla_{\mathbf{y}} \phi_2^s)]\} = \mathcal{O}(\varepsilon), \quad \mathbf{y} \in \mathcal{S}, \tag{51}$$

subject to

$$\varepsilon^{-1}\{\mathbf{n}_s \cdot (\varepsilon^{-\delta} \mathbf{K}^s \nabla_{\mathbf{y}} \phi_0^s)\} + \varepsilon^0 \{\mathbf{n}_s \cdot [\varepsilon^{-\delta} \mathbf{K}^s (\nabla_{\mathbf{x}} \phi_0^s + \nabla_{\mathbf{y}} \phi_1^s)] + 2\varepsilon^\gamma A_0 B_0\} +$$
$$\varepsilon\{\mathbf{n}_s \cdot [\varepsilon^{-\delta} \mathbf{K}^s (\nabla_{\mathbf{x}} \phi_1^s + \nabla_{\mathbf{y}} \phi_2^s)] + 2\varepsilon^\gamma (A_0 B_1 + A_1 B_0)]\} = \mathcal{O}(\varepsilon^2), \quad \mathbf{y} \in \Gamma, \tag{52}$$

B.2 Terms of order $\mathcal{O}(\varepsilon^{-2})$

Collecting the leading-order terms in the mass transport equation and corresponding boundary conditions (49) and (50) leads to

$$\nabla_{\mathbf{y}} \cdot (\mathbf{D}^s \nabla_{\mathbf{y}} c_0^s) = 0, \qquad \mathbf{y} \in \mathcal{S}, \tag{53}$$

subject to the interface condition

$$\mathbf{n}_s \cdot (\mathbf{D}^s \nabla_{\mathbf{y}} c_0^s) = 0, \qquad \mathbf{y} \in \Gamma. \tag{54}$$

Similarly, at the leading order the charge balance equation (51) and the boundary condition yield

$$\nabla_{\mathbf{y}} \cdot (\mathbf{K}^s \nabla_{\mathbf{y}} \phi_0^s) = 0, \qquad \mathbf{y} \in \mathcal{S}, \tag{55}$$

subject to

$$\mathbf{n}_s \cdot (\mathbf{K}^s \nabla_{\mathbf{y}} \phi_0^s) = 0, \qquad \mathbf{y} \in \Gamma. \tag{56}$$

The homogeneity of equations (53)- (56) ensures that the above boundary value problems have both a trivial solution, i.e.

$$c_0^s = c_0^s(\mathbf{x}, t, \tau_{\mathrm{r}}, \tau_{\mathrm{re}}, \tau_{\mathrm{rs}}) \tag{57a}$$

$$\phi_0^s = \phi_0^s(\mathbf{x}, t, \tau_{\mathrm{r}}, \tau_{re}, \tau_{\mathrm{r}s}) \tag{57b}$$

B.3 Terms of order $\mathcal{O}\left(\varepsilon^{-1}\right)$

At the following order, the mass transport equation (49) can be written as

$$\varepsilon^{1+\gamma} \partial_{\tau_{\mathrm{r}}} c_0^s - \nabla_{\mathbf{y}} \cdot [\mathbf{D}^s (\nabla_{\mathbf{x}} c_0^s + \nabla_{\mathbf{y}} c_1^s)] = 0, \quad \mathbf{y} \in \mathcal{S} \tag{58}$$

since $\nabla_{\mathbf{y}} c_0^s \equiv \mathbf{0}$, and it is subject to the boundary condition

$$\mathbf{n}_s \cdot [\mathbf{D}^s (\nabla_{\mathbf{x}} c_0^s + \nabla_{\mathbf{y}} c_1^s)] + 2\varepsilon^{\gamma} A_0 B_0 = 0, \qquad \mathbf{y} \in \Gamma. \tag{59}$$

Integrating (58) over $\mathcal{S}$ with respect to $\mathbf{y}$, while accounting for the boundary condition (59), and the periodicity of the coefficients on the external boundary of the unit cell ∂Y, leads to

$$\varepsilon^{1+\gamma} \partial_{\tau_{\mathrm{r}}} c_0^s = -2\eta \varepsilon^{\gamma} \mathcal{K}^{\star} A_0 B_0. \tag{60}$$

Equation (60) is combined with (58) to eliminate the temporal derivative and obtain

$$\nabla_{\mathbf{y}} \cdot [\mathbf{D}^s (\nabla_{\mathbf{x}} c_0^s + \nabla_{\mathbf{y}} c_1^s)] + 2\eta \varepsilon^{\gamma} \mathcal{K}^{\star} A_0 B_0 = 0. \tag{61}$$

Similarly, the order $\mathcal{O}(\varepsilon^{-1})$ of the charge balance equation (51) can be simplified to

$$\nabla_{\mathbf{y}} \cdot [\mathbf{K}^s (\nabla_{\mathbf{x}} \phi_0^s + \nabla_{\mathbf{y}} \phi_1^s)] = 0, \quad \mathbf{y} \in \mathcal{S}, \tag{62}$$

subject to

$$\mathbf{n}_s \cdot [\varepsilon^{-\delta}\mathbf{K}^s(\nabla_{\mathbf{x}}\phi_0^s + \nabla_{\mathbf{y}}\phi_1^s)] + 2\varepsilon^{\gamma}A_0B_0 = 0, \quad \mathbf{y} \in \Gamma. \tag{63}$$

Equations (61) and (62) subject to (59) and (63) form a boundary value problem for c_1^s and ϕ_1^s, respectively. As outlined in the previous appendix, a solution exist in the following form:

$$\begin{aligned} c_1^s(\mathbf{x},\mathbf{y},t,\tau_{\mathrm{r}},\tau_{\mathrm{me}},\tau_{\mathrm{ms}}) &= \boldsymbol{\chi}_3(\mathbf{y}) \cdot \nabla_{\mathbf{x}} c_0^s(\mathbf{x},t,\tau_{\mathrm{r}},\tau_{\mathrm{me}},\tau_{\mathrm{ms}}) + \overline{c}_1^s(\mathbf{x},t,\tau_{\mathrm{r}},\tau_{\mathrm{me}},\tau_{\mathrm{ms}}), \\ \phi_1^s(\mathbf{x},\mathbf{y},t,\tau_{\mathrm{r}},\tau_{\mathrm{me}},\tau_{\mathrm{ms}}) &= \boldsymbol{\chi}_4(\mathbf{y}) \cdot \nabla_{\mathbf{x}} \phi_0^s(\mathbf{x},t,\tau_{\mathrm{r}},\tau_{\mathrm{me}},\tau_{\mathrm{ms}}) + \overline{\phi}_1^s(\mathbf{x},t,\tau_{\mathrm{r}},\tau_{\mathrm{me}},\tau_{\mathrm{ms}}). \end{aligned} \tag{64}$$

Substitution of (64) into (61) and (59) leads to the following cell problem for the closure variable $\boldsymbol{\chi}_3(\mathbf{y})$,

$$2\eta\varepsilon^{\gamma}\mathcal{K}^{\star}A_0B_0 + \nabla_{\mathbf{y}} \cdot [\mathbf{D}^s(\mathbf{I} + \nabla_{\mathbf{y}}\boldsymbol{\chi}_3)\nabla_{\mathbf{x}}c_0^s] = 0, \qquad \mathbf{y} \in \mathcal{S}, \tag{65a}$$

subject to $\langle \boldsymbol{\chi}_3 \rangle_s = 0$ and

$$\mathbf{n}_s \cdot [\mathbf{D}^s(\mathbf{I} + \nabla_{\mathbf{y}}\boldsymbol{\chi}_3)\nabla_{\mathbf{x}}c_0^s] + 2\varepsilon^{\gamma}A_0B_0 = 0, \qquad \mathbf{y} \in \Gamma. \tag{65b}$$

The boundary-value problem (65) couples the pore scale with the continuum scale, in the sense that the closure variable $\boldsymbol{\chi}_3(\mathbf{y})$—a solution of the pore-scale cell problem (65) —is influenced by the continuum scale through its dependence on the macroscopic concentration $c_0^s(\mathbf{x})$. This coupling is incompatible with the general representation (64). This inconsistency is resolved by imposing the following constraint on the exponent γ, namely $\gamma > 0$. This condition on γ ensures that $\boldsymbol{\chi}_3$ is independent of c_0^s, and the cell problem (65) can be simplified to

$$\nabla_{\mathbf{y}} \cdot [\mathbf{D}^s(\mathbf{I} + \nabla_{\mathbf{y}}\boldsymbol{\chi}_3)] = 0, \qquad \mathbf{y} \in \mathcal{S}, \tag{66a}$$

$$\mathbf{n}_s \cdot [\mathbf{D}^s(\mathbf{I} + \nabla_{\mathbf{y}}\boldsymbol{\chi}_3)] = 0, \qquad \mathbf{y} \in \Gamma. \tag{66b}$$

Similarly, substitution of (64) into the $\mathcal{O}(\varepsilon^{-1})$-charge balance equation (62) and its boundary condition (63) leads to the following cell problem for the closure variable $\boldsymbol{\chi}_4(\mathbf{y})$,

$$\nabla_{\mathbf{y}} \cdot [\mathbf{K}^s(\mathbf{I} + \nabla_{\mathbf{y}}\boldsymbol{\chi}_4)\nabla_{\mathbf{x}}\phi_0^s] = 0, \qquad \mathbf{y} \in \mathcal{S}; \tag{67a}$$

subject to $\langle \boldsymbol{\chi}_4 \rangle_s = 0$ and

$$\mathbf{n}_s \cdot [\varepsilon^{-\delta} \mathbf{K}^s (\nabla_{\mathbf{y}} \boldsymbol{\chi}_4 + \mathbf{I})] \nabla_{\mathbf{x}} \phi_0^s] + \varepsilon^{\gamma} (A_0 B_0) = 0, \qquad \mathbf{y} \in \Gamma, \tag{67b}$$

where $\boldsymbol{\chi}_4(\mathbf{y})$ is a Y-periodic vector field. Separation between pore- and continuum-scales requires $\gamma + \delta > 0$. Under this condition (67), simplifies to

$$\nabla_{\mathbf{y}} \cdot [\mathbf{K}^s (\mathbf{I} + \nabla_{\mathbf{y}} \boldsymbol{\chi}_4)] = 0, \qquad \mathbf{y} \in \mathcal{S}, \tag{68a}$$

$$\mathbf{n}_s \cdot [\mathbf{K}^s (\mathbf{I} + \nabla_{\mathbf{y}} \boldsymbol{\chi}_4)] = 0, \qquad \mathbf{y} \in \Gamma. \tag{68b}$$

In (66) and (68), the diffusion and conductivity tensors are functions of concentration c^e and potential ϕ^e. With an order ε approximation $\mathbf{D}^e \approx \mathbf{D}^e(c_0^e, \phi_0^e)$ and $\mathbf{K}^e \approx \mathbf{K}^e(c_0^e, \phi_0^e)$. Then, $\boldsymbol{\chi}_4 = \boldsymbol{\chi}_3 =: \boldsymbol{\chi}^s(\mathbf{y})$, where $\boldsymbol{\chi}^s$ is a solution of the closure problem

$$\nabla_{\mathbf{y}} \cdot (\mathbf{I} + \nabla_{\mathbf{y}} \boldsymbol{\chi}^s) = 0, \qquad \mathbf{y} \in \mathcal{S}, \tag{69a}$$

$$\mathbf{n}_s \cdot (\mathbf{I} + \nabla_{\mathbf{y}} \boldsymbol{\chi}^s) = 0, \qquad \mathbf{y} \in \Gamma. \tag{69b}$$

B.4 Terms of order $\mathcal{O}(\varepsilon^0)$

At the leading order, the mass transport equation in the electrode (49)

$$\begin{aligned} &\partial_t c_0^s + \varepsilon^{-\alpha} (\partial_{\tau_{\mathrm{me}}} c_0^s + \varepsilon^{\beta-\gamma} \partial_{\tau_{\mathrm{ms}}} c_0^s) + \varepsilon^{1+\beta} \partial_{\tau_{\mathrm{r}}} c_1^s - \varepsilon^{\beta-\gamma} \nabla_{\mathbf{x}} \cdot [\mathbf{D}^s (\nabla_{\mathbf{x}} c_0^s + \nabla_{\mathbf{y}} c_1^s)] \\ &\quad - \varepsilon^{\beta-\gamma} \nabla_{\mathbf{y}} \cdot [\mathbf{D}^s (\nabla_{\mathbf{x}} c_1^s + \nabla_{\mathbf{y}} c_2^s)] = 0, \qquad \mathbf{y} \in \mathcal{S}, \end{aligned} \tag{70}$$

subject to

$$\mathbf{n}_s \cdot [\mathbf{D}^s (\nabla_{\mathbf{x}} c_1^s + \nabla_{\mathbf{y}} c_2^s)] + 2\varepsilon^{\gamma} (A_0 B_1 + A_1 B_0) = 0, \qquad \mathbf{y} \in \Gamma. \tag{71}$$

Integrating (70) over $\mathcal{S}$ with respect to $\mathbf{y}$ and using the interface condition (71) leads to

$$\begin{aligned} &\partial_t \langle c_0^s \rangle_s + \varepsilon^{-\alpha} (\partial_{\tau_{\mathrm{me}}} \langle c_0^s \rangle_s + \varepsilon^{\beta-\gamma} \partial_{\tau_{\mathrm{ms}}} \langle c_0^s \rangle_s) + \varepsilon^{1+\beta} \partial_{\tau_{\mathrm{r}}} \langle c_1^s \rangle_s - \varepsilon^{\beta-\gamma} \nabla_{\mathbf{x}} \cdot (\mathbf{D}^{s\star\star} \nabla_{\mathbf{x}} c_0^s) \\ &\quad + 2\varepsilon^{\beta-\gamma} \eta \mathcal{K}^{\star} (\langle A_0 \rangle_{\mathcal{B}} \langle B_1 \rangle_{\Gamma} + \langle A_1 \rangle_{\Gamma} \langle B_0 \rangle_{\mathcal{B}}) = 0, \end{aligned} \tag{72}$$

where $\mathbf{D}^{s\star\star} = \langle \mathbf{D}^s(\mathbf{I} + \nabla_{\mathbf{y}}\boldsymbol{\chi}^s)\rangle_s$. Similarly, the leading order of the charge transport equation is

$$\nabla_{\mathbf{x}} \cdot [\mathbf{K}^s(\nabla_{\mathbf{x}}\phi_0^s + \nabla_{\mathbf{y}}\phi_1^s) + \nabla_{\mathbf{y}} \cdot [\mathbf{K}^s(\nabla_{\mathbf{x}}\phi_1^s + \nabla_{\mathbf{y}}\phi_2^s)] = 0, \qquad \mathbf{y} \in \mathcal{S}, \tag{73}$$

subject to

$$\mathbf{n}_s \cdot [\varepsilon^{-\delta}\mathbf{K}^s(\nabla_{\mathbf{x}}\phi_1^s + \nabla_{\mathbf{y}}\phi_2^s)] + 2\varepsilon^{\gamma}(A_0B_1 + A_1B_0) = 0, \qquad \mathbf{y} \in \Gamma. \tag{74}$$

Multiplying both (73) and (74) by ε and adding them to (58) and (59), respectively, and then integrating over $\mathcal{S}$, leads to the effective equation

$$\varepsilon^{1-\delta}\nabla_{\mathbf{x}} \cdot (\mathbf{K}^{s\star\star}\nabla_{\mathbf{x}}\langle\phi_0^s\rangle_s) = \varepsilon^{\gamma}\eta\mathcal{K}^{\star}\langle A_0\rangle_{\mathcal{B}}\langle B_1\rangle_{\Gamma} + \langle A_1\rangle_{\Gamma}\langle B_0\rangle_{\mathcal{B}}), \tag{75}$$

where $\mathbf{K}^{s\star\star} = \langle \mathbf{K}^s(\mathbf{I} + \nabla_{\mathbf{y}}\boldsymbol{\chi}_4)\rangle_s$.

Following the procedure outlined in A.4 and assuming that $\langle\boldsymbol{\chi}^s\rangle_s \approx \langle\boldsymbol{\chi}^s\rangle_{\Gamma}$, equations (72) and (75) lead to the macroscopic equations for mass and charge transport in the electrode (2.37) and (2.38), respectively.

Appendix C Development of the FHM Model and Parameter Identification Studies

This appendix aims to serve as a user guide for the development of the FHM model that describes mass and charge transport of lithium in the active particle and electrolyte phases of a lithium-ion cell. This model is developed in COMSOL Multiphysics®, a software platform designed for the modeling and simulation of physics-based problems in electrical, mechanical, chemical, and electrochemical domains. The user-friendly interface of COMSOL enables the development of different models using pre-defined and user-defined mathematical equations. COMSOL Multiphysics® version 5.0 was used for the development of the FHM model.

Following the development of the model, the implementation of model parameter identification studies using a co-simulation framework involving COMSOL and MATLAB® software is presented. This is possible due to the presence of a recently developed COMSOL feature called the MATLAB® LiveLink™ that establishes an interface for communication between both the software platforms. Thanks to this feature, simulation results from the COMSOL environment can be exported to Matlab for data processing and analysis. Variables can be monitored and modified in the Matlab platform and transferred to the COMSOL interface in a systematic manner, which yields an efficient way of optimizing the parameters involved in the study of complex systems.

The implementation of the FHM model in 1-D Cartesian coordinates, in the direction perpendicular to the current collectors, is presented here. In the first step, all the model parameters that are part of the mathematical equations of the 1-D FHM model are defined in the COMSOL *Model Builder* under the *Global* node. Both constant parameters as well as parameters that are a function of time or a time-dependent model variable are defined here. Following this step, the 1-D geometry is defined in which the coupled non-linear PDEs of the FHM are resolved as a function of time. The anode, separator, and cathode domains are defined in this step. The next step is to define the model variables for the respective domains. A systematic and organized approach to define the model variables for each domain makes it easier to identify anomalies during simulations.

After defining the model parameters and the geometry in which the model variables must be resolved, the following step involves the selection of a pre-defined physics-based interface for resolving the variables of the FHM model. This is achieved using the *Add Physics* feature of COMSOL. Suitable physics-based interfaces are selected for each variable and the coefficients of the pre-defined equations are defined

according to the mathematical formulation of the mass and charge transport equations. The final step before the beginning of simulations is to define the mesh and solver settings for the resolution of the model variables. A time-dependent study is conducted to evaluated the dynamic variation of the model variables as a function of time. Following the completion of simulations, the results can be analyzed for each model variable at each location in the domain that they were resolved. The desired results can then be exported from the COMSOL environment in the form of a spreadsheet. Finally, the use of the MATLAB® LiveLink™ tool to perform the co-simulation studies is presented, and the identification procedure to optimize the parameters of the FHM COMSOL model using the PSO technique is summarized at the end of this appendix. Additional information about the use of the MATLAB® LiveLink™ feature of COMSOL can be obtained from [197, 198].

Creating a 1-D COMSOL Model

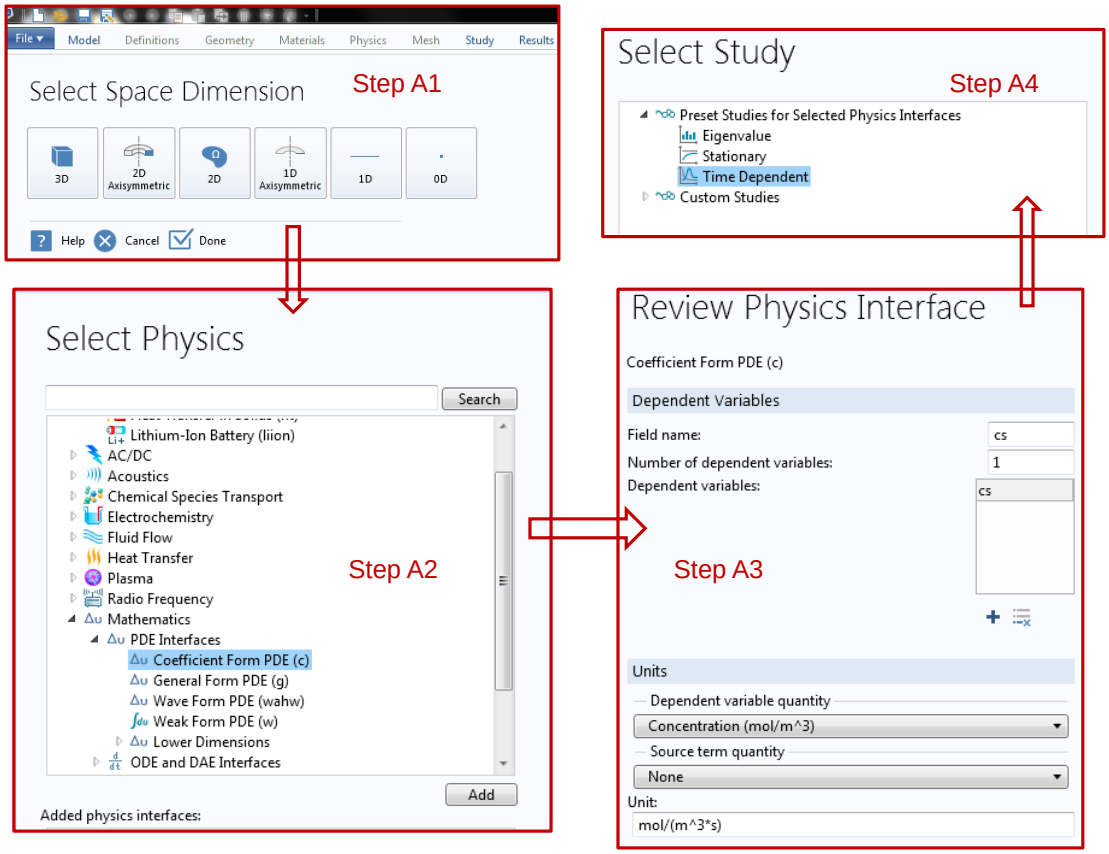

Figure 1: Sequence of steps for the creation of a 1-D COMSOL model for time-dependent studies.

The following steps must be followed to create a 1-D COMSOL model, and is depicted in Fig. 1:

1. Step A1: When a new COMSOL *.mph* file is opened for the very first time, the spatial domain in which the model is developed must be defined. Under *Select Space Dimension*, the *1D* tab must be selected.

2. Step A2: The next step is to select the physics-based interface to define the equations of the model. Since the equations of the FHM model are PDEs, the *Coefficient Form PDE* interface is chosen from the *Mathematics/PDE Interfaces* icon and added using the *Add* tab.

3. Step A3: This step can be modified at any time before beginning the simulations, but it is a good practice to define the model variable and provide its dimensional unit. Under *Review Physics Interface*, the field name and the name of the dependent variable is defined. Then the dimensions of the variable can be selected from the list of available options, and confirmed using the *Study* tab.

4. Step A4: The last step in this phase is to select the type of study that will be performed using the model. Among the pre-defined types of studies for the selected physics interface, click on *Time Dependent* and confirm this study using the *Done* tab.

Defining Model Parameters and Input

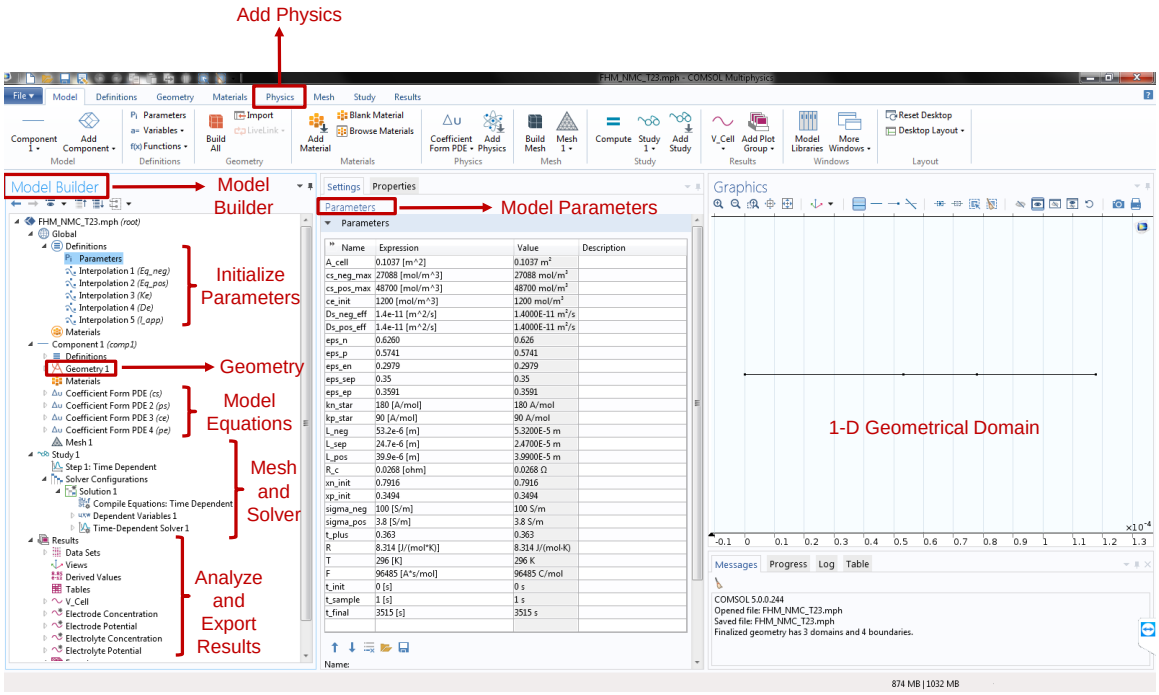

Figure 2: An overview of different features of the COMSOL interface used for the modeling and simulation of the FHM model.

Figure 2 presents a general overview of commonly used features in the COMSOL software platform to develop a physics-based model. The equations of mass and charge transport of the FHM model are summarized in Table 4.1. The four model variables that must be resolved as a function of time are $\bar{c}_s$, $\bar{c}_e$, $\bar{\phi}_s$, and $\bar{\phi}_e$. In COMSOL, they are represented by the variables *cs*, *ce*, *ps*, and *pe*, respectively. The boundary and the initial conditions for these variables are summarized in Table 4.5 and Table 4.6, respectively. Table 1 summarizes the representation of the different model parameters in COMSOL. The effective transport properties are determined using the approach presented in section §2.3. The pore-scale parameters K^e and D^e are a function of $\bar{c}_e$. They are defined in COMSOL as *Ke* and *De*, respectively. They are used to define the corresponding effective coefficients in the FHM model. Additional parameters are defined for the time-dependent study. After creating the 1-D model, these parameters must be defined and initialized next.

Table 1: Parameters of the FHM model and their corresponding representation in COMSOL.

Parameter	COMSOL Representation	Parameter	COMSOL Representation
A_{cell}	A_cell	$\eta_{e,p}$	eps_ep
$c_{s,n,max}$	cs_neg_max	L_{neg}	L_neg
$c_{s,p,max}$	cs_pos_max	L_{sep}	L_sep
$\bar{c}_e(t=0)$	ce_init	L_{pos}	L_pos
$D_{e,n}^{eff}$	*De*(*ce*)×(0.192)	$K_{e,n}^{eff}$	*Ke*(*ce*)×(0.192)
$D_{e,sep}^{eff}$	*De*(*ce*)×(0.244)	$K_{e,sep}^{eff}$	*Ke*(*ce*)×(0.244)
$D_{e,p}^{eff}$	*De*(*ce*)×(0.254)	$K_{e,p}^{eff}$	*Ke*(*ce*)×(0.254)
$D_{s,n}^{eff}$	Ds_neg_eff	$K_{s,n}^{eff}$	(sigma_neg)×(0.584)
$D_{s,p}^{eff}$	Ds_pos_eff	$K_{s,p}^{eff}$	(sigma_pos)×(0.513)
$\eta_{s,n}$	eps_n	$\bar{c}_{s,n}(t=0)$	(xn_init)×(cs_neg_max)
$\eta_{s,p}$	eps_p	$\bar{c}_{s,p}(t=0)$	(xp_init)×(cs_pos_max)
$\eta_{e,n}$	eps_en	R_c	R_c
$\eta_{e,sep}$	eps_sep	t_+	t_plus
$U_{0,n}$	*Eq_neg*	$U_{0,p}$	*Eq_pos*
J_{Li}	J_Li	I_{app}	*I_app*

The following steps must be followed to initialize model parameters and input:

1. Step B1: The first icon in the *Model Builder* is the *Global* icon. Use the right click button on *Definitions* and select *Parameters*. Each model parameter must be defined with a numerical value and its unit. For convenience, the intercalation current density term of the FHM model is expressed in COMSOL in the following manner:

$$J_{Li,j} = \frac{\varepsilon_j^{-1}\mathcal{K}_{|}^{*}\eta_{e,j}}{L_j}\cdot k_j\cdot\sqrt{\bar{c}_{e,j}\cdot\bar{c}_{s,j}\cdot\Big(1-\frac{\bar{c}_{s,j}}{c_{s,max,j}}\Big)}\cdot 2\sinh\Big(\frac{F}{2RT}\big[\bar{\phi}_{s,j}-\bar{\phi}_{e,j}-U_{0,j}\big]\Big)$$
$$= k_j^{\star}\cdot\sqrt{\bar{c}_{e,j}\cdot\bar{c}_{s,j}\cdot\Big(1-\frac{\bar{c}_{s,j}}{c_{s,max,j}}\Big)}\cdot 2\sinh\Big(\frac{F}{2RT}\big[\bar{\phi}_{s,j}-\bar{\phi}_{e,j}-U_{0,j}\big]\Big), \tag{76}$$

where $k_j^{\star}$ [A/mol] is used to express the electrode intercalation reaction rate. In COMSOL, kn_star and kp_star are used to express the anode and cathode reaction rates, respectively.

2. Step B2: The non-constant parameters of the model are the anode OCP *Eq_neg*, the cathode OCP *Eq_pos*, the pore-scale electrolyte diffusion *De*, and the pore-scale electrolyte conductivity *Ke*. The OCP of each electrode is a function of its stoichiometric coefficient. *De* and *Ke* are a function of *ce*. An interpolation function is used to input the values of these parameters. Use the right click button on

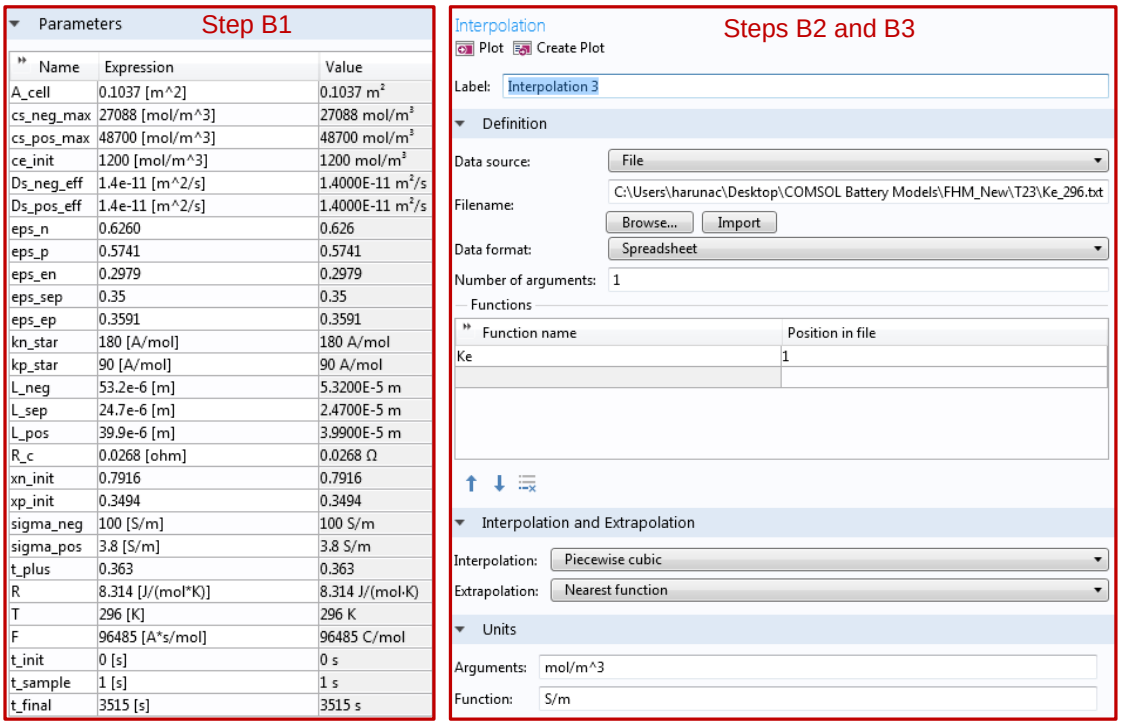

Figure 3: Initialization of the constant model parameters and *Ke* as a function of the model variable *ce*.

Definitions and select *Interpolation* from the *Functions* icon.

3. Step B3: The parameters of the FHM model are initialized as shown in Fig. 3. To define *Ke*, a notepad source file, Ke_296.txt, is created with two columns of data. The first column consists of a range of *ce* values, and the second column consists of the corresponding *Ke* values. This file is uploaded into COMSOL, and a piecewise cubic function is used to interpolate the value of *Ke* for different *ce* values.

4. Step B4: Repeat steps B2 and B3 for the other parameters. *Eq_neg* is defined in terms of xn_init, *Eq_pos* in terms of xp_init, *De* in terms of *ce*, and *I_app* is defined as a function of time.

Defining the Geometry

The following steps must be followed to create the 1-D geometry, and is depicted in Fig. 4:

1. Step C1: Use the right click button on *Geometry 1* and select *Interval*. This will allow the creation of the three domains of the 1-D model: anode, separator, and cathode.

2. Step C2: Under the *Interval* settings, change the number of intervals to *Many*. The 1-D geometry is created by defining the coordinates of the end points of each domain. Since there are three domains,

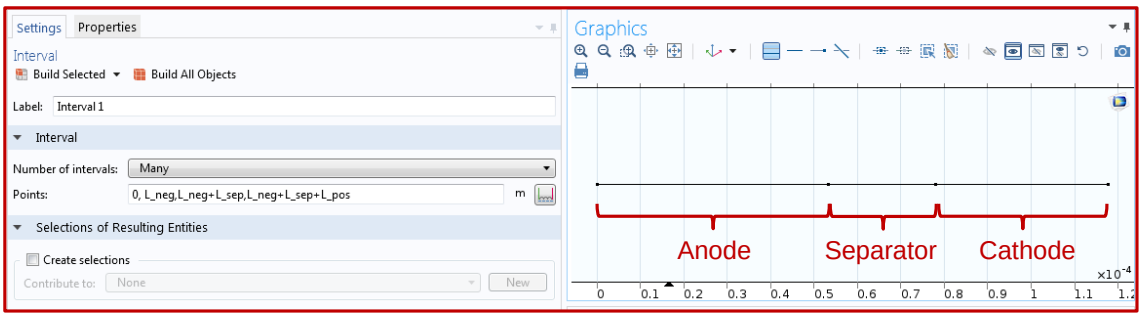

Figure 4: Creating the 1-D geometry in which the four variables of the FHM model are resolved.

four end points must be defined in total.

3. Step C3: Corresponding to *Points*, provide the following input: (0, L_neg, L_neg + L_sep, L_neg + L_sep + L_pos). Then click on the *Build All Objects* tab to generate three domains of lengths L_neg, L_sep, and L_pos, respectively.

Defining Model Parameters in each Domain

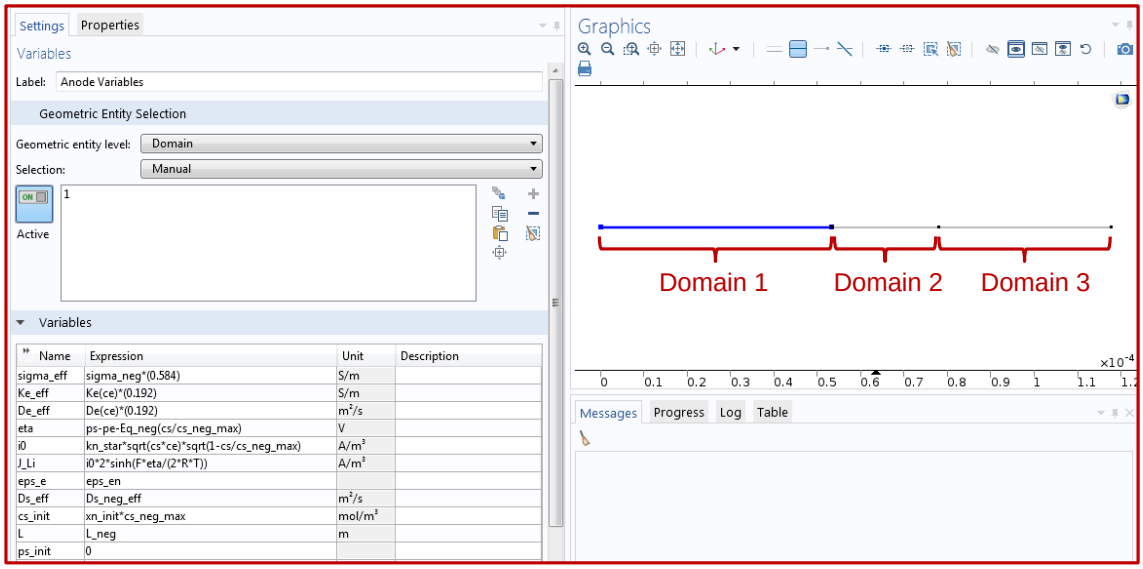

Figure 5: Defining the parameters in the anode domain of the 1-D model.

The steps to define the parameters of the FHM model for each of the three domains is presented here. Fig. 5 depicts the model parameters that are defined in the anode domain of the 1-D model. The following steps must be executed:

1. Step D1: Use the right click button on *Definitions* that is located under the *Component 1* icon. Select the first option *Variables*, and rename it as *Anode Variables*.

2. Step D2: In the *Variable* settings, change the geometric entity level to *Domain*. Change the selection to *Manual*, and select the first domain 1 that represents the anode.

3. Step D3: Under the *Variable* tab, the different model parameters are defined. The parameters defined in the anode domain are: effective diffusion parameters Ds_eff and De_eff, effective conductivity parameters Ks_eff and Ke_eff, electrolyte volume fraction eps_e, thickness L, initial active material lithium concentration cs_init, initial electrode potential ps_init, and the intercalation current density J_Li, which is the COMSOL representation of the term $J_{Li,j}$ in the FHM model.

4. Step D4: Repeat the steps D1 to D3 for defining the model parameters in the second domain 2 for the separator, and the third domain 3 for the cathode. The parameters defined in the cathode are the same as the ones defined in the anode. The values of the corresponding model parameters must be entered for the cathode domain. In the separator domain, only the electrolyte transport equations are resolved. The parameters defined in this domain are: effective diffusion De_eff, effective conductivity Ke_eff, and electrolyte volume fraction eps_e. Since there are no active particles in the separator, there are no reactions involved. Hence the value of J_Li is set to zero.

Defining the FHM Model Equations

a) Model Variable *cs*

Figure 6 depicts the approach to define the electrode mass transport equation in the 1-D model. The following steps must be executed:

1. Step E1: The first step is to add a physics-based interface to resolve the FHM model variables. *cs* is chosen first and the electrode mass transport equation is defined initially. Click on the *Physics* tab shown in Fig. 2, and select *Add Physics*. Select the *Coefficient Form PDE* interface that is located in *Mathematics/PDE Interfaces*. Confirm this selection by clicking on *Add to Component*. This study interface is then added to *Component 1* where the geometry and model parameters were defined earlier. This step is very similar to step A2 depicted in Fig. 1.

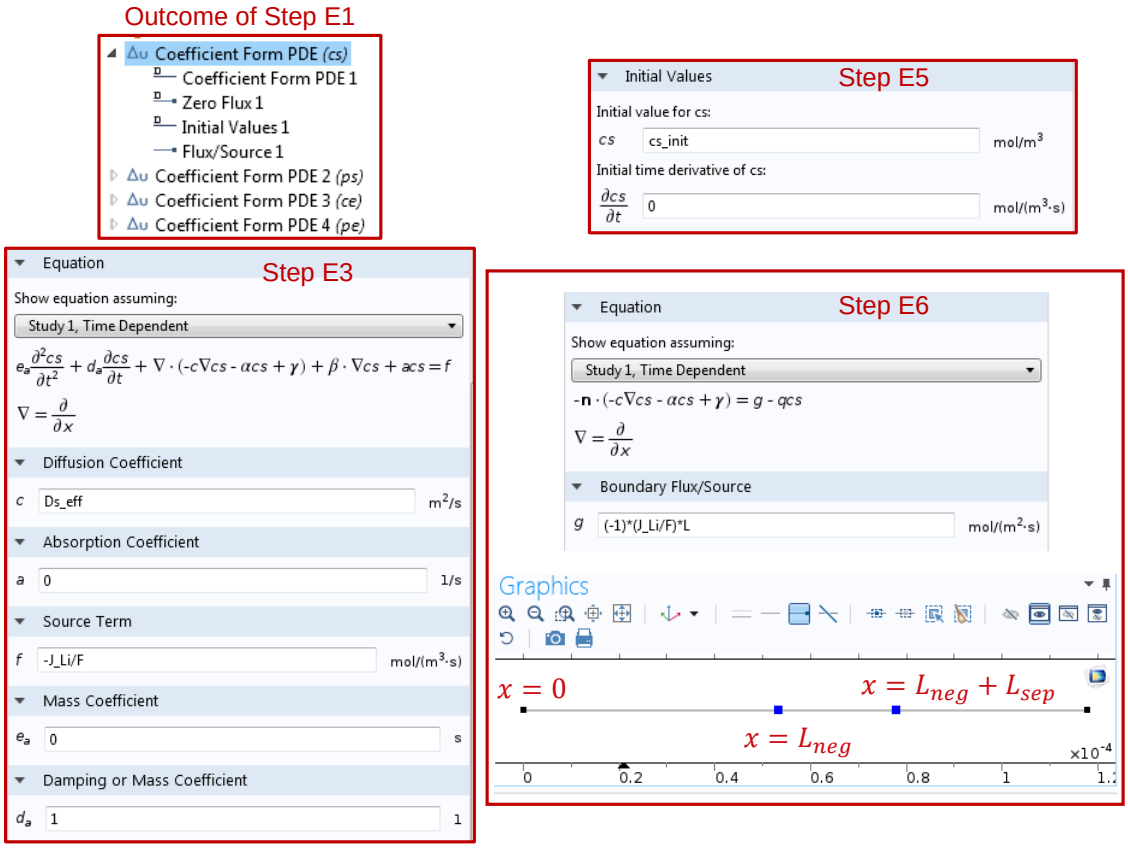

Figure 6: Defining the electrode mass transport equation to resolve the variable *cs*.

2. Step E2: In the *Coefficient Form PDE (cs)* settings, under *Domain Selection*, manually select domains 1 and 3 where *cs* will be resolved. Define the units of the dependent variable quantity and the source term quantity exactly as shown in step A3 of Fig. 1.

3. Step E3: Modify the coefficients of the default coefficient form PDE equation to represent the mass transport equation to resolve *ps*. Set the value under the *Diffusion Coefficient* to Ds_eff, the value under the *Source Term* to -J_Li/F, and the *Damping or Mass Coefficient* to 1. This is depicted in Fig. 6. All the other coefficients are set to 0.

4. Step E4: By default, zero flux is selected at the locations x = 0 of domain 1, and x = L_neg + L_sep + L_pos of domain 3. These are the correct settings, so no additional modification is necessary.

5. Step E5: Under *Initial Values 1*, set the initial value for *cs* to cs_init, and the value of the initial time derivative of *cs* to zero.

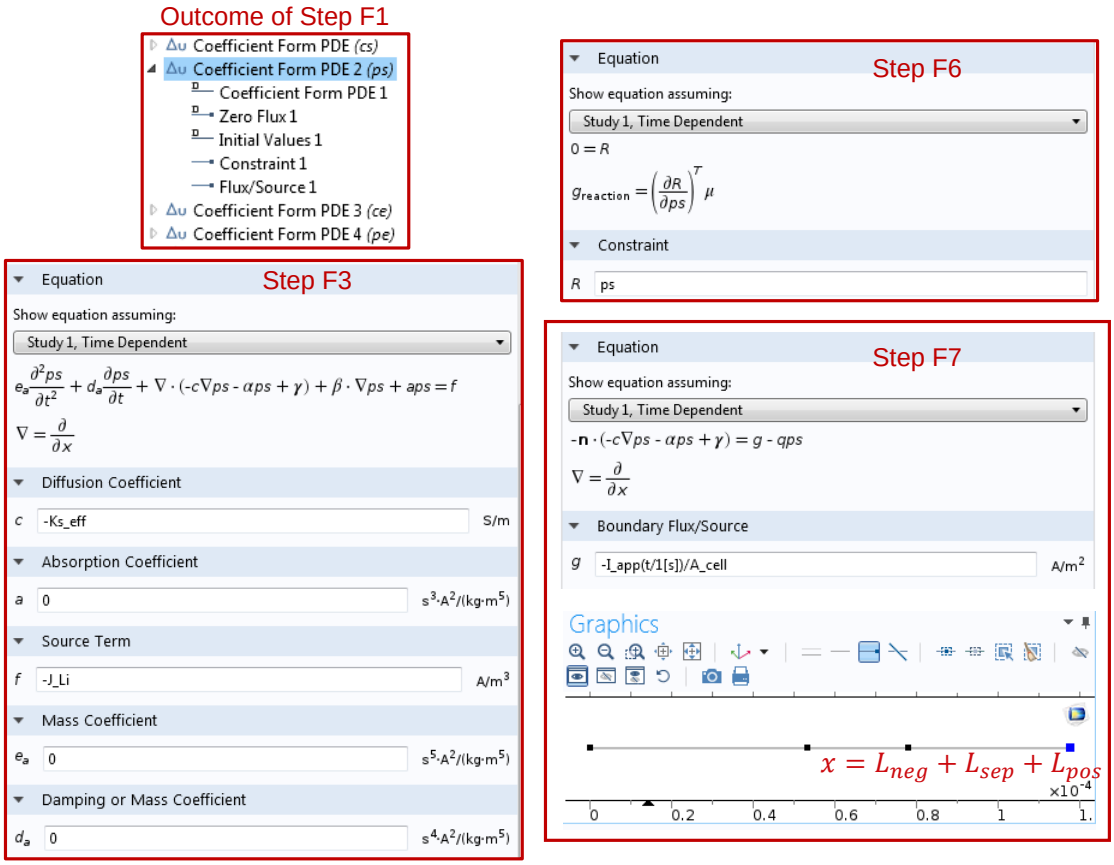

Figure 7: Defining the electrode charge transport equation to resolve the variable *ps*.

6. Step E6: Use the right click button on *Coefficient Form PDE (cs)* and select *Flux/Source 1*. Set the value under *Boundary Flux/Source* to (-J_Li/F)×L. Following this, in the *Flux/Source* settings, under *Boundary Selection*, manually select boundaries 2 and 3. Boundary 2 represents the location x = L_neg, which is an end point of domain 1. Boundary 3 represents the location x = L_neg + L_sep, which is an end point of domain 3. These locations are highlighted by the blue dots in Fig. 6.

b) Model Variable *ps*

Figure 7 depicts the approach to define the electrode charge transport equation in the 1-D model. The following steps must be executed:

1. Step F1: Repeat step E1 to add a physics-based interface to resolve the FHM model variable *ps*.

2. Step F2: In the *Coefficient Form PDE (ps)* settings, under *Domain Selection*, manually select domains 1 and 3 where *ps* will be resolved. Under the *Units* tab, select *Electric potential (V)* for the dependent

variable quantity, and provide the units [A/m^3] for the source term quantity. This is similar to step A3 that is depicted in Fig. 1.

3. Step F3: Modify the coefficients of the default coefficient form PDE equation to represent the charge transport equation to resolve *ps*. Set the value under the *Diffusion Coefficient* to -Ks_eff, and the value under the *Source Term* to -J_Li. This is depicted in Fig. 7. All the other coefficients are set to 0.

4. Step F4: Verify that zero flux is applied at the locations x = L_neg of domain 1 and x = L_neg + L_sep of domain 3. This must be applied by default.

5. Step F5: Under *Initial Values 1*, set the initial value for *ps* to ps_init, and the value of the initial time derivative of *ps* to zero.

6. Step F6: Use the right click button on *Coefficient Form PDE (ps)* and select *Constraint 1*. Set the value under *Constraint* to ps.

7. Step F7: Use the right click button on *Coefficient Form PDE (ps)* and select *Flux/Source 1*. Set the value under the *Boundary Flux/Source* to -I_app(t/1[s])/A_cell. Following this, in the *Flux/Source* settings, under *Boundary Selection*, manually select boundary 4. Boundary 4 represents the location x = L_neg + L_sep + L_pos, which is an end point of domain 3. This location is highlighted by the blue dot in Fig. 7.

c) Model Variable *ce*

Figure 8 depicts the approach to define the electrolyte mass transport equation in the 1-D model. The following steps must be executed:

1. Step G1: Repeat step E1 to add a physics-based interface to resolve the FHM model variable *ce*.

2. Step G2: In the *Coefficient Form PDE (ce)* settings, under *Domain Selection*, manually select domains 1, 2, and 3 where *ce* will be resolved. Provide the same values for the dependent variable quantity and the source term quantity as done for the variable *cs* in step E2.

3. Step G3: Modify the coefficients of the default coefficient form PDE equation to represent the mass transport equation to resolve *ce*. Set the value under the *Source Term* to J_Li/F, the value of the *Damping or Mass Coefficient* to eps_e, and the value of the *Conservative Flux Source* to:
$(-1)\times\left[\,(\text{De\_eff})^{*}\text{cex} + (-1)\times(\text{R}\times\text{T}\times\text{t\_plus}^2\times\text{Ke\_eff}/(\text{F}^2\times\text{ce}))\times\text{cex}\right]$.

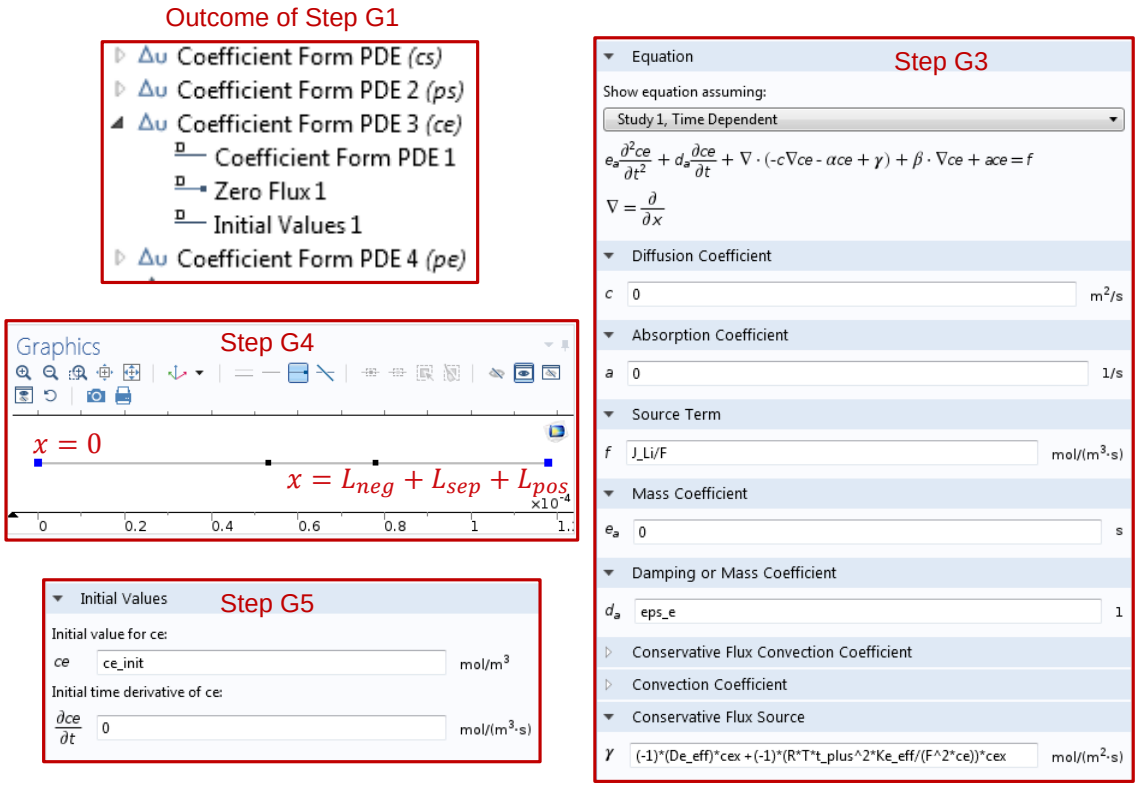

Figure 8: Defining the electrode charge transport equation to resolve the variable *ce*.

The term cex in COMSOL represents the partial derivative of the variable *ce* with respect to x. This is depicted in Fig. 8. All the other coefficients are set to zero. Note that the electrolyte mass and charge transport equations are coupled because of the presence of both variables *ce* and *pe* in these model equations.

4. Step G4: Verify that zero flux is applied at the locations x = 0 of domain 1 and x = L_neg + L_sep + L_pos of domain 3. This must be applied by default. These locations are highlighted by the blue dots in Fig. 8.

5. Step G5: Under *Initial Values 1*, set the initial value for *ce* to ce_init, and the value of the initial time derivative of *ce* to zero.

d) Model Variable *pe*

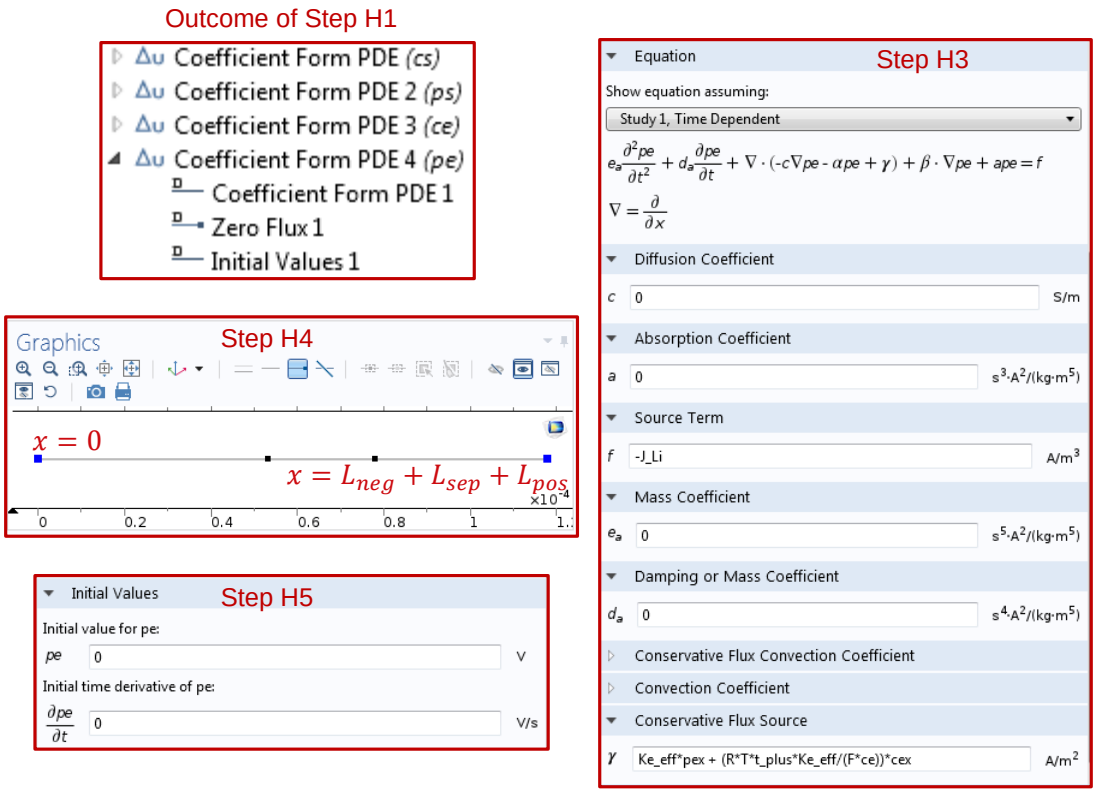

Figure 9: Defining the electrode charge transport equation to resolve the variable *pe*.

Figure 9 depicts the approach to define the electrolyte charge transport equation, following the steps listed . The following steps must be executed:

1. Step H1: Repeat step E1 to add a physics-based interface to resolve the FHM model variable *pe*.

2. Step H2: In the *Coefficient Form PDE (pe)* settings, under *Domain Selection*, manually select domains 1, 2, and 3 where *pe* will be resolved. Under the *Units* tab, select *Electrolyte potential (V)* for the dependent variable quantity, and provide the units [A/m^3] for the source term quantity.

3. Step H3: Modify the coefficients of the default coefficient form PDE equation to represent the charge transport equation to resolve *pe*. Set the value under the *Source Term* to -J_Li, and the value of the *Conservative Flux Source* to:
   $\left[\text{(Ke\_eff)*pex} + \text{(R}\times\text{T}\times\text{t\_plus}\times\text{Ke\_eff/(F}\times\text{ce))}\times\text{cex}\right]$.

The term pex in COMSOL represents the partial derivative of the variable *pe* with respect to x. This is depicted in Fig. 9. All the other coefficients are set to zero.

4. Step H4: Verify that zero flux is applied at the locations x = 0 of domain 1 and x = L_neg + L_sep + L_pos of domain 3. This must be applied by default. These locations are highlighted by the blue dots in Fig. 9.

5. Step H5: Under *Initial Values 1*, set the initial value for *pe* to 0, and the value of the initial time derivative of *pe* to zero.

Defining the Mesh and Solver Settings

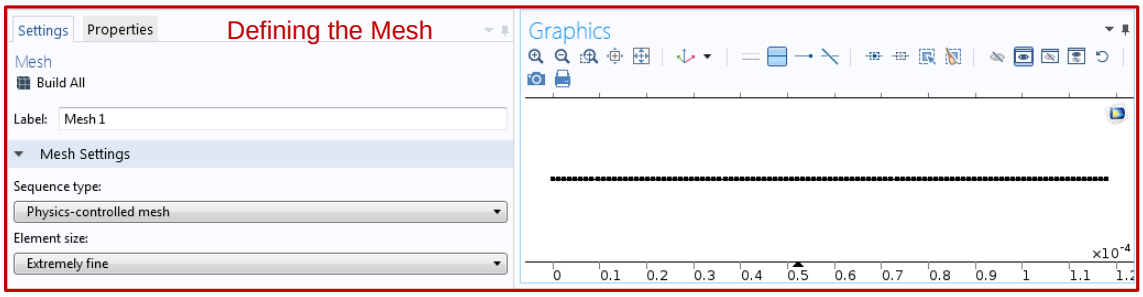

Figure 10: Defining the mesh to resolve the FHM model variables.

Following the setup of the four model variables using the *Coefficient Form PDE* physics-based study interface, the next steps involve the setup of the mesh and solver settings. The following steps must be executed:

1. Step I1: Click on *Mesh 1*. In the mesh settings, under the sequence type, select *Physics-controller mesh*. Under the element size, select *Extremely fine*. This selection and its corresponding outcome are depicted in Fig. 10.

2. Step I2: Under the *Study 1* tab, click on *Step 1: Time Dependent*. Under the study settings, select a time unit of *s*, and provide the following range for the simulation time:

   range(t_init,t_sample,t_final)

   t_init represents the time at the beginning of the simulation, and is set to 0. t_final represents the time at the end of the simulation. Based on experimental data from the capacity test conducted on an 18650 NMC cell at 23°C, it is set to 3515 s. t_sample represents the time increments at which data points are

stored during simulation, and it is set to 1. The relative tolerance is set to 0.001 and activated. The model is considered converged when the estimated error in the iterative solver is less than 0.001 [199].

3. Step I3: Under the *Time-Dependent Solver 1* tab, click on *Direct*. Among the different solvers, choose the *PARDISO* solver. It is a direct solver based on LU decomposition, is the fastest solver among the available options in COMSOL, and is capable of storing the solution *out-of-core*, thereby transfering some of the computational burden to the hard-disk [199].

4. Step I4: The four model variables are fully coupled non-linear PDEs, and must be resolved simultaneously. To handle any computational issues associated with the high non-linearity of the model, click on *Fully Coupled 1* and under the *Method and Termination* tab, select the *Automatically highly non-linear (Newton)* method. Then, set the termination technique to *Tolerance* and increase the maximum number of iterations to 800. This will enable sufficient number of iterations to ensure that the model converges based on the initially defined tolerance value. The execution of steps I2 to I4 is depicted in Fig. 11.

Defining the Stopping Criteria

To ensure that there are no numerical instabilities developed due to the generation of complex values of the intercalation current density term J_Li, three stopping criteria are defined in the model. Model simulation is terminated at the time instant when the condition defining any of the three stopping criteria is breached. These conditions are defined based on the allowable operating range of the lithium-ion cell for which the FHM model is used to predict its voltage response. The following steps must be implemented to setup and activate these conditions during simulations:

1. Step J1: The first stopping criteria is to ensure that lithium concentration in the anode remains positive at all times during the simulation. A minimum value of $32\ \left[\text{molm}^{-3}\right]$ is chosen, which is approximately 0.1% of the initial anode lithium concentration. Use the right click button on *Definitions* that is located under the *Component 1* icon. Move the cursor to *Component Couplings* and select *Integration* from the available options. Rename the operator name as *Positive_Anode_cs*. Under the source selection tab, select *Boundary* for the geometric entity level, and manually select boundary 2. Under the *Advanced* tab, set the method to *Integration*, the integration order to 4, and the frame to *Spatial (x, y, z)*. This means that the lithium concentration dynamics is monitored at each time instant at the location x = L_neg.

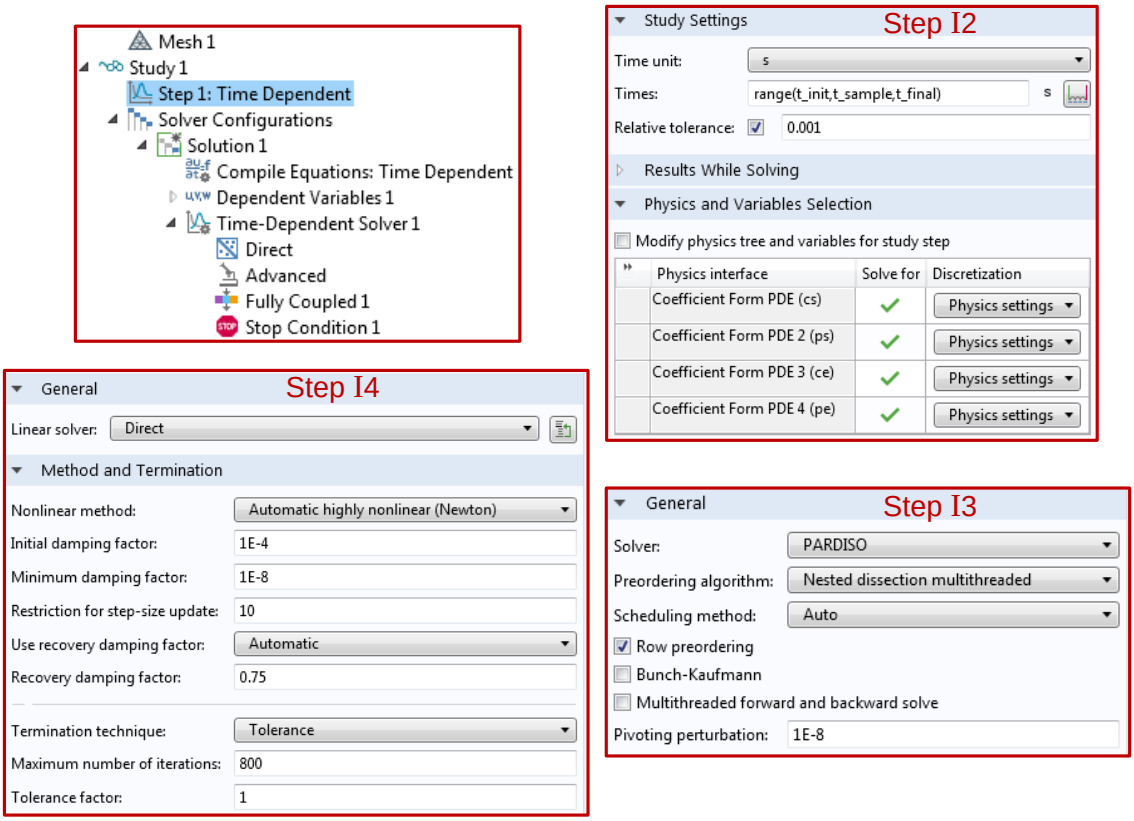

Figure 11: Defining the solver settings to resolve the FHM model variables.

2. Step J2: The second stopping criteria is to ensure that lithium concentration in the cathode does not exceed its maximum storage limit at all times during the simulation. A maximum value of $\left(cs\_\text{pos\_max} - 32\right)$ $\left[\text{molm}^{-3}\right]$ is chosen, which ia approximately 99.9% of the maximum cathode lithium storage limit. Follow the same steps as step J1, but rename the operator name as *Limit_Cathode_cs* and select boundary 3 instead of boundary 2.

3. Step J3: Since the minimum operating voltage limit of the 18650 NMC cell is 2.50 V, the final stopping criteria is to ensure that the model-predicted cell voltage does not drop to lower than 2.50 V during the simulation. Under the *Time-Dependent Solver 1* tab, click on *Direct*. The equation for the model-predicted voltage as a function of time is described in equation (4.9). Since the anode electrostatic potential is constrained to zero, and the electrostatic potential in the cathode is the same at all locations in domain 3, the difference between the cathode electrostatic potential and the term (I_app$\times$R_c) is monitored at each time instant. The same point defined in step J2 can be used to monitor the voltage dynamics.

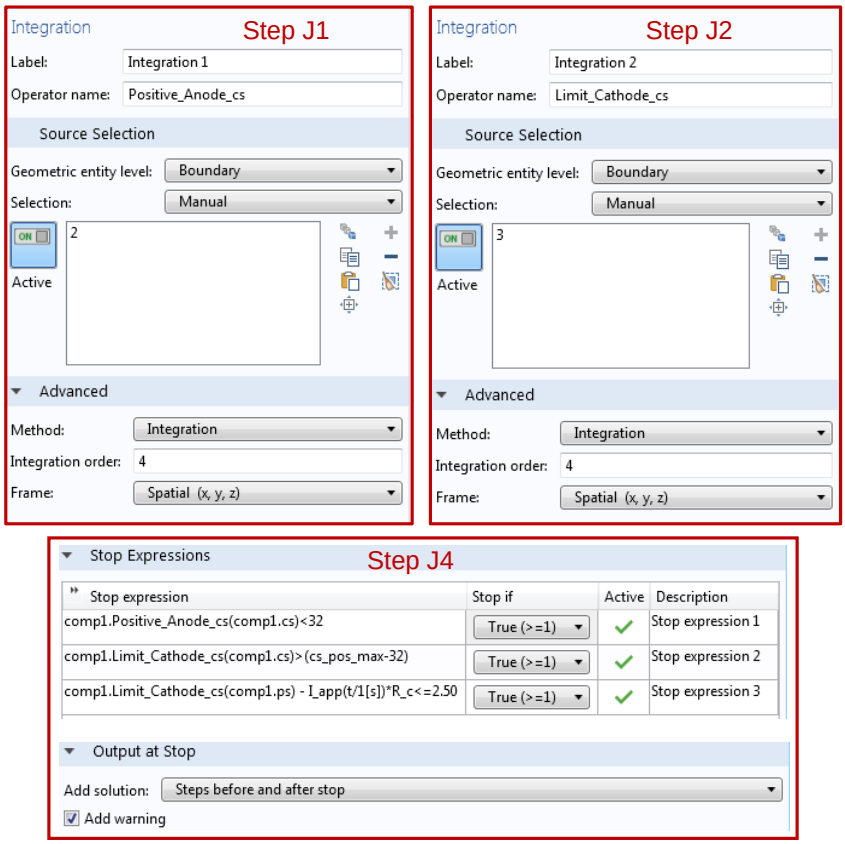

Figure 12: Defining the stopping criteria for the FHM model simulations.

4. Step J4: The final step in this process is to define the three stop conditions. Click on *Stop Condition 1*, depicted earlier in Fig. 11, and define these conditions under *Stop Expressions* as follows:

Stopping Criteria 1	comp1.Positive_Anode_cs(comp1.cs) $<$ 32
Stopping Criteria 2	comp1.Limit_Cathode_cs(comp1.cs) $>$ (cs_pos_max-32)
Stopping Criteria 3	comp1.Limit_Cathode_cs(comp1.ps) - I_app(t/1[s])$\times$R_c $\leq$ 2.50

For each of the stop expressions, set the *Stop If* condition to *True ($\geq$1)* and activate them. Under the *Output at Stop* tab, choose *Steps before and after stop* in order to store the solution of the model simulations until the time instant when a stop condition was violated. Enabling the warning sign indicates the stopping criteria that was violated and the time instant at which it occurred. The execution of steps J1 to J4 is depicted in Fig. 12.

Analysis and Export of Results

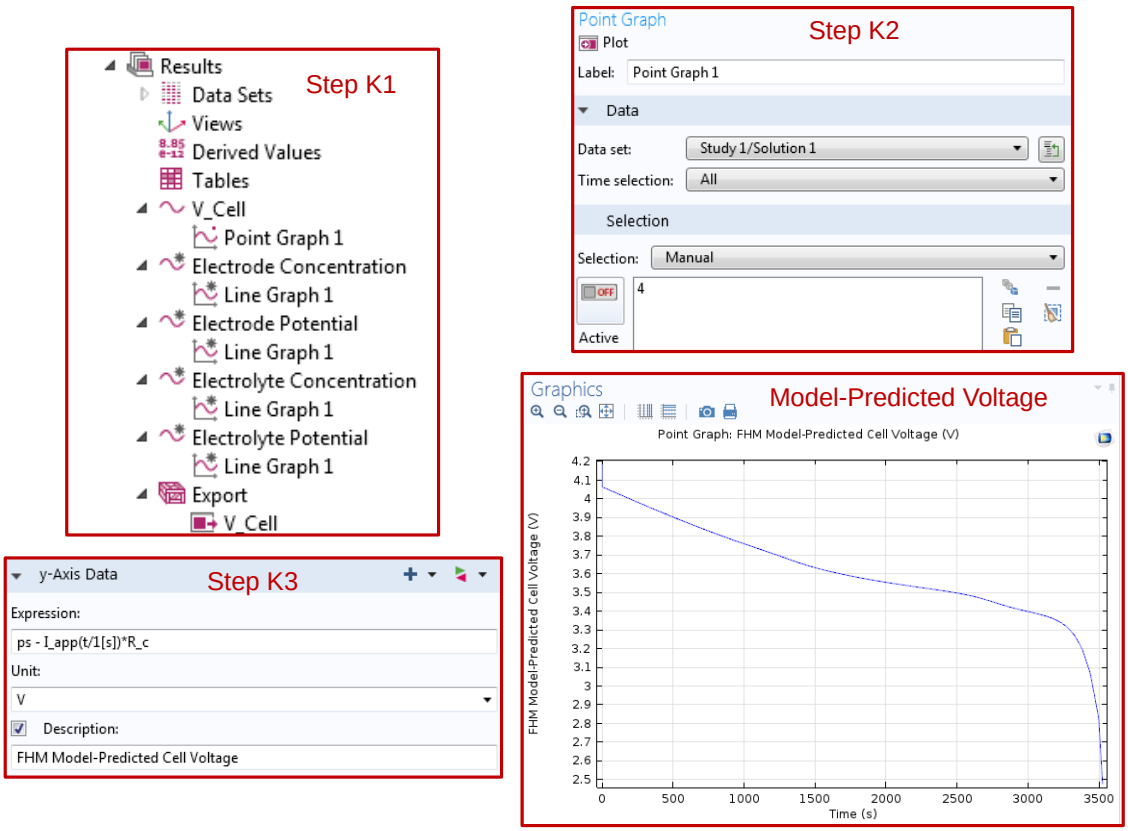

Figure 13: Analysis of the model-predicted voltage at the end of the simulation.

At the end of a simulation, the resolved values of the four model variables as a function of time and their respective domain of resolution are displayed under the *Results* tab. The following steps describe how to analyze the results and export data from the COMSOL environment:

1. Step K1: Use the right click button on the *Results* tab and select *1D Plot Group*. Rename the resulting icon as *V_cell*. Use the right click button on *V_cell* and select *Point Graph*.

2. Step K2: The model-predicted cell voltage is the difference between the cathode electrostatic potential *ps* and the voltage loss at the current collectors, (I_app×R_c). Under *Point Graph*, select the data set *Study 1/Solution 1* that consists of the results from the simulations. Under time selection, choose all the data points from beginning to end of the simulation. Then manually select the location of the cathode current collector, x = L_neg + L_sep + L_pos, which is boundary 4.

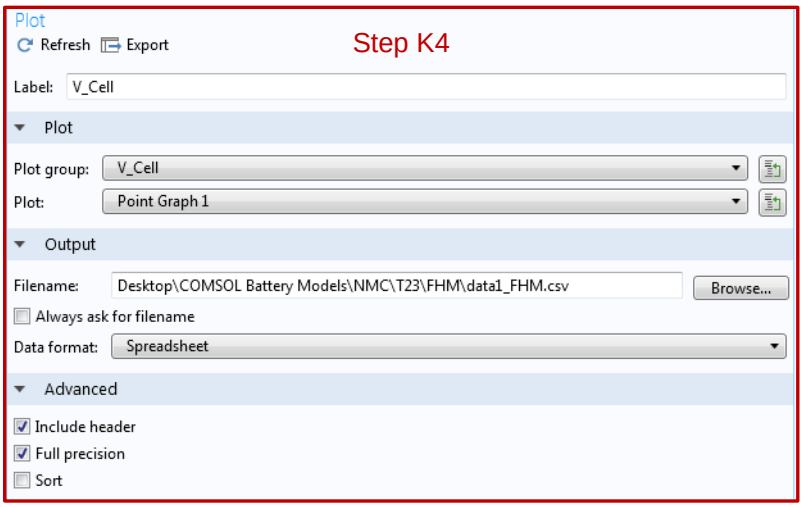

Figure 14: Exporting the FHM model-predicted voltage data from the COMSOL environment.

3. Step K3: Under the *y-Axis Data*, the expression for the model-predicted voltage is provided:

   (ps - I_app(t/1[s])×R_c)

   Under the plot description, type *FHM Model-Predicted Cell Voltage*. Finally, click on the *Plot* icon. The sequence of steps J1 to J3 and the resulting plot are depicted in Fig. 13.

4. Step K4: To export the model-predicted voltage data from the COMSOL platform, start by using the right click button on the *Point Graph* tab located under *V_cell*. Select *Add Plot Data to Export*. The export icon is generated along with a tab for *V_cell*. Under this tab, provide the name of the file, the folder directory where the file must be saved, and the format in which data is saved. Choose the *Spreadsheet* data format from the available options, and click on the *Export* tab located at the top. This will save the data in a .csv file format, and be opened using Microsoft® Excel® software. This step is depicted in Fig. 14.

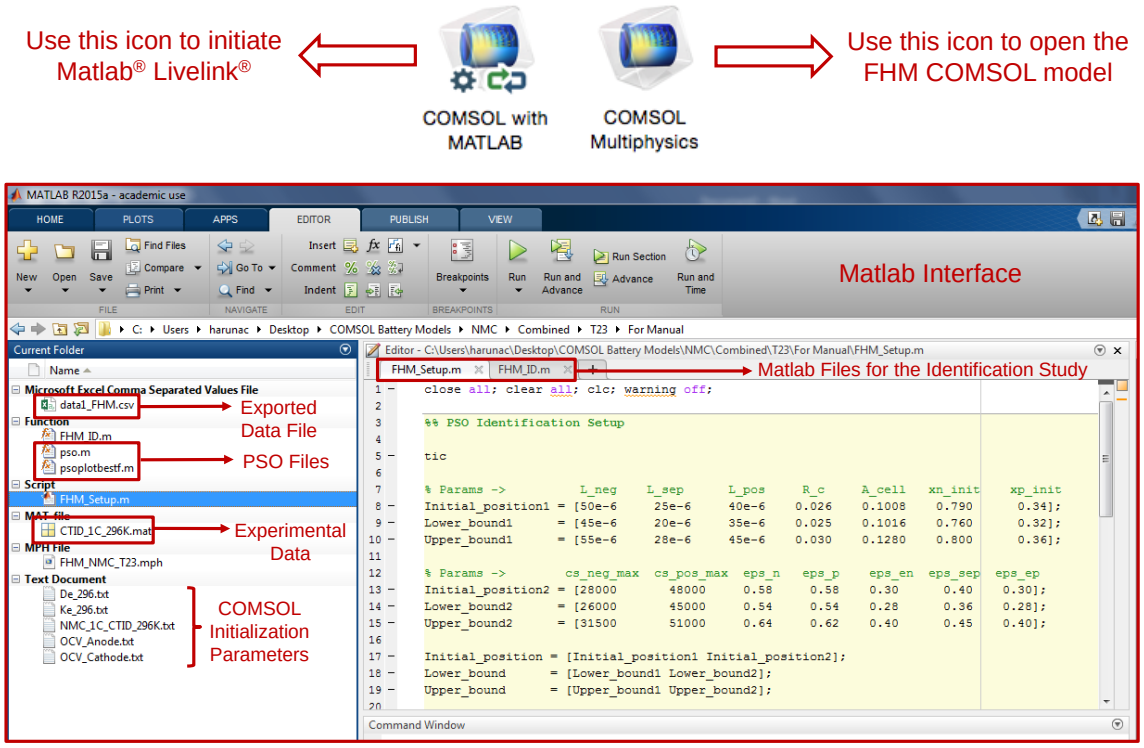

Figure 15: Matlab interface for conducting parameter identification studies using the FHM COMSOL model.

MATLAB® LiveLink™ for Model Parameter Identification

The parameter identification study using the co-simulation framework of COMSOL Multiphysics® and MATLAB®, the MATLAB® LiveLink™ is launched using the *COMSOL with Matlab* icon shown in Fig. 15. This opens the MATLAB interface and initiates communication with the COMSOL interface. The parameter identification study is conducted using the PSO algorithm. As depicted in Fig. 15, all the files required to conduct the parameter identification study must be located in the same folder directory. The following documents are required: a) Script files to execute the PSO algorithm, b) A MATLAB script file FHM_Setup.m to setup the problem for the identification study and a MATLAB function script file FHM_ID.m to run the COMSOL model and evaluate the cost function at the end of each iteration, c) A .mat file containing experimentally measured current, voltage, and time information, d) Text files containing data for the initialization of certain COMSOL parameters, and e) Exported data file from the COMSOL environment that consists of the model-predicted voltage response as a function of time.

The objective of the identification study is to determine the most optimum values of the model parameters that minimize the RMS error between the experimental and model-predicted voltage response as much as possible. The 14 parameters of the FHM COMSOL model are identified in the PSO-based study depicted in Fig. 16. Initial values, and upper and lower bounds are provided for each of these parameters, which specify the range in which these parameters can vary during the iterations. The pso.m script file consists of different options associated with the identification study, and some of them are modified to suit the requirements of the current study. The *swarm* population size is set to 200 and the total number of generations is set to 10. The stall limit indicates the number of successive generations with no change in the cost function, and is used as a criteria to terminate the identification study. The values for the other options depicted in Fig. 16 have been chosen according to [186].

Figures 17 and 18 depict the MATLAB function script file to initialize and simulate the COMSOL model at each iteration, export the model-predicted voltage data from the COMSOL environment and analyze them in MATLAB, evaluate the cost function, and provide the updated set of parameter values for the next iteration. The first step involves loading the experimental data. Then the parameters of the FHM model are initialized in MATLAB. For the very first iteration, the parameter values are selected from the *Initial_Position* vector. For successive iterations, the PSO algorithm provides the parameter values. The FHM COMSOL model is then loaded and initialized through the MATLAB interface. It is not necessary to have the COMSOL model open during identification. The simulation of the COMSOL model for all the iterations is completely controlled from the MATLAB interface. The *model.param.set* feature of LiveLink^{TM} is used to input the corresponding simulation time parameter values and the model parameter values for every iteration.

The *model.study* feature is used to simulate the COMSOL model for one complete run from the initial to the final time of simulation that was defined earlier in the code in Fig. 17. The solver configuration settings for every simulation run is defined using the *model.sol* feature of Livelink^{TM} and has been chosen according to [197]. At the end of the simulation, data is exported from the COMSOL environment in a .csv spreadsheet format using the *model.result.export* feature. This data is analyzed in MATLAB and the model-predicted voltage vector as a function of time is saved in the workspace to calculate the cost function.

For certain values of the model parameters, the predicted voltage can either reach the lower cut-off value of 2.50 V before the final time of simulation, or have a value greater than 2.50 V after the final time of simulation. A penalty function is added to the calculated RMS error in these cases. This ensures that the PSO algorithm optimizes the parameter values such that the model-predicted voltage reaches lower cut-off voltage at time instant (t = t_final). At the end of the parameter identification study, a state.mat MATLAB file

is generated which contains the optimized values of the identified parameters of the FHM model. The results of the parameter identification studies presented in this dissertation are summarized in sections §4.5 and §4.6 of Chapter 4.

```
close all;
clear all;
clc;
warning off;

%% PSO Identification Setup

tic

% Params ->          L_neg    L_sep     L_pos     R_c     A_cell    xn_init    xp_init
Initial_position1    = [50e-6    25e-6    40e-6    0.026    0.1008    0.790      0.34];
Lower_bound1         = [45e-6    20e-6    35e-6    0.025    0.1016    0.760      0.32];
Upper_bound1         = [55e-6    28e-6    45e-6    0.030    0.1280    0.800      0.36];

% Params ->       cs_neg_max    cs_pos_max    eps_n    eps_p    eps_en    eps_sep    eps_ep
Initial_position2    = [28000          48000          0.58      0.58      0.30       0.40       0.30];
Lower_bound2         = [26000          45000          0.54      0.54      0.28       0.36       0.28];
Upper_bound2         = [31500          51000          0.64      0.62      0.40       0.45       0.40];

Initial_position     = [Initial_position1 Initial_position2];
Lower_bound          = [Lower_bound1  Lower_bound2];
Upper_bound          = [Upper_bound1  Upper_bound2];

% Options
options                          = pso;
options.PopulationSize       = 200;
options.PlotFcns             = @psoplotbestf;
options.Display              = 'iter';
options.Vectorized           = 'off';
options.TolFun               = 0.5e-6;
options.Generations          = 10;
options.StallGenLimit        = 10;
options.InitialPopulation    = Initial_position;
options.CognitiveAttraction = 0.3;
options.SocialAttraction     = 3.6;
options.BoundaryMethod     = 'absorb';

% Problem
problem = struct;
problem.fitnessfcn           = @FHM_ID;
problem.nvars                = 14;
problem.lb                   = Lower_bound;
problem.ub                   = Upper_bound;
problem.options              = options;

% Optimization
[x,fval,exitflag,output] = pso(problem);

toc
```

Figure 16: MATLAB code to setup the PSO algorithm for parameter identification.

```
function [ RMS ] = FHM_ID( x )

% Load Experimental Data

load CTID_1C_296K.mat;
V_exp = voltage_296K_1C; % Experimentally measured voltage
time_exp = time_296K_1C;

% Identification Parameters

L_neg          = x(1);
L_sep          = x(2);
L_pos          = x(3);
R_c            = x(4);
A_cell         = x(5);
xn_init        = x(6);
xp_init        = x(7);
cs_neg_max     = x(8);
cs_pos_max     = x(9);
eps_n          = x(10);
eps_p          = x(11);
eps_en         = x(12);
eps_sep        = x(13);
eps_ep         = x(14);

% Load FHM Comsol Model

model = mphload('FHM_NMC_T23.mph');

t_init = 0;
t_sample = 1;
t_final = time_exp(end);

model.param.set('t_init', [num2str(t_init)  '[s]']);
model.param.set('t_final', [num2str(t_final)  '[s]']);
model.param.set('t_sample', [num2str(t_sample)  '[s]']);

% Load Parameters

model.param.set('L_neg', [num2str(L_neg)  '[m]']);
model.param.set('L_sep', [num2str(L_sep)  '[m]']);
model.param.set('L_pos', [num2str(L_pos)  '[m]']);
model.param.set('R_c', [num2str(R_c)  '[ohm]']);
model.param.set('A_cell', [num2str(A_cell)  '[m^2]']);
model.param.set('xn_init', [num2str(xn_init)  '[m/m]']);
model.param.set('xp_init', [num2str(xp_init) '[m/m]']);
model.param.set('cs_neg_max', [num2str(cs_neg_max)  '[mol/m^3]']);
model.param.set('cs_pos_max', [num2str(cs_pos_max)  '[mol/m^3]']);
model.param.set('eps_n', [num2str(eps_n)  '[m/m]']);
model.param.set('eps_p', [num2str(eps_p)  '[m/m]']);
model.param.set('eps_en', [num2str(eps_en)  '[m/m]']);
model.param.set('eps_sep', [num2str(eps_sep)  '[m/m]']);
model.param.set('eps_ep', [num2str(eps_ep)  '[m/m]']);
```

Figure 17: The first part of the MATLAB function code where the FHM COMSOL model and its parameters are defined and initialized.

```
% Run FHM Model

model.study('std1').run;

% Solver Configuration Settings

model.sol('sol1').feature('v1').set('initmethod', 'sol');
model.sol('sol1').feature('v1').set('initsol', 'sol');
model.sol('sol1').feature('v1').set('notsolmethod', 'sol');
model.sol('sol1').feature('v1').set('notsol', 'sol');

% Data Extraction from COMSOL

model.result.export('plot1').run;

filename1 = ['data1_FHM.csv'];
alldata1 = csvread(filename1,8,0);

time_sim = alldata1(:,1);
V_sim = alldata1(:,2); % Model-predicted voltage

% RMS Error Calculation

V_meas = interp1(time_exp,V_exp,time_sim,'linear');
error_V = nansum((V_meas-V_sim).^2);
rms_1 = sum(sqrt(1/(length(time_sim))*error_V));

if V_sim(end)<= 2.50
    err_v = 0;
else
    err_v = 1000;
end

RMS = rms_1 + err_v;

end
```

Figure 18: The second part of the MATLAB function code where the FHM COMSOL model is run and the model-predicted response is analyzed to determine the cost function at the end of the iteration.

Bibliography

[1] M. Hannan, M. Lipu, A. Hussain, and A. Mohamed, "A review of lithium-ion battery state of charge estimation and management system in electric vehicle applications: Challenges and recommendations," *Renewable and Sustainable Energy Reviews*, vol. 78, pp. 834–854, 2017.

[2] A. G. Boulanger, A. C. Chu, S. Maxx, and D. L. Waltz, "Vehicle Electrification: Status and Issues," *Proceedings of the IEEE*, vol. 99, no. 6, pp. 1116–1138, 2011.

[3] B. Guan, R. Zhan, H. Lin, and Z. Huang, "Review of the state-of-the-art of exhaust particulate filter technology in internal combustion engines," *Journal of Environmental Management*, vol. 154, pp. 225–258, 2015.

[4] T. V. Johnson and A. Joshi, "Directions in vehicle efficiency and emissions," *Combustion Engines*, vol. 55, 2016.

[5] H. Wei, T. Zhu, G. Shu, L. Tan, and Y. Wang, "Gasoline engine exhaust gas recirculation–a review," *Applied Energy*, vol. 99, pp. 534–544, 2012.

[6] B. Guan, R. Zhan, H. Lin, and Z. Huang, "Review of state of the art technologies of selective catalytic reduction of no_x from diesel engine exhaust," *Applied Thermal Engineering*, vol. 66, no. 1, pp. 395–414, 2014.

[7] J. Li, L. Zou, F. Tian, X. Dong, Z. Zou, and H. Yang, "Parameter Identification of Lithium-Ion Batteries Model to Predict Discharge Behaviors Using Heuristic Algorithm," *J. Electrochem. Soc*, vol. 163, no. 8, pp. A1646–A1652, 2016.

[8] L. H. Saw, Y. Ye, and A. A. Tay, "Integration issues of lithium-ion battery into electric vehicles battery pack," *Journal of Cleaner Production*, vol. 113, pp. 1032–1045, 2016.

[9] J. F. Peters, M. Baumann, B. Zimmermann, J. Braun, and M. Weil, "The environmental impact of Li-Ion batteries and the role of key parameters–A review," *Renewable and Sustainable Energy Reviews*, vol. 67, pp. 491–506, 2017.

[10] V. Ramadesigan, "Electrochemical-engineering-based models for lithium-ion batteriespast, present, and future," *The Electrochemical Society Interface*, vol. 26, no. 2, pp. 69–71, 2017.

[11] L. Zhang, L. Wang, G. Hinds, C. Lyu, J. Zheng, and J. Li, "Multi-objective optimization of lithium-ion battery model using genetic algorithm approach," *J. Power Sources*, vol. 270, pp. 367–378, 2014.

[12] S. Basu, R. S. Patil, S. Ramachandran, K. S. Hariharan, S. M. Kolake, T. Song, D. Oh, T. Yeo, and S. Doo, "Non-isothermal electrochemical model for lithium-ion cells with composite cathodes," *J. Power Sources*, vol. 283, pp. 132–150, 2015.

[13] M. Xu, Z. Zhang, X. Wang, L. Jia, and L. Yang, "A pseudo three-dimensional electrochemical-thermal model of a prismatic LiFePO4 battery during discharge process," *Energy*, vol. 80, pp. 303–317, 2015.

[14] K. Somasundaram, E. Birgersson, and A. S. Mujumdar, "Model for a bipolar Li-ion battery module: Automated model generation, validation and verification," *Appl. Math. Comput.*, vol. 219, pp. 2231–2245, 2012.

[15] G. M. Goldin, A. M. Colclasure, A. H. Wiedemann, and R. J. Kee, "Three-dimensional particle-resolved models of li-ion batteries to assist the evaluation of empirical parameters in one-dimensional models," *Electrochim. Acta*, vol. 64, pp. 118–129, 2012.

[16] J. Christensen, V. Srinivasan, and J. Newman, "Optimization of lithium titanate electrodes for high-power cells," *J. Electrochem. Soc*, vol. 153, no. 3, pp. A560–A565, 2006.

[17] Q. Sun, Q. Wang, X. Zhao, J. Sun, and Z. Lin, "Numerical study on lithium titanate battery thermal response under adiabatic condition," *Energy Convers. Manage.*, vol. 92, pp. 184–193, 2015.

[18] X. Zhao, B. M. Sánchez, P. J. Dobson, and P. S. Grant, "The role of nanomaterials in redox-based supercapacitors for next generation energy storage devices," *Nanoscale*, vol. 3, no. 3, pp. 839–855, 2011.

[19] R. Padbury and X. Zhang, "Lithium–oxygen batteriesLimiting factors that affect performance," *J. Power Sources*, vol. 196, no. 10, pp. 4436–4444, 2011.

[20] K.-J. Lee, K. Smith, and G.-H. Kim, "Three-Dimensional Thermal-Electrochemical Coupled Model for Spirally Wound Large-Format Lithium-Ion Batteries (Presentation)," tech. rep., National Renewable Energy Laboratory (NREL), Golden, CO., 2011.

[21] C. Sprouse and C. Depcik, "Review of organic Rankine cycles for internal combustion engine exhaust waste heat recovery," *Applied Thermal Engineering*, vol. 51, no. 1, pp. 711–722, 2013.

[22] R. Klein, N. A. Chaturvedi, J. Christensen, J. Ahmed, R. Findeisen, and A. Kojic, "Electrochemical model based observer design for a lithium-ion battery," *IEEE Transactions on Control Systems Technology*, vol. 21, no. 2, pp. 289–301, 2013.

[23] C. Sbarufatti, M. Corbetta, M. Giglio, and F. Cadini, "Adaptive prognosis of lithium-ion batteries based on the combination of particle filters and radial basis function neural networks," *J. Power Soc.*, vol. 344, pp. 128–140, 2017.

[24] D. Bartlett, T. Herman, and A. Klinkman, "Business Models for Extracting More Useful Life From Lithium Ion Battery Systems," master Project, Duke University, 2017.

[25] A. Fotouhi, D. J. Auger, K. Propp, S. Longo, and M. Wild, "A review on electric vehicle battery modelling: From Lithium-ion toward Lithium-Sulphur," *Renewable and Sustainable Energy Reviews*, vol. 56, pp. 1008–1021, 2016.

[26] J. W. Choi and D. Aurbach, "Promise and reality of post-lithium-ion batteries with high energy densities," *Nature Reviews Materials*, vol. 1, p. 16013, 2016.

[27] A. Jha, *Next-generation batteries and fuel cells for commercial, military, and space applications*. CRC Press, 2012.

[28] J. Zhang and J. Lee, "A review on prognostics and health monitoring of li-ion battery," *J. Power Sources*, vol. 196, no. 15, pp. 6007–6014, 2011.

[29] S. Al Hallaj, H. Maleki, J.-S. Hong, and J. R. Selman, "Thermal modeling and design considerations of lithium-ion batteries," *J. Power Sources*, vol. 83, no. 1, pp. 1–8, 1999.

[30] G. Pistoia, *Lithium-ion batteries: advances and applications*. Newnes, 2013.

[31] K. A. Smith, "Electrochemical control of lithium-ion batteries [applications of control]," *IEEE Control Systems*, vol. 30, no. 2, pp. 18–25, 2010.

[32] S. Malifarge, B. Delobel, and C. Delacourt, "Determination of Tortuosity Using Impedance Spectra Analysis of Symmetric Cell," *J. Electrochem. Soc*, vol. 164, no. 11, pp. E3329–E3334, 2017.

[33] A. M. Bizeray, J.-H. Kim, S. R. Duncan, and D. A. Howey, "Identifiability and parameter estimation of the single particle lithium-ion battery model," *arXiv preprint arXiv:1702.02471*, 2017.

[34] L. Zheng, L. Zhang, J. Zhu, G. Wang, and J. Jiang, "Co-estimation of state-of-charge, capacity and resistance for lithium-ion batteries based on a high-fidelity electrochemical model," *Applied Energy*, vol. 180, pp. 424–434, 2016.

[35] M. A. Rahman, S. Anwar, and A. Izadian, "Electrochemical model parameter identification of a lithium-ion battery using particle swarm optimization method," *J. Power Soc.*, vol. 307, pp. 86–97, 2016.

[36] M. Farag, M. Fleckenstein, and S. Habibi, "Continuous piecewise-linear, reduced-order electrochemical model for lithium-ion batteries in real-time applications," *J. Power Soc.*, vol. 342, pp. 351–362, 2017.

[37] J. B. Goodenough and Y. Kim, "Challenges for rechargeable Li batteries," *Chemistry of materials*, vol. 22, no. 3, pp. 587–603, 2009.

[38] J. B. Goodenough and K.-S. Park, "The Li-Ion Rechargeable Battery: A Perspective," *Journal of the American Chemical Society*, vol. 135, no. 4, pp. 1167–1176, 2013.

[39] B. Scrosati, J. Hassoun, and Y.-K. Sun, "Lithium-ion batteries. A look into the future," *Energy & Environmental Science*, vol. 4, no. 9, pp. 3287–3295, 2011.

[40] S. Sripad and V. Viswanathan, "Evaluation of Current, Future, and Beyond Li-Ion Batteries for the Electrification of Light Commercial Vehicles: Challenges and Opportunities," *J. Electrochem. Soc.*, vol. 164, no. 11, pp. E3635–E3646, 2017.

[41] P. G. Bruce, "Energy storage beyond the horizon: Rechargeable lithium batteries," *Solid State Ionics*, vol. 179, no. 21, pp. 752–760, 2008.

[42] J. Bhattacharya and A. Van der Ven, "Phase stability and nondilute Li diffusion in spinel Li_1+xTi_2O_4," *Physical Review B*, vol. 81, no. 10, p. 104304, 2010.

[43] R. Malik, D. Burch, M. Bazant, and G. Ceder, "Particle size dependence of the ionic diffusivity," *Nano Letters*, vol. 10, no. 10, pp. 4123–4127, 2010.

[44] R. T. Purkayastha and R. M. McMeeking, "An integrated 2-D model of a lithium ion battery: the effect of material parameters and morphology on storage particle stress," *Computational Mechanics*, pp. 1–19, 2012.

[45] X. Zhang, W. Shyy, and A. M. Sastry, "Numerical simulation of intercalation-induced stress in Li-ion battery electrode particles," *J. Electrochem. Soc.*, vol. 154, no. 10, pp. A910–A916, 2007.

[46] R. E. Garcia, Y.-M. Chiang, W. C. Carter, P. Limthongkul, and C. M. Bishop, "Microstructural Modeling and Design of Rechargeable Lithium-Ion Batteries," *J. Electrochem. Soc.*, vol. 152, no. 1, pp. A255–A263, 2005.

[47] M. Smith, R. E. Garcia, and Q. C. Horn, "The Effect of Microstructure on the Galvanostatic Discharge of Graphite Anode Electrodes in LiCoO_2-Based Rocking-Chair Rechargeable Batteries," *J. Electrochem. Soc.*, vol. 156, no. 11, pp. A896–A904, 2009.

[48] C.-W. Wang and A. M. Sastry, "Mesoscale modeling of a Li-ion polymer cell," *J. Electrochem. Soc.*, vol. 154, no. 11, pp. A1035–A1047, 2007.

[49] M. Doyle, T. F. Fuller, and J. Newman, "Modeling of Galvanostatic Charge and Discharge of the Lithium/Polymer/Insertion Cell," *J. Electrochem. Soc*, vol. 140, no. 6, pp. 1526–1533, 1993.

[50] C. Y. Wang and W. B. Gu, "Micro-Macroscopic Coupled Modeling of Batteries and Fuel Cells," *J. Electrochem. Soc*, vol. 145, no. 10, pp. 3407–3417, 1998.

[51] S. Whitakera, *The Method of Volume Averaging*. Springer, Netherlands, 1999.

[52] U. Hornung, *Homogenization and Porous Media*. Springer, New York, 1997.

[53] K. Kumaresan, G. Sikha, and R. E. White, "Thermal Model for a Li-Ion Cell," *J. Electrochem. Soc*, vol. 155, no. 2, pp. A164–A171, 2008.

[54] W. Fang, O. J. Kwon, and C.-Y. Wang, "Electrochemical–thermal modeling of automotive li-ion batteries and experimental validation using a three-electrode cell," *International Journal of Energy Research*, vol. 34, no. 2, pp. 107–115, 2010.

[55] K. Smith and C.-Y. Wang, "Power and thermal characterization of a lithium-ion battery pack for hybrid-electric vehicles," *J. Power Sources*, vol. 160, no. 1, pp. 662–673, 2006.

[56] M. Guo and R. E. White, "Thermal Model for Lithium Ion Battery Pack with Mixed Parallel and Series Configuration," *J. Electrochem. Soc*, vol. 158, no. 10, pp. A1166–A1176, 2011.

[57] G.-H. Kim, K. Smith, K.-J. Lee, S. Santhanagopalan, and A. Pesaran, "Multi-Domain Modeling of Lithium-Ion Batteries Encompassing Multi-Physics in Varied Length Scales," *J. Electrochem. Soc*, vol. 158, no. 8, pp. A955–A969, 2011.

[58] B. Y. Liaw, G. Nagasubramanian, R. G. Jungst, and D. H. Doughty, "Modeling of lithium ion cellsA simple equivalent-circuit model approach," *Solid State Ionics*, vol. 175, no. 1, pp. 835–839, 2004.

[59] J. Gomez, R. Nelson, E. E. Kalu, M. H. Weatherspoon, and J. P. Zheng, "Equivalent circuit model parameters of a high-power Li-ion battery: Thermal and state of charge effects," *J. Power Sources*, vol. 196, no. 10, pp. 4826–4831, 2011.

[60] H. He, R. Xiong, and J. Fan, "Evaluation of lithium-ion battery equivalent circuit models for state of charge estimation by an experimental approach," *Energies*, vol. 4, no. 4, pp. 582–598, 2011.

[61] X. Hu, S. Li, and H. Peng, "A comparative study of equivalent circuit models for Li-ion batteries," *J. Power Sources*, vol. 198, pp. 359–367, 2012.

[62] K. A. Smith, C. D. Rahn, and C.-Y. Wang, "Control oriented 1D electrochemical model of lithium ion battery," *Energy Conversion and Management*, vol. 48, no. 9, pp. 2565–2578, 2007.

[63] C. Speltino, D. D. Domenico, G. Fiengo, and A. Stefanopoulou, "Comparison of reduced order lithium-ion battery models for control applications," in *Proceedings of the 48th IEEE Conference on CDC/CCC*, pp. 3276–3281, 2009.

[64] L. Cai and R. E. White, "Reduction of Model Order Based on Proper Orthogonal Decomposition for Lithium-Ion Battery Simulations," *J. Electrochem. Soc*, vol. 156, no. 3, pp. A154–A161, 2009.

[65] T.-S. Dao, C. P. Vyasarayani, and J. McPhee, "Simplification and order reduction of lithium-ion battery model based on porous-electrode theory," *J. Power Sources*, vol. 198, pp. 329–337, 2012.

[66] G. L. Plett, "Battery management system algorithms for HEV battery state-of-charge and state-of-health estimation," *Advanced materials and methods for lithium-ion batteries*, 2007.

[67] M. Rubagotti, S. Onori, and G. Rizzoni, "Automotive battery prognostics using dual Extended Kalman Filter," in *Proceedings of the ASME 2009 Dynamic Systems and Control Conference*, pp. 257–263, 2009.

[68] M. J. Rothenberger, D. J. Docimo, M. Ghanaatpishe, and H. K. Fathy, "Genetic optimization and experimental validation of a test cycle that maximizes parameter identifiability for a Li-ion equivalent-circuit battery model," *Journal of Energy Storage*, vol. 4, pp. 156–166, 2015.

[69] R. Ahmed, J. Gazzarri, S. Onori, S. Habibi, R. Jackey, K. Rzemien, J. Tjong, and J. LeSage, "Model-based parameter identification of healthy and aged li-ion batteries for electric vehicle applications," *SAE International Journal of Alternative Powertrains*, vol. 4, no. 2015-01-0252, pp. 233–247, 2015.

[70] H. Perez, X. Hu, S. Dey, and S. Moura, "Optimal Charging of Li-Ion Batteries with Coupled Electro-Thermal-Aging Dynamics," *IEEE Transactions on Vehicular Technology*, 2017.

[71] X. Lin, H. E. Perez, S. Mohan, J. B. Siegel, A. G. Stefanopoulou, Y. Ding, and M. P. Castanier, "A lumped-parameter electro-thermal model for cylindrical batteries," *J. Power Sources*, vol. 257, pp. 1–11, 2014.

[72] H. E. Perez, J. B. Siegel, X. Lin, A. G. Stefanopoulou, Y. Ding, and M. P. Castanier, "Parameterization and validation of an integrated electro-thermal cylindrical lfp battery model," in *ASME 2012 5th Annual Dynamic Systems and Control Conference, Dynamic Systems and Control Division, ASME*, pp. 41–50, 2012.

[73] X. Lin, A. G. Stefanopoulou, H. E. Perez, J. B. Siegel, Y. Li, and R. D. Anderson, "Quadruple adaptive observer of the core temperature in cylindrical Li-ion batteries and their health monitoring," in *American Control Conference (ACC), 2012*, pp. 578–583, IEEE, 2012.

[74] X. Lin, H. E. Perez, J. B. Siegel, A. G. Stefanopoulou, Y. Li, R. D. Anderson, Y. Ding, and M. P. Castanier, "Online parameterization of lumped thermal dynamics in cylindrical lithium ion batteries for core temperature estimation and health monitoring," *IEEE Transactions on Control Systems Technology*, vol. 21, no. 5, pp. 1745–1755, 2013.

[75] L. Serrao, S. Onori, G. Rizzoni, and Y. Guezennec, "A novel model-based algorithm for battery prognosis," *IFAC Proceedings Volumes*, vol. 42, no. 8, pp. 923–928, 2009.

[76] P. Spagnol, S. Onori, N. Madella, Y. Guezennec, and N. John, "Aging and characterization of li-ion batteries in a hev application for lifetime estimation," in *Adv. Automotive Control, 2010*, pp. 186–191, July 2010.

[77] A. Millner, "Modeling lithium ion battery degradation in electric vehicles," in *Innovative Technologies for an Efficient and Reliable Electricity Supply (CITRES), 2010 IEEE Conference on*, pp. 349–356, IEEE, 2010.

[78] L. Serrao, S. Onori, A. Sciarretta, Y. Guezennec, and G. Rizzoni, "Optimal energy management of hybrid electric vehicles including battery aging," in *American Control Conference (ACC), 2011*, pp. 2125–2130, IEEE, 2011.

[79] S. Onori, G. Rizzoni, and A. Cordoba-Arenas, "A prognostic methodology for interconnected systems: preliminary results," *IFAC Proceedings Volumes*, vol. 45, no. 20, pp. 1125–1130, 2012.

[80] F. Todeschini, S. Onori, and G. Rizzoni, "An experimentally validated capacity degradation model for Li-ion batteries in PHEVs applications," *IFAC Proceedings Volumes*, vol. 45, no. 20, pp. 456–461, 2012.

[81] B. S. Haran, B. N. Popov, and R. E. White, "Determination of the hydrogen diffusion coefficient in metal hydrides by impedance spectroscopy," *J. Power Sources*, vol. 75, no. 1, pp. 56–63, 1998.

[82] D. Zhang, B. N. Popov, and R. E. White, "Modeling lithium intercalation of a single spinel particle under potentiodynamic control," *J. Electrochem. Soc.*, vol. 147, no. 3, pp. 831–838, 2000.

[83] G. Ning and B. N. Popov, "Cycle life modeling of lithium-ion batteries," *J. Electrochem. Soc.*, vol. 151, no. 10, pp. A1584–A1591, 2004.

[84] V. Ramadesigan, P. W. C. Northrop, S. De, S. Santhanagopalan, R. D. Braatz, and V. R. Subramanian, "Modeling and Simulation of Lithium-Ion Batteries from a Systems Engineering Perspective," *J. Electrochem. Soc*, vol. 159, no. 3, pp. R31–R45, 2012.

[85] T. R. Tanim, C. D. Rahn, and C.-Y. Wang, "A temperature dependent, single particle, lithium ion cell model including electrolyte diffusion," *Journal of Dynamic Systems, Measurement, and Control*, vol. 137, no. 1, p. 011005, 2015.

[86] N. Baba, H. Yoshida, M. Nagaoka, C. Okuda, and S. Kawauchi, "Numerical simulation of thermal behavior of lithium-ion secondary batteries using the enhanced single particle model," *J. Power Sources*, vol. 252, pp. 214–228, 2014.

[87] S. Santhanagopalan and R. E. White, "Online estimation of the state of charge of a lithium ion cell," *J. Power Sources*, vol. 161, no. 2, pp. 1346–1355, 2006.

[88] T. R. Tanim, C. D. Rahn, and C. Y. Wang, "State of charge estimation of a lithium ion cell based on a temperature dependent and electrolyte enhanced single particle model," *Energy*, vol. 80, pp. 731–739, 2015.

[89] A. Bartlett, J. Marcicki, S. Onori, G. Rizzoni, X. G. Yang, and T. Miller, "Model-based state of charge estimation and observability analysis of a composite electrode lithium-ion battery," in *Decision and Control (CDC), 2013 IEEE 52nd Annual Conference on*, pp. 7791–7796, IEEE, 2013.

[90] A. Bartlett, J. Marcicki, S. Onori, G. Rizzoni, X. G. Yang, and T. Miller, "Electrochemical model-based state of charge and capacity estimation for a composite electrode lithium-ion battery," *IEEE Transactions on Control Systems Technology*, vol. 24, no. 2, pp. 384–399, 2016.

[91] D. Di Domenico, G. Fiengo, and A. Stefanopoulou, "Lithium-ion battery state of charge estimation with a kalman filter based on a electrochemical model," in *Control Applications, 2008. CCA 2008. IEEE International Conference on*, pp. 702–707, IEEE, 2008.

[92] D. Di Domenico, A. Stefanopoulou, and G. Fiengo, "Lithium-ion battery state of charge and critical surface charge estimation using an electrochemical model-based extended kalman filter," *Journal of Dynamic Systems, Measurement, and Control*, vol. 132, no. 6, p. 061302, 2010.

[93] C. Speltino, D. Di Domenico, G. Fiengo, and A. Stefanopoulou, "Experimental validation of a lithium-ion battery state of charge estimation with an extended kalman filter," in *Control Conference (ECC), 2009 European*, pp. 4828–4833, IEEE, 2009.

[94] C. Speltino, D. Di Domenico, G. Fiengo, and A. Stefanopoulou, "Experimental identification and validation of an electrochemical model of a lithium-ion battery," in *Control Conference (ECC), 2009 European*, pp. 1053–1058, IEEE, 2009.

[95] S. Dey, B. Ayalew, and P. Pisu, "Adaptive observer design for a Li-ion cell based on coupled electrochemical-thermal model," *ASME Paper No. DSCC2014-5986*, 2014.

[96] S. Dey, B. Ayalew, and P. Pisu, "Nonlinear robust observers for state-of-charge estimation of lithium-ion cells based on a reduced electrochemical model," *IEEE Transactions on Control Systems Technology*, vol. 23, no. 5, pp. 1935–1942, 2015.

[97] J. C. Forman, S. Bashash, J. Stein, and H. Fathy, "Reduction of an electrochemistry-based Li-ion battery health degradation model via constraint linearization and Padé approximation," *Ann Arbor*, vol. 1001, p. 48109, 2010.

[98] J. Marcicki, F. Todeschini, S. Onori, and M. Canova, "Nonlinear parameter estimation for capacity fade in lithium-ion cells based on a reduced-order electrochemical model," in *American Control Conference (ACC), 2012*, pp. 572–577, IEEE, 2012.

[99] S. J. Moura, J. C. Forman, J. L. Stein, and H. K. Fathy, "Control of film growth in lithium ion battery packs via switches," in *2009 ASME Dynamic Systems and Control Conference*, 2009.

[100] S. J. Moura, J. C. Forman, S. Bashash, J. L. Stein, and H. K. Fathy, "Optimal control of film growth in lithium-ion battery packs via relay switches," *IEEE Transactions on Industrial Electronics*, vol. 58, no. 8, pp. 3555–3566, 2011.

[101] A. A. Franco, "Multiscale modelling and numerical simulation of rechargeable lithium ion batteries: concepts, methods and challenges," *RSC Adv.*, vol. 3, pp. 13027–13058, 2013.

[102] P. W. Northrop, M. Pathak, D. Rife, S. De, S. Santhanagopalan, and V. R. Subramanian, "Efficient simulation and model reformulation of two-dimensional electrochemical thermal behavior of lithium-ion batteries," *J. Electrochem. Soc.*, vol. 162, no. 6, pp. A940–A951, 2015.

[103] L. Terborg, S. Weber, F. Blaske, S. Passerini, M. Winter, U. Karst, and S. Nowak, "Investigation of thermal aging and hydrolysis mechanisms in commercial lithium ion battery electrolyte," *J. Power Sources*, vol. 242, pp. 832–837, 2013.

[104] B. Stiaszny, J. C. Ziegler, E. E. Krauß, J. P. Schmidt, and E. Ivers-Tiffée, "Electrochemical characterization and post-mortem analysis of aged LiMn_2O_4–Li (Ni_0.5 Mn_0.3 Co_0.2) o_2/graphite lithium ion batteries. Part i: Cycle aging," *J. Power Sources*, vol. 251, pp. 439–450, 2014.

[105] B. Stiaszny, J. C. Ziegler, E. E. Krauß, M. Zhang, J. P. Schmidt, and E. Ivers-Tiffée, "Electrochemical characterization and post-mortem analysis of aged LiMn_2O_4–NMC/graphite lithium ion batteries part II: Calendar aging," *J. Power Sources*, vol. 258, pp. 61–75, 2014.

[106] M. Grützke, V. Kraft, B. Hoffmann, S. Klamor, J. Diekmann, A. Kwade, M. Winter, and S. Nowak, "Aging investigations of a lithium-ion battery electrolyte from a field-tested hybrid electric vehicle," *J. Power Sources*, vol. 273, pp. 83–88, 2015.

[107] N. Balke, S. Jesse, A. Morozovska, E. Eliseev, D. Chung, Y. Kim, L. Adamczyk, R. Garcia, N. Dudney, and S. Kalinin, "Nanoscale mapping of ion diffusion in a lithium-ion battery cathode," *Nature Nanotechnology*, vol. 5, no. 10, pp. 749–754, 2010.

[108] R. García-García and R. E. García, "Microstructural effects on the average properties in porous battery electrodes," *J. Power Sources*, vol. 309, pp. 11–19, 2016.

[109] M. B. Pinson and M. Z. Bazant, "Theory of SEI Formation in Rechargeable Batteries: Capacity Fade, Accelerated Aging and Lifetime Prediction," *J. Electrochem. Soc*, vol. 160, no. 2, pp. A243–A250, 2013.

[110] R. Narayanrao, M. M. Joglekar, and S. Inguva, "A Phenomenological Degradation Model for Cyclic Aging of Lithium Ion Cell Materials," *J. Electrochem. Soc*, vol. 160, no. 1, pp. A125–A137, 2013.

[111] M. Safari, M. Morcrette, A. Teyssot, and C. Delacourt, "Multimodal Physics-Based Aging Model for Life Prediction of Li-Ion Batteries," *J. Electrochem. Soc*, vol. 156, no. 3, pp. A145–A153, 2009.

[112] S. K. Rahimian, S. C. Rayman, and R. E. White, "Maximizing the Life of a Lithium-Ion Cell by Optimization of Charging Rates," *J. Electrochem. Soc*, vol. 157, no. 12, pp. A1302–A1308, 2010.

[113] F. Ciucci and W. Lai, "Derivation of Micro/Macro Lithium Battery Models from Homogenization," *Transp. Porous Media*, vol. 88, no. 2, pp. 249–270, 2011.

[114] Y. Davit, C. G. Bell, H. M. Byrne, L. A. C. Chapman, L. S. Kimpton, G. E. Lang, K. H. L. Leonard, J. M. Oliver, N. C. Pearson, R. J. Shipley, S. L. Waters, J. P. Whiteley, B. D. wood, and M. Quintard, "Homogenization via formal multiscale asymptotics and volume averaging: How do the two techniques compare?," *Adv. Water Resour.*, vol. 62, pp. 178–206, 2013.

[115] A. Salvadori, E. Bosco, and D. Grazioli, "A computational homogenization approach for Li-ion battery cells: Part 1 formulation," *J. Mech. Phys. Solids*, vol. 65, pp. 114–137, 2014.

[116] A. Vadakkepatt, B. Trembacki, S. R. Mathur, and Y. J. Murthy, "Bruggeman's exponents for effective thermal conductivity of lithium-ion battery electrodes," *J. Electrochem. Soc*, vol. 163, no. 2, pp. A119–A130, 2016.

[117] J. Newman and K. E. Thomas-Alyea, *Electrochemical Systems*. John Wiley & Sons, 2012.

[118] S. Onori, P. Spagnol, V. Marano, Y. Guezennec, and G. Rizzoni, "A new life estimation method for lithium-ion batteries in plug-in hybrid electric vehicles applications," *Int. J. Power Electronics*, vol. 4, no. 3, pp. 302–319, 2012.

[119] K. E. Thomas and J. Newman, "Thermal Modeling of Porous Insertion Electrodes," *J. Electrochem. Soc*, vol. 150, no. 2, pp. A176–A192, 2003.

[120] H. J. Ploehn, P. Ramadass, and R. E. White, "Solvent Diffusion Model for Aging of Lithium-Ion Battery Cells," *J. Electrochem. Soc*, vol. 151, no. 3, pp. A456–A462, 2004.

[121] A. J. Smith, A. C. Burns, X. Zhao, D. Xiong, and J. R. Dahn, "A High Precision Coulometry Study of the SEI Growth in Li/Graphite Cells," *J. Electrochem. Soc*, vol. 158, no. 5, pp. A447–A452, 2011.

[122] M. B. Pinson and M. Z. Bazant, "Theory of SEI Formation in Rechargeable Batteries: Capacity Fade, Accelerated Aging and Lifetime Prediction," *J. Electrochem. Soc*, vol. 160, no. 2, pp. A243–A250, 2013.

[123] J. L. Lee, A. Chemistruck, and G. L. Plett, "One-dimensional physics-based reduced-order model of lithium-ion dynamics," *J. Power Sources*, vol. 220, pp. 430–448, 2012.

[124] S. K. Rahimian, S. Rayman, and R. E. White, "Extension of physics-based single particle model for higher charge–discharge rates," *J. Power Sources*, vol. 224, pp. 180–194, 2013.

[125] M. Torchio, L. Magni, R. B. Gopaluni, R. D. Braatz, and D. M. Raimondo, "Lionsimba: A Matlab Framework Based on a Finite Volume Model Suitable for Li-Ion Battery Design, Simulation, and Control," *J. Electrochem. Soc.*, vol. 163, no. 7, pp. A1192–A1205, 2016.

[126] S. J. Moura, F. B. Argomedo, R. Klein, A. Mirtabatabaei, and M. Krstic, "Battery state estimation for a single particle model with electrolyte dynamics," *IEEE Transactions on Control Systems Technology*, vol. 25, no. 2, pp. 453–468, 2017.

[127] W. F. Fang, O. J. Kwon, C. Y. Wang, and Y. Ishikawa, "Modeling of Li-ion battery performance in hybrid electric vehicles," *SAE International Journal of Passenger Cars-Electronic and Electrical Systems*, vol. 2, no. 2009-01-1388, pp. 418–423, 2009.

[128] J. Smekens, J. Paulsen, W. Yang, N. Omar, J. Deconinck, A. Hubin, and J. V. Mierlo, "A Modified Multiphysics model for lithium-ion batteries with a $Li_xNi_{1/3}Mn_{1/3}Co_{1/3}O_2$ electrode," *Electrochimica Acta*, vol. 174, pp. 615–624, 2015.

[129] P. R. Shearing, L. E. Howard, P. S. Jørgensen, N. P. Brandon, and S. J. Harris, "Characterization of the 3-dimensional microstructure of a graphite negative electrode from a Li-ion battery," *Electrochemistry Communications*, vol. 12, no. 3, pp. 374–377, 2010.

[130] J. R. Wilson, J. S. Cronin, S. A. Barnett, and S. J. Harris, "Measurement of three-dimensional microstructure in a $LiCoO_2$ positive electrode," *J. Power Sources*, vol. 196, pp. 3443–3447, 2011.

[131] B. Vijayaraghavan, D. R. Ely, Y.-M. Chiang, R. G. Garcia, and R. E. Garcia, "An analytical method to determine tortuosity in rechargeable battery electrodes," *J. Electrochem. Soc*, vol. 159, no. 5, pp. A548–A552, 2012.

[132] W. Lai and F. Ciucci, "Mathematical modeling of porous battery electrodesRevisit of Newman's model," *Electrochim. Acta*, vol. 56, no. 11, pp. 4369–4377, 2011.

[133] I. Battiato and D. M. Tartakovsky, "Applicability regimes for macroscopic models of reactive transport in porous media," *J. Contam. Hydrol.*, vol. 120-121, pp. 18–26, 2011.

[134] Y. Efendiev, O. Iliev, and V. Taralova, *Upscaling of an isothermal Li-ion battery model via the Homogenization Theory*. Fraunhofer Inst. für Techno-und Wirtschaftsmathematik, ITWM, 2013.

[135] J. Newman and W. Tiedemann, "Porous-Electrode Theory with Battery Applications," *AIChE J.*, vol. 21, no. 1, pp. 25–41, 1975.

[136] A. Latz and J. Zausch, "Thermodynamic consistent transport theory of Li-ion batteries," *J. Power Sources*, vol. 196, no. 6, pp. 3296–3302, 2011.

[137] E. Martinez-Rosas, R. Vasquez-Medrano, and A. Flores-Tlacuahuac, "Modeling and simulation of lithium-ion batteries," *Comput. Chem. Eng.*, vol. 35, no. 9, pp. 1937–1948, 2011.

[138] G. B. Less, J. H. Seo, S. Han, A. M. Sastry, J. Zausch, A. Latz, S. Schmidt, C. Wieser, D. Kehrwald, and S. Fell, "Micro-Scale Modeling of Li-Ion Batteries: Parameterization and Validation," *J. Electrochem. Soc*, vol. 159, no. 6, pp. A697–A704, 2012.

[139] J. Smekens, J. Paulsen, W. Yang, N. Omar, J. Deconinck, A. Hubin, and J. Van Mierlo, "A Modified Multiphysics model for lithium-ion batteries with a Li_x Ni_1/3 Mn_1/3 Co_1/3 o_2 electrode," *Electrochim. Acta*, vol. 174, pp. 615–624, 2015.

[140] A. H. Wiedemann, G. M. Goldin, S. A. Barnett, H. Zhu, and R. J. Kee, "Effects of three-dimensional cathode microstructure on the performance of lithium-ion battery cathodes," *Electrochim. Acta*, vol. 88, pp. 580–588, 2013.

[141] C. Taborelli, S. Onori, S. Maes, P. Sveum, S. Al-Hallaj, and N. Al-Khayat, "Advanced battery management system design for SOC/SOH estimation for e-bikes applications," in *International Journal of Powertrains, 2015 to appear*, p. to appear, May 2015.

[142] S. J. Moura, N. A. Chaturvedi, and M. Krstic, "Adaptive Partial Differential Equation Observer for Battery State-of-Charge/State-of-Health Estimation Via an Electrochemical Model," *J. Dyn. Sys., Meas., Control*, vol. 136, no. 1, 2013.

[143] D.-W. Chung, M. Enber, D. R. Ely, V. Wood, and R. E. Garcia, "Validity of the Bruggeman relation for porous electrodes," *Modelling and Simulation in Materials Science and Engineering*, vol. 21, no. 7, p. 074009, 2013.

[144] X. Zhang and D. M. Tartakovsky, "Effective Ion Diffusion in Charged Nanoporous Materials," *J. Electrochem. Soc*, vol. 164, no. 4, pp. E53–E61, 2017.

[145] D. S. McLachlan, J. H. Hwang, and T. O. Mason, "Evaluating Dielectric Impedance Spectra using Effective Media Theories," *J. Electroceram.*, vol. 5, no. 1, pp. 37–51, 2000.

[146] "The openFOAM Foundation." `http://www.openfoam.org/`. Accessed: 2017.

[147] L. Zhang, L. Wang, G. Hinds, C. Lyu, J. Zheng, and J. Li, "Multi-objective optimization of lithium-ion battery model using genetic algorithm approach," *J. Power Sources*, vol. 270, pp. 367–378, 2014.

[148] M. Ebner, D. W. Chung, R. E. Garcia, and V. Wood, "Tortuosity Anisotropy in Lithium-Ion Battery Electrodes," *Advanced Energy Materials*, vol. 4, no. 5, 2014.

[149] S. J. Moura, , N. A. Chaturvedi, and M. Krstic, "Pde estimation techniques for advanced battery management systems - part i: Soc estimation," in *American Control Conference (ACC), 2012*, pp. 559–565, June 2012.

[150] S. J. Moura, , N. A. Chaturvedi, and M. Krstic, "Pde estimation techniques for advanced battery management systems - part ii: Soh identification," in *American Control Conference (ACC), 2012*, pp. 566–571, June 2012.

[151] N. A. Chaturvedi, R. Klein, J. Christensen, J. ahmed, and A. Kojic, "Algorithms for Advanced Battery-Management Systems," *IEEE Control Syst. Mag.*, vol. 30, no. 3, pp. 49–68, 2010.

[152] S. Santhanagopalan, Q. Guo, P. Ramadass, and R. White, "Review of models for predicting the cycling performance of lithium ion batteries," *J. Power Sources*, vol. 156, no. 2, pp. 620–628, 2006.

[153] P. Albertus, J. Christensen, and J. Newman, "Experiments on and Modeling of Positive Electrodes with Multiple Active Materials for Lithium-Ion Batteries," *J. Electrochem. Soc*, vol. 156, no. 7, pp. A606–A618, 2009.

[154] L. Cai and R. E. White, "An Efficient ElectrochemicalThermal Model for a Lithium-Ion Cell by Using the Proper Orthogonal Decomposition method," *J. Electrochem. Soc*, vol. 157, no. 11, pp. A1188–A1195, 2010.

[155] S.-C. Chen, Y.-Y. Wang, and C.-C. Wang, "Thermal Analysis of Spirally Wound Lithium Batteries," *J. Electrochem. Soc*, vol. 153, no. 4, pp. A637–A648, 2006.

[156] N. Baba, H. Yoshida, M. Nagaoka, C. Okuda, and S. Kawauchi, "Numerical simulation of thermal behavior of lithium-ion secondary batteries using the enhanced single particle model," *J. Power Sources*, vol. 252, pp. 214–228, 2014.

[157] Y. Ye, Y. Shi, and A. A. O. Tay, "Electro-thermal cycle life model for lithium iron phosphate battery," *J. Power Sources*, vol. 217, pp. 509–518, 2012.

[158] M. Guo, G. Sikha, and R. E. White, "Single-Particle Model for a Lithium-Ion Cell: Thermal Behavior," *J. Electrochem. Soc*, vol. 158, no. 2, pp. A122–A132, 2011.

[159] P. Gambhire, N. Ganesan, S. Basu, K. S. Hariharan, S. M. Kolake, T. Song, D. Oh, T. Yeo, and S. Doo, "A reduced order electrochemical thermal model for lithium ion cells," *J. Power Sources*, vol. 290, pp. 87–101, 2015.

[160] G. Ning and B. N. Popov, "Cycle Life Modeling of Lithium-Ion Batteries," *J. Electrochem. Soc*, vol. 151, no. 10, pp. A1584–A1591, 2004.

[161] J. Park, J. H. Seo, G. Plett, W. Lu, and A. M. Sastry, "Numerical Simulation of the Effect of the Dissolution of LiMn2O4 Particles on Li-Ion Battery Performance," *J. Electrochem. Soc*, vol. 14, no. 2, pp. A14–A18, 2011.

[162] L. O. Valoen and J. N. Reimers, "Transport Properties of LiPF6-Based Li-Ion Battery Electrolytes," *J. Electrochem. Soc*, vol. 152, no. 5, pp. A882–A891, 2005.

[163] M. Tang, P. Albertus, and J. Newman, "Two-Dimensional Modeling of Lithium Deposition during Cell Charging," *Journal of the Electrochemical Society*, 2009.

[164] G. F. Kennell and R. W. Evitts, "Two-Dimensional Lithium-Ion Battery Modeling with Electrolyte and Cathode Extensions," *Advances in Chemical Engineering and Science*, 2012.

[165] C.-W. Wang and A. M. Sastry, "Mesoscale Modeling of a Li-Ion Polymer Cell," *Journal of the Electrochemical Society*, 2007.

[166] S. Mazumder and J. Lu, "Faster-Than-Real-Time Simulation of Lithium Ion Batteries with Full Spatial and Temporal Resolution," *International Journal of Electrochemistry*, 2013.

[167] P. Gambhire, K. S. Hariharan, A. Khandelwal, S. M. Kolake, T. Yeo, and S. Doo, "A physics based reduced order aging model for lithium-ion cells with phase change," *Journal of Power Sources*, 2014.

[168] J. Marcicki, *Modeling, Parametrization, and Diagnostics for Lithium-Ion Batteries with Automotive Applications*. PhD thesis, The Ohio State University, 2012.

[169] T. R. Jou, K. Xu, O. Borodin, and M. Ue, *Electrolytes for Lithium and Lithium-Ion Batteries*. Springer, Newyork, 2014.

[170] A. Nyman, M. Behm, and G. Lindbergh, "Electrochemical characterisation and modelling of the mass transport phenomena in $LiPF_6$–EC–EMC electrolyte," *Electrochimica Acta*, 2008.

[171] E. Prada, D. D. Domenico, Y. Creff, J. Bernard, V. Sauvant-Moynot, and F. Huet, "Simplified Electrochemical and Thermal Model of $LiFePO_4$-Graphite Li-Ion Batteries for Fast Charge Applications," *Journal of the Electrochemical Society*, 2012.

[172] U. Kumar, A. K. Metya, N. Ramakrishnan, and J. K. Singh, "A Study of Transport Properties and Stress Analysis Using Atomistic and Macro Simulations for Lithium-ion batteries," *J. Electrochem. Soc.*, vol. 161, no. 9, pp. A1453–A1460, 2014.

[173] S. Tippmann, D. Walper, L. Balboa, B. Spier, and W. G. Bessler, "Low-temperature charging of lithium-ion cells part I: Electrochemical modeling and experimental investigation of degradation behavior," *Journal of Power Sources*, 2014.

[174] M. Takahashi, S. Tobishima, K. Takei, and Y. Sakurai, "Reaction behavior of $LiFePO_4$ as a cathode material for rechargeable lithium batteries," *Solid State Ionics*, 2002.

[175] G. Sikha, R. E. White, and B. N. Popov, "A Mathematical Model for a Lithium-Ion Battery/Electrochemical Capacitor Hybrid System," *Journal of the Electrochemical Society*, 2005.

[176] X.-Y. Qiu, Q.-C. Zhuang, Q.-Q. Zhang, R. Cao, P.-Z. Ying, Y.-H. Qiang, and S.-G. Sun, "Electrochemical and electronic properties of $LiCoO_2$ cathode investigated by galvanostatic cycling and EIS," *Physical Chemistry Chemical Physics*, 2012.

[177] E. Prada, D. D. Domenico, Y. Creff, J. Bernard, V. S-Moynot, and F. Huet, "A Simplified Electrochemical and Thermal Aging Model of LiFePO4-Graphite Li-ion Batteries: Power and Capacity Fade Simulations," *J. Electrochem. Soc*, vol. 160, no. 4, pp. A616–A628, 2013.

[178] A. C. Arenas, S. Onori, Y. Guezennec, and G. Rizzoni, "Capacity and power fade cycle-life model for plug-in hybrid electric vehicle lithium-ion battery cells containing blended spinel and layered-oxide positive electrodes," *J. Power Sources*, vol. 278, pp. 473–483, 2015.

[179] K. Kumaresan, Q. Guo, P. Ramadass, and R. E. White, "Cycle life performance of lithium-ion pouch cells," *J. Power Sources*, vol. 158, pp. 679–688, 2006.

[180] Y. Ye, Y. Shi, and A. A. O. Tay, "Electro-thermal cycle life model for lithium iron phosphate battery," *J. Power Sources*, vol. 217, pp. 509–518, 2012.

[181] P. Gambhire, K. S. Hariharan, A. Khandelwal, S. M. Kolake, T. Yeo, and S. Doo, "A physics based reduced order aging model for lithium-ion cells with phase change," *J. Power Sources*, vol. 270, pp. 281–291, 2014.

[182] J. Park, J. H. Seo, G. Plett, W. Lu, and A. M. Sastry, "Numerical Simulation of the Effect of the Dissolution of LiMn2O4 Particles on Li-Ion Battery Performance," *J. Electrochem. Soc*, vol. 14, no. 12, pp. A14–A18, 2011.

[183] G. L. Plett, *Battery Management Systems, Volume I: Battery Modeling*. Artech House, 2015.

[184] W. Du, N. Xue, W. Shyy, and J. R. R. A. Martins, "A Surrogate-Based Multi-Scale Model for Mass Transport and Electrochemical Kinetics in Lithium-Ion Battery Electrodes," *J. Electrochem. Soc*, vol. 161, no. 8, pp. E3086–E3096, 2014.

[185] H. Arunachalam, S. Onori, and I. Battiato, "On Veracity of Macroscopic Lithium-Ion Battery Models," *J. Electrochem. Soc*, vol. 162, no. 10, pp. A1940–A1951, 2015.

[186] S. Ebbesen, P. Kiwitz, and L. Guzzella, "A generic particle swarm optimization matlab function," in *Proceedings of the American Control Conference (ACC)*, pp. 1519–1524, IEEE, 2012.

[187] N. Chakraborti, R. Jayakanth, S. Das, E. D. Çalişir, and Ş. Erkoç, "Evolutionary and Genetic Algorithms applied to Li^{+}-C System: Calculations Using Differential Evolution and Particle Swarm Algorithm," *Journal of Phase Equilibria and Diffusion*, vol. 28, pp. 140–149, 2007.

[188] J. C. Forman, S. J. Moura, J. L. Stein, and H. K. Fathy, "Genetic identification and fisher identifiability analysis of the Doyle-Fuller-Newman model from experimental cycling of a LiFePO_4 cell," *J. Power Sources*, vol. 210, pp. 263–275, 2012.

[189] M. Charkhgard and M. Farrokhi, "State-of-charge estimation for lithium-ion batteries using neural networks and EKF," *IEEE Transactions on Industrial Electronics*, vol. 57, no. 12, pp. 4178–4187, 2010.

[190] J. Xu, C. C. Mi, B. Cao, J. Deng, Z. Chen, and S. Li, "The state of charge estimation of lithium-ion batteries based on a proportional-integral observer," *IEEE Transactions on Vehicular Technology*, vol. 63, no. 4, pp. 1614–1621, 2014.

[191] M. Doyle and J. Newman, "The use of Mathematical Modeling in the design of Lithium/Polymer Battery Systems," *Electrochim. Acta*, vol. 40, no. 13-14, pp. 2191–2196, 1995.

[192] V. R. Subramanian, D. Tapriyal, and R. E. White, "A boundary condition for porous electrodes," *Electrochemical and Solid-State Letters*, vol. 7, no. 9, pp. A259–A263, 2004.

[193] L. Cai and R. E. White, "Reduction of model order based on proper orthogonal decomposition for lithium-ion battery simulations," *J. Electrochem. Soc.*, vol. 156, no. 3, pp. A154–A161, 2009.

[194] J. C. Forman, S. Bashash, J. L. Stein, and H. K. Fathy, "Reduction of an Electrochemistry-Based Li-Ion Battery Model via Quasi-Linearization and Pade Approximation," *J. Electrochem. Soc*, vol. 158, no. 2, pp. A93–A101, 2011.

[195] J. L. Auriault and P. M. Adler, "Taylor dispersion in porous media: Analysis by multiple scale expansions," *Adv. Water Resour.*, vol. 18, no. 4, pp. 217–226, 1995.

[196] Y. Efendiev, O. Iliev, and V. Taralova, "Upscaling of an isothermal Li-ion battery model via the Homogenization Theory," *Scientific Report of Fraunhofer ITWM*, vol. 230, 2013.

[197] A. COMSOL, "Livelink for matlab user's guide," *Part Number CM020008*, 2014.

[198] D. Kern and N. Framke, "Automation of comsol multiphysics parameter studies using the matlab livelink, 2012," 2014.

[199] "Solutions to Linear Systems of Equations: Direct and Iterative Solvers." `https://www.comsol.com/blogs/solutions-linear-systems-equations-direct-iterative-solvers/`. Accessed: 2017-10-21.